



HAL
open science

Activity and morphology of neuronal cultures: a study on spatio-temporal patterns of activity in neuronal networks and neurons morphology in 2D cultures

Mallory Dazza

► **To cite this version:**

Mallory Dazza. Activity and morphology of neuronal cultures: a study on spatio-temporal patterns of activity in neuronal networks and neurons morphology in 2D cultures. *Neurons and Cognition* [q-bio.NC]. Université Paris Cité, 2021. English. NNT: 2021UNIP7116 . tel-03724888

HAL Id: tel-03724888

<https://theses.hal.science/tel-03724888>

Submitted on 15 Jul 2022

HAL is a multi-disciplinary open access archive for the deposit and dissemination of scientific research documents, whether they are published or not. The documents may come from teaching and research institutions in France or abroad, or from public or private research centers.

L'archive ouverte pluridisciplinaire **HAL**, est destinée au dépôt et à la diffusion de documents scientifiques de niveau recherche, publiés ou non, émanant des établissements d'enseignement et de recherche français ou étrangers, des laboratoires publics ou privés.



Université de Paris

Thèse de doctorat de l'Université de Paris
De l'École Doctorale **Physique en Île-de-France** (ED 564)
Collaboration **Lab. Matière & Systèmes Complexes - Institut Curie**

Thèse de Doctorat de Physique

Activity and morphology of neuronal cultures

A study on spatio-temporal patterns of activity in neuronal networks and neurons morphology in 2D cultures

Par *Mallory Dazza*

Dirigée par
Pr. Samuel Bottani
Dr. Catherine Villard

Co-encadrée par
Dr. Pascal Monceau
Dr. Stéphane Métens

Soutenue publiquement le 22 Juillet 2021 devant un jury composé de

Pr. Lucilla DE ARCANGELIS	Università Luigi Vanvitelli	Rapporteur
Dr. Païkan MARCAGGI	Université Aix-Marseille	Rapporteur
Dr. Alain DESTEXHE	Université Paris-Saclay	Examineur
Dr. Anna LEVINA	Universität Tübingen	Examineur
Dr. Julien DERR	Université de Paris	Examineur
Pr. Samuel BOTTANI	Université de Paris	Directeur
Dr. Catherine VILLARD	Université Paris Sciences & Lettres	Co-directeur



Cette thèse est placée sous licence [Creative Commons](https://creativecommons.org/licenses/by-nc-nd/4.0/)

Summary

The goal of my thesis is to understand the relationship between neuronal network structures and spatio-temporal dynamics of neurons' activity, either recorded in vitro, or simulated with mathematical models. My work focuses on neuronal cultures, as these experimental set-ups are increasingly studied in technical applications, but lack detailed theoretical characterisation and understanding.

The theoretical modeling involves two levels of interests: the activity and the establishment of connections in neuronal cultures. I was interested in two different models of activity: the static quorum percolation model and the dynamical adaptive exponential integrate and fire. Network connectome of neuronal culture is taken into account with a network embedded in the two-dimensional space. I investigate the phase transition of the Quorum Percolation Model and identify a transition between 2 types of propagating dynamics. With a phase specifically designed to investigate neuronal activity, I propose a novel method to analyse and identify the periodic bursting regime both in time and space. This analysis reveals specific characteristics of bursting initiation that help us in the understanding of the fundamental principles that relate the spatial network and the collective neuronal activity.

The second part of my thesis is experimental: the goal is to investigate and quantify neurons morphology in 2D cultures. Indeed, although many studies indicate that spatial correlations are a key parameter to understand the propagating bursting dynamics in culture, the underlying network structure is poorly characterized. The challenge is to observe a single cell in a culture dense biological medium. With viral infection, controlled in its quantity, we were able to observe individual cells, expressing the green fluorescent protein, in a complex biological environment. The confocal images are automatically processed with a python program able to extract and quantify neurites' morphology. Such measurements will be of great help in order to refine theoretical network models, and for future microfluidic devices that aim at controlling the network structure. I identify two regimes in the correlation of neurite path showing the interaction between neurite stiffness and adhesion to its environment and estimate the average connection length in a biological network with a simple *toy model*.

Keywords

NEURONS · CULTURE · NETWORK · MORPHOLOGY · BURSTS · AVALANCHE

NUCLEATION · DYNAMICS · PROPAGATION · PHASE ·

Resumé

L'objectif de mon étude est de comprendre la relation entre la structure spatiale d'un réseau de neurones à deux dimensions et l'activité, soit mesurée expérimentalement soit résolu par des modèles mathématiques.

La partie théorique porte sur le comportement spatio-temporel des bouffées d'activité d'une culture de neurones et est basée sur deux modèles. Un premier, statique, de type percolation à quorum et un second dynamique du type "adaptive exponential integrate-and-fire". En utilisant un modèle de réseau inscrit dans l'espace 2D et une phase spécifiquement adaptée à une activité sous forme de potentiel d'action nous arrivons à mettre en évidence des caractéristiques spécifiques de l'activité : temps et longueur caractéristiques, vitesse de propagation, zone et neurone initiateurs (leader), etc... Ces propriétés nous permettent de mieux comprendre les mécanismes fondamentaux de l'initiation des bouffées d'activité dans les cultures et leurs relations avec le réseau spatial. J'étudie la transition de phase du modèle de Quorum Percolation au sein de réseau spatiaux et identifie une transition entre deux dynamiques de propagation spatiales.

La seconde partie de ma thèse, de nature expérimentale, vise l'exploration du réseau spatial en culture et la quantification de la morphologie de neurones corticaux. En effet, alors même que différentes études théoriques indiquent clairement que les corrélations spatiales sont déterminantes pour la dynamique collective dans les cultures, la structure des réseaux reste encore très mal élucidée. Après quelques jours de croissance *in vitro* il est impossible d'observer une cellule unique, noyée dans l'ensemble de la culture. En utilisant une infection virale en quantité précisément contrôlée, permettant l'expression de la protéine fluorescente GFP, nous arrivons à observer une cellule unique dans un réseau biologique. Nous pouvons ainsi suivre la croissance de cellule unique par imagerie confocale. Ces images sont par la suite analysées automatiquement par un programme python permettant de quantifier précisément la morphologie de neurones corticaux *in vitro*. Ces mesures sont un outil précieux pour nourrir les modèles de réseaux spatiaux, mais également pour le design d'environnement microfluidique dont l'objectif est le contrôle de la morphologie. Par une modélisation simple de la connectivité du réseau, j'établis un ordre de grandeur de la longueur de connexion. L'analyse morphologique des neurites révèle deux régimes de longueur différents, dont l'origine encore mal identifiée pourrait permettre de quantifier le rôle des interactions cellules-cellules dans la morphologie des neurones.

Mots Clés

NEURONES · CULTURE · RÉSEAU · MORPHOLOGIE · BOUFFÉES · AVALANCHE
NUCLÉATION · DYNAMIQUE · PROPAGATION · PHASE ·

Detailed Contents

Summary	i
Resumé	ii
Detailed Contents	iii
INTRODUCTION	1
1 Why are neuronal cultures interesting ?	2
1.1 Mind, brain and neuronal activity	2
The Game of Life	2
Cellular automaton	3
The brain complexity	4
1.2 2D neuronal cultures	6
A model of the brain ?	6
Microfluidic devices	7
1.3 State of the art	8
Recorded activity	8
Theoretical descriptions	13
MODEL OF NEURONAL NETWORK ACTIVITY IN 2D SPATIALLY EM- BEDDED NETWORKS	18
2 Spatio-temporal Dynamics of the Quorum Percolation Model	19
2.1 Overview of the QPM	19
2.2 Simulation of the QPM	21
Network Model	21
Simulation methods	23
2.3 Propagating dynamics	26
Exploration of the phase space (λ, m)	26
Characterization of the propagating dynamics	37
Dynamics: first-to-fire and propagation	42
2.4 Discussion	47
3 Spatio-temporal Dynamics in bursts of synchronized Pacemakers	49
3.1 Introduction	50
Motivations	51
Objectives	53

3.2	Materials and methods	53
	Numerical simulations	53
	Spike time analysis	55
	Spatial Spike Analysis	61
3.3	Results	64
	Burst initiation	64
	Spatial initiation: Cluster algorithm performance	65
	Looking for leaders	66
3.4	Discussion	68
	Dynamical regimes	68
	Experimental data	71
3.5	Conclusion	71
3.6	Chapter's appendix	73
	Simulation of Neuronal Network	73
	Analysis with the Izhikevich model, synaptic depression and stochastic inputs	76
	Firing rate and first spike probability distribution	79
 NEURONS MORPHOLOGY IN 2D CULTURES		85
4	Neuron morphology in complex networks	86
4.1	Neuronal morphogenesis in vivo	86
	Development of the neuronal tree	86
	Extension process: The Growth cone	88
	Neurite structure	89
4.2	Methods and Protocols	92
	Primary culture of cortical neurons	92
	Data acquisition	95
4.3	Results	105
	Morphological properties	105
	Growth properties	109
	Persistence length	110
 CONCLUDING REMARKS AND PERSPECTIVES		113
Understanding neuronal networks		114
 APPENDIX		117
A Neuronal culture confinement		118
 Bibliography		123

Figures

1.1	Wilson Bentley snowflakes' photographs	2
1.2	Examples of The Game of Life two-dimensional patterns	3
1.3	Rule 126 of the elementary cellular automaton	3
1.4	Recoding of neuronal culture with micro electrode array - Masquelier et al. (2013)	9
1.5	Spatio-temporal pattern of avalanche - Beggs et al. (2003)	10
1.6	Scale free behavior dissociated neuronal cultures - Pasquale et al. (2008)	10
1.7	Nucleation points probability density function - Orlandi et al. (2013)	12
1.8	Network burst generation phases	13
1.9	Quorum percolation model	14
1.10	Quorum percolation order parameter	15
1.11	Schematic of a subcritical cluster	15
1.12	Experimental results of Quorum Percolation	16
2.1	Statistical properties of EDR networks	22
2.2	Statistical properties of EDR networks - Focus on the degree	23
2.3	Transition of dynamics in the Quorum Percolation Model	26
2.4	Quorum Percolation Model - Propagation in space $m/\overline{k}_i = 0.2$ and 0.3	27
2.5	Quorum Percolation Model - Propagation in space $m/\overline{k}_i = 0.4, 0.5$ and 0.6	28
2.6	Quorum Percolation Model - Propagation in space $m/\overline{k}_i = 0.7$ and 0.8	29
2.7	Number of iterations as function of m and λ at the critical point f^*	29
2.8	Representation of a Branching Process	31
2.9	Branching rate as function of the iteration time step in the QPM	32
2.10	Interruption of propagation in an EDR network	32
2.11	Examples of propagation in an EDR network	33
2.12	Branching rate σ_t as functions of the time step in the QPM	34
2.13	Stable branching rate σ_∞ as function of the quorum and EDR scale	35
2.14	The expected number of activated nodes in the QPM, as function of the time step	35
2.15	Limited propagation in the Quorum Percolation Model	36
2.16	Example of avalanches in the QPM	37
2.17	Avalanche size distribution in the QPM	38
2.18	Average avalanche size in the QPM with small connectivity scale	38
2.19	Fractured propagation in a network with EDR scale $800 \mu\text{m}$ and quorum 4	39
2.20	Average avalanche size in the QPM as function of the connectivity scale	39
2.21	Edge activation probability distribution	39
2.22	Weakly connected component with high edge activation probability	40
2.23	Fractured propagation in a network with EDR scale $25 \mu\text{m}$ and quorum 4	40
2.24	Schematic of the performance	43
2.25	Average performance for network EDR scale 150 and $800 \mu\text{m}$	44

2.26	Area of the initiation surface as function of the EDR scale	44
2.27	Schematic of the distance to the surface initiation	45
2.28	Expansion paramater as fuction of the time of activation - nucleation centres drawn in the 2D space	46
2.29	Propagation velocity as function of the EDR scale	46
2.30	Propagation velocity as function of the quorum	47
3.1	Burst detection with the extremum of the network phase $\Phi(t)$	56
3.2	The network phase and corresponding raster plot of experimental data from Lonardoni et al.	59
3.3	DBSCAN search for an initiation area	60
3.4	Optimization of parameters in the DBSCAN search in a circular culture	62
3.5	Optimization of parameters in the DBSCAN search in a triangular culture	63
3.6	Probability density function of spiking time in a burst initiation	64
3.7	Performance as function of the detected clusters surface	67
3.8	First-to-fire statistics with for two EDR scale λ	68
3.9	Performance as function of the detectd clusters surface with experimental data from Lonardoni et al. (2017)	70
3.10	Phase space and Interspike of the considered Pacemakers	74
3.11	Neuron Phase plotted in space for 2 bursts of the Izhikevic simulation	78
3.12	Spatio-temporal analysis of an Izhikevich model simulation, with synpatic de- pression and stochastic inputs	79
3.13	Time reference chnages the probability density of spiking time	80
3.14	Neurons' phases plotted in space, for IB pacemakers	81
3.15	Neurons' phases plotted in space, for RS pacemakers	82
3.16	Neurons' phases plotted in space, for RS pacemakers	83
3.17	Neurons' phases plotted in space, for ND pacemakers	84
4.1	Morphology of a stage 5 neuron	86
4.2	Developmental stage 1 to 4 of an hippocampal neuron	87
4.3	Fluorescent imaging of microtubules and actin filaments in a growth cone	88
4.4	Droplet patterns for photolithography mask	94
4.5	CytBow neurons in patterned culture	96
4.6	Phase contast image of DIV 4 cortical neurons, with one expressing the GFP in speudocolour	97
4.7	Ratio of cell density expressing the GFP and the total density versus the volume of added virus	98
4.8	A drilled dish to support glass coverslips	100
4.9	GFP Fluorescent image from DIV4 cortical culture	101
4.10	Morphology of a cortical neuron at DIV4	101
4.11	Example of a branching point	102
4.12	Definition of the angles in a branching point	102
4.13	Schematic of the (u,v) branch	102
4.14	Neuron morphology and growth direction seen as a tree-like graph	103

4.15 A single cortical neuron at DIV6 in a 180 mm^{-2} density culture.	103
4.16 Subsampling of the B-spline approximation of branches to computed the tangent angle θ_s	105
4.17 Axon and dendrites curvilinear length distribution	105
4.18 Branch Tortuosity distribution	106
4.19 Number and distance between branching points distributions	107
4.20 Branching angle distribution	107
4.21 Presence probability of an axon branch at a distance r from the soma	108
4.22 Computation of the probability connection	108
4.24 Growth ratio distribution	109
4.23 Connection probability as function of the inter neurons distance	109
4.25 Growth cone speed distribution	110
4.26 Correlation of neurite paths orientation	111
4.27 Correlation of neurite orientation path as function of the curvilinear distance	111
4.28 Image of DIV6 axon within a complex biological environment	111
4.29 Image of DIV5 neuron within a complex biological environment	112
4.30 Image of DIV5 axon and growth cone within a complex biological environment	112
A.1 Design of microfluidics chips	119
A.2 Patterned culture of cortical neurons in millimeter scale chip	120
A.3 Culture of cortical neurons with inverse pattern	121
A.4 Pattern of PDMS	122

Tables

3.1 Parameters Values	75
4.1 number of recorded neurons and volume of virus added	99

INTRODUCTION

Why are neuronal cultures interesting ?

1.1 Mind, brain and neuronal activity	2
The Game of Life	2
Cellular automaton	3
The brain complexity	4
1.2 2D neuronal cultures	6
A model of the brain ?	6
Microfluidic devices	7
1.3 State of the art	8
Recorded activity	8
Theoretical descriptions	13

This chapter presents the interdisciplinary field that neurophysics aims to be. Coping with the complex subtleties of biological systems, physicist try to further the understanding of neuronal mechanisms. Widening the scope of neurobiology by introducing new approaches, this research domain also find its roots in the wonder of consciousness and the hope that someday we might understand how our thoughts emerge and change. These metaphysical questions are probably what keep many neurophysicists going on.

My personal understanding of neuronal processes comes from my physics training. To my mind, the sophisticated and highly efficient processing power of cognitive systems belong to the class of emergent behaviours. From snowflakes to ant societies, the biosphere is overflowing with examples of large scale complex order absent in the microstates.

In this section I will present a mathematical object, that can be though as a "toy model" for neuronal systems and may represent the elementary brick for information processing. Then I will present the fundamental notions needed to understand my doctoral work.

1.1 Mind, brain and neuronal activity

Universal computing with The Game of Life

You cannot play this game with your family. You play with the game itself, and create your own mathematical world with birth, life, and death. In the late 1960s, the mathematician John Horton Conway invented a set of very simple rules to create geometrical drawings: they are the living soul of the world you will create. The drawings are embedded in a square grid, and are transformed according to these very rules. Each square cell has 8 nearest neighboring cells. If 2 or 3 of them are painted, then the cell stays painted (is alive), otherwise the cell dies, and is erased. A birth, meaning a new cell is painted, happens when there are 3 painted neighboring



Figure 1.1: Two snowflakes' photographs of Wilson Bentley [1]

cells. After choosing your very own initial pattern, you just have to let it evolve and observe it creating new patterns, or maybe die out. I can only advise you to go and have a little fun: [The Game Of Life](#)

This game became popular in the mathematical world for its rules are simple, but the possibilities are tremendous: a real zoo of patterns, life forms, has been identified [2]. Let's look at some of them. The blinker, 3 aligned square, is an oscillator: every two generation the pattern returns to its original state. The beehive, or the boat (see figure 1.2) consists on two patterns that do not change from one generation to the next. The glider (see figure 1.2) is an example of pattern that travels across the grid: it is in perpetual motion.

The game of life has taught us that transferring information is easy, as long as you follow some basic rules. Information can be one of the 5 generation of the glider, and after letting it travel some distance, the same pattern appears elsewhere in another 3 by 3 square. Much more than this naive example the game of life can be used to compute every logic gates: it is a universal Turing Machine [3]. The 1 and 0 can be think as the existence or not of gliders, and different patterns can be used to accomplish the different logic gates. In this Turing Machine, the computation is done with specific spatio-temporal patterns. Anyone who looks at both the retinal waves, captured by Meister et al. or Butts et al. [4, 5] and a random realisation of Conway's game of life will notice the uncanny resemblance.

A paradigm for the emergence of complex organization: Cellular automaton

Conway's game of life is an example of what is now called, a cellular automaton: a set of rules that describe the evolution of cells in a square grid. Stephen Wolfram studied and classified the 256 one-dimensional cellular automaton. For example, all generations of a single alive cell, submitted to the iteration rule 126 represent a Sierpinski triangle, (see figure 1.3) a well-known fractal structure, that repeats itself endlessly at every scale. This macroscopic property emerges from the elementary rule 126 that describes microstates. In 2004 Matthew Cook [6] demonstrated that the iteration rule 110 is a Universal Turing Machine, like Conway's Game of

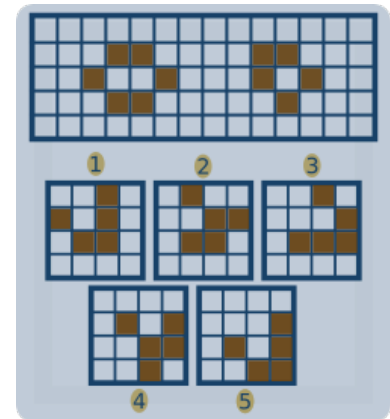


Figure 1.2: Examples of patterns in Conway's Game of Life. The **Top** grid displays examples of a beehive (left) and a boat (right). The **bottom** five square display the 5 generation of a gliders that make him travel across the square diagonal

[3]: Rendell (2011), 'A Universal Turing Machine in Conway's Game of Life'

[4]: Meister et al. (1991), 'Synchronous bursts of action potentials in ganglion cells of the developing mammalian retina'

[5]: Butts et al. (1999), 'Retinal Waves Are Governed by Collective Network Properties'

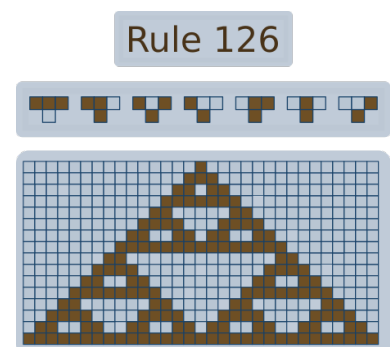


Figure 1.3: The **Top** frame represents the set or iteration rules in the 126 elementary cellular automaton. The **Bottom** frame shows the first 16 iteration with a single live cell at the initial state.

[6]: Cook (2004) 'Universality in Elementary Cellular Automata'

Life. In both of these examples (rules 126 and 110), local and simple rules have been able to create macroscopic, coherent and complex structures.

However, out of the 256 one-dimensional cellular automaton, not many of them exhibit such remarkable behavior. The fundamental mechanism, the rationale that makes rule 110 to be different, to be better (?) is entirely unknown. Why specific rules of propagation allow certain macroscopic behavior whereas some repress any large scale structure ? In another domain, synchronization is a widely spread phenomenon in physics. It describes the collective behaviour of multiple subsystems and emerges from the coupling between intrinsically oscillating units. Is there any equivalent, in the world of 'physics laws' that can explain why certain sets of rules appear as boring, when others create wonders ? Is the reductionism paradigm even relevant ?

Food For Thoughts Methodological reductionism claims that a high level of organization can be explained and understood from a lower level of organization. Physics, and many other domains of sciences, are often associated to reductionism. It has been very successful for the understanding of heredity, through its macro-molecule organization as genes, or the understanding of macroscopic properties like magnetization through a molecular scale interaction. In mathematics, it has led Ernst Friedrich Ferdinand Zermelo to try developing a common foundation for mathematics, nowadays called the axiomatic set theory. However, Kurt Gödel incompleteness theorem is a strong argument that can nuance the idea that there exists such foundation, or that it has any worth. In the exploration of emerging properties, scientists [7, 8] have raised the question about the fruitfulness and relevancy of reductionism. "The ability to reduce everything to simple fundamental laws does not imply the ability to start from those laws and reconstruct the universe." ~ *Philip Warren Anderson*

[7]: Gazzaniga (2010), 'Neuroscience and the correct level of explanation for understanding mind'

[8]: Anderson (1972), 'More Is Different'

From a simple paradigm to the brain complexity

The two-dimensional cellular automaton presented here are not so different from models of neuronal networks. Indeed, a straightforward and simplistic approach to describe neurons behaviour can be to consider them as black and white units:

either active (a painted cell) or silent (a white cell). These Ising-like models are vastly studied. [9–11] In such neuronal model of cellular automaton, the iteration rule then takes into account that inhibitory cells remove active cells, whereas excitatory cells create them. Is it possible that a macroscopic coherent structure emerges from such a simple system? And if so, what is the role of the biological complexity of the brain?

Emergent behaviour can be classified into several categories. [12] For instance, an emergent *property* like the temperature is a property of an ensemble of particles, an emergent *structure* like 3 lines form a triangle or a *real* emergence like the computing capacity of the Game of Life. Is the mind a macroscopic property of an ensemble of excitable units, or a real emerging, just like a cell is alive whereas the molecules of which it is made are not? Do those weak categories of emergence even apply to the brain? A new tailored definition may be required to investigate the complex mind-brain relationship.

The intricate multi-scale structure of the brain is the major obstacle to understand fully the mind-brain mechanisms [12]. From the couple of centimetres of anatomical and functional brain regions, to the molecular interactions, the brain is made of modular interacting components at every spatio-temporal scales. Minicolumns are structures of 30 microns in diameter that represent 100 neurons. [13] They are the anatomical basis of the cerebral cortex structure made of columns, subareas, areas and lobes. The temporal scaling of neuronal activity is also evidently related to its complexity and processing power. Large scale brain activity [14] has been recorded from 1 to 200 Hz, whereas synaptic plasticity involves molecular changes in a matter of seconds (short term plasticity) to hours (long term plasticity). [15]

Macroscopic neuroimaging techniques that quantify the relationship between mind and brain states are showing accurate correlations, [16, 17] however do not bring us closer to understanding the origin of this relationship. Moreover, there is no evidence, to my knowledge, that there exists a direct bijective relationship between brain state, however it is measured, and mind state. There is still no proper understanding of the emergence of macroscopic behaviour, like the consciousness, from its microscopic elements, and interactions. All this, question our ability to properly describe, scientifically, the consciousness, and its relationship with the physical brain.

[9]: Hernández-Navarro et al. (2017), 'Dominance of Metric Correlations in Two-Dimensional Neuronal Cultures Described through a Random Field Ising Model'

[10]: Schneidman et al. (2006), 'Weak pairwise correlations imply strongly correlated network states in a neural population'

[11]: Tkacik et al. (2006), 'Ising models for networks of real neurons'

[13]: Hagmann et al. (2008), 'Mapping the Structural Core of Human Cerebral Cortex'

[14]: Salinas et al. (2001), 'Correlated neuronal activity and the flow of neural information'

[15]: Abbott et al. (2004), 'Synaptic computation'

[16]: Damoiseaux et al. (2009), 'Greater than the sum of its parts'

[17]: Raichle et al. (2007), 'A default mode of brain function'

" Perhaps most simply, emergence - of consciousness or otherwise - in the human brain can be thought of as characterizing the interaction between two broad levels: the mind and the physical brain. To visualize this dichotomy, imagine that you are walking with Leibniz through a mill. Consider that you can blow the mill up in size such that all components are magnified and you can walk among them. All that you find are mechanical components that push against each other but there is little if any trace of the function of the whole mill represented at this level. This analogy points to an important disconnect in the mind-brain interface: although the material components of the physical brain might be highly decomposable, mental properties seem to be fundamentally indivisible "

Danielle S. Bassett and Michael S. Gazzaniga [12]

[12]: Bassett et al. (2011), 'Understanding complexity in the human brain'

To my very own disappointment, I am not going to propose a theoretical framework able to solve this immensely complicated question. However, looking at neuronal cultures is a way to reduce the inherent complexity of the brain, and study a system closer to a cellular automaton where the reductionism paradigm may still be relevant.

1.2 Neuronal cultures in practice

A model of the brain ?

Compared to 3D structure of the brain, the 2D neuronal network growing in a dish is a much simpler system. The main reasoning behind this is a matter of order of magnitude. For example, in the 1D cellular automaton, there are $2^3 = 256$ different¹ possible rules. There are $2^{2^9} = 10^{154}$ possible 2D cellular automaton and $2^{2^{27}}$ 3D cellular automaton, which is infinity according to any computer in 2021, and maybe ever. Scaling down one dimension drastically reduces the complexity. Also, for a theoretical physicist playing with numerical simulations, it makes it much more easy to treat without heavy machinery. The human brain is large, with approximately 85 billion neurons² [18], with each creating thousands of synapses. Neuronal cultures typically contain 10^3 to 10^5

1: One need to consider 3 cells, each of them can be alive or dead, hence 2^3 combination, and each of these combinations can create a cell either dead or alive.

2: that is $8 \cdot 10^{13}$

[18]: Herculano-Houzel (2012), 'The remarkable, yet not extraordinary, human brain as a scaled-up primate brain and its associated cost'

neurons making it easier to model with computational methods.

In 1907, the American Ross Granville Harrison [19] reported the first culture of frog neurons which allowed him to identify several morphological scales in growing nerve fibres. " One fiber was observed to lengthen almost 20 μm in 25 minutes. " Much more than just a report on the size, and growth speed of nerve fibres, R.G. Harrison demonstrated that living neuronal tissues from vertebrates can grow outside the body. A century after this demonstration, as I am writing this, the key word 'neuronal culture' gives 761 results in PubMed search engine. They are all articles published in the 3 first months of 2021. Being able to study neurons in a controlled medium (in ions concentration, temperature, pH etc...) has led to a tremendous number of successful study. Jerome Pine, in 1980, and Guenter W. Gross et al. in 1982 [20, 21] recorded neurons' activity with the help of micro-electrode arrays. They started the idea that neuronal cultures could be used as a model to investigate activity in the brain. The intricate three-dimensional structure of the brain and the large amount of external stimuli is an impediment that neuronal culture overcome. Our understanding and modelling of single neuron behaviour is greatly due to recordings of cultures. They became also extensively used for drug testing and the investigation of neurodegenerative diseases and epileptiform of activity. [22, 23]

Microfluidic devices: a new perspective

The structured organization of the brain, in the form of a complex network is the support of our cognitive functions. This network emerges as neurons grow, axons get longer, the dendritic tree get denser, and continue changing once the synapses are formed according to plasticity rules and cellular apoptosis³. The resulting network is highly predetermined, and little is due to randomness. Mastering the growth of healthy biological neurons in a dish allows testing of multiple theories, but does not necessarily reflect the brain mechanisms. Is the extrapolation from unconstrained neuronal cultures to the brain relevant ? The advantage of neuronal culture were that neurons could grow freely, actually move it away from the subject at hand: the neuronal network in the brain.

[19]: Harrison et al. (1907), 'Observations of the living developing nerve fiber'

[20]: Pine (1980), 'Recording action potentials from cultured neurons with extracellular microcircuit electrodes'

[21]: Gross et al. (1982), 'Recording of spontaneous activity with photoetched microelectrode surfaces from mouse spinal neurons in culture'

[22]: Schlachetzki et al. (2013), 'Studying neurodegenerative diseases in culture models'

[23]: Dichter (2009), 'MODELS | The use of Cell Culture Models to Study Mechanisms Related to Epilepsy and Antiepileptic Drugs'

3: 50 % of the network connectivity might come from apoptosis [24]

[25]: J. Millet et al. (2010), 'Guiding neuron development with planar surface gradients of substrate cues deposited using microfluidic devices'

[26]: Peyrin et al. (2011), 'Axon diodes for the reconstruction of oriented neuronal networks in microfluidic chambers'

[29]: Renault et al. (2016), 'Asymmetric axonal edge guidance'

[30]: Forro et al. (2021), 'Electrophysiology Read-Out Tools for Brain-on-Chip Biotechnology'

[31]: Jahromi et al. (2019), 'Microfluidic Brain-on-a-Chip'

[32]: Wagenaar et al. (2006), 'An extremely rich repertoire of bursting patterns during the development of cortical cultures'

[33]: Masquelier et al. (2013), 'Network Bursting Dynamics in Excitatory Cortical Neuron Cultures Results from the Combination of Different Adaptive Mechanism'

[34]: Okujeni et al. (2017), 'Mesoscale Architecture Shapes Initiation and Richness of Spontaneous Network Activity'

Advances in microfluidics and chemical patterning techniques in the last 15 years made possible the design of precised and controlled environment at the micrometer scale. Controlling the environment also means controlling the growth.[25] Millet et al. were able to guide neuronal growth with chemical cues deposited on a glass substrate, whereas Peyrin et al. built an oriented neuronal network with asymmetrical 3D microchannels. With cleverly designed devices, researchers [26] have made possible to partly reconstruct the brain architecture as a network with non-random long range connections. This reconstruction made possible to investigate the role of synaptic connections in Alzheimer's and Parkinson's disease. [27, 28] The devices used to create directed links in populations of neurons become more and more efficient [29] and new discoveries may possibly appear from modern Brain-On-chip enthusiasm. [30, 31] .

1.3 Dynamics of cultured neuronal networks, what do we know ?

Recorded activity in culture

The periodic bursting regime

A couple of days after plating dissociated neurons, cultures exhibit one stereotypical activity in the form of periodic synchronized bursting event. From the firsts recordings [21] in the 80s, using either electrodes [32–34] or calcium imaging techniques people have reported that neuronal cultures main activity is formed by a several hundred milliseconds of intense firing over the whole network, separated by long windows of sparse activity. This bursting activity keeps on for as long as the culture is alive and is persistent over multiple biochemical manipulation. For instance, cancelling inhibition does not stop this spontaneous dynamics. Such robustness implies the existence of a fundamental mechanism governing this collective behaviour.

[27]: Deleglise et al. (2014) 'beta-amyloid induces a dying-back process and remote trans-synaptic alterations in a microfluidic-based reconstructed neuronal network'

[28]: Deleglise et al. (2013) 'Synapto Protective Drugs Evaluation in Reconstructed Neuronal Network'

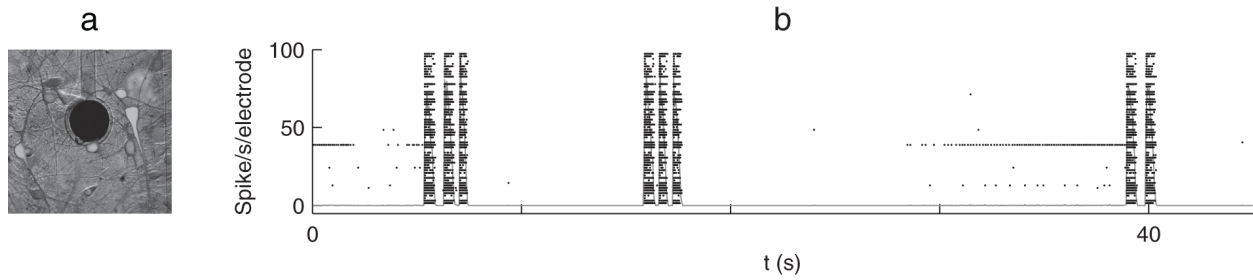


Figure 1.4: **a.** Cortical network growing over a micro electrode array. The black dot is a $30\ \mu\text{m}$ diameter electrode. **b.** Raster plot of the recorded activity with 60 electrodes as function of time. Each black dots represent a spike. Figure from Masquelier et al. [33]

Characteristics of neuronal activity: a question of perspective

When Masquelier et al. [33] reported their findings on bursts in culture, they identified what they called network spikes: events of consistently the same duration, where almost every cell in the culture is activated. These network spikes, as can be observed in figure 1.4, come in series with short interval between them (less than a second) such that you can observe 3 network spikes in the first 2 bursts, and only 2 in the last one. Conceptually, the identified network spikes are considered as distinct events because they were temporally distant: neurons' action potentials are gathered in a single system size event of duration several hundreds of milliseconds. Gathering spikes in time bins is the strategy used by John M. Beggs and Dietmar Plenz [35–37] to analyse brain slices activity. They were interested in identifying avalanches: consecutively activated neurons related all together by one or several initial spikes.

Following an analogy with snow avalanches, aftershocks in earthquakes or the dynamics of a pile of rice, neuronal avalanches are continuous spatio-temporal patterns of correlated activity up to the triggering initial spike(s). It has been observed that the size distribution of the number of aftershocks or rice avalanches, [38–40] follows a power law such that an initial event (shock under the earth crust, or a spike) can be a single isolated event as well as it can trigger a system size avalanche. Such dynamics is characteristic of a scale free behaviour in the sense that there is no scale, there is no typical length, or time duration able to properly characterize it. On the contrary, an example can be a propagating wave, characterized by its wavelength and frequency.

[35]: Beggs et al. (2003), 'Neuronal Avalanches in Neocortical Circuits'

[36]: Beggs (2004), 'Neuronal Avalanches Are Diverse and Precise Activity Patterns That Are Stable for Many Hours in Cortical Slice Cultures'

[37]: Plenz et al. (2007), 'The organizing principles of neuronal avalanches'

[38]: Bak et al. (1989), 'Earthquakes as a self-organized critical phenomenon'

[39]: Baiesi et al. (2004), 'Scale-free networks of earthquakes and aftershocks'

[40]: Frette et al. (1996), 'Avalanche dynamics in a pile of rice'

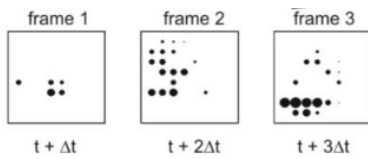


Figure 1.5: Pattern in space of one avalanche recorded by Beggs et al. [36]

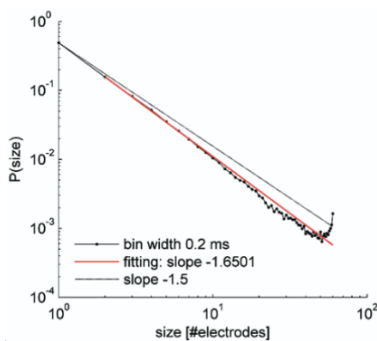


Figure 1.6: Avalanche size distribution in dissociated neuronal cultures. Figure from Pasquale et al. 2008

[41]: Pasquale et al. (2008), ‘Self-organization and neuronal avalanches in networks of dissociated cortical neurons’

[42]: Yaghoubi et al. (2018), ‘Neuronal avalanche dynamics indicates different universality classes in neuronal cultures’

Neuronal avalanches

Neuronal avalanches are the spatio-temporal patterns of activity emerging from spike propagation through the network. They are identified in experimental recordings able to pinpoint action potential as a function of time and space. Spike times are sorted out in time bins of size Δt , close to the millisecond. Avalanches are then consecutive time bins with at least one spike, and with empty bins before and after them. The avalanche duration is the sum of all the time bins, and the avalanche size is the number of activated electrodes, or neurons during this time interval. Figure 1.5 represents the spatial pattern of an avalanche of 3 time bins.

This definition, although rarely stated in scientific papers, implies that neurons’ activity in an avalanche follows the causality law. Hence, spike in the n^{th} time bins are mainly related to previous spike of this avalanche, and not previous activity. The avalanche typical scale in time, and in space is the correlation time or length.

According to John M. Beggs and Dietmar Plenz [35–37] neuronal avalanches are also scale free. They reported that the size distribution is a power law, with a $-\frac{3}{2}$ exponent (see figure 1.6). Latter studies, [41, 42] also reported scale free behaviour in neuronal cultures with similar data analysis. The report of scale free behaviour in neuronal propagating dynamics has raised a great deal of interest in the neuroscience community, because the fundamental origin of scale invariance is often the divergence of the correlation length, and it always occurs in critical systems.

Remarks on critical systems in neuroscience

In the description of an emergent property one may find oneself faced with what is called a phase transition: as a system variable is changed the observable (called the order parameter) changes radically and rapidly. For instance, as the temperature (the system variable) of a liquid is increased, the density of molecules (the order parameter) is rather constant, except at one point, where the liquid becomes a gas and the density decreases drastically. The critical point is the temperature value at which the transition occurs. At a critical point, systems follow universal laws related only to properties of

symmetry: the macroscopic observable (order parameter) of two systems with similar symmetries behave similarly.

The neural criticality hypothesis suppose that the brain autonomously stays at a critical state (see [43] for a review). This hypothesis imply that neural systems are able to target a critical point during their growth and astutely tune a control parameter to stay close to the critical point. This is an example of self-organized critical system [44–46]. The system variable is here controlled by the system itself in order to stay in the critical state. The relevant question being is their an advantage for neuronal system to put efforts into staying at criticality.

Critical states are efficient for multiple neural related tasks. Critical neuronal avalanches are reported [47] to ensure maximal sensitivity to sensory stimuli allowing to flexibly switch of dynamics/state by small changes [45]. The allegedly optimized information processing [48] of neuronal systems come from the divergence of the correlation scales at criticality. Both temporal and spatial correlation scales diverge at the critical point. These experimental recordings and theoretical predictions are at the origin of a vast debate in the neuroscience community, and has been the center of attention of many scientists.

Although it is closely related, the self organized criticality is not the main subject of my doctoral work. I have been focused on the spatio-temporal characterization of (avalanche-like) neuronal activity. I do hope it will help in understanding it, the origin and relevancy of self-organized criticality in neuronal systems will not be debated here.

Spatial characteristics

In their studies, Beggs et al. [36] claim that neuronal avalanches are stable patterns of activity over many hours. They reported that neuronal cultures spontaneously produce 5000 avalanches per hour, representing 30 different spatio-temporal patterns of propagation. In a more recent study, Javier G. Orlandi et al [49] reported with calcium imaging techniques, that the nearly periodic bursting activity is controlled by the nucleation, and propagation of circular waves. The nucleation centres appears to be randomly chosen in a set of

[43]: Hesse et al. (2014), ‘Self-organized criticality as a fundamental property of neural systems’

[44]: Bak et al. (1988), ‘Self-organized criticality’

[45]: Wilting et al. (2018), ‘Operating in a Reverberating Regime Enables Rapid Tuning of Network States to Task Requirements’

[46]: Zeraati et al. (2021), ‘Self-organization toward criticality by synaptic plasticity’

[48]: Beggs (2008), ‘The criticality hypothesis’

[49]: Orlandi et al. (2013), ‘Noise focusing and the emergence of coherent activity in neuronal cultures’

[47]: Kinouchi et al. (2006) ‘Optimal Dynamical Range of Excitable Networks at Criticality’

4: CMOS-MEA: complementary metal-oxide semiconductor micro-electrodes-array

[50]: Lonardoni et al. (2017), 'Recurrently connected and localized neuronal communities initiate coordinated spontaneous activity in neuronal networks'

[51]: Gandolfo et al. (2010), 'Tracking burst patterns in hippocampal cultures with high-density CMOS-MEAs'

[52]: Eytan et al. (2006), 'Dynamics and Effective Topology Underlying Synchronization in Networks of Cortical Neurons'

[53]: Ikegaya et al. (2004), 'Synfire Chains and Cortical Songs'

[54]: Eckmann et al. (2008), 'Leader neurons in population bursts of 2D living neural networks'

[55]: Zbinden (2010), 'Leader neurons in living neural networks and in leaky integrate and fire neuron models'

specific points in the culture (see figure 1.7). They reported propagation velocity close to $10 \text{ mm}\cdot\text{s}^{-1}$ with an increase as the inhibition is suppressed with bicuculine. Others research teams also reported a propagating dynamics with high resolution array of electrodes⁴. [50, 51] .

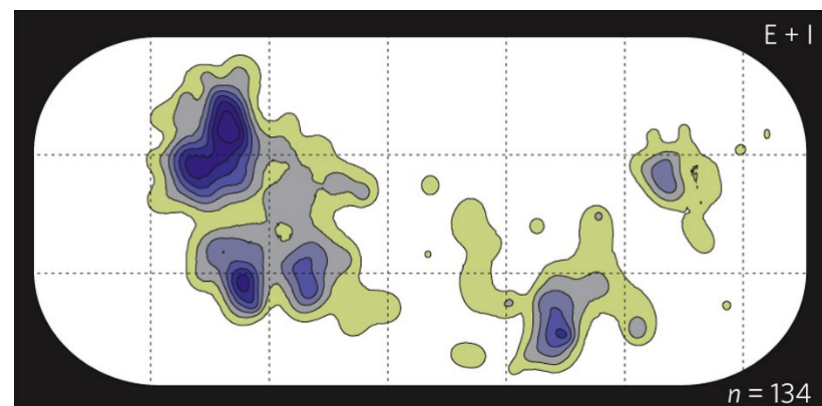
Overall, the most recent studies show that neuronal cultures bursting regime are made of an initiation of activity, leading to the nucleation and propagation of a wave. To these three phases (initiation, nucleation, propagation) one may add a possible reverberating phase, once the activity spread to the whole culture.[51]. Several parts of the culture may act as nucleation centres, creating a non-uniform distribution in space.

Leader neurons

What is the role of each individual neuron in a burst ? As it has been observed, some may lie close to the nucleation centre, making them among the firsts to fire. Are they always the first one to fire ? Is the phase (initiation, nucleation, propagation, reverberation) in which a neuron spike constrained or random ? According to D. Eytan and S. Marom [52] some neurons consistently spike at earliest phase of the burst, whereas other are most frequently activated at latter stage. Similarly to the 30 stable avalanche families observed by Beggs et al. [36], it seems that all *in vitro* neuronal systems activity exhibit sequences of spiking that regularly repeat themselves in a constrained order. [53–55]

Leader neurons are at the centre of scientific theories trying to model the fundamental mechanisms for neuronal culture to *spontaneously* generate periodic bursts of propagating activity. Although developing neural circuits *en vivo* are known to

Figure 1.7: Nucleation points probability density function. The probability to be a nucleation center is not uniform in space. 134 bursts were analysed. Figure from Orlandi et al. 2013 [49]



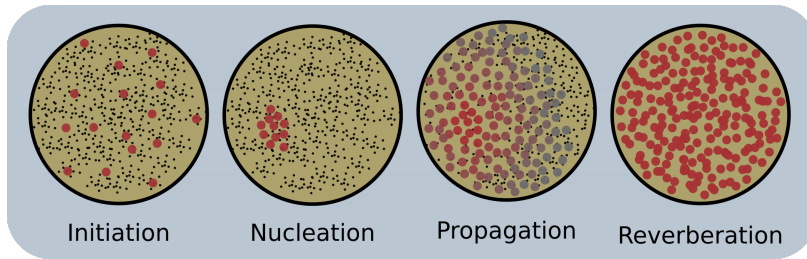


Figure 1.8: A schematic representation of network burst generation phases. Small black dots represent non active neurons, whereas colored neurons are active. The initiation may happens sparsely in the network. The nucleation is localized in one specific point. The propagation starts at this point. The reverberation constitute the majority of the burst duration after its growth.

behave similarly [56, 57] it is still unclear what makes leader neurons, leader, or what govern the initiation dynamics.

Mechanisms, and theoretical description

Noise Driven: Quorum Percolation model

Without any external drive, neuronal cultures are unexpectedly able to display intense activity. One possible mechanism comes from the stochastic synaptic noise. Typical communication pathway between neurons is the release of vesicle in the synaptic shaft evoked by an action potential-induced Ca^{2+} influx. Independently of any presynaptic depolarization, spontaneous release of vesicle has been reported [58–60] to occur at each synapse as a random event with typical frequency of 10 Hz⁵. These spontaneous releases represent a fraction of action potential evoked releases which in turn are associated with a miniature Excitatory Post Synaptic Potential (mPSP). This constant uniform excitation may be able to bring the membrane potential above threshold of activation. The depolarization of some neurons may then propagate and spread to the whole network. The theoretical framework able to describe such phenomenon is called percolation.

Historically, it refers to the flow of liquids going through porous materials. The word percolation comes from the Latin *percolare*, which means to trickle through, to filter. Like hot water has to cross ground coffee beans, neuronal activity has to propagate through a complex network. There are multiple kinds of percolation [61], and the one we are interested in is called quorum percolation, a variation of the bootstrap percolation in directed networks.

[56]: Feller (1999), ‘Spontaneous Correlated Activity in Developing Neural Circuits’

[57]: Blankenship et al. (2010), ‘Mechanisms underlying spontaneous patterned activity in developing neural circuits’

[58]: Kavalali (2015), ‘The mechanisms and functions of spontaneous neurotransmitter release’

[59]: Kaeser et al. (2014), ‘Molecular Mechanisms for Synchronous, Asynchronous, and Spontaneous Neurotransmitter Release’

[60]: Sibarov et al. (2015), ‘Characteristics of Postsynaptic Currents in Primary Cultures of Rat Cerebral Cortical Neurons’

5: It appears that the frequency is age dependant, [60] Sibarov et al. reported that the frequency increase exponentially from 1 Hz to 15 Hz between days in vitro 1 and 20.

[61]: Miller (2016), ‘Equivalence of several generalized percolation models on networks’

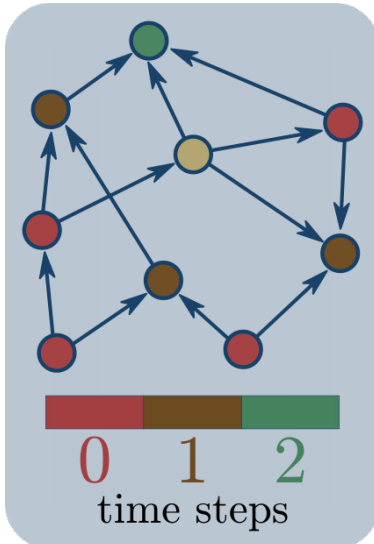


Figure 1.9: Schematic of propagation in the quorum percolation model with a threshold $m = 2$. The **red** nodes are activated at $t = 0$. Then the **brown** nodes are activated at second time step, then the **green** node. The **gold** node will never activate.

[62]: Izhikevich (2007), *Dynamical systems in neuroscience*

[63]: Baxter et al. (2010), 'Bootstrap percolation on complex networks'

[64]: Amini (2010), 'Bootstrap Percolation in Living Neural Networks'

The Quorum Percolation Model

The quorum percolation model describes the ability of a network to recruit a giant connected component G_{cc} under the random activation of an initial proportion f . It is a model with discrete time, where the proportion of active nodes at time $t + 1$ depends only on the number of active nodes at t . A node is activated at $t + 1$ if and only if it had at least m activated incoming neighbours at time t . This dynamics of propagation in networks is represented in figure 1.9

Dynamical models of neuron's membrane potential often consider a threshold above which a spike is artificially emitted. Excitatory post synaptic potentials (initiated by neighbours spiking) bring the membrane potential closer to threshold making the neuron more easily activated. In such framework, the Quorum Percolation Model suppose that the number of excitatory input needed to reach the threshold is:

$$m = \frac{V_{th} - V_{eq}}{V_{PSP}}$$

with V_{th} the potential threshold, V_{eq} the equilibrium potential and V_{PSP} the increase in the post synaptic potential after one activated incoming neighbours. Note that the existence of a threshold can be criticized, see page 3 of [62]

This model exhibits a complex phase transition diagram. [63, 64] The order parameter that best illustrate the transitions is the size of the giant active *connected* component G_{cc} in the infinite time limit. The system stable state changes depending on the number of initially active nodes. As one can see with the brown and red curves of figure 1.10 for two specific values f_{c1} and f_{c2} there is a meaningful change in the order parameter. For $f < f_{c1}$, there is no giant connected component and the order parameter G_{cc} is null. For $f > f_{c1}$ a giant connected component appears and the order parameter *continuously* increases from zero. At $f = f_{c2}$ one observes a discontinuity in the order parameter: there is a finite jump in the size of the active giant connected component. This is the distinctive feature of first order phase transition. For $f > f_{c2}$ the order parameter keeps continuously increasing. Hence, the phase transition diagram presents two phase transitions,

a second order phase transition at f_{c1} , and a first order one at f_{c2} .

Origin of the discontinuity: subcritical clusters

In undirected networks, cascades of activations happen when some nodes are at the edges of switching on: they have $m - 1$ active neighbours. We call subcritical clusters groups of connected nodes with $m - 1$ active neighbours at the infinite time limit. Figure 1.11 illustrates a small subcritical cluster. The activation of a single vertex in the overall neighbourhood of this cluster is sufficient to activate all of its nodes. Just as in bond percolation, where the connected components mean size diverges close to threshold, as f approaches f_{c2} from below, the mean size of subcritical clusters diverges. Hence, the avalanche of activation originating from a single activated node in the network, results in a finite jump of the order parameter.

It can be shown [63] that the mean size of subcritical cluster follow, $\bar{s}_{subc} \underset{p \rightarrow p_c}{\sim} (f_{c2} - f)^{-1/2}$. This divergence comes from the subcritical cluster size distribution at the critical point. The distribution is known to scale as $s^{-3/2}$ in the undirected complex networks, and other simpler ones like Bethe lattices. [65]

A complex picture: the two-dimensional phase diagram

Because quorum percolation utilizes a parameter m in its dynamical process, it also exhibits a more complex transition. Increasing the value of the threshold, one can understand that when m is above the mean in-degree \bar{k}_i the propagation is jammed by low in-degree nodes and the discontinuity can not exist any more. There is a value m_c above which the number of active nodes at the infinite time limit is a continuous function of the initially ignited fraction f . For such values the size of the giant active connected component is continuous: zero below f_{c1} and non-zero above (see figure 1.10). The complete picture of quorum percolation phase transition has to be drawn in a two-dimensional phase space, where the critical points f_{c1} and f_{c2} are functions of the threshold m .

Quorum Percolation in Neuronal Cultures

In the hope to quantify neuronal network statistical properties, Breskin et al [66, 67] introduced the idea that the re-

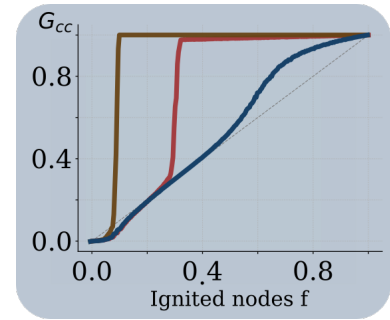


Figure 1.10: Size of the giant active connected component as functions of the initially ignited fraction for threshold values m being 5 (brown), 9 (red) and 13 (blue) in an Erdős Rényi with 1000 nodes and a mean degree of 15.

[63]: Baxter et al. (2010), 'Bootstrap percolation on complex networks'

[65]: Shukla (2008), 'Dynamics of bootstrap percolation'

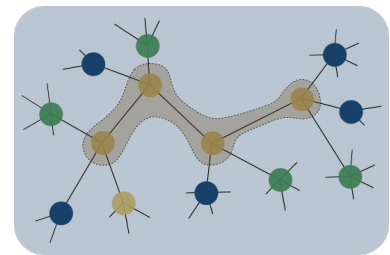


Figure 1.11: Schematic of a subcritical cluster highlighted in gold for a threshold of 3. Nodes in green represent the active fraction at the start, blue ones are activated at the stable state and gold are not active. One can notice that if a single node of the cluster is activated, the whole cluster will be. A single activation is able to create a discontinuity in the size of the giant active component.

[66]: Breskin (2006), 'Connectivity in living neural networks'

[67]: Eckmann et al. (2007), 'The physics of living neural networks'

6: With CNQX: 6-cyano-7-nitroquinoxaline-2,3-dione

[68]: Soriano et al. (2008), 'Development of input connections in neural cultures'

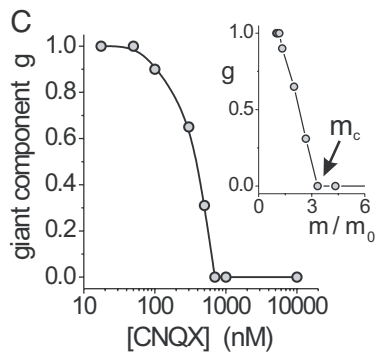


Figure 1.12: Experimental results of the quorum percolation experiments from [68]. They showed the estimation of the jump in the order parameter as functions of the threshold m , or the concentration [CNQX].

[69]: Tazerart et al. (2008), 'The Persistent Sodium Current Generates Pacemaker Activities in the Central Pattern Generator for Locomotion and Regulates the Locomotor Rhythm'

[70]: Sipilä et al. (2006), 'Intrinsic bursting of immature CA3 pyramidal neurons and consequent giant depolarizing potentials are driven by a persistent Na⁺ current and terminated by a slow Ca²⁺-activated K⁺ current'

response to an external electrical stimulation can be understood through the lens of percolation. They recorded the number of activated neurons G_a as function of the excitation potential V while chemically⁶ weakening the original network and observed a discontinuous jump in the response curve $G_a(V)$. They latter introduced [68] a control parameter to assess the quorum percolation threshold m as a function of the CNQX concentration, that quantify the network damage. The idea is that this chemical does not behave as an on and off switch, but decrease slowly the synaptic strength by blocking some synaptic receptors.

The average number of inputs m_o for a neuron to fire, in the undamaged network, is related to the potential threshold and synaptic efficiency (see section Section 4). The synaptic strength is affected by the concentration of CNQX according to the available receptors concentration c that are not blocked by it. Some bio-chemical analyses easily gives, $c = \frac{K_d}{K_d + [CNQX]}$, where K_d is the CNQX dissociation constant ($K_d = 300 \text{ nmol.L}^{-1}$). The quorum percolation threshold as a function of the synaptic strength is then $m = \frac{m_o}{c} = 1 + \frac{[CNQX]}{K_d}$, which presents a critical value above which the size of the giant active component is continuous. Figure 1.12 shows the estimation of the critical value m_c , or equivalently the concentration [CNQX] above which there is no discontinuity in the number of active neurons.

Synchronization: intrinsically oscillating neurons

Pacemaker neurons are able to drive neuronal circuits into bursting regime. They are spontaneously activated, even in the absence of synaptic input. The depolarization of their membrane potential comes from a persistent active sodium conductance [69, 70], and is followed by an after-spike hyperpolarization that last 1 to 6 seconds. These neurons are believed to be clustered at the nucleation centre of propagating events in the cerebellum and hippocampus. [57]

The existence of intrinsically oscillating neurons, with stable frequencies, leads us to believe that the observed bursting regime is a specific case of synchronization of oscillators. Indeed, a phase transition, from an asynchronous activity to a phase locked synchronized burst has indeed been observed experimentally in culture of hippocampal neurons. Y. Penn

et al [71] demonstrated that the rhythmic bursting regime appears when the concentration of calcium is increased. They claim that such biological networks are established with 60 % of pacemaker-like neuron, that display various types of bursting patterns, with an inter-burst interval ranging from 1 to 20 s⁷.

This phase transition has been qualitatively reproduced with a dynamical model in Tanguy Fardet thesis. [72] Taking into account that a the diminution of calcium induces a reduction in the vesicle release and of the after-spike hyperpolarisation⁸, the adaptive exponential integrate-and-fire model [73] in a Gaussian network reproduces the phase transition, with the decrease of inter-burst interval as the calcium concentration is increased.

Reaching a synchronous state is not obvious, and this model is able to reproduce the observed synchronization because it belongs to the family of relaxation oscillators. The Mermin-Wagner theorem [74] states that harmonic oscillators cannot reach synchronous state in 2D locally coupled networks. However, relaxation oscillators are driven by the fastest ones, hence the possibility to synchronize in spatially embedded 2D networks. It has been proven that relaxation oscillators coupled locally synchronize at an exponential rate, a feature observed experimentally [52] in neuronal cultures.

[71]: Penn et al. (2016), 'Network synchronization in hippocampal neurons'

7: Although it is in the same order of magnitude, this long interval seems incongruent with the 1 to 6 seconds of after-spike hyperpolarization.

[72]: Fardet (2018), 'Growth and activity of neuronal cultures'

[73]: Brette et al. (2005), 'Adaptive Exponential Integrate-and-Fire Model as an Effective Description of Neuronal Activity'

8: The AHP is mediated by calcium activated potassium conductance [57]

[74]: Mermin et al. (1966), 'Absence of Ferromagnetism or Antiferromagnetism in One- or Two-Dimensional Isotropic Heisenberg Models'

[52]: Eytan et al. (2006), 'Dynamics and Effective Topology Underlying Synchronization in Networks of Cortical Neurons'

**MODEL OF NEURONAL NETWORK
ACTIVITY IN 2D SPATIALLY
EMBEDDED NETWORKS**

Spatio-temporal Dynamics of the Quorum Percolation Model

2

In the introduction chapter we have seen that the spatial dynamics of neuronal culture activity in two-dimensional space is still unclear, and requires more in depth analysis to provide an accurate model of neuronal population activity. Also, I have presented the model of quorum percolation, used to describe neuronal culture response to an excitation and the transition to a fully active state with an elementary ingredient of neuronal dynamics: a threshold based interaction.

In this chapter, I will first briefly present an overview of the Quorum Percolation Model (QPM) extensions to specific neuronal dynamics in order to grasp a more detailed understanding of this model, and more specifically of the critical point m_c above which the phase transition is continuous. Then, I will use this model in networks embedded in space in order to explore the theoretical possibilities offered by such simplified model of activation. I will define and quantify different regimes of 2D spatial propagation and introduce the idea that spatial correlation changes the first order phase transition.

2.1 Overview of the QPM	19
2.2 Simulation of the QPM	21
Network Model	21
Simulation methods	23
2.3 Propagating dynamics	26
Exploration of the phase space (λ, m)	26
Characterization of the propagating dynamics	37
Dynamics: first-to-fire and propagation	42
2.4 Discussion	47

2.1 An overview of the QPM variants

Connectomics with the QPM

After a successful description of stimulated neuronal cultures, [66] the QPM has been used to estimate properties of the neuronal network degree distribution. The experimental measure of the critical threshold m_c is in agreement with simulations of the QPM with network described by a Gaussian in-degree distribution of average degree between 60 and 150 depending on neurons' origins and culture density. [68]

In a mean field approach of the QPM, a neuron with in-degree k is activated when the proportion of active neurons is higher than $\frac{m}{k}$. Hence, the conjecture that the degree distribution tail is responsible for the initiation of bursts in culture. Eckmann et al [75] claim that a power law tail with exponent -2 is able

[66]: Breskin (2006), 'Connectivity in living neural networks'

[68]: Soriano et al. (2008), 'Development of input connections in neural cultures'

[75]: Eckmann (2010) 'Leaders of neuronal cultures in a quorum percolation model'

[52]: Eytan et al. (2006), ‘Dynamics and Effective Topology Underlying Synchronization in Networks of Cortical Neurons’

[76]: Renault et al. (2014), ‘Effective non-universality of the quorum percolation model on directed graphs with Gaussian in-degree’

[68]: Soriano et al. (2008), ‘Development of input connections in neural cultures’

[77]: Fardet et al. (2018), ‘Effects of inhibitory neurons on the quorum percolation model and dynamical extension with the Brette–Gerstner model’

[78]: Renault et al. (2013), ‘Memory decay and loss of criticality in quorum percolation’

to reproduce the exponential rise in the number of active neurons observed *in vitro*. [52] The superposition of a Gaussian distribution of incoming connections and this power law tail is able to reproduce the following supra-exponential growth, in agreement with their previous studies [66].

The degree distribution has also been shown to strongly influence the first order phase transition. The critical value m_c above which the transition is continuous has been shown to depend on the mean degree and standard deviation in Gaussian networks. Monceau et al. [76] identified the relationship as

$$\frac{m_c}{k_i} \approx 1 - 1.3 \frac{\sigma}{k_i} + 1.5 \left(\frac{\sigma}{k_i} \right)^2 \quad (2.1)$$

with σ the in-degree standard deviation.

Extension of the quorum percolation model

The QPM has been refined to best describe neuronal cultures. As expected, [68] the effect of $\leq 20\%$ inhibitory neurons has been shown to be equivalent to a rewiring of a purely excitatory network and only shift the critical point to smaller values: $m_c(\eta) = m_c(\eta = 0) - 2\bar{k}\eta$. [77]

In order to take some aspect of neurons dynamics into account, Renault et al. have introduced the probability p_d that a neuron deactivates at each time step of the simulation δt . [78]

The duration of activation scale is then: $\tau_{QP} = \frac{\delta t}{\ln(1 - p_d)}$ The decay reduces the effective size of the network, and changes the behaviour of the observed first order phase transition. They found out that, even for small decay p_d values, the size of the giant component is not discontinuous anymore. The transition with decay is of second order, as long as the threshold $m > 1$. Thus, memory decay decreases the threshold to $m_c = 1$. Along with a shift in m_c they showed that the apparent size of the discontinuity, if measured experimentally would be underestimated if decay is not taken into account.

Quorum Percolation in spatially embedded networks

Although the theoretical framework developed here seems to describe some features of neuronal population activation properly, the model lacks an important parameter. Cultured

[66]: Breskin (2006) ‘Connectivity in living neural networks’

neurons grow in the 2D space, and develop synaptic connections accordingly. The assumption of random graphs, where any neuron can connect with any other neuron in the culture is unrealistic. One need to take into account that the network is embedded in space: there exists a typical finite distance of connection λ . As a result the dynamic of activation is different. In metric networks, the activation of a finite number of neurons, m in a disk of radius λ is enough to trigger a system size event. In random graph, such nuclei able to initiate a propagating activation does not exist, and a large excitation is needed.

2.2 Simulation of the the Spatial Quorum Percolation Model

Network Model

The Exponential Distance Rule (EDR) model [72] can reproduce a Gaussian-like in-degree distribution, the observed adirectionality and the finite connection distance. [79] It is an Erdős-Rényi like network, where the connection probability depends exponentially on the Euclidean distance. The network is built under the condition of fixed mean degree, from a random selection of somata positions in a circular culture with strict border conditions. Each pair of somata separated by a distance d is connected with the probability:

$$p(d) = p_0 e^{-d/\lambda} \quad (2.2)$$

with p_0 a normalization factor. The exponential characteristic length λ (also called EDR scale) is equal to the mean connectivity length in the thermodynamic limits.

Network properties and the EDR scale

In order to better understand this model, we introduce a characteristic scale λ_c with the network mean in-degree \bar{k}_i , and the culture spatial density η :

$$\lambda_c = \sqrt{\frac{\bar{k}_i}{\pi\eta}} = R\sqrt{\frac{\bar{k}_i}{N}} \quad (2.3)$$

[72]: Fardet (2018), ‘Growth and activity of neuronal cultures’

[79]: Barral et al. (2016), ‘Synaptic scaling rule preserves excitatory–inhibitory balance and salient neuronal network dynamics’

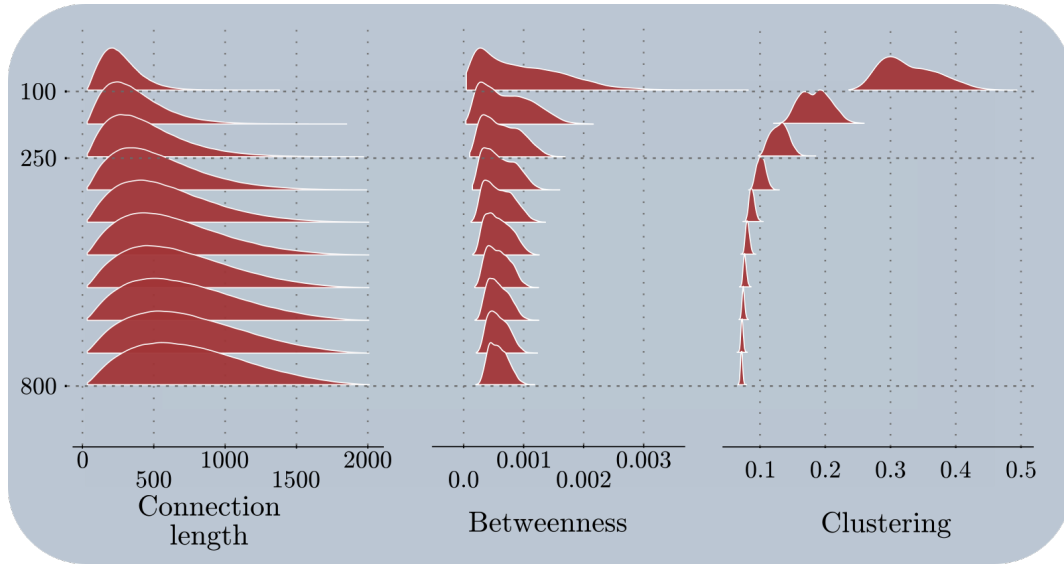


Figure 2.1: Graphical representation of the EDR model properties as function of the spatial scale λ (vertical axis). The simulated networks are set with a spatial density of $500 \text{ cells} \cdot \text{mm}^{-2}$ in a circular environment of radius 1mm. The mean in-degree is 100, hence $\lambda_c = 250 \mu\text{m}$. Values of λ are given on the left. The **left** frame displays the distribution of connection length (in μm). The **middle** frame displays the betweenness distribution and the **right** frame the clustering distribution. Beware that the vertical scale changes for better visualization, so that the total area is always 1. Every curve in this figure is a probability density normalized to 1.

With R the culture radius, and N the number of neurons. This scale represents the radius of a circle that covers \bar{k}_i neuron, depending on the density and is much smaller than the radius. Indeed, typical values of N and \bar{k}_i are in range of 10^4 and 100 (respectively), hence

$$\lambda_c \sim \frac{R}{10}$$

Emergence of clusters

Figure 2.1 shows EDR networks properties as function of the EDR scale. The characteristic scale λ_c appears to be a transition point between two behaviours. Although much smaller than the culture radius, for values of the EDR scale λ close to 800 microns, the network is very close to an Erdős-Rényi one and heterogeneities are not yet clearly observable. However, for values of λ close to λ_c , locality emerges as a widening of the clustering and betweenness¹⁰. Interestingly, the maximum of the betweenness distribution shifts towards low values showing a decrease for the majority of nodes, whereas some have increasingly high values. This is characteristic of densely connected clusters, interconnected with high centrality nodes.

10: A centrality measure that quantifies the importance of a node in the network information flow. For a node n , its value is related to the number of smallest paths between all pairs of nodes (u, v) going through the node n .

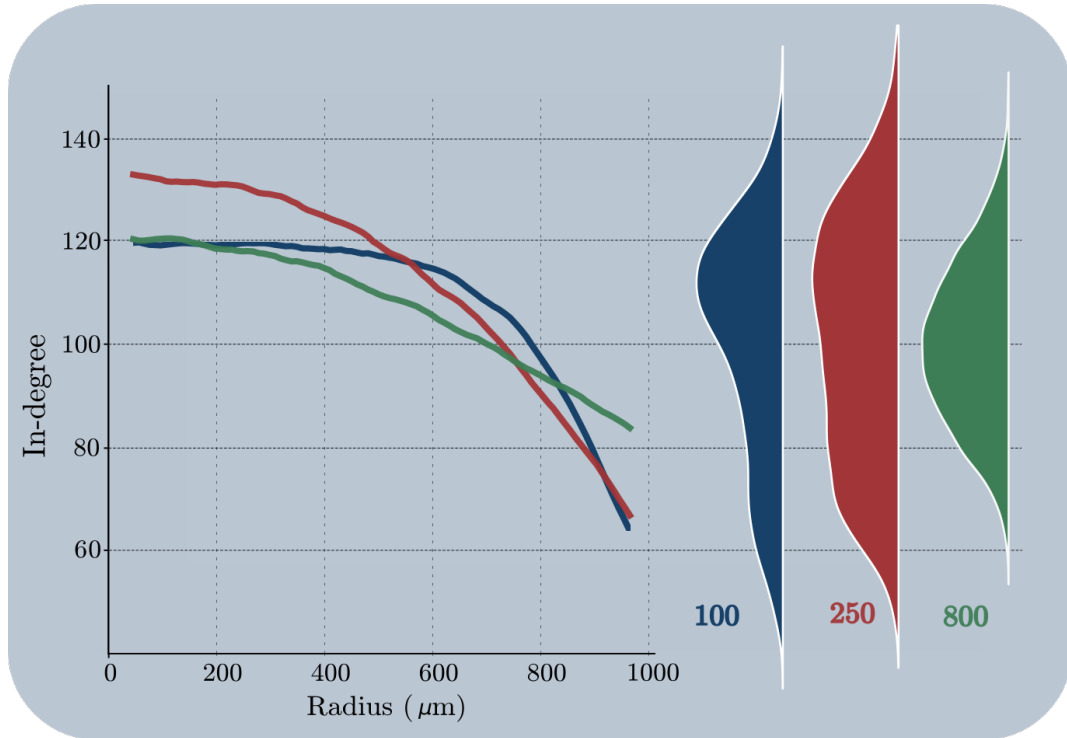


Figure 2.2: Graphical representation of the EDR model degree distribution for three values of the spatial scale λ , 100 (blue), 250 (red) and 800 (green) microns. The simulated networks are set with a spatial density of $500 \text{ cells} \cdot \text{mm}^{-2}$ in a circular environment of radius 1mm. The mean in-degree is 100, hence $\lambda_c = 250 \mu\text{m}$. The **right** graphs represent the in-degree distribution. The **left** frame represents nodes' degree as a function of their position in polar coordinates. The curves are an average over 100 instances of the EDR model.

Correlation with space

Figure 2.2 shows the correlation of the in-degree with the node position¹¹ in the two-dimensional culture. As the EDR scale decreases, nodes close to the environment border are constrained to a smaller degree, because of the lack of close neighbors. Close to λ_c the distribution is broad, with the highest in-degree at the centre of the culture. As λ decrease below λ_c the degree appears constant for a large portion of the environment and decrease rapidly at the border. Hence, the highly asymmetrical¹² degree distribution. Note the non-monotonous evolution of the degree $\bar{k}_i(r)$ as λ is changed: the highest in-degree appears when λ is close to λ_c and at $r \approx 0$

11: Characterized by its distance to the culture center

12: The distribution is almost bimodal: nodes close to the boundary have low in-degree,

Numerical simulation methods

Explicit simulations of the QPM

The QPM dynamics can be described in discrete time as follows:

1. For every node n a variable $s_n(t = 0)$ is initiated to 0.

- A **random fraction** of the network, \mathcal{F} is activated such that $\forall n \in \mathcal{F}, s_n(t = 0) = m$
2. Any node n_a activated at the time step $t - \Delta t$ sends at t one signal to each of its outgoing neighbors.
 3. The variable $s_n(t)$ for all nodes n is incremented by 1 for each signal received at time t . If $s_n(t)$ is greater than the threshold m , the node n is activated at time t
 4. Once a node is activated, it remains in this state until the end: when the number of activated neurons at time t is equal to the number of activated neurons at time $t + \Delta t$

Once the number of activated node is constant over one iteration, the system has reached a *stable state*. One cascade of activation produced by the QPM is terminated, and the macroscopic state reached by the model can be analyzed. From a statistical physics point of view, this state is described by the size of the giant active connected component G_{cc} . The observable G_{cc} depends on the complex network, of spatial scale λ and the fraction of initially ignited nodes f . The QPM is solved with random instances of both the EDR network and the fraction of initially ignited nodes. Thus, the observable is to be averaged over the two associated configurations in order to obtain the function $G_{cc}(\lambda, f)$. Only then, the behaviour of $G_{cc}(\lambda, f)$ will be smoothed of statistical dependency. It is worth noticing, however, that the activation dynamics are entirely deterministic.

In our specific case, we are interested in the propagation of activity in one specific instance of the EDR network model. In order to relate the observed QPM dynamics to properties of the network and not only to the connection length λ we will keep the network fixed and average observables over 10000 instances of different fractions of initially ignited nodes only.

Thus, the behaviour observed as function of the EDR scale λ cannot be taken as hard proof since it may come from statistical variability and must be understood as conjectures. On the contrary, the behaviour observed as function of the quorum threshold m is not associated to statistical variability since m is constant over the network. Also, the conclusions one can draw from the analysis in the following sections are limited by the finite size of the simulated system which will be discussed.

The fraction of initially ignited neurons f

As explained in the previous chapter, there is a first order phase transition in the size of the giant active connected component. If the random fraction of initially activated neurons is too low there is no giant connected component, whereas once above a critical value, there is a giant active connected component. I want to characterize the spread of activity in the two-dimensional space. Hence, the quantity of interest is the number of iterations NOI to reach the stable state. It is fairly intuitive that for small values of initially activated neurons, there are only few propagating events and the number of iterations is small. The same thing happens when the fraction of initially ignited neurons is high: only a few number of time steps is sufficient to activate the whole network. Thus, I will first look at the specific point f^* where the number of iterations reaches its maximal value. For values $m < m_c$ it corresponds to the first order phase transition f_{c2} . Indeed, the number of iteration to reach the stable configuration is commonly used to find the critical point of the first order phase transition. [80] However, it is not restricted to this phase transition. For $m \geq m_c$ the number of iterations also goes through a maximum, and allows us to study the propagating dynamics above the transition.

The propagating dynamics is constrained by the network size. The more nodes there is, the longer the propagation will be. I will study networks of 10000 nodes. Since the computational time for simulating the model, and analyzing the result can be extensively long, I coded a program able to work with multiple processes. The time saving advantage, and the simplicity of implementation are the main arguments for this choice, however it requires more memory than multithreading. Hence, the size of the considered network could not be too large. This restricted me to an in-degree of 10, but allowed me to simulate ~ 10 networks at the same time without overloading the memory.

The simulated EDR networks' in-degree distribution sets the typical order of magnitude for the thresholds m_c . According to equation 2.1: $m_c/\overline{k_i} \approx 0.7^{13}$. In the following analysis the quorum will be express in terms of $m/\overline{k_i}$ and one need to keep in mind that above 0.7 the size of the giant active connected component is continuous in an equivalent Gaussian network.

[80]: Gao et al. (2015), 'Bootstrap percolation on spatial networks'

13: The standard deviation is sufficiently constant for all EDR scale and is approximated well by the square root of the mean in-degree like any Erdős-Rényi network

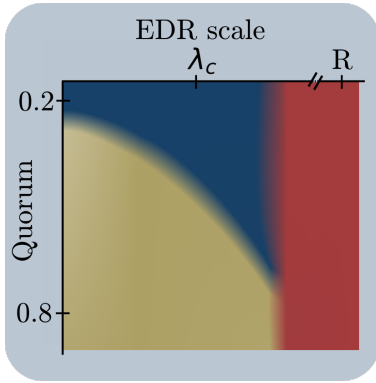


Figure 2.3: Schematic representation of the propagating dynamics transitions in the Quorum Percolation Model, with EDR network. The quorum is expressed as m/\bar{k}_i . The **blue** region represents a dynamics of localized nucleation. The **red** region represents a dynamics where no propagating front can be identified. The **gold** region represents a dynamics of fractured propagation. R is the culture radius, and λ_c computed with equation 2.3

14: Note that for high values of the quorum, the observation is made difficult by the high number of initially active nodes

15: In order to distinguish this dynamics, I tend to use the word nucleation when there is a rotational symmetry.

The QPM and synchronous bursting activity

A single instance of the QPM is understood as the initiation of a single burst. The fraction of initially activated nodes f and the threshold m represent (respectively) a uniform noisy excitation of the network and its excitability. The QPM can highlight the condition under which a network is able to produce a burst and if it is, the initiation dynamics can be analyzed.

2.3 Propagating dynamics

Exploration of the phase space (λ, m)

Before looking for quantification of the activity, it is interesting to observe the overall behaviour for different values of the connection length λ and the quorum m/\bar{k}_i . One specific instance of the QPM can be plotted in space, with the time step at which a node is activated being the observable. The different dynamics identified here, are summarized in the figure 2.3. They are all example of one of the longest propagation at the considered phase point (m, λ, f^*) . There are 3 patterns clearly identifiable.¹⁴

- ▶ **Localized nucleation:** For small values of the quorum m/\bar{k}_i and small values of the EDR scale λ , we observe a localized nucleation of activity and a propagation invariant by rotation. After the nucleation, the propagation respect a rotational symmetry around the nucleation centres. See figure 2.4, plot with EDR scale $\lambda = 150\mu\text{m}$: propagation starts in the middle blue-ish region and spread in every directions. There can be multiple nucleation centres (see on the same figure, plots with smaller EDR scale).¹⁵
- ▶ **Fractured propagation:** For larger values of the quorum m/\bar{k}_i and small values of the EDR scale λ , we observe a localized nucleation of activity, with an asymmetrical propagation. The propagation seems to be highly restricted by the network and create fractured patterns of activity. See for example, plots of figure 2.5 with an EDR scale $\lambda < 75\mu\text{m}$. The typical scale of the fractured patterns seems related to the quorum and EDR scale: they increase when m decreases, and when λ increases.

- **Non-propagating:** For high values of the EDR scale λ , we do not observe any propagating front correlated to space. The higher values of the quorum m/\bar{k}_i may indicate that there is a relationship with the mean degree: activated nodes are mainly in the centre, where the degree is higher (see figure 2.2). See plots with EDR scale larger than $400 \mu\text{m}$ in figures 2.4 to 2.6.

Figures 2.4 to 2.6 displays examples of these dynamics. One can notice that there is a clear difference between the *localized nucleation* and *fractured propagation*. The (m, λ) phase space is separated in (at least) two domains by a curve $m_1(\lambda)$. For $m < m_1(\lambda)$ the propagation is locally nucleated, whereas for $m > m_1(\lambda)$ the propagation is fractured. In the following sections, I will investigate this curve $m_1(\lambda)$ and try to characterize the different dynamics.

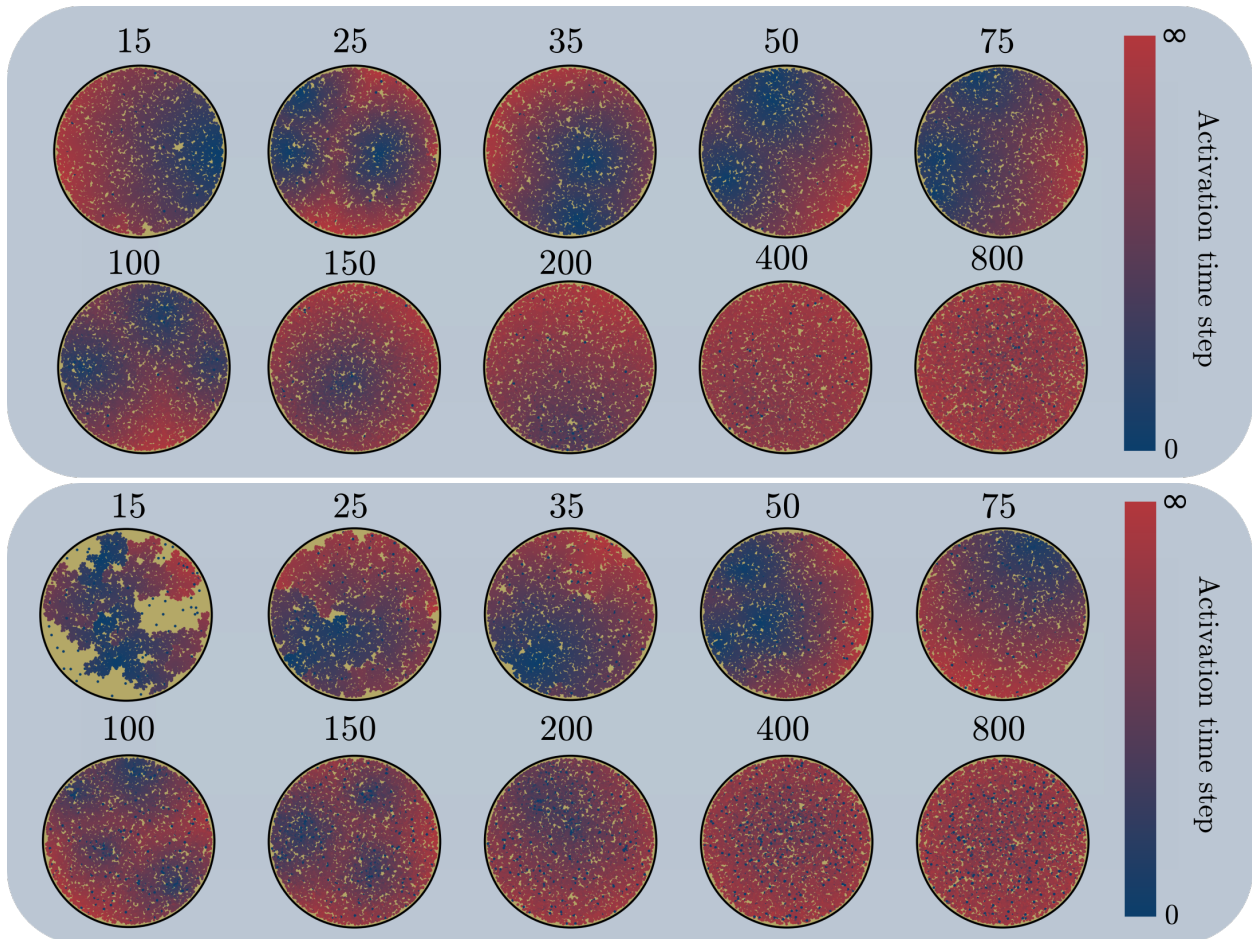


Figure 2.4: Representation in the 2D space of one instance of the Quorum Percolation Model, with threshold quorum $m/\bar{k}_i = 0.2$ (**top**) and $m/\bar{k}_i = 0.3$ (**bottom**). Colours represent the time of activation, from **blue** at the initial time to **red**, at the stable configuration in the infinite time limit. The corresponding EDR scale is written on top of each frame (in microns).

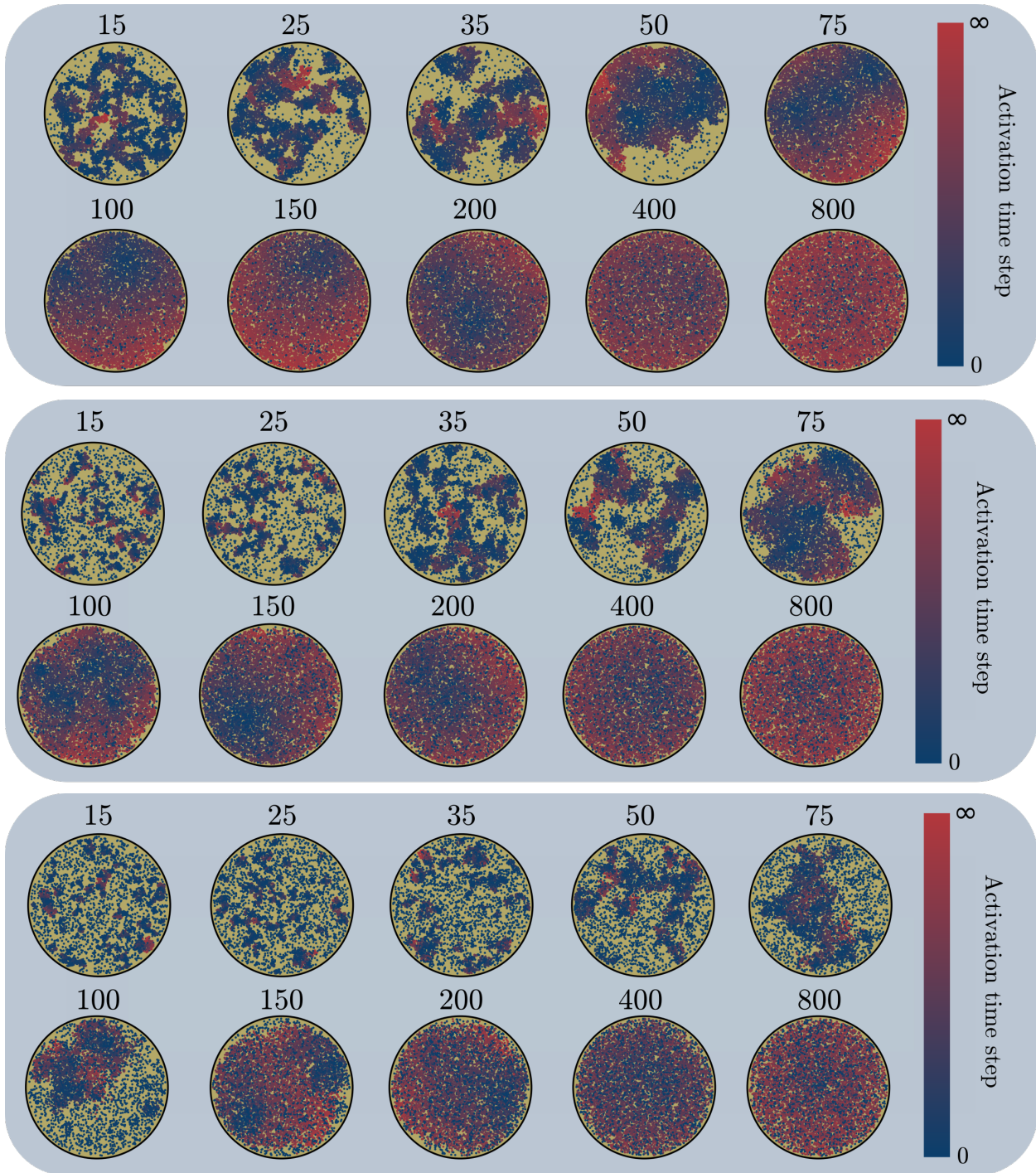


Figure 2.5: Representation in the 2D space of one instance of the Quorum Percolation Model, with threshold quorum $m/\bar{k}_i = 0.4$ (**top**), $m/\bar{k}_i = 0.5$ (**middle**) and $m/\bar{k}_i = 0.6$ (**bottom**). Colours represent the time of activation, from **blue** at the initial time to **red**, at the stable configuration in the infinite time limit. The corresponding EDR scale is written on top of each frame (in microns).

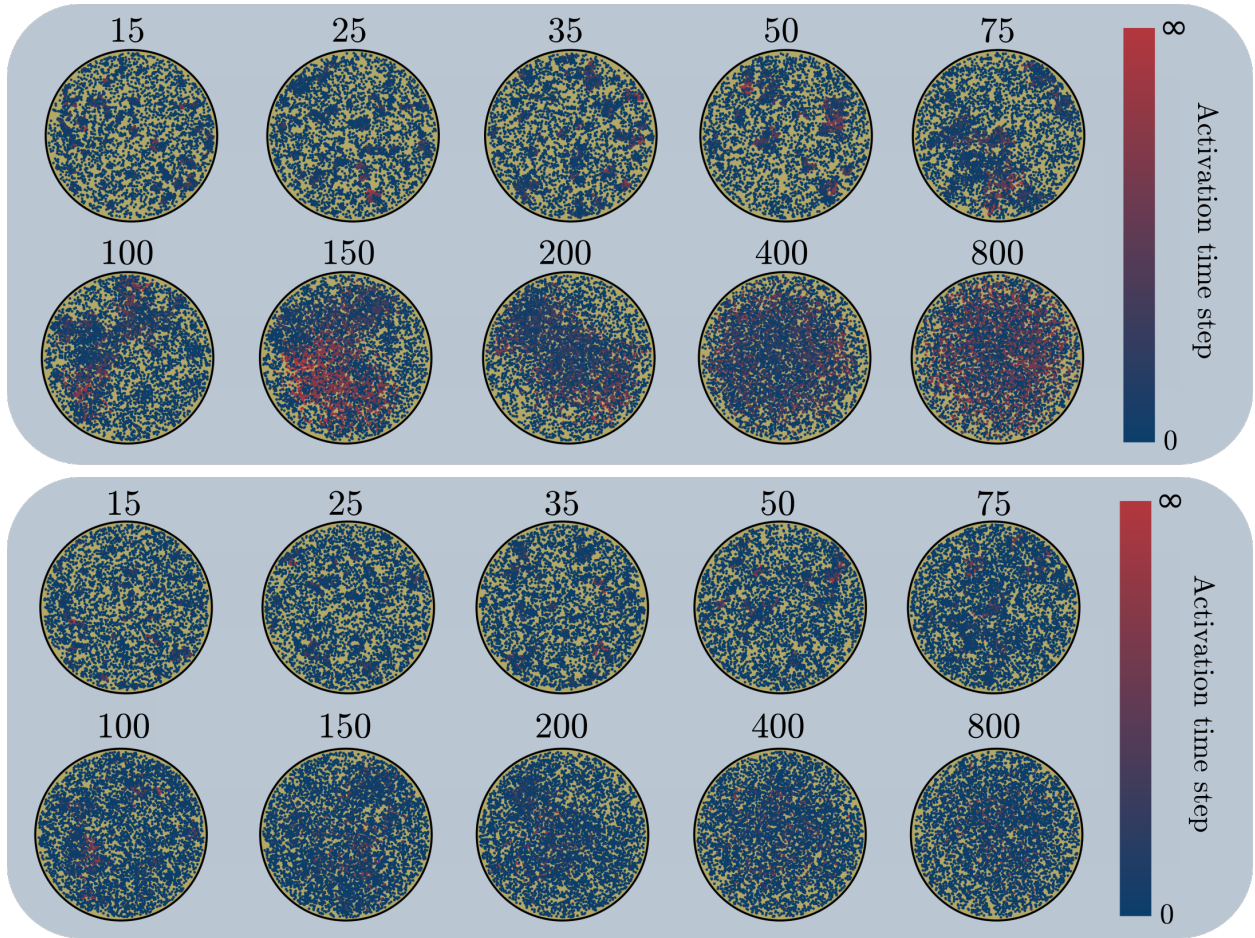


Figure 2.6: Representation in the 2D space of one instance of the Quorum Percolation Model, with threshold quorum $m/\bar{k}_i = 0.7$ (**top**) and $m/\bar{k}_i = 0.8$ (**bottom**). Colours represent the time of activation, from **blue** at the initial time to **red**, at the stable configuration in the infinite time limit. The corresponding EDR scale is written on top of each frame (in microns).

Number of iterations

Figure 2.7 shows the average number of iterations at the critical point, NOI^* as function of the quorum. We can see that there is a maximum for all values of the EDR scale. As λ is varied, this maximum decreases down to a constant value for $\lambda \sim 400 \mu\text{m}$, where all curves $\text{NOI}^*(m)$ merge into one. This behaviour seems related to the dynamics identified above: for an EDR scale higher than $400 \mu\text{m}$, there is no propagation front, hence the number of iteration does not depend on the EDR scale. On the contrary, when the EDR scale is smaller, the number of iterations depends on the network spatial structure and shows a maximum. This maximum can be associated with the transition between two dominating behaviours.

Unsurprisingly, the number of iterations depends on the propagating dynamics. On the one hand, slower propagating dy-

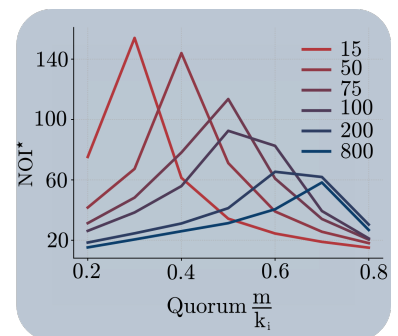


Figure 2.7: Number of iteration at the critical point, NOI^* , as function of the quorum m/\bar{k}_i , for different values of the EDR scale λ in range $[15, 800]$ microns. For values of λ higher than $\sim 400 \mu\text{m}$, all curves merge into one.

16: As we will see later, the propagation velocity increases with the EDR scale in the localized nucleation dynamics regime

namics will last longer because it will take them more time to reach the system size. On the other hand, the net number of recruitable nodes impacts the number of iterations. The maximum of NOI^* separates two regimes: one where the propagation is possible but slowed down by the typical connection length¹⁶, and a second where the propagation is jammed by the quorum threshold.

When the quorum is small with respect to the in-degree, long range connections make the propagation faster, thus the number of iterations decreases for increasing values of λ . However, when the quorum increases close to the smallest values of the in-degree distribution the propagation follows the only possible path in the network, made of the highest in-degree nodes. Hence, the propagation may be slow down, or even stop because of network local structure. The number of iterations decreases for higher values of the quorum. In between the two situations, there is a maximum describe by the $m_1(\lambda)$ function.

Branching parameter

Definition: Branching Process

[81]: Kendall (1966), 'Branching Processes Since 1873'

The branching process theory began with Sir Francis Galton and Reverend Henry William Watson. [81] Sir Francis Galton, an explorer, mathematician, geographer and so on was an ardent proponent of social Darwinism and presumably coined the term of eugenics in 1884. He was interested in the disappearance of family names, [82] and formulated the following problem: s

[82]: Galton (1873), 'Problem 4001'

Problem 4001: A large nation, of whom we will only concern ourselves with the adult males, N in number, and who each bear separate surnames, colonise a district. Their law of population is such that, in each generation, a_0 per cent of the adult males have no male children who reach adult life; a_1 have one such male child; a_2 have two; and so on up to a_5 who have five.

In a modern approach, a branching process is a model for population growth with discrete time. The population evolves according to a simple rule: in every generation $i = 0, 1, 2, \dots$ each individual produces in the next generation a random number of offsprings, independently of others. The model is governed by the probability of offspring, $p_n = P(\text{number of offsprings} = n)$.

Let X_n with $n \in \mathbb{N}^*$ be random variables drawn in the offspring distribution, and A_i with $i \in \mathbb{N}$ be the number of offspring at generation i . Then the transition probabilities, of state with k individuals, to state with n , can be written as

$$P(A_{i+1} = n | A_i = k) = P(X_1 + X_2 + \dots + X_k = n)$$

From this equation, it is possible to show¹⁷ that the expected value for the number of individual at generation i , $E(A_i) = \mu_i$ is governed by the expected value of offsprings, $E(X) = E(A_1) = \sigma$ (we consider that there is one individual at the initial time, $A_0 = 1$):

$$\mu_i = \sigma^i \Leftrightarrow \sigma = \frac{\mu_{i+1}}{\mu_i} \tag{2.4}$$

Hence, the population dies out if $E(X)$ is less than 1, and grows to infinity otherwise. This parameter, $E(X)$, is called the branching parameter. It corresponds to the average number of offsprings computed over the probability p_n : $\sigma = \sum_{n=0}^{\infty} np_n$

It is here assumed that

$$\forall (n, m) \in \mathbb{N}^{*2}, E(X_n) = E(X_m) = \sigma \tag{2.5}$$

Each individual is equivalent, and being born in a different generation does not change the expected number of offsprings. This is a stationnary branching process. Also, there is no interaction between the generation $i - 2$ and the generation i . In the case of quorum percolation, the population can be understood as the number of active nodes and the propagation can be studied with an equivalent of the branching parameter σ .

Branching rate in the QPM

In quorum percolation simulations, one can quantify the propagating dynamics with an equivalent of the branching parameter. In a time evolution process, we introduce $W(t)$ the number of activated nodes at time t . One can define the branching rate, a time dependent variable as:

$$\frac{E(W(t + \Delta t))}{E(W(t))} = \sigma_t \tag{2.6}$$

17: One can find it in many mathematics textbook on stochastic processes such as [83]

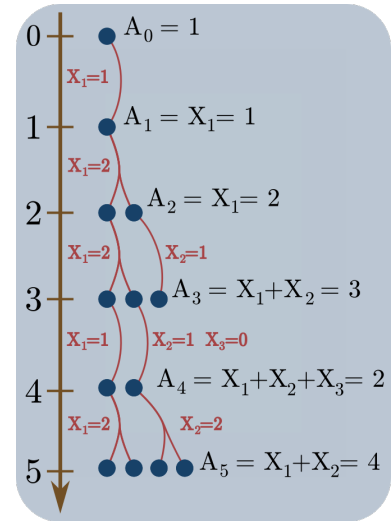


Figure 2.8: Representation of the first 5 generations of a Branching Process. For instance, the number of individuals at the 4th generation is 2 because the 3 individuals of generation 3 have only 2 offsprings in total: the random variables X_1, X_2 and X_3 drawn in the distribution of offsprings p_n are respectively evaluated to 1, 1 and 0.

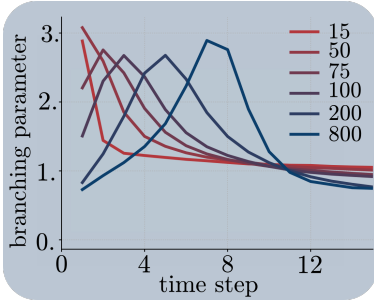


Figure 2.9: Branching rate σ_t , computed with eq. 2.6 in the firsts time steps of the quorum percolation model with EDR network of different spatial scale (displayed in microns). The quorum is $m/k_i = 0.2$.

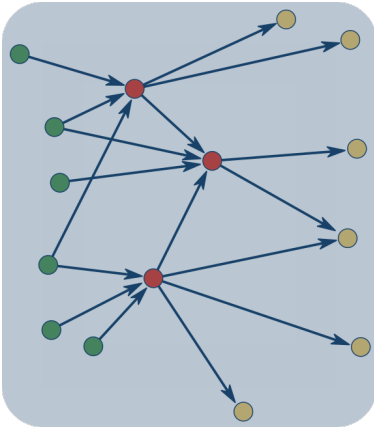


Figure 2.10: Schematic of an EDR network in the QPM. Only the connections going from left to right are shown. The **green** nodes are activated and **gold** nodes are not. Because of local fluctuation of seeding density, and a small EDR scale the **red** nodes have few connections going from left to right. They are unable to propagate the activity in this direction. Note that they have a high betweenness: the smallest path from the green to the gold nodes have to cross one of the red one.

The branching rate relates nodes activated at the time step $t + \Delta t$ to nodes activated at t . The question the branching rate can help us solve is whether the propagation can be sustained or not. There are two limiting factors able to stop the propagation of activity: the network size and the network locality¹⁸. Firstly, one can expect a decrease of the branching rate when the propagating front reaches the boundaries of the two-dimensionnal spatial network. The propagation is stopped because it has reach the limit of the environment. Secondly, the network may not be able to self-maintain the activity, because of local structural characteristics: see figure 2.10 for a schematic representation of how locality can interrupt the propagation.

Figure 2.9 shows the branching rate during the firsts time steps of the QPM simulation. One can understand the first order transition in the QPM with network embedded in space with this figure. Depending on the spatial connectivity scale, the emergence of a giant active component does not come from similar dynamics:

- ▶ For small values of the EDR scale, the initially activated nodes can represent a very high local excitation. The reason is that locally, the density of activable edges at $t = 0$ is in some area much higher than on the overall network, because of some nodes with high clustering values (see figure 2.1). Hence, at the firsts time steps the branching rate has a very high value: for each ignited node at t , 3 are ignited at $t + \Delta t$. However, this clustered network is not suited for propagation and the branching rate rapidly decreases, because of nodes with high betweenness (see figure 2.1).
- ▶ For larger values of the EDR scale, the clustering and betweenness are uniform in space. Hence the effective initial excitation is uniform in the network, and there is no particular region of higher excitation. However, the network is efficient in information transfer and the excitation is rapidly increased and propagated across the network.

The branching rate in the propagating dynamics transition

Figure 2.12 displays the branching rate σ_t as functions of the time step in the QPM. The branching rate's decrease due to the network size can be observed in localized nucleation dynamics (see top frame of figure 2.11), when the quorum and the EDR scale are low. This decrease happens with a relatively good statistics, meaning that most of the instances behave very similarly. We can observe that the time step at which this happens depends on the EDR scale and quorum. Hence, one may expect that the propagation speed and nucleation size depend on the quorum and EDR scale. We will look into it in latter sections.

Closer to the transition point m_1 where the dynamics appear fractured (see middle frame of figure 2.11), the branching rate does not show this slow decrease, but stays relatively constant with a significant decrease in the statistics. This seems to indicate a very irregular dynamics, where some realizations are able to propagate activity for a very long time whereas other cannot.

When the dynamics appear clearly fractured ($m > m_1(\lambda)$), the branching rate reaches a stable value σ_∞ lower than 1, with also a decreasing statistics as the time step goes up. The stable value σ_∞ depends on the EDR scale and the quorum (see figure 2.13). It decreases with increasing λ and m , showing that the network locality is the limiting factor for propagation in this regime. In the fractured propagation regime, the network is fundamentally unable to propagate activity up to the system size.

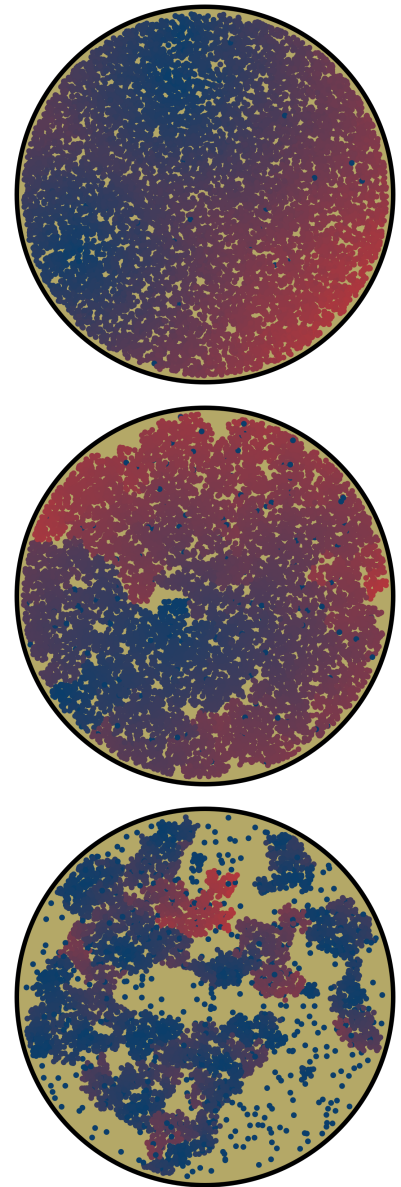


Figure 2.11: **Top** frame shows an example of a localized nucleation dynamics in a network with EDR scale 50 and a quorum $m/\bar{k}_i = 0.2$. **Middle** frame shows an example close to the transition point $m_1(\lambda)$ in a network with EDR scale 25 and a quorum $m/\bar{k}_i = 0.3$. **Bottom** frame shows an example of a fractured propagation dynamics in a network with EDR scale 25 and a quorum $m/\bar{k}_i = 0.4$.

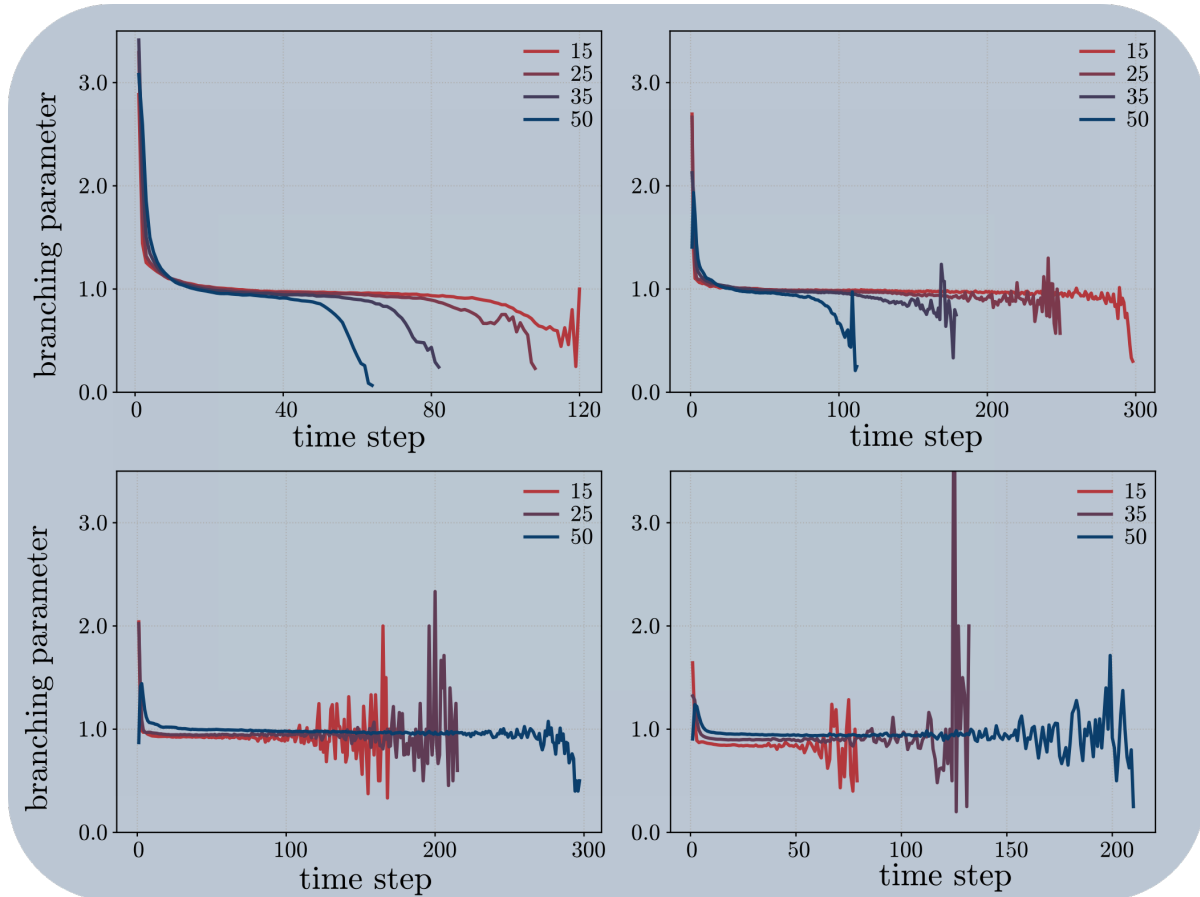


Figure 2.12: The branching rate, computed with eq. 2.6, for different values of the quorum and the EDR scale. Note that the y-axis is the same for all frames, whereas the x-axis is not. Also, the represented EDR scale is not the same in the two bottom frames for better visualization. The **top left** frame corresponds to a quorum $m/\bar{k}_i = 0.2$. The **top right** frame corresponds to a quorum $m/\bar{k}_i = 0.3$. The **bottom left** frame corresponds to a quorum $m/\bar{k}_i = 0.4$. The **bottom right** frame corresponds to a quorum $m/\bar{k}_i = 0.5$. It is interesting to know that the visible noise at the end of the activity comes from a lack of statistics. The longer the propagation, the more uncommon it is, hence the reduced number of realization in these time step ranges.

Close to the transition point $m_1(\lambda)$, σ_∞ is very close to one, hence the possibility to reach a system size event. See the middle plot of figure 2.11 with $\lambda = 25\mu\text{m}$ and $m/\bar{k}_i = 0.3$, the fractured dynamics spread to the whole environment. On the contrary, further away from the transition point ($m > m_1(\lambda)$), σ_∞ is smaller than one. The number of activated nodes at each time step, $W(t)$ decreases over time. We can expect the typical scale of avalanches in this regime to be finite, and dependent on the EDR scale, characterizing the ability or inadequacy of the network to propagate a complex signal.

We understand from figure 2.12 that the branching rate behaviour as function of the time step can be used to identify the transition $m_1(\lambda)$ from localized nucleation to fractured propagation in small EDR scale networks. When the EDR scale increases, m_1 increases close to the critical point of the quorum percolation phase transition m_c ¹⁹.

In figure 2.14, the evolution of the expected value $E(W(t))$ shows the emergence of a monotonically decreasing function when the quorum is higher than $m/\bar{k}_i \approx 0.7$ with a connectivity scale of $150\mu\text{m}$. This value is the critical point above which the quorum percolation phase transition is of second order. For high values of the EDR scale, the branching rate's decrease is to be associated with the quorum percolation phase transition. In this regime, the quorum m has reached the smallest values of the in-degree distribution: $m \approx m_c$ and the propagation is limited by nodes' in-degree. Looking at plots in figure 2.6 for large values of the EDR scale ($400, 800\mu\text{m}$) the propagation stops even if the border of the culture has not been reached. The apparent rotational symmetry seem to correlate with the in-degree (see figure 2.2) showing that the propagation is limited by nodes' in-degree.

Figure 2.15 shows the different limiting factors of propagation in the QPM in the (m, λ) phase space.

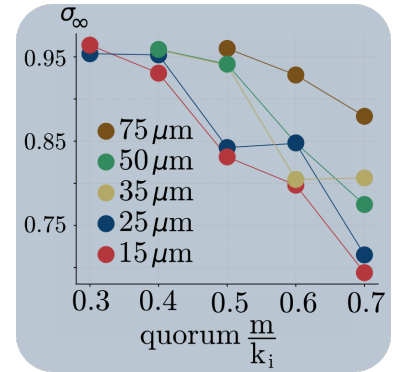


Figure 2.13: Stable branching rate σ_∞ as function of the quorum m/\bar{k}_i for different EDR scale.

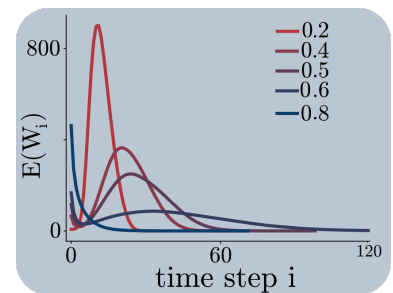


Figure 2.14: The expected number of activated nodes as function of the time step $E(W(t))$ for different quorum values (color scale). The quorum is expressed in terms of m/\bar{k}_i and the EDR scale is $150\mu\text{m}$

19: Remember the size of the giant active connected component is continuous if $m > m_c$, and in Gaussian network with equivalent degree distribution, $m_c/\bar{k}_i \approx 0.7$

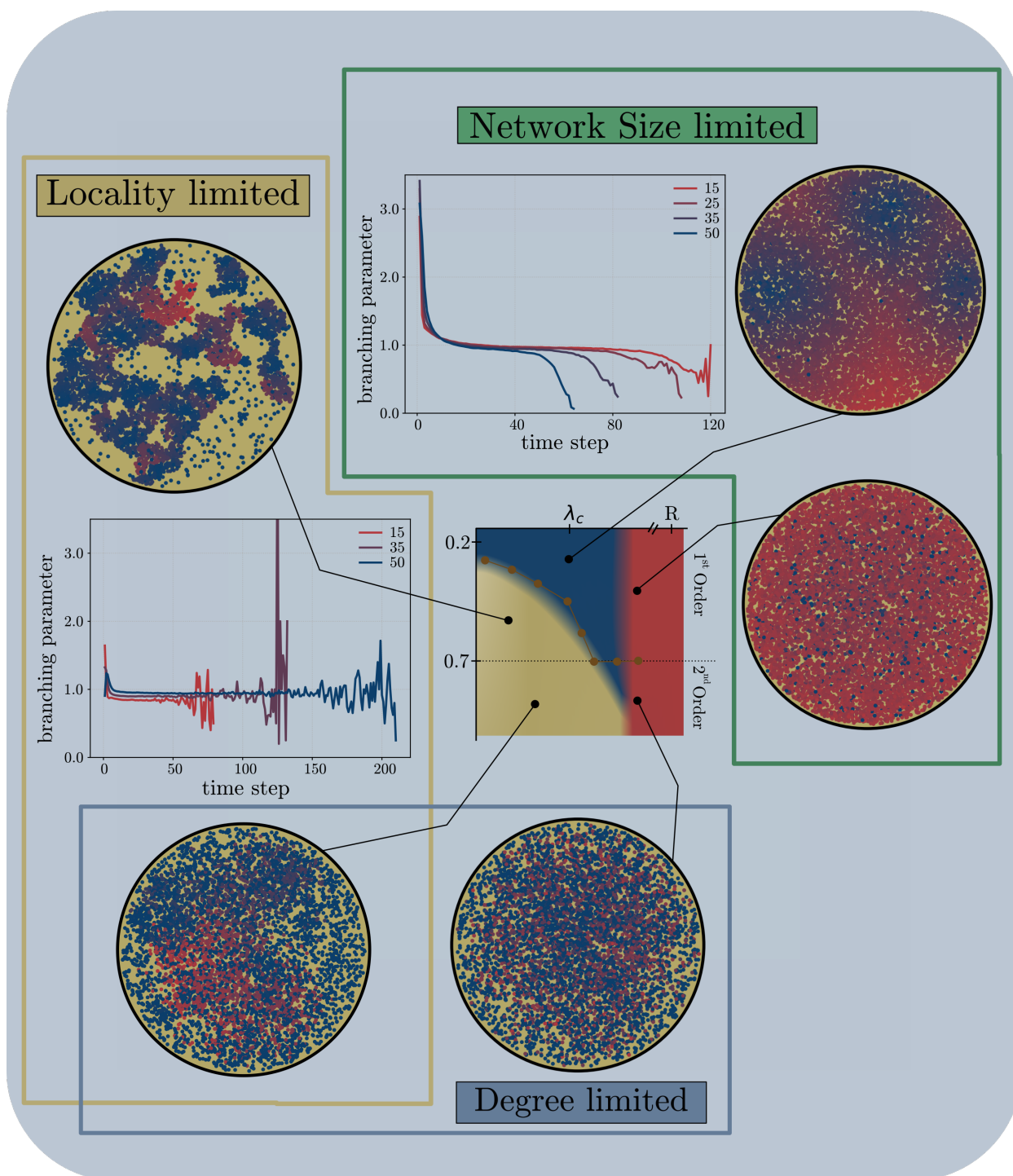


Figure 2.15: Representation of the limiting factors of propagation in the (m, λ) phase space. The **blue** region represents the localized nucleation dynamics. The **red** region represents non-propagating dynamics. The **gold** region represent the fractured propagation dynamics. The quorum value of 0.7 is the quorum percolation critical value in a space-free gaussian network: it separate first order to second order phase transition in the limit $\lambda \rightarrow \infty$. The **Network Size** is a limiting factor when the quorum percolation phase transition is of first order. In the localized nucleation regime this is characterized by the branching rate decrease when the propagating front reach the 2D culture boundaries. The **degree** is a limiting factor when the quorum percolation phase transition is of second order. The **locality** is a limiting factor when the EDR scale is small and $m > m_1(\lambda)$.

Characterization of the propagating dynamics

Avalanche: causal propagation of activity

Simulations of the QPM on a specific network allow looking for avalanches as correlated events. With the knowledge of both the activation time and the connections one can identify the active connected component that respect the network *and* time causality. The fraction of initially activated nodes act as an excitation of the network. This excitation being uniform, it may lead to several avalanches not in any way related to one another. One single instance of the QPM can create several avalanches of different sizes. One need to identify them properly in order to know there sizes.

I compute an avalanche size as the number of node in one connected component of a subgraph of the network (see figure 2.16 for graphical representation). First only activated nodes are taken into account in the subgraph. Second, we consider only the connections respecting the time causality. The connection from node A to B is kept in the subgraph, only if A has been activated before B. The resulting subgraph can be looked for connected components.²⁰ One connected component is made of active nodes with at least one path connecting any pair of nodes (A,B) such that A is activated before B. This is an avalanche. Hence, the number of node in individual connected component is the avalanche size. Figure 2.17 shows the avalanche size probability distribution in the QPM with spatially embedded networks.

The avalanche size distributions shows two different behaviours. Depicted in the left frame of figure 2.17, with small connectivity scale and large quorum values, the distribution displays a finite cut-off. This cut-off does not seem to be related to the initial excitation, since it decreases when the fraction of initially activated node f^* increases. It seems to indicate that for high quorum value, the propagation is jammed and cannot reach a system size event. The large number of activated nodes is formed of multiple small avalanches. There is again, a transition point where it appears that all scales of avalanches are represented in a distribution that may be close to a power-law with exponent $-3/2$. Nonetheless, this possibly scale free behaviour is not as easily observable in larger EDR scale, even close to the transition point m_1 .

20: In the search for connected components, the direction is not taken into account, and I look for what is called 'weakly connected components'

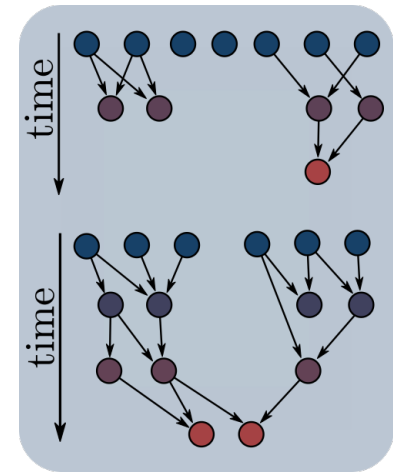


Figure 2.16: Example of avalanches in the QPM model. This sketch represents 2 instances of the QPM, only the connection going forward in time are represented. The **blue** dots are activated at $t = 0$. In the **Top** one there are 1 avalanche of size 4, 2 avalanche of size 1 and 1 avalanche of size 6. In the **bottom** one there is only 1 avalanche of size 15.

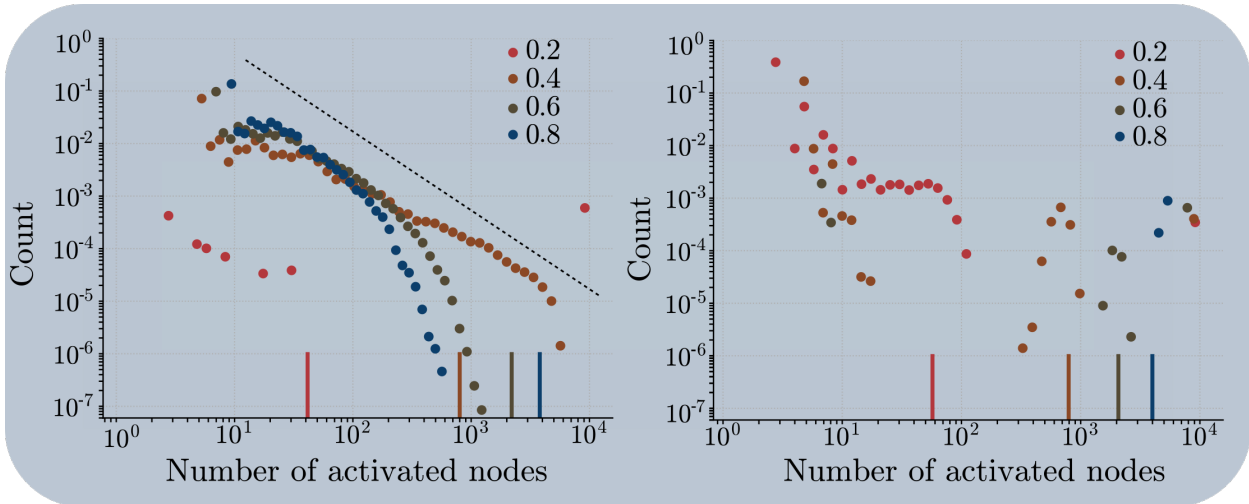


Figure 2.17: Normalized avalanche size probability distribution in the QPM with connectivity scale of $15 \mu\text{m}$ (**left**) and $800 \mu\text{m}$ (**right**). The quorum is expressed in terms of m/\bar{k}_i with a colorscale and the vertical lines show the value of the initially activated nodes $f^* \times N$, with N the total number of nodes. The dashed line in the left frame shows a -1.5 slope as reference. Note that the bins are logarithmically distributed, hence the amplitude may not be mistaken with the count of instances. For instance, in the case $m/\bar{k}_i = 0.2$ in red, the number of instances with an event of the size of the system is close to the total number of instances. However, the amplitude for an avalanche size of 10^4 node is similar to the one for an avalanche size of 10 which very rarely occurred. Note also that there is a gap without any avalanches in between 10^2 and 10^4 for the quorum $m/\bar{k}_i = 0.2$ on the left frame.

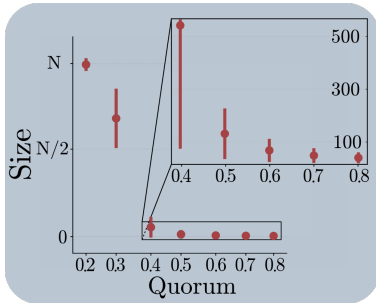


Figure 2.18: Average size of avalanches in the QPM with $\lambda = 15 \mu\text{m}$. The bar length represents the standard deviation of the distribution. The quorum is expressed in terms of m/\bar{k}_i and N is the number of nodes.

Figure 2.18 displays the average size of avalanches in network with $15 \mu\text{m}$ EDR scale. We can notice the change in the avalanche dynamics. For small a quorum value, all avalanches encompass the whole network. For larger values of the quorum, the activity is formed of multiple small avalanches with a typical size in the range of 100 nodes (1% of the network). The transition point, is characterized, like many critical systems by an increase of the variability, represented by the standard deviation in the figure. Figure 2.20 shows that the typical avalanches' size depends on the EDR scale. As the connectivity scale increases the number of node in an avalanche increases. This represents the idea that network locality is responsible for jamming the activity propagation.

The localized nucleation dynamics is more difficult to characterize with the correlated activity of avalanches. One may want to remember that it is mainly formed of a system size event, however more frequently than I would have expected smaller avalanches are also present with a non-trivial distribution.

When the EDR scale is large (see the right frame of figure 2.17), the avalanche size statistics represents the first order phase transition: the vast majority of QPM instances are of the size of the system, and only a few instances do not percolate.

These small avalanches' size scale is directly related to the initial excitation f^* . This type of dynamics corresponds of the non propagating dynamics (see figure 2.19).

Regularity of propagation ?

Is there a certain stability in avalanches ? We have seen that in the fractured propagation dynamics, there are avalanches with a finite size (see figures 2.17, 2.18 and 2.20). Are those avalanches random, or does it exists a frequent sequence of node activation ? We want to find a group of nodes $A, B, C \dots$ such that the sequence of activation $A \rightarrow B \rightarrow C$ etc... is more frequent than expected.

We define the edge activation probability as

$$P_{AB} = \frac{\text{number of instances where B is activated after A}}{\text{number of instances where A is activated}} \quad (2.7)$$

When computing this quantity, one may be careful that the number of realization where A is active is not too small which may result in a biased value.

For every point in the considered phase space (λ, m) , the distribution of P_{AB} was close to a log-normal with mean $1/\overline{k_o}$ the inverse of the mean out-degree(see figure ??). The average behaviour seems that every node activates randomly any of its out going neighbors. The recurrence of activation seems independent of the spatio-temporal dynamics: the overall statistics being relatively close with one another.

Giving a closer look, one may try to find a specific path in the network where the probability P_{AB} is the highest possible. This would represent the most probable propagation given the activation of certain nodes. In other words, we want to find weekly connected components in which the edge activation probability of any connections would be higher than an arbitrary threshold. Figure 2.22 shows such weekly connected components of a networks with EDR scale of $15 \mu\text{m}$. Be careful, this figure does not represent specific nodes with a higher probability to be activated, but the most probable connected components that would be activated if some nodes of this very same component are activated.

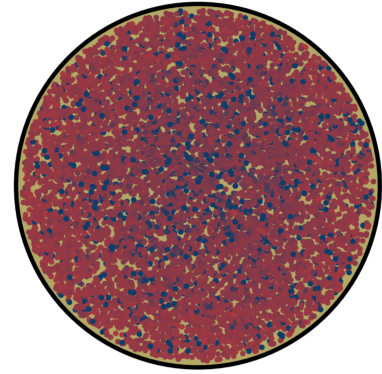


Figure 2.19: Non propagating dynamics in a network of EDR scale $800 \mu\text{m}$ and quorum $m/\overline{k_i} = 0.4$

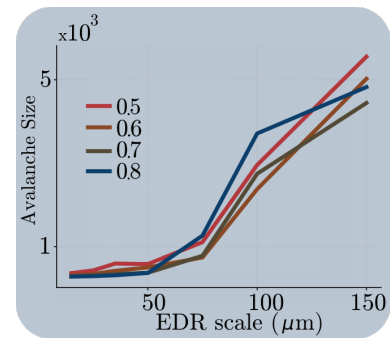


Figure 2.20: Average size of avalanches in the QPM as function of the connectivity scale. The quorum is expressed in terms of $m/\overline{k_i}$.

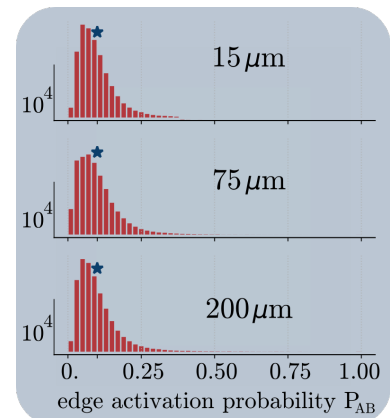


Figure 2.21: Distribution of the edge activation probability computed with equation 2.7 in 3 networks with EDR scale 15, 75 and $200 \mu\text{m}$. The mean value is shown with a blue star and is always 0.1.

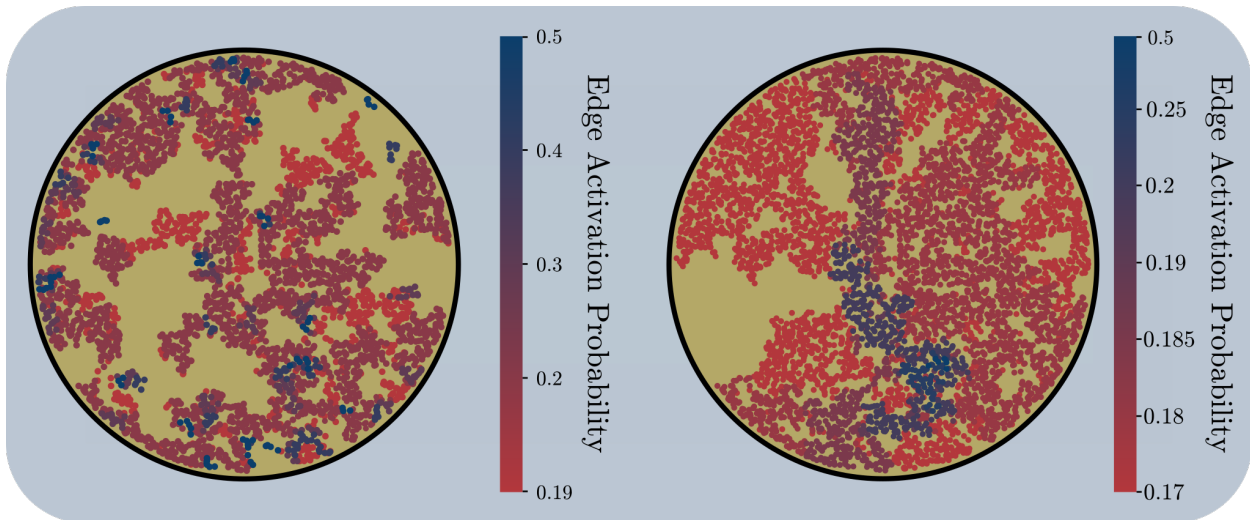


Figure 2.22: Weekly connected components with high edge activation probability in network with $\lambda = 15\mu\text{m}$. The threshold is expressed with the colour scale (Note that the scale is not linear). The **left** frame displays all weekly connected components for a given threshold for the probability P_{AB} . For a given threshold, each individual weekly connected components are drawn with the same colour, although they may be distinct. The **right** frame displays a single weekly connected component for each given threshold for the probability P_{AB} . The drawn component is the one with a specific neuron in it, picked randomly in the ones with highest P_{AB} value. This frame shows the most probable avalanche once this node has been activated.

The first observation is that the edge activation probability is in the large majority smaller 0.4. The edges chosen the most frequently (in blue) are not structured in the 2D space but spread uniformly. We can see that the emergent structure does not present any symmetry: it describes the default type of propagation in the considered regime: fractured propagation (see figure 2.23).

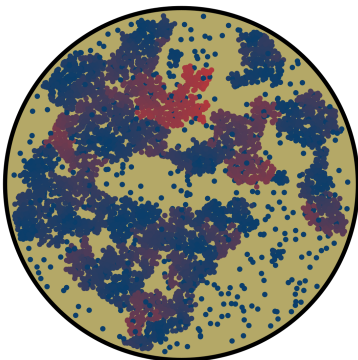


Figure 2.23: Fractured propagation in a network of EDR scale $25\mu\text{m}$ and quorum $m/k_i = 0.4$

The lack of regularity is here expressed in terms of low values of the edge activation probability P_{AB} : at a single node scale, the direction of propagation is chosen randomly within all its out-going neighbors. Also, the uniform distribution in space of the most probable connected component (in blue) indicates that even if some out-going neighbors are more frequently chosen, they are not related to one another in the network: there is no frequent sequence of activation with more than 1 or 2 nodes.

When the dynamics is locally nucleated, the regularity of each realization increases. The largest weekly connected subgraph appears for larger probability threshold. Indeed, the main difference between different realizations is the number and position of nucleation centre. One can understand that changing the centre of nucleation does not change much sequence of activation for neurons away from the centre. Hence, neurons close to the border have a higher probability to be found in

regular avalanches. For this type of dynamics, the centre of initiation and first to be activated neurons are the property able to quantify the regularity.

Remarks on the QPM First let us state that, the QPM is a first order Markov chain because the state of the network at time t depends only on the state of the system at time $t - \Delta t$. Mathematically,

$$\begin{aligned} P(A(t) = a_t | A(t-\Delta t) = a_{t-1}, \dots, A(0) = a_0) \\ = P(A(t) = a_t | A(t - \Delta t) = a_{t-1}) \end{aligned}$$

where $A(t)$ is a random variable listing all the active nodes at time t .

Nonetheless, the sequence of activation is not well represented by a first order markov chain. Let us consider the sequence $A \rightarrow B \rightarrow C$, where A,B and C are nodes in the network. One can write that

$$\begin{aligned} P(A \rightarrow B \rightarrow C) &= P(A \rightarrow B) \times P(A, B \rightarrow C) \\ &= P(A \rightarrow B) \times (P(A \rightarrow C) + P(B \rightarrow C)) \end{aligned}$$

For networks with low clustering values, the probability that the triangle ABC exist is very low. Hence, the propability of a sequence can be approximate with

$$P(A \rightarrow B \rightarrow C) = P(A \rightarrow B) \times P(B \rightarrow C)$$

The sequence probability is dominated by what I defined as the edge activation probability. We showed above that there is no highly frequent sequence of activation. However, in network with high clustering value the probability that the triangle ABC is not uniform in space, and can reach high values. Thus the estimation of the most probable avalanche should in reality take into account this "long range interaction" in the network space.

Dynamics: first-to-fire and propagation

We understand that there is no proof of regular avalanches. It means that there is no regular initiators: the nodes activated at the first time steps are chosen randomly by the initial excitation. In the following section, we are going to look for the initiators, and we can already say that there is no specific region, nor specific nodes that is more frequently a centre of nucleation or a first-to-fire. The typical size of nucleation and the propagating velocity are interesting properties of the dynamics that require to find the firsts activated nodes.

Method

I propose here a procedure to detect the surface of initiation, specifically designed to study the localized nucleation dynamics. The idea is that we are going to map the 2D discrete activation pattern into a time dependent 2D surface $S(t)$. The surface of initiation will be identified as a specific time point in this 2D function.

As a first hypothesis, I consider that the 2D culture is homogeneously and randomly seeded. Secondly, I suppose that a nucleation centre is a surface where the local density of activated nodes is close to the total local density. The initiation of a localized nucleation starts by recruiting all nodes in a given region.

Once identified I will evaluate the surface with two criteria:

1. The number of activated node outside the surface must be small compared to the number of activated node inside the surface.
2. The surface must be the smallest possible.

In order to quantify these two criteria I introduce the surface performance:

$$P(S(t)) = \frac{A_t^S}{A_t^o} \quad (2.8)$$

with A_t^S the number of activated nodes in the surface $S(t)$ at time t , and A_t^o the total number of activated nodes at time t .

The performance extreme values are 0 and 1. A performance $P(S(t))$ close to one, means that the surface $S(t)$ encompass the majority of active nodes. At $t = 0$ the initially activated

nodes are uniformly spread in the 2D space, hence no surface can be found to properly describe the activity: the area $|S(t = 0)| = 0$ and the corresponding performance $P(S(t = 0)) = 0$. As time grows, a nucleation point appears and one can find a surface $S(t)$ that encompass the activated node in this nucleation region. The initial excitation being still present, the performance increases from 0, but is not necessarily close to one. Once the number of nodes in the nucleation centre is close to the number of nodes in the initial excitation the performance is close to one. As time grows, the surface area increase in order to describe the spread of activity and the performance stays relatively close to one. Once the activity has reach the size of the system, the surface will be close the culture and the performance close to 1. This expected behaviour can be found in figure 2.24.

For a localized nucleation, one expect to find a small surface able represents the majority of all activated nodes: the initiation surface. I define this surface as the smallest surface with the maximum performance. It can be found by looking at the maximum of

$$P(S(t)) - \frac{|S|}{|C|} \quad (2.9)$$

with $|S(t)|$ being the surface area, and $|C|$ being the culture area. This maximum is associated with a nucleation time t_n and a surface $S_n = S(t_n)$. Figure 2.24 shows a schematic representation of this computation.

Description of the activity with 2D surfaces

In order to map the observed dynamics (see localized nucleation in figure 2.4), made of multiple centre of nucleation, the surface $S(t)$ has to be computed for each individual instance. The number of regions depends on individual instance of the QPM, and we don't want to fix it to a certain value. Also, we will look for surfaces as circles because the nucleation centre and the propagation are invariant by rotation. One could look at every time step, and draw by hand the surface $S(t)$, however this is extremely time-consuming and lacks reproducibility. The procedure described below is a simple automatic way to identify the surfaces $S(t)$.

Looking for non-connected regions of high activity can be done by looking for clusters of active nodes. A cluster is a group of nodes, sufficiently close from one another in the

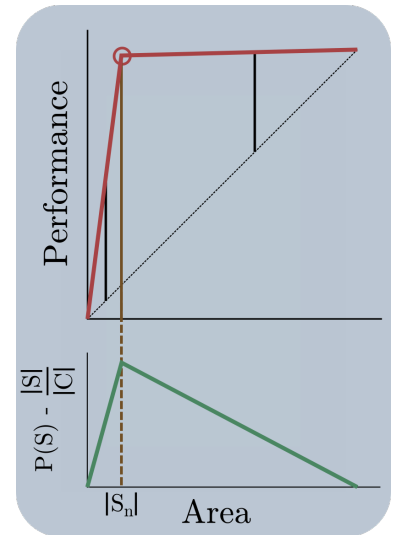


Figure 2.24: Schematic representation of the performance and the corresponding $P(S) - \frac{|S|}{|C|}$. Once the performance is close to unity it stays relatively constant. The circled point corresponds to the point where the surface $S(t)$ is the surface of initiation. It can be computed by calculating the distance between the performance and the first bisecting line and looking for the maximum.

[84]: Ester et al. (1996), 'A Density-Based Algorithm for Discovering Clusters in Large Spatial Databases with Noise'

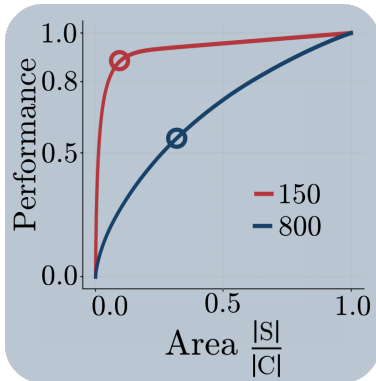


Figure 2.25: Performance average over 1000 realizations of percolating events for network of EDR scale 150 and 800 μm . The circle shows the point of the surface initiation computed with equation 2.9.

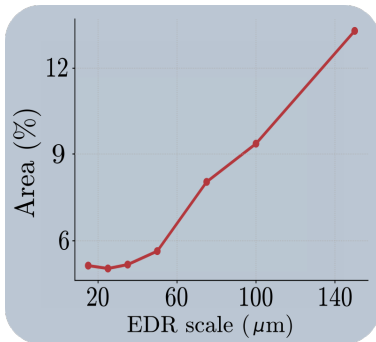


Figure 2.26: Area of the initiation surface as function of the EDR scale. The area is expressed in percentage of the culture area.

2D space. There exists multiple different algorithm able to find different categories of clusters. The one we use here is called DBSCAN [84] because it requires few number of parameters and there is no need to add the number of clusters as input. This algorithm can be run at each time step in order to find separated clusters of activity. Then each cluster is approximated by the smallest disk that encompass every cluster's node. The union of all disks is the surface $S(t)$ at the corresponding time step. As time grows, the total number of active nodes increases along with the surface area of $S(t)$.

The performance of all $S(t)$ surfaces can be computed as a function of the surface area in order to find the surface of initiation. Figure 2.25 displays the performance with a non propagating dynamics and a localized nucleation. As expected, when the dynamics nucleates locally the performance sharply increases close to 1, and then stays constant. On the contrary, when the initiation is not localized the performance increases slowly, because there is no localized region of high activity. The surface of initiation is then much larger, here close to 40% of the culture but still represents poorly the overall nodes' activation.

Hence, the performance is able to represent the typical size of the nucleation region, with the maximum of equation 2.9, and quantify the locality of the activation pattern, with the curve $P(S)$. The more $P(S)$ is close to the first bisector line, the less localize the initiation is.

Figure 2.26 shows that the area of the initiation surface increases with the EDR scale. With the hypothesis that the density is homogeneous, the bigger the area the more neurons there are in the surface. With a larger connectivity length, the clustering decreases and the interconnected nodes are further apart, hence a region with 100% recruited node is larger. Also, as the EDR scale increases there is a slight increase (above 50 μm for $m/\bar{k}_i = 0.2$) in the fraction of initially ignited nodes f^* . Thus, the number of activated nodes outside the surface is effectively larger, decreasing the performance and resulting in a larger surface of initiation.

Initiation of activity

Because several nucleation centres may be resent simultaneously with different radii, computing the propagation is

not straightforward. In order to estimate the propagation velocity from a nucleation centre to any node in the network, one needs to estimate the distance to the closest border of the initiation disks (computed above). A simple way to do this is to enlarge the initiation surface boundaries by a quantity r in every direction. Then, the distance from any node n is the value of the corresponding expansion r_n . Figure 2.27 shows such expansion of initiation surface made of 3 distinct nucleation centres. This process respects the rotational symmetry of the propagation with multiple centre of symmetry.

The expansion parameter r can be plotted as a function of average time of activation to compute the velocity with a linear regression. Figure 2.28 shows the expansion parameter r plotted versus the time activation for one realization with a network of EDR scale $50 \mu\text{m}$. The first observation is that the velocity is constant over time: correlation coefficients of all realizations are close to $r^2 = 0.99$. The linear evolution demonstrates the rotational symmetry observed and that the propagation velocity depends only on the QPM simulation parameters (λ, m) and not the position in the 2D space.

Figure 2.28 shows values of the expansion parameter r smaller than zero. They correspond to the initiation surface shrinking and are also associated with a linear propagation. The initiation surface boundaries do not correspond to a shift in dynamics, from a non-propagative nucleation to a propagation front. In figure 2.28, the right frame shows the first time step of a percolating event. We can see that the propagation starts at $t = 1$ for both nucleation centres. There is no proof of an initiation/nucleation phase after $t = 0$ where the dynamics would be different from a propagating front. The closest phase to an initiation/nucleation one can think of is the initial excitation $t = 0$. In a continuous excitation process, where a single node is activated per time step, the initiation/nucleation can be understood as the time required for a quorum to be activated in a group of interconnected nodes. However, in the QPM the excitation being concentrated at $t = 0$ the initiation/nucleation is constrained to this single time step.

Because the nucleation is concentrated in $t = 0$ each individual nucleation centres are synchronized. Again, in a continuous excitation process, with a single node being activated per time step, different centres of nucleation might be out of sync with each others. The corresponding phase difference, if too large, would make this analysis dysfunctional. Because nucleation centres in the QPM are synchronized at $t = 0$,

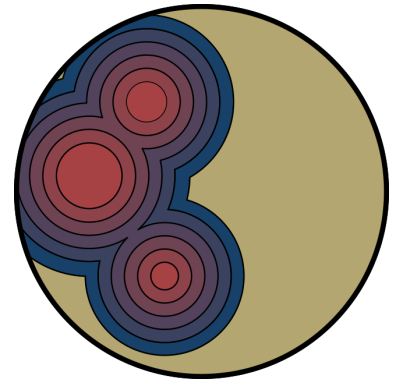


Figure 2.27: Computation of the distance to the initiation surface. The surface S_n , consisting of 3 disks, is here represented in bright red. The distance from S_n is represented by the colour scale.

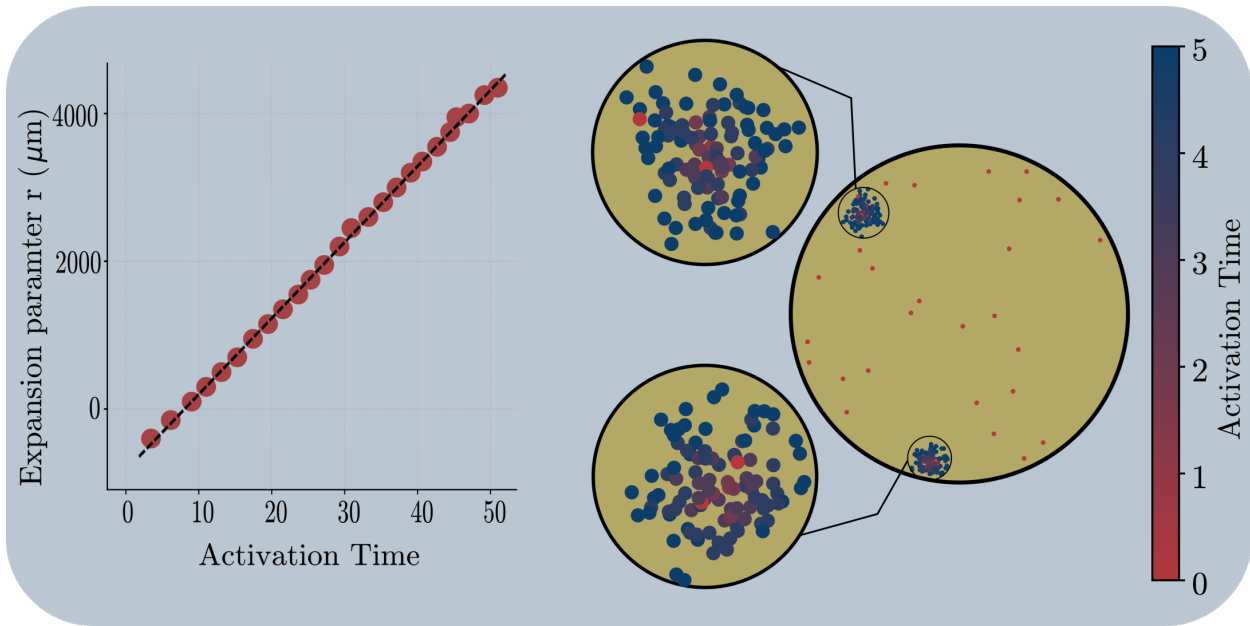


Figure 2.28: The left frame shows the expansion parameter r as a function of the time of activation. Negative values of r correspond to the initiation surface shrinkage. Only a fraction of the data points are shown for better visualisation and the dashed line represents the linear regression. The right frame displays the first activation time in the 3000 μm radius circular culture. The initiation surface is made of 2 disks of radius 450 (top) and 400 (bottom) μm .

their corresponding propagation front meet one another at the equidistant line from the nucleation centres.

Propagation velocity

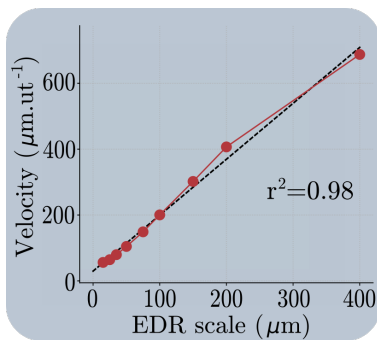


Figure 2.29: Propagation velocity as function of the EDR scale. The quorum is $m/\bar{k}_i = 0.2$ corresponding to localized nucleation. The velocities fall onto a linear evolution as functions of λ . The correlation coefficient is $r^2 = 0.98$ and the slope is 1.7 ut (ut refers to unit of time)

Instinctively, one may expect the propagation velocity to depend on the connectivity length scale λ and even predict that for each consecutive time step, the propagation front advances by a quantity equal to the mean connectivity length. Figure 2.29 displays the propagation velocity as function of the EDR scale λ . The linear evolution seems to indicate that the propagation front advances by a quantity higher than the connectivity length. The distance covered by the growing front is 1.7 times the EDR scale. Also, this relation seems to hold over an entire decade. Figure 2.1 shows that the connection length distribution widens close to λ_c and stays similar as λ increases. Thus, the long range connections do not seem to be at the origin of this fast propagation.

One may wonder why the evolution of the velocity with respect to the EDR scale correlates so well with a linear curve. First, one may argue that the method used here is biased and forces the linear relationship. However, I believe that it is

related to that fact that each realization is done on an effective different network. We have seen that there is no specific centre of initiation and the nucleation point changes for every realization. Thus, from the point of view of the couple of first-to-fire nodes and the propagating front the network is effectively different one realization from the other.

The interaction between the mean in-degree and quorum is expected to be a relevant quantity. Figure 2.30 shows that the velocity is indeed linearly correlated with the quorum m/\bar{k}_i . The higher the quorum, the slower the dynamics is.

2.4 Discussion

We have studied the spatio-temporal dynamics of the quorum percolation model in spatially embedded networks, described by the mean connection length λ . Three dynamics of propagation have been identified in the (λ, m) phase space. In the limit of long range connection, $\lambda \gg \lambda_c$, the dynamics does not exhibit a propagating front. The only correlation with the 2D space that exist with the activation patterns is as the quorum got closer to $m_c = \bar{k}_i$. In this regime the propagation is highly limited by the in-degree and does not reach the circular culture boundaries.

In the short range limit, $\lambda \leq \lambda_c$, the dynamics is correlated with the 2D space. We have shown evidences of a transition from a propagation that respects a rotational symmetry centred on specific nucleation points, and a propagation seemingly random and erratic. This erratic propagation, named 'fractured propagation', exists for a quorum smaller than a value m_1 . This transition point m_1 depends on the mean connectivity scale λ . The localized nucleation dynamics appears in a confined region of the phase space ($\lambda < \lambda_c, m < m_1(\lambda)$). We have shown that m_1 is a monotonically increasing function of EDR scale up to a certain point, ($\lambda > \lambda_c, m < m_c$) where the localized nucleation does not exist any more and the transition shifts toward the non-propagating dynamics.

We have shown that below m_1 , the correlated propagation of activity is predominantly made of percolating system size events. There exists only a fraction of finite scale correlated events. On the contrary above $m_1(\lambda)$, the fractured propagation dynamics exhibit multi-scale correlated events. The

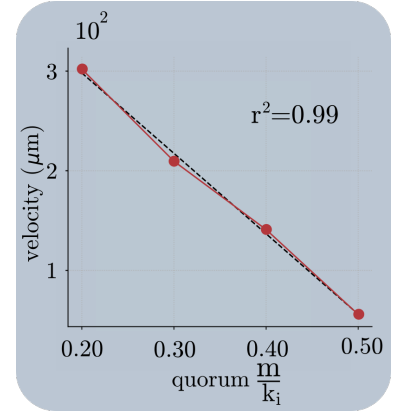


Figure 2.30: Propagation velocity as function of the quorum m/\bar{k}_i for an EDR network with $\lambda = 150\mu\text{m}$. The velocities falls onto a linear evolution with a correlation coefficient is $r^2 = 0.99$ and the slope $-800 \mu\text{m}\cdot\text{ut}^{-1}$ (ut refers to unit of time)

transition point m_1 may even be related to a scale-free behaviour, with a power law of exponent $-3/2$.

The analysis conducted here suggests that the critical value m_c above which the first order transition become a second order one depends on the connectivity spatial scale. Locality is able to jam the signal propagation, reducing the possibility for a system scale events to appears discontinuously.

The discontinuity is associated with the power-law distribution of subcritical clusters just below the critical point of initially ignited nodes f_{c2} , which resonates with the distribution of neuronal avalanches. However, we have shown that below m_c the QPM exhibits only system size correlated avalanche. The subcritical clusters are unable to produce multi-scale avalanches, because once activated they are part of a much bigger avalanche. Still, it seems that the sought scale-free behaviour of correlated avalanches may be present at the critical point $f = f_{c2}$ and $m = m_c$. However, in space-free random network the large value of $m_c = \overline{k_i}$ imply a large value of f_{c2} , such that most of the activated nodes are activated at the initial time $t = 0$ and not through the percolating event. One may wonder the relevance of this in the framework of spontaneous neuronal avalanches. However, following the idea that the critical point m_c depends on the EDR scale, it is possible for small initial fractions f_{c2} to initiate a scale-free avalanche distribution in a quorum percolation model with spatially embedded networks. Locality is a critical parameter in the search for multi scale correlated avalanches.

It is important to keep in mind neuronal cultures order of magnitude. The in-degree ranges from 60 to 150 and the density from 100 to 1000 mm^{-2} . These values correspond to $\lambda_c \sim \frac{\overline{k_i}}{d}$ ranging from 0.25 to 1.25 mm. The typical size of axons, in mature cultures, is expected to be closer to a couple of millimetres, making the neuronal culture probably closer to a space-free random network than a spatially embedded one. However, the experimental recordings are not entirely consistent with one another. Some show a scale-free behaviour, others a complex propagation or a localized nucleation. After making my very own neuronal culture I can see how the local density and its fluctuation may have an extremely important role in understanding of recorded activity. The scale λ_c may appear as a something to keep in mind when interpreting neuronal activity.

Spatio-temporal Dynamics in bursts of synchronized Pacemakers

3

In the previous chapter, we saw that the Quorum percolation model, although assumed to describe only the response to an excitation, may be able to capture some features of *spontaneous* neuronal activity. The model is indeed simplistic and does not take inner neurons dynamics into account. A model of neuronal population dynamics needs to go beyond the simple response to an excitation and

In this chapter I investigate one specific type of dynamics: pacemaker neurons. As we have seen in the introduction, pacemakers are present in multiple neuronal systems and may be able to explain the synchronization in a bursting regime observed neuronal cultures. This work is based on my publication: “A novel methodology to describe neuronal networks activity reveals spatiotemporal recruitment dynamics of synchronous bursting states” [85] which is presented here reformatted and with only some minor modifications.

Abstract

We propose a novel phase based analysis with the purpose of quantifying the periodic bursts of activity observed in various neuronal systems. The way bursts are initiated and propagate in a spatial network is still insufficiently characterized. In particular, we investigate here how these spatiotemporal dynamics depend on the mean connection length. We use a simplified description of a neuron’s state as a time varying phase between firings. This leads to a definition of network bursts, that does not depend on the practitioner’s individual judgment as the usage of subjective thresholds and time scales. This allows both an easy and objective characterization of the bursting dynamics, only depending on system’s proper scales. Our approach thus ensures more reliable and reproducible measurements. We here use it to describe the spatiotemporal processes in networks of intrinsically oscillating neurons. The analysis rigorously reveals the role of the mean connectivity length in spatially embedded networks in determining the existence of “leader” neurons during burst initiation, a feature incompletely understood observed in several neuronal cultures experiments. The precise definition of a

3.1 Introduction	50
Motivations	51
Objectives	53
3.2 Materials and methods	53
Numerical simulations	53
Spike time analysis . .	55
Spatial Spike Analysis	61
3.3 Results	64
Burst initiation	64
Spatial initiation: Cluster algorithm performance . .	65
Looking for leaders . .	66
3.4 Discussion	68
Dynamical regimes . .	68
Experimental data . . .	71
3.5 Conclusion	71
3.6 Chapter’s appendix . .	73
Simulation of Neuronal Network	73
Analysis with the Izhikevich model, synaptic depression and stochastic inputs	76
Firing rate and first spike probability distribution .	79

burst with our method allowed us to rigorously characterize the initiation dynamics of bursts and show how it depends on the mean connectivity length. Although presented with simulations, the methodology can be applied to other forms of neuronal spatiotemporal data. As shown in a preliminary study with MEA recordings, it is not limited to *in silico* modeling.

Keywords Network Burst · Synchronization · Dynamics · Phase · Initiation · Propagation

3.1 Introduction

With experimental recordings or numerical simulations from the whole brain to neuronal cultures [49, 86–88] scientists try to understand the information processing [89] underlying propagating activities in complex neuronal networks. Phenomena of rhythmic activity coupled to propagation are extensively studied in complex neuronal systems. In a bottom up approach, exploring the variety of activity patterns that exists is a relevant path in order to understand higher brain functions, or diseases. As an example, propagating waves have been identified as the default activity of cortical structures. They are observed in various conditions, during sleep in the healthy brain, or during epileptic epochs, and at different scales: from thousands of neurons in less than a millimeter in culture, to billions of neurons through the whole cortical layer. [90, 91] In order to go even deeper in the understanding of neuronal wave activity, one needs reproducible and unbiased quantitative measurements adapted to the considered phenomena.

We propose here a methodological approach of such phenomena motivated by studies on neuronal culture activity. [92–94] Although recorded at different scales, activity observed *in vitro* are thought to be a well suited model for propagating phenomenon in the brain either similar to slow wave sleep [95] or to epileptic activity [96, 97]. Indeed, recent studies on young 2D neuronal cultures have forwarded evidences that

[86]: Olmi et al. (2019), ‘Controlling seizure propagation in large-scale brain networks’

[87]: Massimini et al. (2004), ‘The Sleep Slow Oscillation as a Traveling Wave’

[88]: Paraskevov et al. (2017), ‘A spatially resolved network spike in model neuronal cultures reveals nucleation centers, circular traveling waves and drifting spiral waves’

[49]: Orlandi et al. (2013), ‘Noise focusing and the emergence of coherent activity in neuronal cultures’

[90]: Sanchez-Vives et al. (2017), ‘Shaping the Default Activity Pattern of the Cortical Network’

[91]: Sanchez-Vives (2015), ‘Slow wave activity as the default mode of the cerebral cortex’

[92]: Renault et al. (2015), ‘Combining Microfluidics, Optogenetics and Calcium Imaging to Study Neuronal Communication In Vitro’

[93]: Yamamoto et al. (2018), ‘Impact of modular organization on dynamical richness in cortical networks’

[94]: Tibau et al. (2018), ‘Neuronal spatial arrangement shapes effective connectivity traits of *in vitro* cortical networks’

[95]: Sanchez-Vives et al. (2000) ‘Cellular and network mechanisms of rhythmic recurrent activity in neocortex’

[96]: Derchansky et al. (2008) ‘Transition to seizures in the isolated immature mouse hippocampus’

[97]: McCormick et al. (2001) ‘On The Cellular and Network Bases of Epileptic Seizures’

specific regions are able to initiate a propagating front of activity going through the whole network during what is now called a network burst [49, 50, 88]. A rhythmic activity takes place within the culture, formed by long periods of silence and shorter epochs of intense firing at the culture scale, that constitute a burst. Although morphological properties of neurons grown in culture may vary from healthy brain tissues, this process of localised initiation and/or propagation has been observed during many activity routing in the brain: during epileptic seizures, slow wave sleep, retinal development [5, 87, 97, 98] or in cortical areas in anesthetized and awake conditions [99].

Motivations

Spatiotemporal analysis of collective rhythms and waves is not straightforward, as shown by the multiple number of methods used in the literature. How to faithfully quantify neuronal network activity in time *and* space is still an open question. The most common approach uses a binning strategy: neurons' activity is considered to be a series of consecutive discrete events in time and space thus easy to count within specific time bin of size Δt . The obtained function can afterwards be used to compute a firing rate as a function of time [52, 54, 71, 100, 101], a degree of synchrony with cross/auto-correlations [14, 71, 102–104], a global network activation (percentage of active units within a time bin) [93], spatial properties

[49]: Orlandi et al. (2013), 'Noise focusing and the emergence of coherent activity in neuronal cultures'
 [50]: Lonardoni et al. (2017), 'Recurrently connected and localized neuronal communities initiate coordinated spontaneous activity in neuronal networks'
 [88]: Paraskevov et al. (2017), 'A spatially resolved network spike in model neuronal cultures reveals nucleation centers, circular traveling waves and drifting spiral waves'

[71]: Penn et al. (2016), 'Network synchronization in hippocampal neurons'
 [54]: Eckmann et al. (2008), 'Leader neurons in population bursts of 2D living neural networks'
 [52]: Eytan et al. (2006), 'Dynamics and Effective Topology Underlying Synchronization in Networks of Cortical Neurons'
 [100]: Gritsun et al. (2012), 'Growth Dynamics Explain the Development of Spatiotemporal Burst Activity of Young Cultured Neuronal Networks in Detail'
 [101]: Bologna et al. (2010), 'Low-frequency stimulation enhances burst activity in cortical cultures during development'

-
- [5]: Butts et al. (1999) 'Retinal Waves Are Governed by Collective Network Properties'
 [87]: Massimini et al. (2001) 'The Sleep Slow Oscillation as a Traveling Wave'
 [97]: McCormick et al. (2001) 'On The Cellular and Network Bases of Epileptic Seizures'
 [98]: Maccione et al. (2014) 'Following the ontogeny of retinal waves'
 [99]: Muller et al. (2012) 'Propagating waves in thalamus, cortex and the thalamocortical system'
 [14]: Salinas et al. (2001) 'Correlated neuronal activity and the flow of neural information'
 [102]: Stegenga et al. (2008) 'Analysis of Cultured Neuronal Networks Using Intraburst Firing Characteristics'
 [103]: Chiappalone et al. (2006) 'Dissociated cortical networks show spontaneously correlated activity patterns during in vitro development'
 [104]: Wang et al. (1996) 'Gamma Oscillation by Synaptic Inhibition in a Hippocampal Interneuronal Network Model'
 [93]: Yamamoto et al. (2018) 'Impact of modular organization on dynamical richness in cortical networks'

[107]: Chao et al. (2005), 'Effects of Random External Background Stimulation on Network Synaptic Stability After Tetanization'
 [109]: Touboul et al. (2017), 'Power-law statistics and universal scaling in the absence of criticality'
 [110]: Touboul et al. (2010), 'Can Power-Law Scaling and Neuronal Avalanches Arise from Stochastic Dynamics?'

[50]: Lonardoni et al. (2017), 'Recurrently connected and localized neuronal communities initiate coordinated spontaneous activity in neuronal networks'
 [54]: Eckmann et al. (2008), 'Leader neurons in population bursts of 2D living neural networks'
 [111]: Mazzoni et al. (2007), 'On the Dynamics of the Spontaneous Activity in Neuronal Networks'

of information transfer with avalanches [35, 42, 105, 106], a center of activity and trajectory [107], or even very persuasive snapshots displaying the activity in space [88, 100, 108]. However, all those tools are known to display time binning and/or thresholds biases [109, 110]. We call here biased, any computation that uses arbitrary parameters that may modify the result. For example, the avalanches size distribution may or may not resemble a critical-like power law distribution depending on Δt [35]. Moreover, the discrete nature of neuron communicating system as action potential should not be taken as the characteristic of a two state dynamical system: either active or inactive. Action potentials are simple hallmarks of a much complex dynamics. However, a binning strategy represents the idea that neurons are either active or silent and thus neglects their dynamical properties.

Let us also note that the very nature of the observed periodic activity in culture is ill-defined, and different definitions of a network burst are found in the literature [50, 54, 111]. Along with different definitions (and namings), various methods exist to detect bursting states. Cotterill et al. [112] concluded, after analysing 8 algorithms, that there is still need for an accurate burst detection method to be adopted at a single unit level. The variety of methods and definitions [50, 52, 54, 103] used at the network level is an impediment to a

[35]: Beggs et al. (2003) 'Neuronal Avalanches in Neocortical Circuits'
 [42]: Yaghoubi et al. (2018) 'Neuronal avalanche dynamics indicates different universality classes in neuronal cultures'
 [105]: Zierenberg et al. (2018) 'Homeostatic Plasticity and External Input Shape Neural Network Dynamics'
 [106]: Levina et al. (2006) 'Dynamical Synapses Give Rise to a Power-Law Distribution of Neuronal Avalanches'
 [88]: Paraskevov et al. (2017) 'A spatially resolved network spike in model neuronal cultures reveals nucleation centers, circular traveling waves and drifting spiral waves'
 [100]: Gritsun et al. (2012) 'Growth Dynamics Explain the Development of Spatiotemporal Burst Activity of Young Cultured Neuronal Networks in Detail'
 [108]: Kitano et al. (2007) 'Variability v.s. synchronicity of neuronal activity in local cortical network models with different wiring topologies'
 [112]: Cotterill et al. (2016) 'A comparison of computational methods for detecting bursts in neuronal spike trains and their application to human stem cell-derived neuronal networks'
 [50]: Lonardoni et al. (2017) 'Recurrently connected and localized neuronal communities initiate coordinated spontaneous activity in neuronal networks'
 [52]: Eytan et al. (2006) 'Dynamics and Effective Topology Underlying Synchronization in Networks of Cortical Neurons'
 [54]: Eckmann et al. (2008) 'Leader neurons in population bursts of 2D living neural networks'
 [103]: Chiappalone et al. (2006) 'Dissociated cortical networks show spontaneously correlated activity patterns during in vitro development'

reproducible description of a neuronal synchronized state independent of any arbitrary parameters.

Objectives

The main focus of this article is to show that there exists an unbiased, parameter free quantity that can define and identify bursts in neuronal culture (section 3.2). Along with a clear definition of a network burst (section 3.2), we present, on simulated data, the dynamical process involved in the recruitment of the network during the bursts initiation. The key concept we introduce to properly define network bursts is the network phase function. We illustrate the potential of this definition on a theoretical model of neuronal culture made of oscillatory units and reveal the bursts initiation involved. Rigorously, the firing rate is the single-spike probability density [113], although it is always represented as the spike-count firing rate. Coming back to the original definition of the firing rate, as a probability density, we show that our burst definition reveals the initiation time scale of network bursts (section 3.3). We conclude on the activity in the 2 dimensional real space and discuss the role of the network connectivity length in the burst initiation (section 3.3).

[113]: Peter Dayan et al. (2000), *Theoretical Neuroscience Computational and Mathematical Modeling of Neural Systems*

3.2 Materials and methods

Simulations of neuronal networks

Neurons activity

The methods described in the following sections are studied on simulations of neuronal networks (see Appendix 3.6 for more details). Neuronal activity is modeled via the adaptive exponential integrate and fire model [73] for its computational efficiency and biological relevance.

By controlling both pre and post synaptic mechanisms Penn et al. [71] found that over two thirds of dissociated hippocampal and cortical neurons are pacemaker neurons. Neurons are said to be pacemakers when they regularly spike even when pull apart from any other neurons. They are oscillators. In neuronal cultures, such behavior may come from persistent sodium current $I_{Na,P}$ or gap junctions [69, 70, 114,

[73]: Brette et al. (2005), 'Adaptive Exponential Integrate-and-Fire Model as an Effective Description of Neuronal Activity'

[71]: Penn et al. (2016), 'Network synchronization in hippocampal neurons'

[70]: Sipilä et al. (2006), 'Intrinsic bursting of immature CA3 pyramidal neurons and consequent giant depolarizing potentials are driven by a persistent Na⁺ current and terminated by a slow Ca²⁺-activated K⁺ current'

[69]: Tazerart et al. (2008), 'The Persistent Sodium Current Generates Pacemaker Activities in the Central Pattern Generator for Locomotion and Regulates the Locomotor Rhythm'

[114]: Draguhn et al. (1998), 'Electrical coupling underlies high-frequency oscillations in the hippocampus in vitro'

[115]: Rouach et al. (2003), 'Carbenoxolone Blockade of Neuronal Network Activity in Culture is not Mediated by an Action on Gap Junctions'

[115]. Following these results, we use 3 different parameter sets corresponding to self-sustained oscillating neurons independently of their connectivity. They will be referred to as 'Noise Driven', 'Regular Spiking' and 'Intrinsically Bursting' depending on their spiking patterns (see Appendix 3.6 for further details). We want to raise awareness on the Noise Driven type. Although the name might be misleading, ND neurons are regularly spiking, however the spike interval depends highly on the number and intensity of inputs received (for example noise). Looking at pacemaker neurons comes with significant consequences. Those neurons intrinsically follow their inner dynamics, and pushing them away from their stable cycle demands specific conditions. For instance, the required input to make a pacemaker spike in a small time window, depends on this neuron inner state when the input is received and not only on its strength. The examples illustrating this paper investigate a novel perspective on bursting phenomena with pacemaker neurons.

Network model

[9]: Hernández-Navarro et al. (2017), 'Dominance of Metric Correlations in Two-Dimensional Neuronal Cultures Described through a Random Field Ising Model'

The network metric correlations [9] have been shown to shape network global activation. We take this into account by choosing an Exponential Distance Rule (EDR) model for the neuronal connectivity. [72] This is an Erdős-Rényi like network, where the connection probability depends on the Euclidean distance, with an exponential decrease. The exponential characteristic length λ is later called, the network spatial scale and is equal to the mean connectivity length. The network is built under the condition of fixed mean degree, from a random selection of somata positions in a 800 μm radius circular culture with strict border conditions (more details in the Appendix 3.6). Each pair of somata separated by a distance d is connected with the probability $p(d) = p_0 e^{-d/\lambda}$, with p_0 a normalization factor. It is to be noted that the proposed analysis is not limited to those specific parameters and model. As an example, a different model is analyzed in detail in appendix 3.6.

[72]: Fardet (2018) 'Growth and activity of neuronal cultures'

Temporal spikes analysis

Spike count rate

We consider spikes as identical, discrete events, varying only in their time of emission and emitter position. In other words, we neglect the information that may exist in the spike shapes and sub-threshold membrane oscillations. Usually, the firing rate is approximated with a convolution of the neural response function with a chosen kernel (rectangular, gaussian, exponential, alpha etc...). Although this spike-count rate has been shown to correlate with specific stimuli in neuroscience studies [113], this approach entails huge variability and may not be reproducible depending on the choice of kernel, and its characteristic time scale. In an attempt to provide unbiased estimators of neurons activity, we suggest a different method in order to rid activity analysis of time binning strategies. We use in this paper individual spike times. While our method is specially appropriate for simulations, the required high spatiotemporal resolution necessary to discriminate single spikes is increasingly available through MEA and even fast calcium imaging that reaches the millisecond range with Oregon Green BAPTA-1 calcium indicator [116, 117].

The Network phase

Since pacemaker neurons are characterized by an oscillatory behaviour, concurrently to single spike times, we will use a phase to describe a neuron's state. Pikovsky et al. [118] defined the phase of an oscillatory signal with discrete events as a piecewise continuous function in between two events. We define the phase $\phi_i(t)$ for neuron i , and any time t in between two spikes $t_{i,k}$ and $t_{i,k+1}$ as:

$$\phi_i(t) = \frac{t - t_{i,k}}{t_{i,k+1} - t_{i,k}}, \quad t \in [t_{i,k}, t_{i,k+1}[\quad (3.1)$$

where $t_{i,k}$ is the time of the k^{th} spike of neuron i , in the ordered sequence of spike times. The phase function of a discrete set of events is computed after the recording of the sequence of firing times; its value at some time $t > t_{i,k}$ depending on the knowledge of the following firing time $t_{i,k+1}$. The phase $\phi_i(t)$ is the difference between time t and the closest spike in the past, divided by the instantaneous interspike

[113]: Peter Dayan et al. (2000), *Theoretical Neuroscience Computational and Mathematical Modeling of Neural Systems*

[116]: Tsai et al. (2017), 'A very large-scale microelectrode array for cellular-resolution electrophysiology'

[117]: Grewe et al. (2010), 'High-speed in vivo calcium imaging reveals neuronal network activity with near-millisecond precision'

[118]: Pikovsky et al. (2001), *Synchronization: A universal concept in nonlinear sciences*

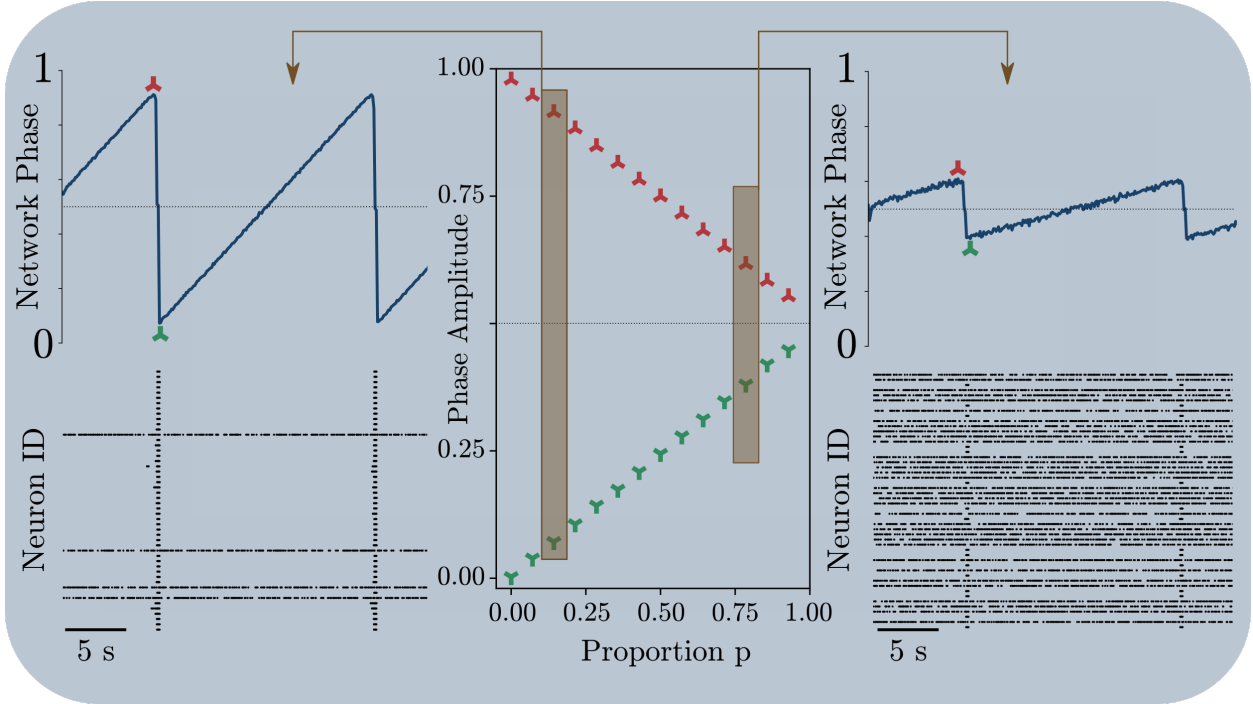


Figure 3.1: Bursting events acting as an epoch of synchronous spiking is visible with large oscillations of the network phase. The middle panel represents the maximum (red) and minimum (green) values of the phase extrema averaged over 50s simulations. In each simulation a proportion p of Intrinsically Bursting neurons, in a synchronous state, have been substituted for a Poisson spiking neuron of rate 10 Hz in order to mimic non-synchronous neurons. As expected (see Eq. 3.4), the proportion of synchronous neurons correlates with the network phase peak values. Left and right panels show the network phase and a raster plot of 50 randomly chosen neurons (in a population of 2000 neurons) as functions of time for two different proportion $p = 0.14$ (left) $p = 0.78$ (right). One can see the two peaks that surround the bursts.

interval at this time t . An oscillatory neuron state can thus be defined by this bounded variable, that embodies both frequency and spike timing. It is the simplest step to estimate a neuron dynamical state, without constraining it to a two state dynamics. We define the network phase as the mean phase:

$$\Phi(t) = \frac{1}{N} \sum_{i=1}^N \phi_i(t) \quad (3.2)$$

with N the total number of neurons. After each spike, the phase of a neuron decreases from 1 to 0 in a discontinuous way. Accordingly, the network phase decreases by an amount in the range of $\frac{1}{N}$. Because of this reset, the network phase decreases more significantly whenever several neurons spike simultaneously, allowing us to detect and define a synchronized bursting regime. The network phase typically increases slowly in between bursts because few neurons spike, and rather irregularly, and it decreases down, and/or oscillates around 0.5, during bursts because of high firing rate (see figure 3.1). Let us stress that the network phase we use here is

a simple way to access the complexity of the spike times' sequence from experimental or simulated data and not a novel modeling of the dynamics.

Burst Definition

Using the network phase, we develop now a mathematical characterization of synchronous bursting states. The network phase $\Phi(t)$ specific behavior in bursting activities (see figure 3.1) guides us towards a definition: bursts are global events observed in between a maximum and minimum of the network phase. Let us show that, a local maximum of the network phase is associated with the synchronization of at least some neurons in the culture. Let us call q the proportion of synchronized neurons that spike in a specific time window, let's call it Δt , around time t . This proportion q of coactivated neurons might not represent the whole network, thus a proportion $p = 1 - q$ does not spike in this time window but at a latter time in the burst. Because the phase between two spikes has a linear evolution, (with the slope being the inverse of the interspike) the network phase variation due to non-synchronous neurons is easily determined. On the contrary, the phase of the spiking neurons goes through the hard reset from 1 to 0 which forces the network phase to decrease by a certain amount $|\Delta\Phi|$. We note N_1 and N_2 the number of synchronous, and non-synchronous neurons (respectively). The synchronous neurons represent the first one to fire in a burst, whereas the non-synchronous neurons represent those who will spike at a latter time, not at all or with an irregular pattern. We can write the quantity $\Delta\Phi$ being equal to:

$$\Delta\Phi = \Phi\left(t + \frac{\Delta t}{2}\right) - \Phi\left(t - \frac{\Delta t}{2}\right)$$

And, given the definition of the network phase (Equation 3.1), the most general form is:

$$\Delta\Phi = \frac{1}{N} \left(\sum_{i=1}^{N_2} \frac{t + \frac{\Delta t}{2} - t_{i,k+1}}{t_{i,k+2} - t_{i,k+1}} - \frac{t - \frac{\Delta t}{2} - t_{i,k}}{t_{i,k+1} - t_{i,k}} \right. \\ \left. + \sum_{i=N_1+1}^{N_2} \frac{\Delta t}{t_{i,k+1} - t_{i,k}} \right)$$

As explained before, because of synchronous spiking neurons, the network phase will decrease when a burst starts. We are looking for the condition for $\Delta\phi$ to be negative. In order to continue the computation without too much complexity, we assume that the instantaneous interspike interval, noted ISI, is the same for both synchronous and non-synchronous populations. This is sufficient to capture the important parameters at play, and reflects data recorded with calcium imaging, where only the first spikes of a burst are accessible with high resolution. For synchronized neurons the ISI corresponds to the interburst interval, while for non-synchronized neurons the ISI represents the interval between irregular firings. We can write:

$$\Delta\Phi = q \left(\frac{\Delta t}{2ISI} - \left(1 - \frac{\Delta t}{2ISI}\right) \right) + p \frac{\Delta t}{ISI} \quad (3.3)$$

The first and second terms describe respectively, the decrease of the network phase due to the synchronous neurons and the increase due to the non-synchronous ones. Thus, the characterization of a synchronous event as we defined it above implies :

$$\frac{\Delta t}{ISI} - q < 0 \quad (3.4)$$

This means that a decrease of the network phase happens if a proportion q of the population spikes in a time scale smaller than $q \times ISI$. This coactivation is associated with a decrease of the network phase by an amount proportional to the size q . A bursting state can thus be detected without any arbitrary parameters and happens in between a maximum and a minimum of the network phase. The amplitude $|\Delta\Phi|$ is related to the proportion of bursting neurons.

With less restrictive assumptions, one can understand that the network phase decreases whenever some neurons are coactivated in a time interval Δt . The network phase decreases by an amount proportional to q , as long as this group phase does not increase back to 1 in this Δt time window. This increase is represented by the last term in equation 3.3: $\left(1 - \frac{\Delta t}{2ISI}\right)$. Hence, the time scale of the synchronization Δt has to be smaller than the fast time scale $q \times ISI_{in_burst}$.

With this definition, the network phase $\Phi(t)$ offers, independently of any arbitrary parameters, a burst starting time reference as a maximum, and an ending time reference as a

minimum. Moreover, as Eq. 3.4 demonstrates it, the difference between the maximum and minimum values of the network phase is a measure of the proportion of synchronous neurons. As figure 3.1 represents it, the minimum and maximum values are linearly correlated with the proportion of synchronous neurons, or equivalently non-synchronous neurons.

The network phase with experimental recording

Large oscillations of the phase, showing bursting regime and different degree of synchronization can also be seen in experimental recordings. Data publicly available, from [50] is represented in figure 3.2. It is a recording of hippocampal cell cultures made with a 64x64 micro-electrode array. Each electrode is considered as an individual unit to compute the phase with, and the network phase is the mean average over the 4096 electrodes.

First spike probability distribution

Eytan et al. [52] have introduced the idea that some neurons in a culture are consistently the first ones to fire over consecutive bursts. Their analysis however depended on an arbitrary threshold on the activity in order to define the sequence of precursors in neuron firing. Our approach allows an unbiased characterization of these. We are going to compute the probability density for the occurrence of a spike close to the burst beginning. Thanks to the time reference for each burst given by its phase's maximum (see section 3.2), we can derive the probability for a neuron to emit its first spike during the burst at time $\tau = t - t_b$ where t_b is the detected burst starting time (see figure 3.1). Note that τ can be above or below zero. This probability is the rigorous definition of the firing rate. Indeed, according to Peter Dayan and L.F. Abbott [113] "The probability density for the occurrence of a spike is, by definition, the firing rate [...]". Here, each trial is an individual burst, and in order to look for the burst initiation, we only take into consideration the first recorded spike of each neuron. Let us note however that in many publications, possibly due to finite number of recordings, the term "firing rate" is more commonly associated with its approximation, the spike count rate. To avoid confusion we will speak in the paper of "spike probability distribution".

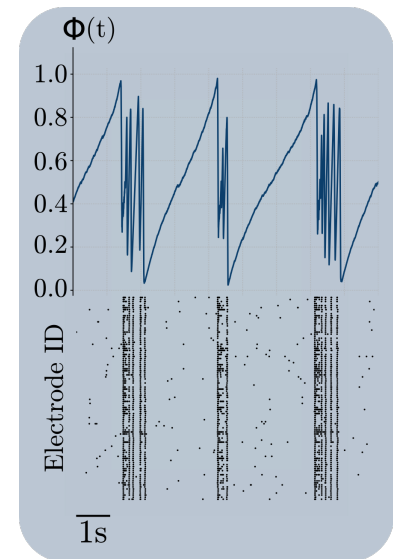


Figure 3.2: Raster plot of 100 electrodes and the network phase as a function of time of experimental recordings from [50]. The burst can clearly be identified. The different sizes of synchronized neurons' groups in the high frequency regime of the bursts is clearly visible with the phase oscillations.

[52]: Eytan et al. (2006), 'Dynamics and Effective Topology Underlying Synchronization in Networks of Cortical Neurons'

[113]: Peter Dayan et al. (2000), *Theoretical Neuroscience Computational and Mathematical Modeling of Neural Systems*

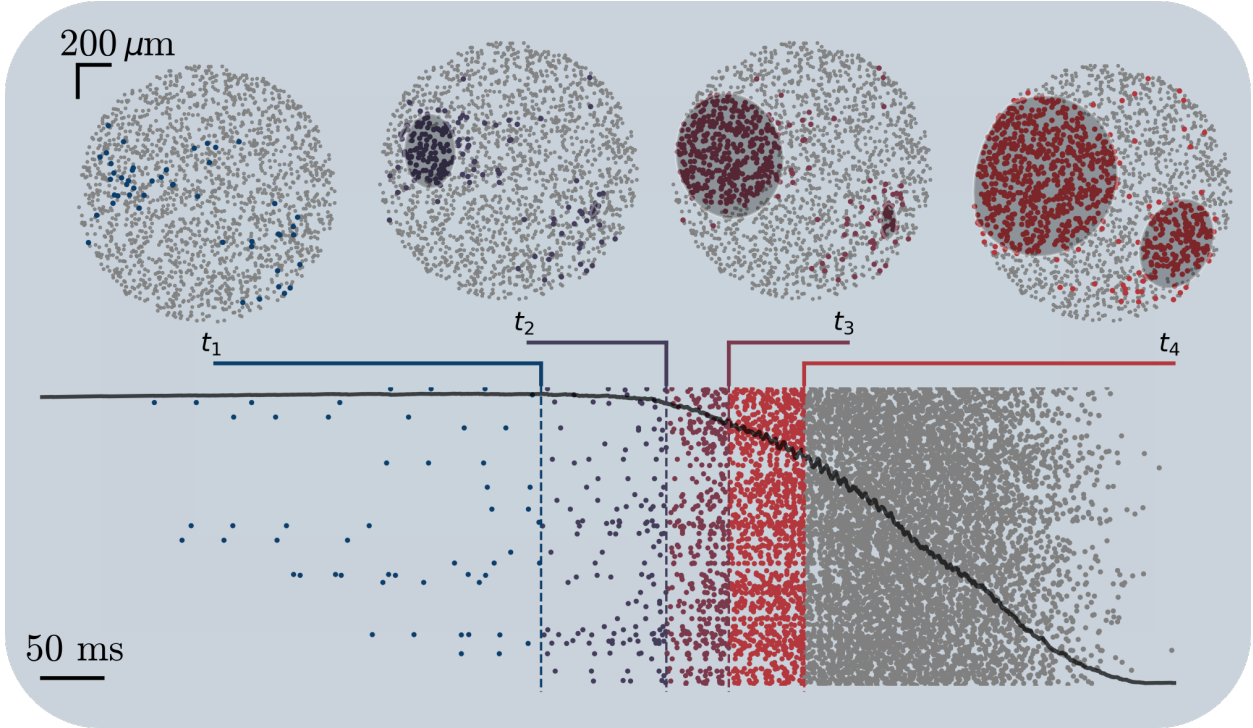


Figure 3.3: Search for initiation area in a bursting activity of Intrinsically Bursting neurons. Bottom panel is a raster plot of the burst, each line is one out of 800 neurons randomly pick in the 2000 neurons simulation. The black line represents the network phase. Top panels represent in space 4 different time points with colored neurons as neurons that have spiked up to the considered time (dashed lines in the raster plot). Neurons that have not yet spiked are plotted in grey. Shadows represent the elliptic initiation area. One can observe that at first, the activity is dispersed and no specific region is detected. Some time after, a region has been sufficiently active to be detected then at a later time an other one appears on the right (last panel) These two regions latter grow up to the size of the culture when all neurons have started spiking.

Although we modeled neurons as pacemaker, the noise added as miniature post synaptic events (see appendix 3.6 for more details) creates some variability and the sequence of action potentials may vary from burst to burst. Hence the need to investigate the initiation in a probabilistic manner. In order to carry out this analysis one needs a time reference coherent over consecutive bursts/trials with the spike sequence probability density.

To compute this quantity, one first detects for each neuron the first spike in a burst and then compute the cumulative activity: $C_b(\tau) = \frac{1}{N} \sum_{n=1}^N \theta(\tau - \tau_{n,b})$, where N is the number of neurons, and $\tau_{n,b}$ is their first spiking time in burst b and θ the Heaviside function. The cumulative activity is then averaged over multiple bursts of the same simulation. Then the numerical derivative F is the first spike time probability density, computed with the time resolution r :

$$F(\tau) = \frac{\langle C_b \rangle(\tau + r) - \langle C_b \rangle(\tau)}{r} \quad (3.5)$$

Spatial Spike Analysis

This section focuses on the initiation in space of bursting dynamics. Many studies [49, 50, 88] either from numerical simulations or experimental recordings in cultures, have reported that bursts start repeatedly in one or several localised regions of the culture. We propose here a method to detect such regions based on a clustering algorithm of spiking neurons. Although we know the in-burst spike times because of the high resolution used in simulations, we will use only the first spike of each neuron in order to look at how does the bursting regime starts.

A specific region of the culture starts spiking before the whole population

As a first hypothesis, one considers that the culture is homogeneously and randomly seeded with neurons. Thus, if one region is to start the activity, it should have a density of spiking neurons close to the density of the culture. This is how we will detect the initiation area. The algorithm DBSCAN from the Scikit Library [84, 119], is a density based algorithm for cluster detection that only requires two parameters and does not need *a priori* guess of the number of clusters. The two parameters are, a radius of search ϵ to look for nearest neighbors, and threshold for the minimum number of neighbors N_{th} required to belong in a cluster. We introduce later an approach to avoid these two arbitrary parameters. Overall, the algorithm can be used at any time point and works as follow:

1. Each burst is identified with the extrema of the network phase
2. For each burst, one looks at the first spike of each neuron. At the considered time point, if a neuron has not spiked yet, it is invisible to the DBSCAN search, if a neuron has spiked, one turns it into a visible state. Visible neurons are neurons that have spiked at least once before the considered time point.
3. The DBSCAN algorithm proceeds as the following:
 - ▶ For each visible neuron i , one counts the number of visible neurons in a radius ϵ , noted n_i
 - ▶ If n_i is larger than or equal to N_{th} , neuron i is said to belong to a cluster

[49]: Orlandi et al. (2013), ‘Noise focusing and the emergence of coherent activity in neuronal cultures’
 [50]: Lonardoni et al. (2017), ‘Recurrently connected and localized neuronal communities initiate coordinated spontaneous activity in neuronal networks’
 [88]: Paraskevov et al. (2017), ‘A spatially resolved network spike in model neuronal cultures reveals nucleation centers, circular traveling waves and drifting spiral waves’

[84]: Ester et al. (1996), ‘A Density-Based Algorithm for Discovering Clusters in Large Spatial Databases with Noise’
 [119]: Pedregosa et al. (2011), ‘Scikit-learn: Machine Learning in Python’

- If two neurons detected in a cluster are closer than ϵ , they are in the same cluster.
4. Initiation areas are approximated with an ellipse overlapping each neuron in a cluster. There can be several regions, and they can overlap too.

The underlying hypothesis for what is here called a visible neuron, is that a spike may have causal influence over very long period of time. One needs to consider here first the propagation delay and second the integration processes in the post-synaptic neuron, which theoretically speaking can be as long as the interspike interval for pacemaker neurons as shown by Izhikevich [62] with the description of the phase response curve.

The algorithm output is a region of the two dimensional culture -sometimes several regions- of high activity, in the sense that this region is not necessarily fast spiking at the moment or near the moment of the computation but most of its neurons have been active up to the point of computation. Figure 3.3 represents this search and the corresponding areas.

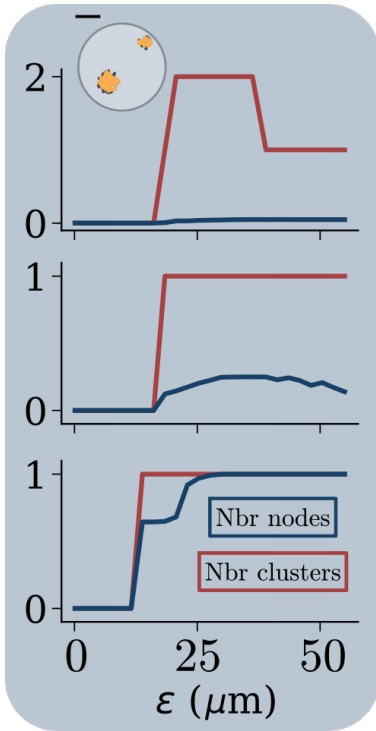


Figure 3.4: Estimation of the optimal parameter ϵ . Each panel shows the number of detected cluster (red) and the number of neurons in it normalized by the total number of neurons (blue) as function of ϵ in circular culture of radius $800 \mu\text{m}$. Scale bar in the inset of the top panel shows $400 \mu\text{m}$. **Bottom frame:** All neurons are visible for the DBSCAN algorithm. **Middle frame:** Only 20% randomly chosen neurons are visible. **Top frame:** Two separate activated regions with a total of 10% visible neurons.

Parameters Estimation

In order to reduce the number of arbitrary parameters we propose to modify the original DBSCAN algorithm. We first choose to relate the minimum number of neighbors threshold N_{th} and the radius of search ϵ to one another. To be identified as the initiation region, almost each neuron in it has to be activated. Thus, the threshold N_{th} has to be the mean number of neuron in a disk of radius ϵ . Given the density d of the culture, we could set $N_{th} = d \times \pi \epsilon^2$. However, doing so, one does not account for the different local densities that arise from the strict condition on the culture boundary. Neurons in the center have necessarily a higher number of neighbors. Thus, we set N_{th} to be the mean number of neurons in a disk, corrected by one standard deviation. In this way, neurons at the border can contribute to a cluster more easily. Under the assumption that the standard deviation scales as the square root of the mean, we set:

$$N_{th} = d \times \pi \epsilon^2 - \sqrt{d \times \pi \epsilon^2} \quad (3.6)$$

[62]: Izhikevich (2007) *Dynamical systems in neuroscience*

To estimate ϵ let us first quote that for small values, some neurons may not be able to reach the threshold N_{th} because there are too few neighbors at this distance. For large ϵ values, because of equation 3.6, the threshold will be high and some neurons may not be able to reach it. This comes from the fact that, locally, the number of neighbors may not scale as fast as N_{th} with ϵ . Thus, there exists a suitable range of values that we are going to look for. Figures 3.4 and 3.5 present an estimation of ϵ for 2 culture geometries based on running the DBSCAN program with different visible neurons. The goals are the following:

- ▶ If each neuron of the culture is visible, the algorithm should detect only one cluster with each neuron in it.
- ▶ If a large percentage of the population (at least more than half) is uniformly spiking in the culture, the algorithm should also detect 1 cluster with most of the spiking neurons in it.
- ▶ It can detect separate regions of activity.

Figures 3.4 and 3.5 present the number of neurons in the initiation area as function of ϵ for different scenarios. One can observe that the 3 goals are to some extent achieved. As predicted, small values of ϵ are not suitable, and large values also miss the clusters. Although a first cluster is detected at $\epsilon \approx 10\mu\text{m}$, each neuron belongs to this cluster only above $25\mu\text{m}$. This sets the minimum value possible. One can observe that the number of neurons in a cluster slightly depends on the culture geometry and density of activity. Sharp edges, with few neurons will be detected in a cluster for larger values of epsilon than culture with aspect ratio 1:1. We also observe that for large ϵ the density of visible neurons can be too low (see middle frame of figure 3.5) for any cluster to be detected: because of equation 3.6, the threshold number of neighbors cannot be reached. However, for a relatively broad range of values the resulting number of neurons in a cluster does not depend on ϵ . This is the range we are interested in. What is important for the following analysis is that the algorithm can localise high densities and treats each neuron equally in order to detect activity near the border as well as in the center. Moreover, it does not necessarily depend on the culture aspect ratio because the most suitable value of ϵ can be adapted to individual cultures.

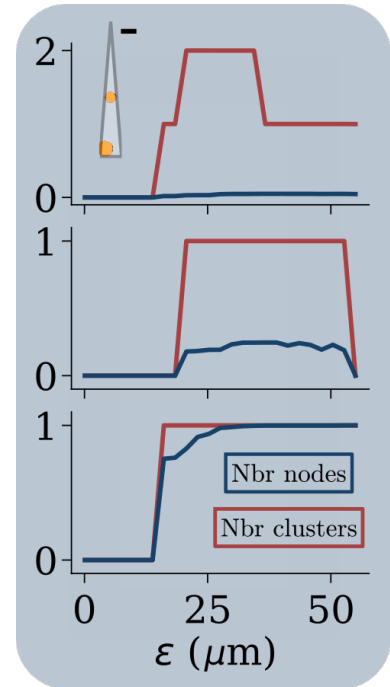


Figure 3.5: Estimation of the optimal parameter ϵ . Each panel shows the number of detected cluster (red) and the number of neurons in it normalized by the total number of neurons (blue) as function of ϵ . Triangular culture, with aspect ratio 1:10. The inset in the top frame presents the result for $\epsilon = 35\mu\text{m}$: orange dots are neurons in a cluster and black dots are visible neurons not in a cluster. Scale bar in the inset of the top panel shows $400\mu\text{m}$. The figures follow the same procedure as in figure 3.4 and the density is the same.

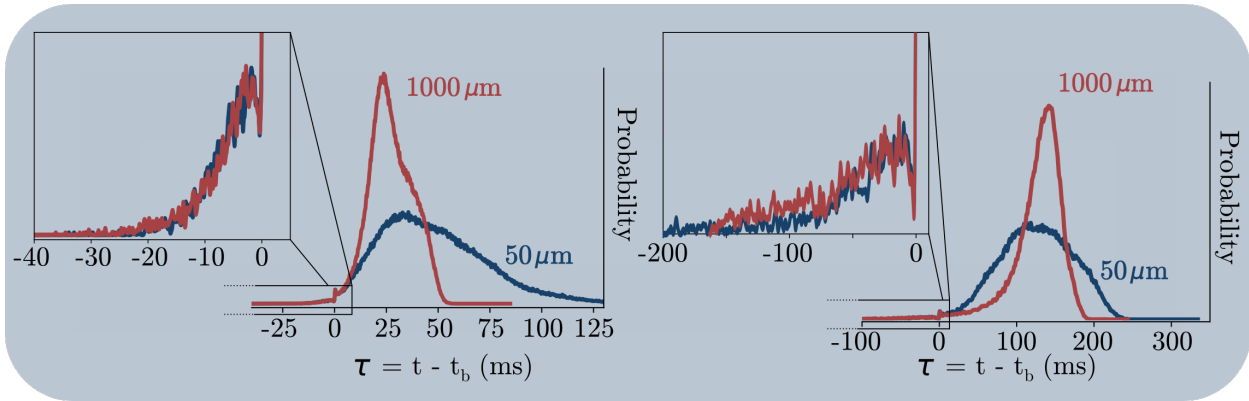


Figure 3.6: Probability density function for any neuron to emit its first spike at time $\tau = t - t_b$, where t_b is the time of the network phase maximum (see burst definition 3.2). The right panel represents the probability function for Noise Driven neurons, and the left panel represents Regular Spiking neurons. Both panels include a zoom-in of the region of interest: first-to-fire neurons for $\tau < 0$. Networks with an EDR scale 1000 (red) and 50 (blue) μm are considered.

3.3 Results

The results presented in this section demonstrate the valuable contribution of the maximum of the phase we introduced before to unambiguously unravel the network dynamics during bursts initiation. Indeed, this extremum defines a specific time point in the dynamics of a burst, coherent over consecutive bursts. With simulated neuronal populations in cultures we illustrate the spatio-temporal dynamics of initiation, uncharacterised until now. Then, with publicly available MEA data from [50] we discuss on the practical use of our methods with experimental data.

[50]: Lonardoni et al. (2017), ‘Recurrently connected and localized neuronal communities initiate coordinated spontaneous activity in neuronal networks’

Burst initiation

We now make use of the probability distribution to reveal different dynamical regimes during bursts. Figure 3.6 displays the temporal dynamics of burst initiation for a set of simulations with different connectivity spatial scales and neuron models. One can observe that the detected time of burst, at $\tau = 0$, appears to be a critical value that separates different behaviors. The probability density for $\tau < 0$ can be used to define a temporal scale for the initiation. With an estimation of the width of the probability density function, we find an initiation duration in the order of 10 ms for regular spiking neurons, and 100 ms for noise driven ones.

Surprisingly enough, the probability distribution for $\tau < 0$ seems independent of the connectivity spatial scale of the

EDR model but depends on the neurons inner dynamics (here modeled through different sets of parameters). This time scale comes from the inner neurons dynamics, and not from the spatial correlation of the network model. On the contrary, for $\tau > 0$ the overall neuronal population is largely characterized by an uni-modal distribution that depends on the network spatial scale. The importance of the spatial correlation emerges in the second regime, ($\tau > 0$) where the curves for two different EDR scale differ from one another.

Spatial initiation: Cluster algorithm performance

In order to quantify the localised initiation, we propose to measure the nucleation site identification performance of our cluster detection algorithm, more simply called performance. As presented before (see 3.2), the clustering algorithm is able to identified a surface $S(t)$ as a set of multiple clusters of concentrated activity. We define the performance of the identified surface $P(S)$ as the number of visible (meaning active) neurons (see 3.2) in the detected region divided by the total number of visible neurons in the population at the calculation time point. As time evolves, one can run the algorithm and compute the performance as function of the estimated region's surface (estimated as the smallest ellipse that encompass each point in it). When the activity starts, it may be sparse and the detected region will probably be of low performance. However, if the activity is indeed localised, in the sense that it is confined into a small region and extends from it, the performance should increase faster than the cluster(s) area and then stay relatively constant as the activity extends to the whole culture.

Moreover, one can estimate the smallest region with the maximum performance looking at the maximum of $P(S(t)) - \frac{|S(t)|}{|C|}$, with $P(S(t))$ the performance of the detected cluster(s), and $|S(t)|$, $|C|$ respectively, the cluster(s) and culture area. This allows us to define consistently what we call "the initiation region". Figure 3.7 represents the performance for two EDR networks with different connectivity scale. One can easily notice that (also reported earlier by Paraskevov et al.[88]), long range connectivity does not exhibit localised initiation. This is noticeable both with the initiation region area being larger than 25% of the culture and the shape of the performance: growing slowly towards 1.

[88]: Paraskevov et al. (2017), 'A spatially resolved network spike in model neuronal cultures reveals nucleation centers, circular traveling waves and drifting spiral waves'

Looking for leaders

[120]: Faci-Lázaro et al. (2019), 'Impact of targeted attack on the spontaneous activity in spatial and biologically inspired neuronal networks'

[54]: Eckmann et al. (2008), 'Leader neurons in population bursts of 2D living neural networks'

A debated topic is whether some neurons behave as “leaders” that display consistently a precursor activity, and what are their characteristics [54, 120]. In order to show the existence of leader neurons in simulations with pacemaker neurons, we focus on the first spike probability density before the burst onset time defined by the maximum of the network phase (see figure 3.6). Neurons that spike in the time lapse described here by $\tau < 0$ display a significantly different dynamics than the rest of the network. The main reason being that this is the only period of time where the probability density does not depend on the network spatial scale but on neurons' inner dynamics. With noise driven neurons, the integral of the curve indicates that there are 20 first-to-fire neurons per bursts. However, they may not always be the same ones. In order to identify leadership in bursting dynamics, we look for first-to-fire statistics. If some neurons are repeatedly first-to-fire, we will call them leaders.

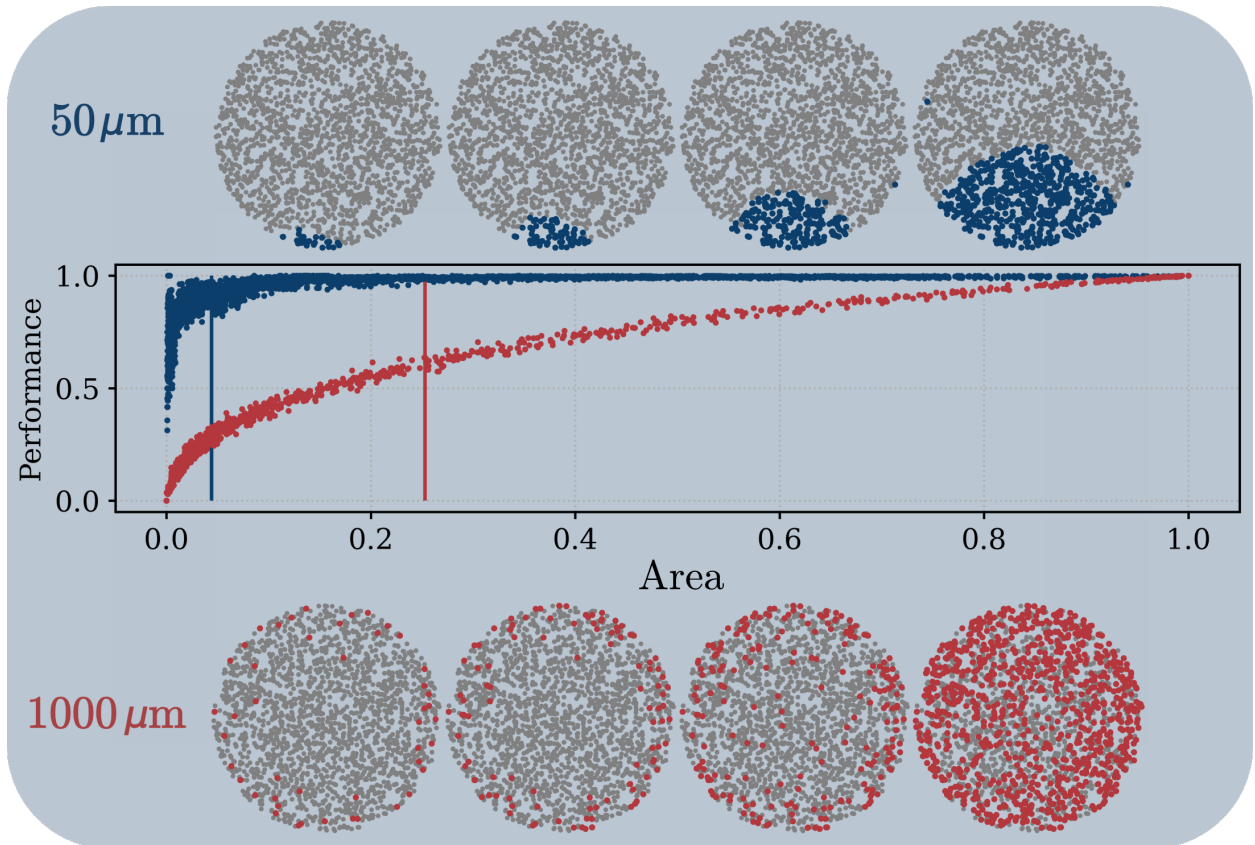


Figure 3.7: Performance as a function of the detected cluster(s) surface area $\frac{|S(t)|}{|C|}$. **Top** panels represent burst initiation in simulations with a network of Regular Spiking neuron and EDR scale of $50 \mu\text{m}$. Snapshots are separated by 20 ms and colored dots represent visible neurons (see 3.2). The activity is manifestly localised. **Bottom** panels represent burst initiation in simulations with the same neuron parameters, but a network with EDR scale of $1000 \mu\text{m}$. Snapshots are separated by 20 ms and colored dots represent visible neurons (see 3.2). The activity is seemingly not-localised. **Middle** panel shows the corresponding performance: the last fifty bursts have been analyzed through the clustering algorithm with a time step smaller than a millisecond. Each data point is here represented. Straight lines represent the maximum of $P(S(t)) - \frac{|S(t)|}{|C|}$. They correspond to top second image and bottom last image.

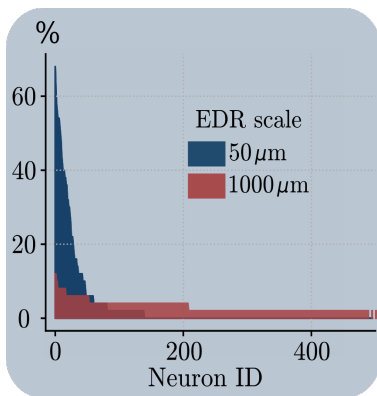


Figure 3.8: Statistics for each neuron to be a first-to-fire over 50 bursts in a simulation with Noise Driven neurons. X-axis has been sorted out to display a decreasing statistic. Blue and red refers to networks where the EDR scale was respectively 50 and 1000 μm . There are 10 first-to-fire neurons present in more than 50% of the considered bursts for the small EDR scale, and most of the culture is never first-to-fire. On the contrary, long connectivity length increase the number of possible first-to-fire up to a third of the culture.

Figure 3.8 displays the first-to-fire statistics for two networks of different EDR scale. Although the distribution probability, figure 3.6 was similar for both of these networks, the first-to-fire statistics is notably different. By using an exponential fit of the distributions of figure 3.8 we estimate the total number of neurons acting as first-to-fire to be 24 and 95 for networks of connectivity scales respectively, 50 and 1000 μm . Thus, in our simulations, with a small EDR scale, the total number of first-to-fire is in the same range as the number of first-to-fire per burst. These short range networks contain leaders: around 20 neurons repeatedly drive the network to a bursting state in simulations with noise driven neurons. On the contrary with large EDR scale, the total number of neurons that act as first-to-fire is much larger than the number of first-to-fire per bursts. Thus, an established group of regular leader neurons does not exist in a network with long range connectivity.

For the culture sizes we simulated, we note a common growth dynamics that requires approximately 20 neurons to initiate a burst for long and short connectivity spatial scales. For short EDR scales, leader neurons exists, they are repeatedly in the burst initiation sequence among other rarely initiation neurons. For larger EDR scales, the variation in the composition of the burst precursor group is much larger and leaders rarefy.

3.4 Discussion

Dynamical regimes

The separation of behavior at $\tau = 0$ in the spike time probability distribution reveals the specific dynamics of what has been reported earlier as leader electrodes. [52, 54]. Using a complex sorting algorithm, Eckmann et al. reported the existence of leader electrodes in neuronal cultures. They used an arbitrary threshold between the probability to spike during a pre-burst period (see [54] for definition of a pre-burst) and the probability to spike at any time during silent periods (low firing rate) to identify leader electrodes.

Here, thanks to the first spike probability distribution, we distinguish naturally the very dynamics of first-to-fire neurons during what Eckmann et al. [54] called the pre-burst. This allowed us to show that the very beginning of these neurons activity is independent of the network spatial correlations.

[54]: Eckmann et al. (2008), 'Leader neurons in population bursts of 2D living neural networks'

[52]: Eytan et al. (2006), 'Dynamics and Effective Topology Underlying Synchronization in Networks of Cortical Neurons'

This property is clearly revealed thanks to our method unique feature to align bursts initiation through the maximum of the phase. The key element of this characterization is that the maximum of the phase is a coherent time point in the synchronization process over consecutive bursts. Because of this, the firing time sequences are properly aligned allowing to compute the first spike time probability distribution and reveal the initiation dynamics time scale. Previous methods making use of arbitrary reference time are not able to separate the spatial scale independent dynamics ($\tau < 0$) from the spatial scale dependent one ($\tau > 0$). This is illustrated in Appendix 3.6 where the first spike time probability distribution is evaluated through a conventional method. There, the burst initiation dynamics is blurred because of the arbitrary time reference.

Our burst initiation alignment method allows us to highlight, on simulations, different regimes during a burst and the role of spatial correlations during initiation and propagation. Indeed, the spike time distributions in figure 5 show distinct initiation and spreading stages. The initiation stage appears insensitive to spatial correlations, while the burst propagation is strongly affected by it.

In addition, the spatial connectivity scale plays a role for the initiation localisation and the existence of leader neurons. Both properties have been found only in networks with small connectivity spatial scale. In order to understand this, we discuss the assumption that neuronal networks activity is made of avalanches. Neuronal avalanches are understood as the spreading of neuronal firings by a cascading process during which neurons that fire at some time t trigger other neuron firing at a later time. The activation of neurons at some time point is predominately determined by the inputs they receive from other neurons of the population just before. Let us first call “causal time”, the time duration between a neuron spike and the last input that may have influenced it. Because of the time delay due to spike propagation or other inner dynamics, a pre-synaptic neuron spike may not influence a post-synaptic neuron future spiking. Thus, there is a causal time below which neurons appearing co-activated are in fact, unrelated with one another, even if they are synaptically connected. Hence, the assumption that neuronal networks activity is made of avalanches tells us that multiple spikes with a time shift smaller than the causal time must have common predecessors that spiked during the avalanche:

[88]: Paraskevov et al. (2017), 'A spatially resolved network spike in model neuronal cultures reveals nucleation centers, circular traveling waves and drifting spiral waves'

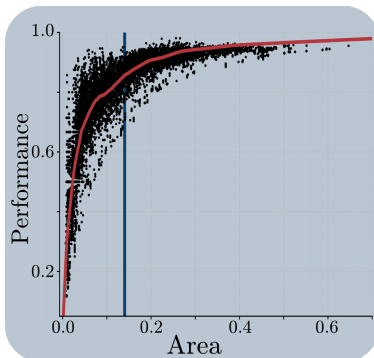


Figure 3.9: Performance computed with a recording on 64x64 MEA from Lonardoni et al. [50], as function of the detected cluster(s) area. The same process is used as in figure 3.7. Black dots are data points, and the red curve is the average curve. The vertical line shows the minimum area for the maximum performance. It corresponds to 14% of the 5.12x5.12 mm² MEA. The activity recorded by the MEA appears to start in a region of 3.5 mm² representing more than 80% of the overall activity during the bursts nucleation. The activity is not uniformly distributed, but is initiated in the identified region.

there is a path in the network (with inverted direction of connections) from those co-activated neurons to the first-to-fire that started the avalanche.

Although we have not reported it here, bursts of activity, when initiated locally, grow with a synchronous propagating front [88] (it can be seen in the activity snapshots in appendix 3.6). These fast synchronous propagating fronts are an example of co-activations in time scale smaller than this causal time. They are synchronous because of the activity of their predecessors, their predecessors were synchronous because of their predecessors, and so on and so forth. The first ones being the first-to-fire in the burst, which spike at their own pace, according to their own dynamics dimly influenced by the network structural characteristics. Hence, the common temporal dynamics observed for different network spatial scale. Then, these first-to-fire neurons project to, and activate the propagating front starting at the phase maximum. The phase maximum corresponds to the time point of the first co-activated neurons in the avalanche: the beginning of the propagating dynamics. This regime depends highly on the network spatial correlations, and corresponds to an avalanche. Because of this avalanche dynamics, first-to-fire neurons can activate a synchronous propagating front if they share common successors. Neurons spatially localised with common successors are numerous in networks with small connectivity spatial scale, and are not likely to exist in networks with long range connections. Hence, the initiation is localised and a synchronous propagating front exists only in network with small connectivity spatial scale.

This scenario is revealed because the maximum of the phase is the time point that separates the leaders' dynamics and the avalanche dynamics. Although, in simulations with pacemaker neurons, the network spatial correlations do not shape the leaders' dynamics, the choice of leaders emerges as a result of the interaction between the network complex structure and the neurons dynamics. Then, the second stage of the burst, dominated by an avalanche dynamics, coupled with a small connectivity spatial scale appears to be the key elements for a propagating front to exist.

Experimental data

Although our methods were developed alongside simulated data, we were concerned about their applicability on experimental data. The application of our analysis on experimental data is mainly dependent on the temporal resolution of the recordings. The decrease of calcium indicators fluorescence signal is too slow in many cases to reach the resolution needed to investigate in-bursts dynamics. However, the increase of the fluorescence signal during the action potential can be sufficiently fast to solve with high resolution the first spike of each burst. The methods presented in this paper can be applied when only the first spike in a burst is known. The computation of the network phase does not require high precision in the burst to pinpoint the starting point. Finally, all the analysis on space and temporal dynamics require only the first spike in each burst. Thus we believe that our methods are also suited for high resolution calcium recordings.

Matrix Electrode Arrays (MEA) provide high temporal resolution sufficient to resolve single spikes. We have looked at recordings from 64x64 MEA, in order to show that spatial resolution is not an issue with modern tools. The sample rate is 7 kHz and the spatial resolution 80 μm . The fast increase of the performance as function of the increasing area of activity, in figure 3.9 proves that the bursts start locally. Like in our simulations, we were able to identify a specific region of the network, representing 14% of the MEA surface that initiates the bursting regime.

With a threshold based burst detection method, Lonardoni et al. [50] were able to show that the bursts initiation sites are related to spatially segregated functional communities. We here find that the surface of initiation, unambiguously identified with our method, represents 14% of the MEA, similar to the size of the functional communities (see figure 4 of their paper). This links activity cross-correlation results from a full recording, with individual bursts initiation.

[50]: Lonardoni et al. (2017), 'Recurrently connected and localized neuronal communities initiate coordinated spontaneous activity in neuronal networks'

3.5 Conclusion

This study presents a novel methodology for characterizing synchronous bursting and propagating events in neuronal cultures. In particular we present the network phase, a natural measure for studying synchronous events. It enables us

[54]: Eckmann et al. (2008), 'Leader neurons in population bursts of 2D living neural networks'

to propose a simple definition and detection criterion for a network burst starting time. This time reference is the basic component in order to determine the first spike time probability distribution which describes the burst initiation dynamics and indicates the existence of leader neurons in networks of naturally oscillating units. It also shows the characteristic time scale of the neuronal population dynamics during what Eckmann et al. [54] called a pre-burst.

We use a modified clustering algorithm in order to detect whether the growing activity is confined in space. To do this, we compute a quantity we call performance which evaluate the location of activity. Its time evolution can highlight localised burst initiation, and pinpoint the area of initiation.

Finally, the presented methods are used to describe the burst initiation dynamics. The time reference we introduce with the network phase, allows us separate the first-to-fire inner dynamics from the regime where avalanches dominate. It shows a separation of behavior both in time and space. Our simulations with spatial networks of pacemaker neurons show that localised initiation happens only with a small connectivity spatial scale breaking the cylindrical symmetry of the simulated culture. Networks with a long connectivity scale display the same pre-burst initiation dynamics as short scale ones. However they do not display a localised initiation.

The methodology developed here makes possible a systemic analysis of bursting states, and the initiation dynamics still under many questionings. The network structural properties that drive specific neurons to be leader of bursting activities is still unknown but is now easier to address. Moreover, thanks to the linear correlation between the network phase and the number of synchronous events, it may become a powerful tool to further the discussion on the keenly debated topic of criticality in neuronal cultures.

In future work we would like to set up similar analysis on high temporal resolution calcium imaging in order to verify the applicability of the methods introduced here, and investigate with precision biological neuronal networks dynamics during bursting regime.

3.6 Chapter's appendix

Simulation of Neuronal Network

Simulate neuronal activity

Simulations are carried out with [73] the adaptive Exponential Integrate and Fire model (aEIF) via the NNGT python library and NEST simulator [121, 122]. Each neuron is described as a two dimensional system with the membrane potential variable V_m (as in the Integrate-and-Fire model) and an adaptation current w which modulate neurons' excitability (as in the Izhikevich model [123]). This model can be solved computationally for large networks in a reasonable amount of time and provide a large variety of activity patterns. [124]

[73]: Brette et al. (2005), 'Adaptive Exponential Integrate-and-Fire Model as an Effective Description of Neuronal Activity'

[123]: Izhikevich (2003), 'Simple model of spiking neurons'

[124]: Naud et al. (2008), 'Firing patterns in the adaptive exponential integrate-and-fire model'

$$\begin{aligned}
 V_m < V_{peak} & \begin{cases} C_m \frac{dV_m}{dt} = -g_L(V_m - E_L) + g_L \Delta_T e^{\frac{V_m - V_{th}}{\Delta_T}} - w + I_e + I_s \\ \tau_w \frac{dw}{dt} = a(V_m - E_L) - w \end{cases} \\
 V_m > V_{peak} & \begin{cases} V_m \leftarrow V_r \\ w \leftarrow w + b \end{cases}
 \end{aligned} \tag{3.7}$$

Where C_m is the membrane capacitance, E_L is the resting potential, g_L is the leak conductance, Δ_T is a potential normalization constant that affect the spiking current, V_{th} is the soft threshold, τ_w is the adaptation time scale, a relates to the sub-threshold adaptation, whereas b gives the spike-triggered adaptation strength and V_r is the reset potential after the potential V_m reaches V_{peak} . I_e and I_s are currents that come from respectively external sources or neighboring spikes. The exponential non-linearity model the pre-spike membrane potential sharp increase and is needed to describe in-burst fast dynamics. In the end, we choose this model because it is more biologically relevant than the Izhikevich model [123], and much less complex than the Hodgkin-Huxley model.

[123]: Izhikevich (2003), 'Simple model of spiking neurons'

To follow indications of neurons in cultures being oscillators even when uncoupled, [71] we simulate the activity with three sets of parameters that display pacemaker neurons:

[71]: Penn et al. (2016), 'Network synchronization in hippocampal neurons'

[121]: Silmathoron et al. (2021) *tfardet/NNGT*

[122]: Gewaltig et al. (2007) 'NEST (NEural Simulation Tool)'

Intrinsically Bursting (IB), Regular Spiking (RS) and Noise Driven neurons (ND) whose behavior is detailed in figure 3.10.

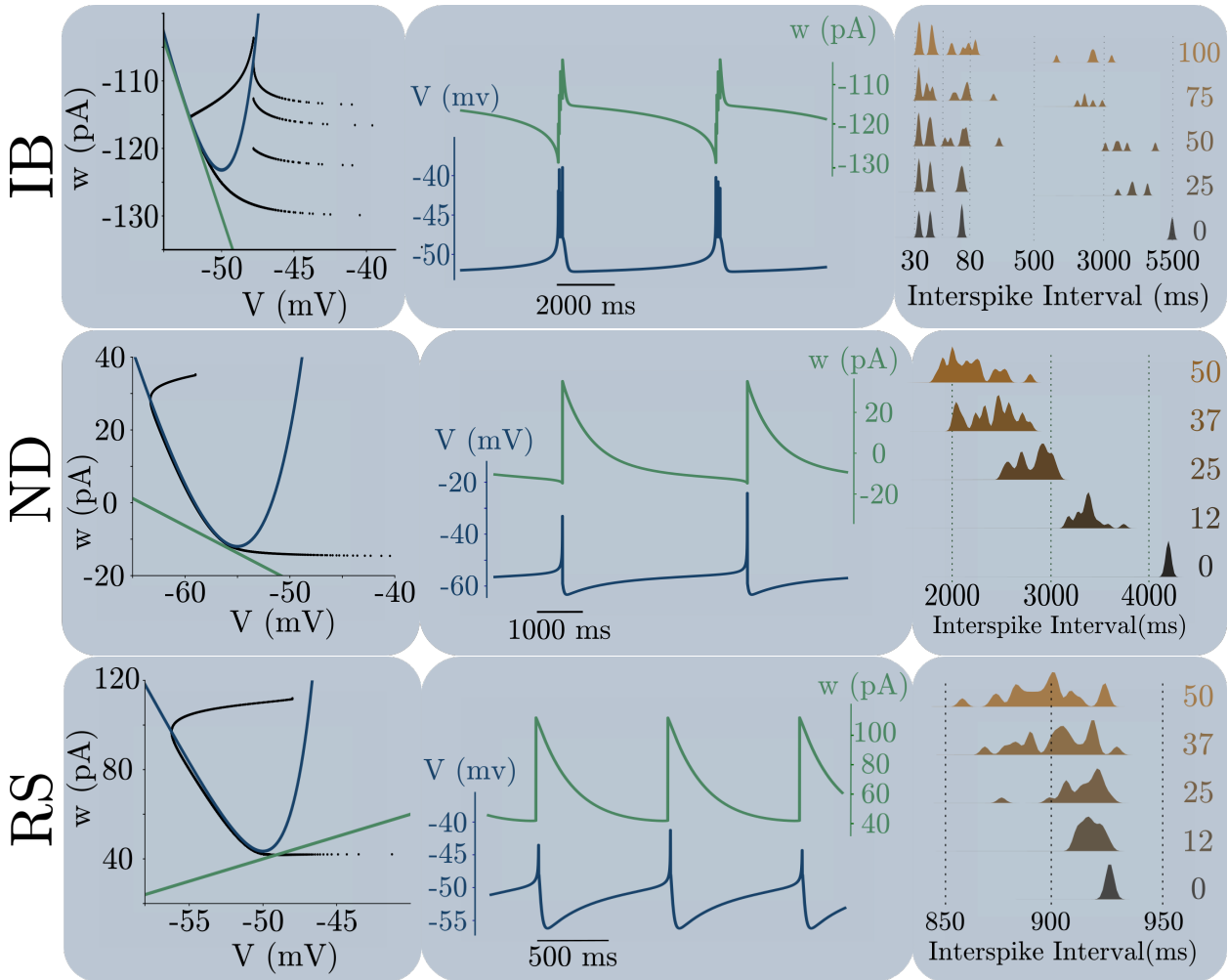


Figure 3.10: Phase space and activity of the considered parameter sets. Each line describes one set of parameters, namely (from top to bottom) Intrinsically Bursting, Noise Driven and Regular Spiking neurons. The (V_m, w) phase plane (left column) is represented with a couple of cycle represented in dark dots. Blue line is the membrane potential nullcline (set of points where $\frac{dV_m}{dt} = 0$) and green line is the adaptation current nullcline (set of points where $\frac{dw}{dt} = 0$). The middle column represents the corresponding membrane potential and adaptive current traces as functions of time. The left column is an histogram of interspike intervals with a poissonian input of rate 15 s^{-1} and increasing weights: from zero noise in black to the highest in brown in pA.

A neuron said Regular Spiking has a very periodic activity even when submitted to noisy input. Its interspike interval varies by 3% when submitted to a 15 s^{-1} poisson spike train. A Noise Driven neuron, on the other hand, is much more dependant on the input it receives: its interspike interval varies by 50 % under the same conditions. Intrinsically Bursting neurons present a more complex frequency pattern: high frequencies are super-imposed over a natural small one. This can be seen in the resetting point after a spike: it is below the V_m nullcline (see figure 3.10). We use in the paper those 3 sets

of parameters to show that the presented methods does not depend on specific values.

Model Parameters

Table 3.1 lists all parameters with their values.

Table 3.1: Parameters Values

Parameters	Values		
	Intrinsically Bursting	Noise Driven	Regular Spiking
Network modeling			
Number of neurons N		2000	
Culture radius R		$800 \mu\text{m}$	
Density d		1000mm^{-2}	
EDR scale λ		$50 - 1000 \mu\text{m}$	
Mean in-degree \bar{k}		100	
Neuron modeling			
Membrane capacitance C_m	400 pF	250 pF	200 pF
Resting Potential E_L	-70 mV	-64.2 mV	-70. mV
Leak conductance g_L	9 nS	10 nS	12.01 nS
Potential normalization Δ_T	2 mV	5.5 mV	1.8 mV
Soft threshold V_{th}	-50 mV	-55 mV	-50 mV
Adaptation time scale τ_w	400 ms	500 ms	300 ms
Sub-threshold adaptation a	-6.5 nS	-1.5 nS	2. nS
Adaptation strength b	10 pA	50 pA	70 pA
Reset Potential V_r	-47.8 mV	-59 mV	-48 mV
Potential spike peak V_{peak}	0 mV	20 mV	30 mV
External current I_e	38.8 pA	25 pA	262 pA
Refractory period Duration τ_{ref}	2 ms	2 ms	2 ms
Synapses modeling			
Synaptic weight g	20 - 50 pA	50 - 125 pA	10 - 50 pA
Synaptic time scale τ_{syn}	0.2 ms	0.2 ms	0.2 ms
Miniature events rate r_{minis}	15s^{-1}	15s^{-1}	15s^{-1}
Miniature events weight g_{minis}	10 - 25 pA	20 - 62 pA	5 - 25 pA
Simulation			
Time step Δt		0.1 ms	
Typical simulation time		300 s	

Spatial Network

To account for the spatial correlations that exist in cultures and shape its activity [9], we use an Exponential Distance Rule (EDR) to connect all neurons. A population of 2000 excitatory neurons is randomly drawn in a circular culture of radius $800 \mu\text{m}$. Then, with the same process as an Erdős-Renyi network generation, one connect node i to j with probability: $p_{ij} = p_0 e^{-d_{ij}/\lambda}$, where d_{ij} is the Euclidean distance between

[9]: Hernández-Navarro et al. (2017), 'Dominance of Metric Correlations in Two-Dimensional Neuronal Cultures Described through a Random Field Ising Model'

them. This results in a directional network, whose topological properties are predetermined by the magnitude of λ , the EDR scale and a sharp border condition: neurons can connect only inside the circular culture.

Post Synaptic Current

Interactions are modeled as fast current injection into the post-synaptic neuron, following a pre-synaptic spike and a space dependent delay. The delay is set as a 3.0 ms constant plus a spike propagation of velocity 0.1 m.s^{-1} , similar to what has been experimentally observed in cultures [79]. Overall, it follows a log-normal distribution of mean 5. to 15. ms for every network. The network metric properties set up both specific connectivity patterns, and the delay in spike propagation with different connection spatial length. Miniature events are also set as a Poisson noise of rate 15 s^{-1} for each synapses and with a post synaptic current (PSC) of half the amplitude of a spike-triggered PSC.

Synaptic weights that determine the post synaptic current amplitude are set such that the rhythmic activity is observed and stable. Stability of this state is estimated with the mean average interspike interval and network phase.

Analysis with the Izhikevich model, synaptic depression and stochastic inputs

We want to show that our methods can be used to analyze simulations with different models. For examples, previous studies [49, 106, 125] described the neuronal activity with dynamical synapses and stochastic inputs. More specifically we want to bring together various point of view in the understanding of bursting networks. Orlandi et al proposed a mechanism called *noise focusing*, based on simulations and experimental recordings, in order to interpret activity during burst initiation. On the other hand, we based our simulations under the assumption that bursting states are an example of oscillator synchronization [71, 126].

Inspired by *in silico* networks in Orlandi et al. [49], the following simulations are done with an EDR network with mean in-degree 70 and scale $100 \mu\text{m}$ in a culture of radius 2.5 mm

[79]: Barral et al. (2016), ‘Synaptic scaling rule preserves excitatory–inhibitory balance and salient neuronal network dynamics’

[49]: Orlandi et al. (2013), ‘Noise focusing and the emergence of coherent activity in neuronal cultures’

[106]: Levina et al. (2006), ‘Dynamical Synapses Give Rise to a Power-Law Distribution of Neuronal Avalanches’

[125]: Levina et al. (2007), ‘Dynamical synapses causing self-organized criticality in neural networks’

[126]: Dhamala et al. (2004), ‘Transitions to Synchrony in Coupled Bursting Neurons’

[71]: Penn et al. (2016), ‘Network synchronization in hippocampal neurons’

[49]: Orlandi et al. (2013) ‘Noise focusing and the emergence of coherent activity in neuronal cultures’

with 5000 neurons, so that the density is 250 mm^{-2} . Following Izhikevich [123] we look for parameters that display regular spiking neurons, who are not intrinsically spiking (synaptic connection and noise create the activity). This model is represented in its reduced form with the following equation

$$\begin{cases} \text{if } V < 30\text{mV} & \begin{cases} \frac{dv}{dt} = 0.04v^2 + 5v + 140 - u + I_s(t) + \eta(t) \\ \frac{du}{dt} = a(bv - u) \end{cases} \\ \text{else } V \geq 30\text{mV} & \begin{cases} v \leftarrow c \\ u \leftarrow u + d \end{cases} \end{cases} \quad (3.8)$$

where v represents the membrane potential and u a membrane recovery variable, which accounts for ionic currents. The parameter a represents the recovery variable time scale, b represents the sub-threshold adaptation, c describes the after-spike polarisation, d the spike-triggered adaptation strenght, and $I_s(t)$ is the post synaptic current. η is a Gaussian White Noise current of mean value 0 and standard deviation 10 pA. It stays constant for a duration of 5 times the simulation time step, then changes values etc... Miniature events are also set as a Poisson noise of rate 50 s^{-1} . We set the following values: $a = 0.02$, $b = 0.25$, $c = -65$ and $d = 8$.

Following previous work, [49, 125, 127] we consider dynamical synapses with the Tsodyks model described by the following equations:

$$\begin{aligned} \frac{dx}{dt} &= \frac{z}{\tau_{rec}} - Ux\delta(t - t_{spk}) \\ \frac{dy}{dt} &= -\frac{y}{\tau_{PSC}} + Ux\delta(t - t_{spk}) \\ \frac{dz}{dt} &= \frac{y}{\tau_{PSC}} - \frac{z}{\tau_{rec}} \end{aligned} \quad (3.9)$$

where x , y and z are the fractions of synaptic resources in a (respectively) recovered (ready), active, and inactive state ; τ_{rec} is the recovery time scale for synaptic depression and is set to 1.2 s and U determines the decrease of available resources used by each presynaptic spike and is set to 0.2; τ_{PSC} is the post synaptic current time scale and is set to 10 ms. Facilitation has been taken away by setting $\tau_{facil} = 0\text{ms}$.

It results in a synaptic current for neuron i given by $I_i = \sum_j^{k_i} g_{ij}y_{ij}(t)$, where g_{ij} is the absolute synaptic strength be-

[123]: Izhikevich (2003), 'Simple model of spiking neurons'

[49]: Orlandi et al. (2013), 'Noise focusing and the emergence of coherent activity in neuronal cultures'

[125]: Levina et al. (2007), 'Dynamical synapses causing self-organized criticality in neural networks'

[127]: Tsodyks et al. (2000), 'Synchrony Generation in Recurrent Networks with Frequency-Dependent Synapses'

tween i and j . The sum runs over all pre-synaptic neurons of i .

Figure 3.11 and 3.12 represent the overall analysis from the network phase maximum detection to the spatial representation of the activity with the neuron's individual phase. The proposed methodology is here able to pinpoint that this model displays a different spatiotemporal dynamics, not seen with simulations of pacemaker neurons presented in the paper. The spike probability distribution does not display the hallmarks of first-to-fire specific dynamics. Since the global activity is high in between burst a co-activation structured in space (a propagation front) can be created without specific initiation. Spatial initiation is still both localised, and structured into a propagation front.

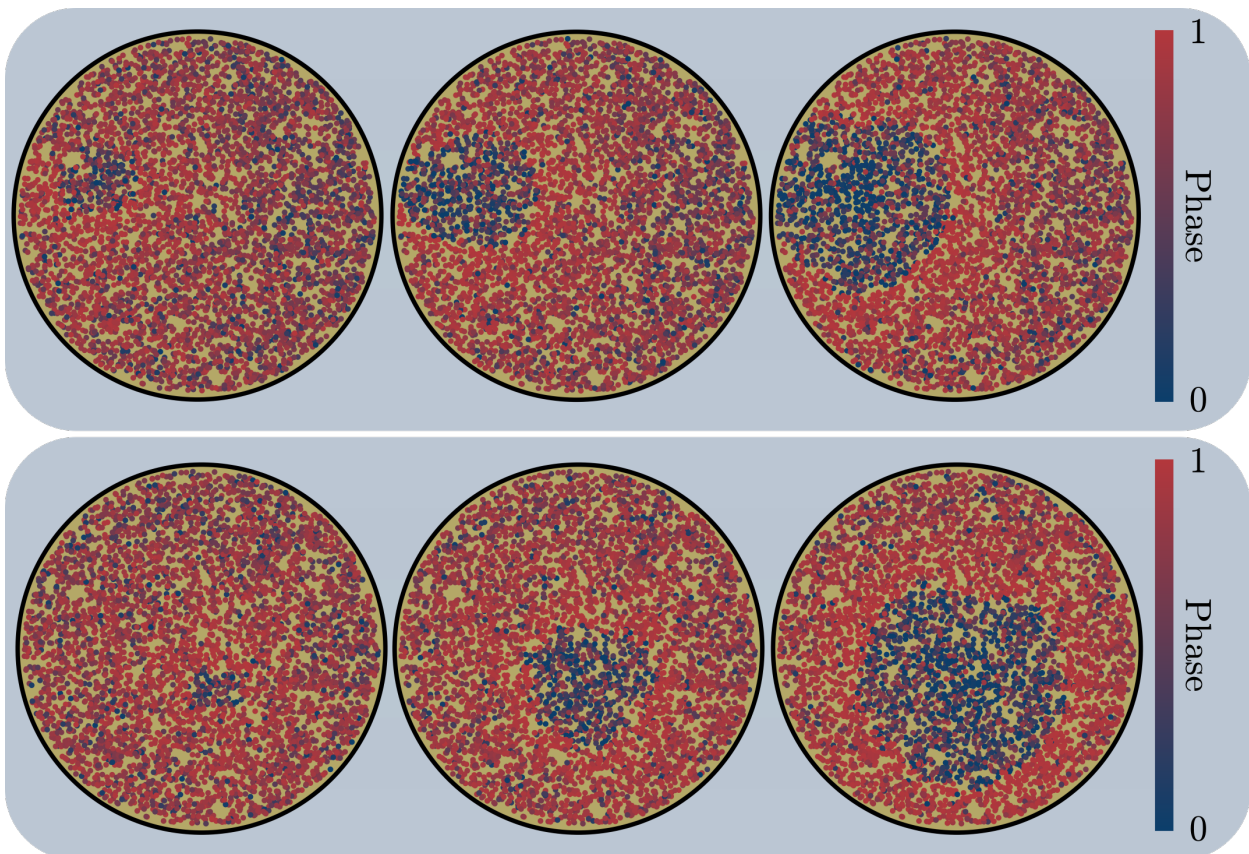


Figure 3.11: Representation in space of 2 bursts (**Top** and **Bottom**) with the neurons' phases in color scale. Culture radius is 2.5mm. The **Middle** frame corresponds to the maximum of the phase time point. 1 ms separate each frame.

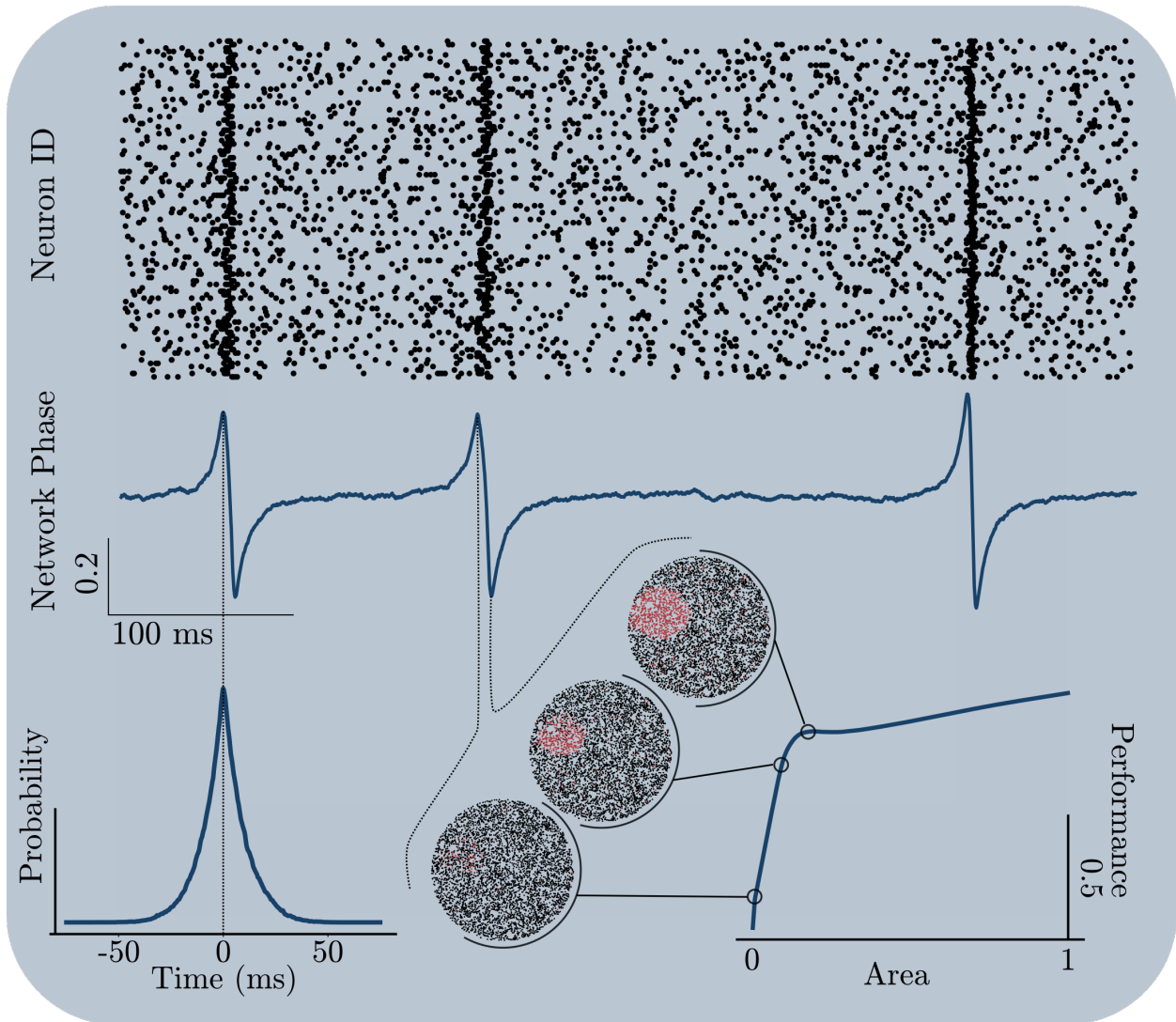
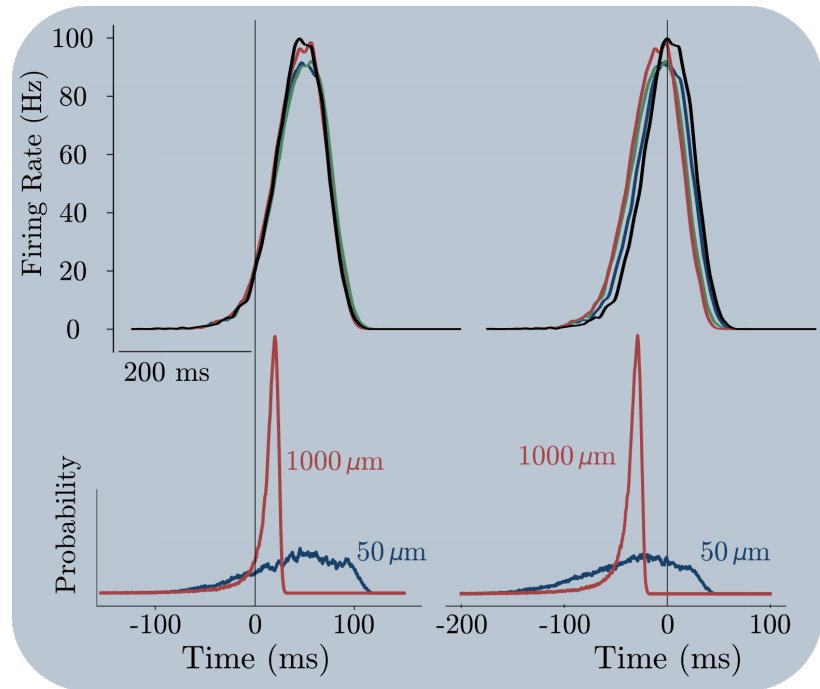


Figure 3.12: Analysis with the Izhikevich model. **Top** panel is a raster plot of 100 randomly selected neurons. **Middle** panel is a trace of the corresponding network phase. Bursts appear as in the paper, between 2 consecutive maxima and minima, however inter burst activity is always high thus the phase stays close to 0.5. **Bottom left** panel shows the first spike time probability distribution. This distribution shows the absence specific dynamics of first-to-fire neurons in this example. **Middle bottom** panel shows the clustering algorithm in space for 3 consecutive time step: visible neurons are represented as red dots, and all other as black dots. The corresponding performance is plotted in the **bottom left** panel. It shows the characteristic curve of localised growth with a region of initiation representing 14% of the total culture.

Firing rate and first spike probability distribution

In order to show that the maximum of the phase represents a specific point in the bursting dynamics, we look at a time reference computed with the spike count rate. This firing rate was computed with a convolution with an exponential kernel first (with temporal scale 3 ms), then gaussian kernel (with temporal standard deviation 3 ms). The resulting function was searched for maximum above a certain threshold to de-

Figure 3.13: Spike time probability density for two different time references. **Top** frames show the spike count rate of 4 consecutive bursts aligned on their maximum (**right**) and on an arbitrary 20 Hz threshold crossing time (**top**). **Bottom** frames show the probability distributions with the corresponding time reference. The simulations correspond to Noise Driven neurons, used in the paper in figure 3.6. One can observe that changing the time reference does not strongly change the distribution shape, however here, we cannot observe first to fire behavior anymore and the curves are arbitrarily translated in time from one another



tect bursting events. This maximum and a 20 Hz threshold value was then used as time references to compute the first spike probability distribution. Figure 3.13 shows an example of firing rate and spike time probability distribution for the same simulations as in the paper (figure 3.6) with two time references. The burst definition presented in the paper is specifically designed to look at the spiking pattern during initiation. It gives a time reference related to the network state with information about previous and future spikes and not only spikes in a couple of milliseconds time window. Hence, this time reference stays coherent over consecutive burst. The arbitrariness in the firing rate threshold method cannot achieve such coherence.

Data and Code Data and code are available in the a github repository: [MalloryDazza/NN_Burst_Dynamics](https://github.com/MalloryDazza/NN_Burst_Dynamics).

Activity snapshots The following figures shows snapshots of the in-burst activity pattern, displayed with neurons individual phases. They correspond to the examples used in the paper.

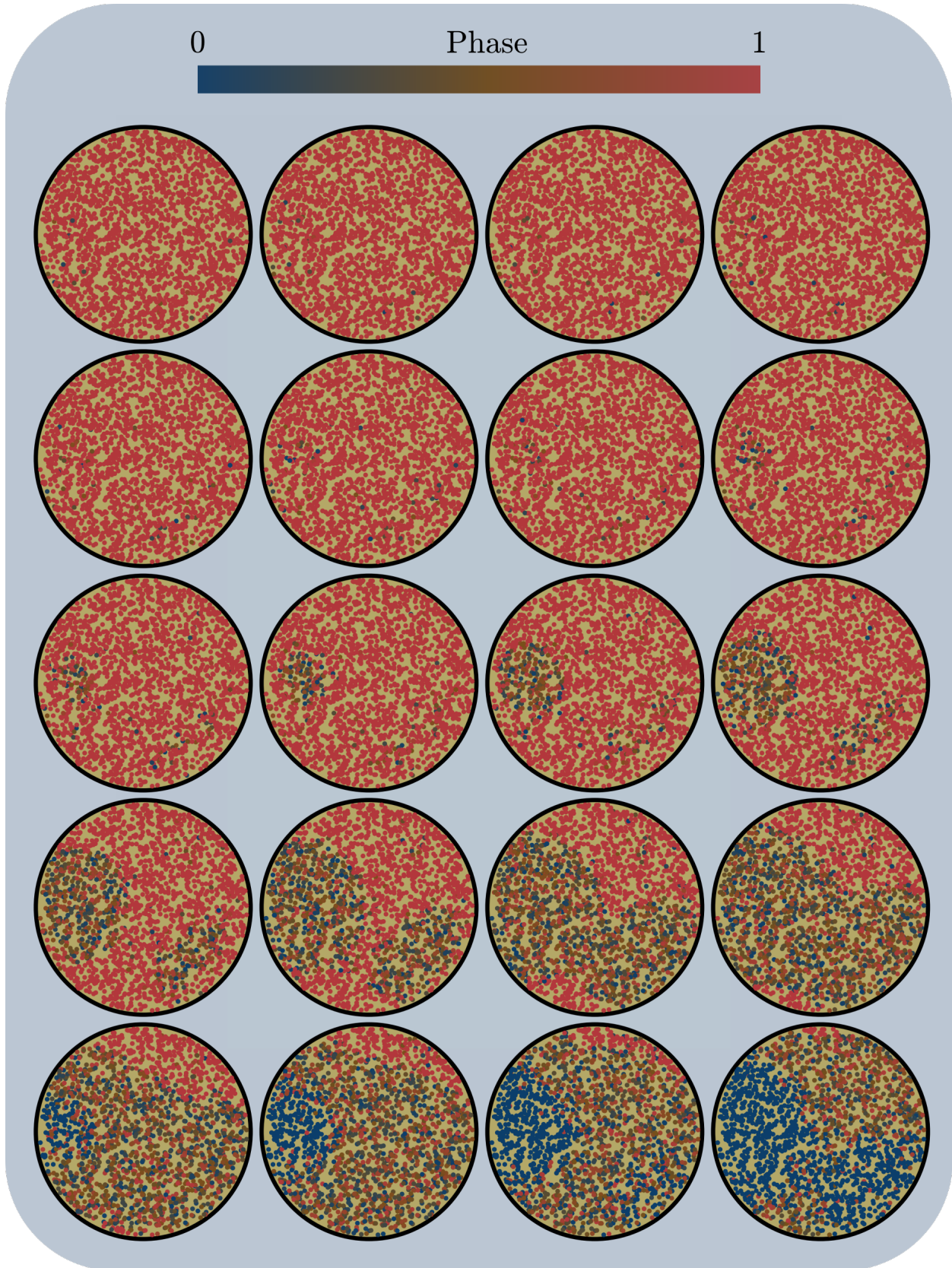


Figure 3.14: Representation in space of the burst used for presenting the spatial cluster detection (figure 2) in the paper. Neurons' phases are plot at the soma location. Each frame are separated by 25 milliseconds. Pacemakers are Intrinsically Bursting, and the EDR scale is $50 \mu\text{m}$.

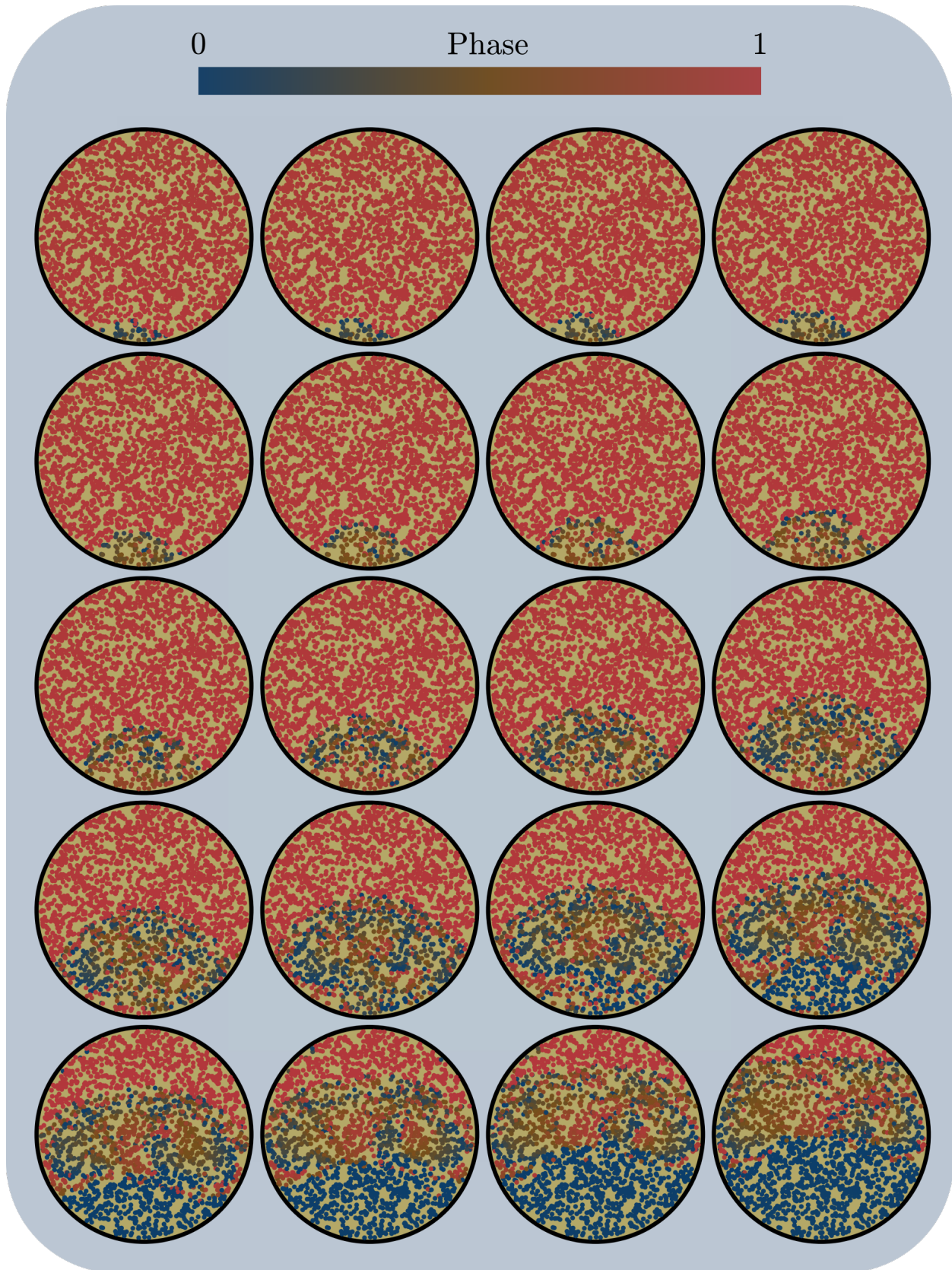


Figure 3.15: Representation in space of the burst used for performance computation (figure 5) in the paper (top activity). Neurons' phases are plot at the soma location. Each frame are separated by 5 milliseconds. Pacemakers are Regular Spiking, and the EDR scale is $50 \mu\text{m}$.



Figure 3.16: Representation in space of the burst used for performance computation (figure 5) in the paper (bottom activity). Neurons' phases are plot at the soma location. Each frame are separated by 5 milliseconds Pacemakers are Regular Spiking, and the EDR scale is $1000 \mu\text{m}.$

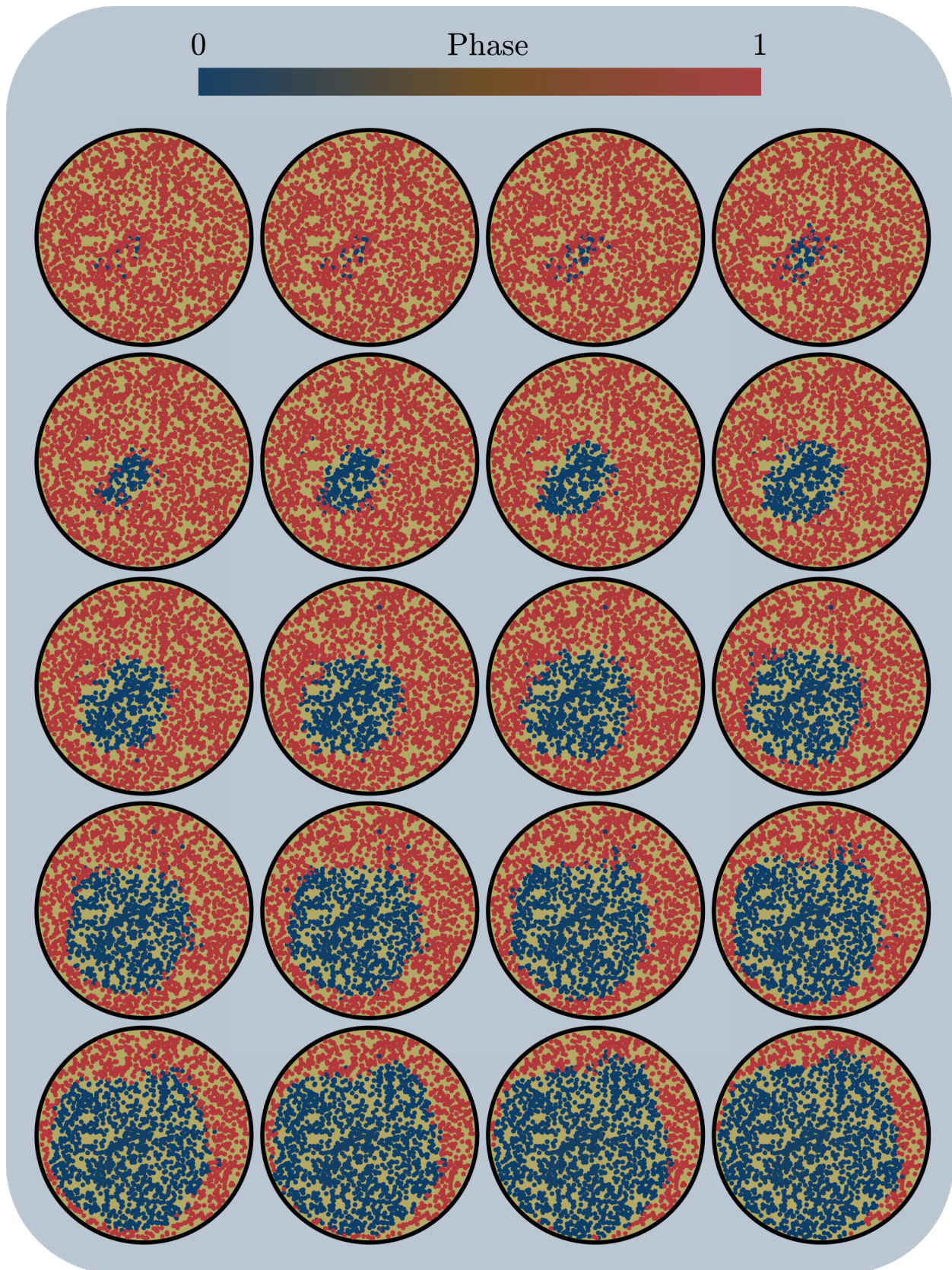


Figure 3.17: Representation in space of the burst used for velocity computation (figure 6) in the paper (left panel). Neurons' phases are plot at the soma location. Each frame are separated by 10 milliseconds. Pacemakers are Noise Driven, and the EDR scale is $50 \mu\text{m}$.

NEURONS MORPHOLOGY IN 2D CULTURES

Neuron morphology in complex networks

4.1 Neuronal morphogenesis in vivo	86
Development of the neuronal tree	86
Extension process: The Growth cone	88
Neurite structure	89
4.2 Methods and Protocols	92
Primary culture of cortical neurons	92
Data acquisition	95
4.3 Results	105
Morphological properties	105
Growth properties	109
Persistence length	110

The previous chapters and other independent studies stress out the importance of spatial correlations in the understanding and forecasting of neuronal network activity. Several network models, like the exponential distance rule model, or growth based models are able to create networks with spatial correlations, however there is a real lack of experimental data to confront the resulting network properties. The challenge is to identify individual neurons morphology in a dense and complex biological environment. This section is a step forward the characterization of two-dimensional neuronal network structure.

The original goal of the experiments I conducted during my thesis was to design a physico-chemical environment able to control the network structural properties. Is it possible to constrain neurons in such a way that the network acquire certain properties ? The firsts examples are the diode and arch microfluidic designs that are able to create directed connections between two populations. Can one goes even further and dream of a physico-chemical design able to control the number of connections, or neurons' clustering ?

Because the investigation and realisation of such environment have been stopped by the Covid-19 pandemic a more modest program has been set up. Although they lack proper characterization, I will still present the firsts attempts in the construction of this physico-chemical design. In this chapter, I will first introduce neurons morphological characteristics, and then present the characterization of the unconstrained neuronal network I have developed.



Figure 4.1: Sketch of a stage 5 neuron, from Baj et al. [128]. Dynamical phase where branches retract (represented by empty arrows) and elongate (represented by black arrows) until a stable form is reached.

4.1 Neuronal morphogenesis in vivo

Development of the neuronal tree

The characteristic neuronal arborescence is made possible by the interaction between a continuous remodelling of its cytoskeleton and the structural support of rigid filaments.

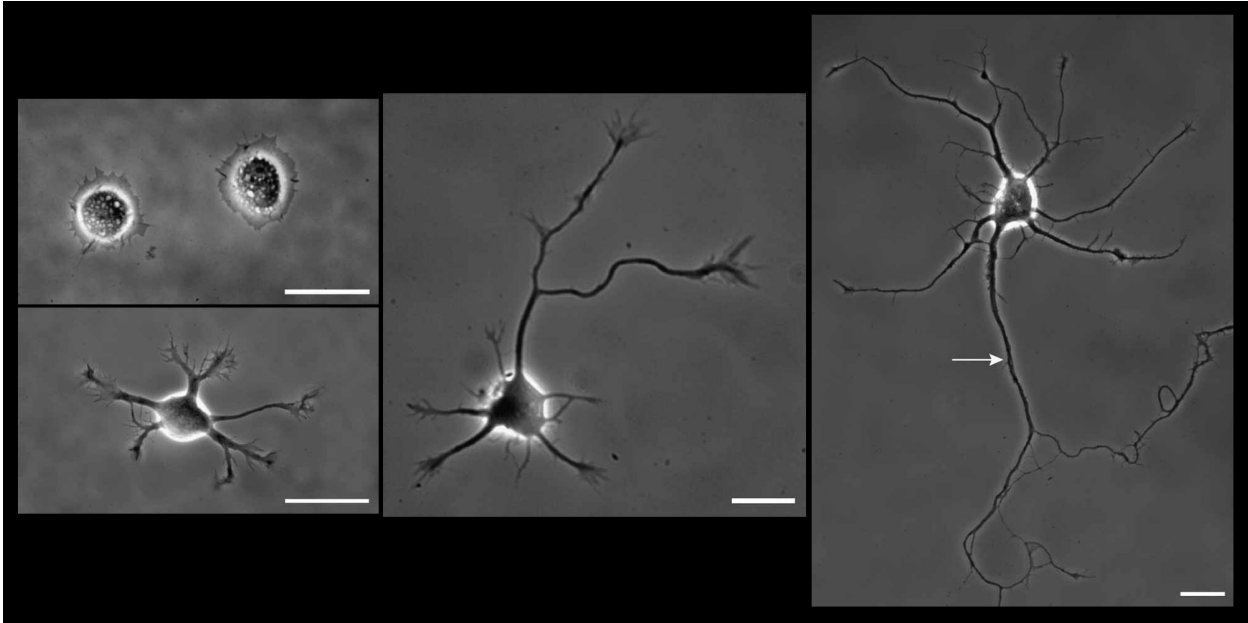


Figure 4.2: Phase-contrast image of an hippocampal neuron at its first stages of development in vitro. **Top left** frame shows a stage 1 neuron: it attaches to the substrate. **Bottom left** frame shows a stage 2 neuron: Minor neurites start to develop with intermittent growth and retraction to 20-30 μm in length. **Middle** frame shows a stage 3 neuron: One neurite, the axon, continuously grows for 2-3 hours becoming 3 times longer than the others. **Right** frame shows a stage 4 neuron: dendrites have begun their growth and the axon extend to several hundreds of microns. In culture, synapses are created on axo-dendritic crossings of different neurons. Images from Kaech et al. [131]. Scale bar is 25 μm .^a

^a [131]: Kaech et al. (2006) 'Culturing hippocampal neurons'

Mature neuron morphology emerges as the final result of a growing and differentiation process, which can be describe by a 5 stage developmental model* [129, 130]. These 5 stages are represented in figures 4.2 and 4.1.

The first two stages are the cell adhesion to its substrate and the emergence of protrusion that will soon become neurites. The creation of a single axon starts when one of the competing immature neurites prevails and grows continuously for a couple of hours. This process of polarization happens 24 hours after plating for 50% of the culture and at the fourth day in vitro, the axon can be half a millimeter long whereas dendrites are less than a hundred microns. During the fourth stage (DIV4-6), axo-dendritic crossing between two cell can see the beginning of synaptogenesis [128, 132] and the dendritic tree extends and stabilizes. Lastly, after seven days in vitro there is fast dynamical phase of branches retraction and extension until a stable morphology is reached. The last stage is the one with the most synaptic changes: the number of

* [128]: Baj et al. (2014) proposed a 6th stage of morphological stabilization during which the dendritic spine shifts from 'stubby' to 'mushroom' types.

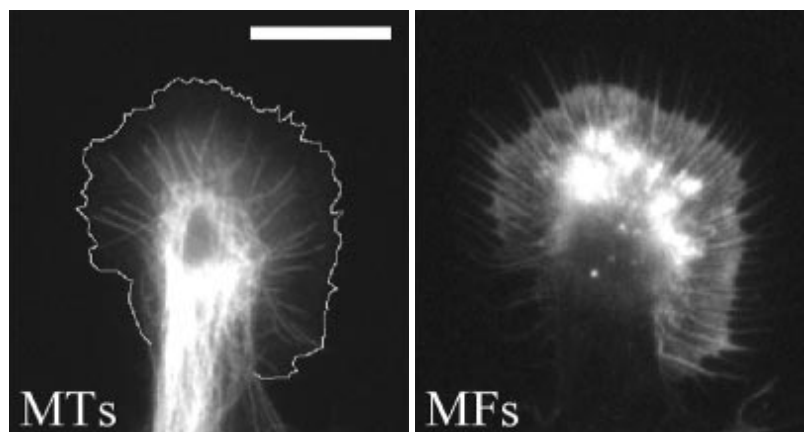
[129]: Dotti et al. (1988), 'The Establishment of Polarity by Hippocampal Neurons in Culture'

[130]: Cáceres et al. (2012), 'Neuronal Polarity'

[132]: Fletcher et al. (1994), 'Synaptogenesis in hippocampal cultures'

[128]: Baj et al. (2014), 'Developmental and maintenance defects in Rett syndrome neurons identified by a new mouse staging system in vitro'

Figure 4.3: Fluorescent imaging of microtubules (**left**) and actin microfilaments (**right**) in a growth cone, from Buck et al. [137]. Scale bar is 10 microns.



[133]: Ganguly et al. (2001), ‘GABA Itself Promotes the Developmental Switch of Neuronal GABAergic Responses from Excitation to Inhibition’

[134]: Harrill et al. (2015), ‘Ontogeny of biochemical, morphological and functional parameters of synaptogenesis in primary cultures of rat hippocampal and cortical neurons’

[135]: Conde et al. (2009), ‘Microtubule assembly, organization and dynamics in axons and dendrites’

[136]: Coles et al. (2015), ‘Coordinating Neuronal Actin–Microtubule Dynamics’

[137]: Buck et al. (2002), ‘Growth Cone Turning Induced by Direct Local Modification of Microtubule Dynamics’

[138]: Kellermeyer et al. (2018), ‘The Role of Apoptotic Signaling in Axon Guidance’

[139]: Koene et al. (2009), ‘NET-MORPH’

[140]: Maskery et al. (2004), ‘Growth Cone Pathfinding: a competition between deterministic and stochastic events’

synapses increase, dendritic spine morphology changes and some excitatory synapses starts to switch to inhibitory [133, 134] .

Extension process: The Growth cone

During the extension of axon and dendrites, the main actor is the growth cone: a mesh of actin filament and microtubule that act as a two-dimensional molecular motor. Figure 4.3 shows the actin filaments and microtubules organization in the growth cone. These two polymers are responsible for the growth cone structure and its ability to steer the neurite growth. [135, 136] When entering a new environment, bundles of actin filament extend the cell membrane by forming filopodia: finger shaped organs able to interact with the environment and create traction forces responsible for the elongation and turning of the growth cone.

The interaction with the bio-chemical environment, also called chemotropic guidance is one of the main mechanisms responsible for the orientation of growth cone movement. Specific chemicals have been shown [137, 138] to initiate biochemical pathways in the growth cone, responsible for the cytoskeleton dynamics and act as attractors, or repellants. The substrate stiffness can also orient growth cone motion: a soft substrate is attractive which explain the preference for neurons to grow over glial cells. However, in a two-dimensional cultures, (if present) guidance cues are uniform and the growth can be well described as a random process [139, 140] .

The growth dynamic cannot be described as a continuous process. Indeed, reports have shown that the growth cone is still more than 50 % of the time. There are period of pausing,

during which the microtubules re-organize into a stable configuration allowing the propagation to continue, and period of retraction [141]. Hence, even in the absence of chemical guidance cues, the growth process depends on the cytoskeleton dynamics and a biologically relevant model needs to take it into account [142]. The run-and-tumble model²³ describes the motion of a self propelled particule as sequences of linear motion (run), interspersed with stochastic change in direction (tumble) according to a uniform law between two extrem values $[\theta_m, -\theta_m]$. The tumble can represent the re-organization pause of the growth cone whereas the run represent the period of rapid motion (the growth cone instantaneous speed is in the order of $10 \mu\text{m.h}^{-1}$)

Neurite structure

Tortuous neurites' morphology is not only due to the erratic growth cone motility. Imagine sliding a sewing thread on a 2D surface from its tip. After a couple of centimeters you will notice that the thread shape does not follow exactly the tip motion. There are two reasons for this, firstly the thread does no adhere to the surface and is allowed to move relatively freely. Secondly, the thread stiffness protect it from sharp angles: these are not stable configuration of the filament. Same thing happens for neurites, mature neurites' shape depends on the interaction with the substrate, and the cytoskeleton rigidity, made of a bundle of microtubules. Microtubules rigidity is quantified through the bending stiffness: $Y \times I$ with Y the Young modulus and I the second moment of area. The bending stiffness quantifies how much force is required to bend the microtubule up to a certain curvature κ , such that:

$$\kappa = \frac{YI}{F\Delta x} \approx \frac{\Delta y}{\Delta x^2}$$

with F the applied force, Δx the length of the microtubule rod and Δy its deflection. It is well known [144, 145] that the order of magnitude of microtubule bending stiffness in vitro is 10^{-23} N.m^2 , thus the tension required to bend a single $10 \mu\text{m}$ long microtubule, to an aspect ratio $\frac{\Delta y}{\Delta x} = \frac{1}{10}$ is 10^{-5} nN. The rest tension of axon has been found to be in range of 1-10 nN, both in vivo and in vitro [146, 147]. Thus, a single microtubule is easily bend by forces present in the cell. The large gap in order of magnituded indeed shows that

[141]: Smirnov et al. (2014), 'The effects of confinement on neuronal-growth cone morphology and velocity'
[142]: Rauch et al. (2013), 'Forces from the rear'

23: for a detailed mathematical description of run-and-tumble and brownian particle motion see [143] Solon et al., (2015)

[144]: Gittes et al. (1993), 'Flexural rigidity of microtubules and actin filaments measured from thermal fluctuations in shape.'

[145]: Suresh (2007), 'Biomechanics and biophysics of cancer cells'

[146]: Hällström et al. (2010), 'Fifteen-Piconewton Force Detection from Neural Growth Cones Using Nanowire Arrays'

[147]: Rajagopalan et al. (2010), 'Drosophila Neurons Actively Regulate Axonal Tension In Vivo'

24: Independant filaments would linearly increase the total stiffness of a material, such that

$$\kappa_{bundle} = N_{bundle} \kappa_{MT}$$

[148]: Landau et al. (1959), *Theory of Elasticity, Volume 7 of Course of Theoretical Physics*

[144]: Gittes et al. (1993), 'Flexural rigidity of microtubules and actin filaments measured from thermal fluctuations in shape.'

[149]: Rivetti et al. (1996), 'Scanning Force Microscopy of DNA Deposited onto Mica'

[150]: Abels et al. (2005), 'Single-Molecule Measurements of the Persistence Length of Double-Stranded RNA'

25: It can be computed from the distribution eq. 4.2

[151]: Howard (2001), *Mechanics of Motor Proteins & the Cytoskeleton*

neurite stable configuration is due to both a rigid bundle of interacting microtubule which increases its stiffness²⁴ and the biochemical interaction with its environment.

The quantity used to described bending of elongated stream-lined systems is the persistence length. It has been used to quantify polymer chains stiffness or the path formed by random walker. In the study of polymer chains, the persistence lengths is defined relatively to the mechanical properties of the chain. [144, 148–150] The energy required to bend by an angle θ a chain of size d , in a 2D plane is:

$$E = \frac{YI\alpha^2}{2d} = k_B T \frac{l_p}{2d} \theta^2 \quad (4.1)$$

where k_B is the Boltzmann constant, T the absolute temperature, Y the Young modulus, I the chain second moment of area and $l_p = \frac{EI}{k_B T}$ the persistence length. Hence, the thermal fluctuation of θ follows a Gaussian distribution, of mean zero and standard deviation $\sigma = \sqrt{d/l_p}$:

$$P(\theta) = \sqrt{\frac{l_p}{2\pi d}} \exp\left(-\frac{l_p \theta^2}{2d}\right) \quad (4.2)$$

Such distribution, and stiffness, has a major consequence on the chain shape. The persistence length l_p corresponds to the distance over which the neurite is close to straight line. This can be quantify by the correlation of the direction. Let us denote $\theta(s)$ the tangent angle of the neurite at a curvilinear axis s . Under the hypothesis of the equipartition principle, one can show²⁵ that in a 2D plane (see pages 317-318 of Jonathan Howard's book [151]):

$$\langle \cos(\theta(s) - \theta(0)) \rangle = \exp\left(-\frac{s}{2l_p}\right) \quad (4.3)$$

In the absence of stiffness, or spatial "memory" the persistence length is null and the correlation falls to zero. This is the case of a Brownian Motion where each directions are taken independently of the previous ones. With a certain rigidity, or spatial memory the persistence length has a finite value, directly related to the mechanical (for a polymer) or motility (for a Brownian Motion) properties. If the angle θ is determined by the thermal fluctuation, then the distribution

of theta values is a Gaussian and the persistence length is the orientation correlation length (see equation 4.3).

Lastly, in order to properly characterize the neuronal network, one has to investigate the formation of synaptic connections. Synaptogenesis is a long process which occurs during the last stages of development from DIV4 to DIV15. They typically happen on overlapping regions between a pre-synaptic axon and a post-synaptic dendrite and can reach an extremely high density in mature culture. Dzyubenko et al. [152] reported 10 synapses. μm^{-2} in typical hippocampal neurons and astrocyte co-cultures with 200 mm^{-2} cells.

[152]: Dzyubenko et al. (2016), 'Colocalization of synapse marker proteins evaluated by STED-microscopy reveals patterns of neuronal synapse distribution in vitro'

From a single cell to complex network

Our main goal is to characterize the network of neuronal cultures. As in the theoretical models used in the previous chapters the network is made of nodes, represented by the neurons' soma, and directional connections from a pre-synaptic neuron to a post-synaptic one. Hence we are interested in the possibility to create synapses between two specific neurons. It seems obvious that if they are too far apart, they will never be connected. It is impossible for the axon to grow over very long distances (typically several millimeters for mice). For close by neurons, a connection in the network is created only if at least one synapse is formed, thus an axon and a dendrite have to overlap over a certain distance. Because of the complex neurites' growth process, the Euclidian distance between the soma is not a relevant parameter to estimate the probability of connections. Axon tortuosity, branching, or the interaction with its biochemical environment are all specific features of neuronal growth and morphology that influence the network properties: the number of connections per neurons (the degree), the probability of triangles and loops (clustering), the centrality of specific nodes (betweenness) etc...

Neurons morphological characteristics, obtained from cultures of cortical neurons, can be directly implemented into growth simulations in order to reproduce biologically relevant networks. Also, I will present a *toy model* to estimate the typical connection Euclidian length in network of real neurons that take into account neurites tortuosity, branching etc...

4.2 Methods and Protocols

Primary culture of cortical neurons

Dissection and cell plating

Dissections were done by Audric Jan with the occasional help of Terence Saulnier and Josquin Courte. Hence, the protocol follows the one presented in Audric Jan PhD thesis[153].

[153]: Jan (2021), 'Fasciculation axonale et dynamique du cône de croissance en environnement confiné'

26: 0.5mL of GBSS (Sigma 9779) completed to 6mL with 100 g.L⁻¹ D-(+)-glucose in calcium and magnesium free D-PBS (Gibco 14190-094)

27: Papain Sigma, 76220

28: DMEM Gibco, 31966-021

Wild type gestating mice at embryonic day 15-16 were dissected in order to extract the embryos' cortexes. They rest during the dissection and until the digestion step on ice in Glucosed Gey's Balanced Salt Solution²⁶ (GBSS_g). After removing the majority of the GBSS_g solution, the papain²⁷ at 15 U.mL⁻¹ in DMEM with high glucose and supplemented with GlutaMAX and sodium pyruvate²⁸ and filtered at 0.22μm is added. The solution is incubated at 37°C for 8 to 10 minutes and gently flipped every 3 minutes. The enzymatic dissociation is stopped with 0.5mL of serum.

After changing the supernatant to DMEM we mechanically dissociate cells with pipettes of varying sizes. It is important to limit the number of air bubbles to a minimum and stopped the trituration once there is no macroscopic piece visible anymore to preserve cell viability. The cell suspension is then centrifugated 6 minutes at 700 rpm at room temperature. After extracting the DMEM, cells are suspended in the seeding medium the closest possible to the seeding concentration. Before seeding, cells are counted with a Malassez hemocytometer. Since the density I seek is close to several hundreds of cells per squared millimetre, the number of cells in a 24x24 mm² coverslip are in the order of 300 000. The concentration depends on the volume added, which depends on the substrate (chips or 'open-air' culture).

In microfluidic chips, the plating medium composition is (percentages in volume):

- ▶ 5% Fetal bovine serum
- ▶ 2% B27 supplement (Gibco, 17504-044)
- ▶ 1% N2 supplement (Gibco, 17502-048)
- ▶ 92% high glucose DMEM, supplemented with pyruvate and GlutaMAX (Gibco, 31966-021)

In 'open-air' culture, the plating medium composition is (percentages in volume):

- ▶ 5% Horse serum

- ▶ 2% B27 supplement (Gibco, 17504-044)
- ▶ 1% N2 supplement (Gibco, 17502-048)
- ▶ 1% Glutamine (Gibco, A2916801)
- ▶ 1% Sodium Pyruvate (Gibco, 11360-070)
- ▶ 90% Glutamine free MEM (Gibco, 21090-022)

The plating medium is changed the day after the dissection to a maintenance medium of composition (percentage in volume):

- ▶ 1% Horse serum
- ▶ 2% B27 supplement (Gibco, 17504-044)
- ▶ 1% Glutamine (Gibco, A2916801)
- ▶ 96% Neurobasal (Gibco, 21103-049)

After plating, cells are stored in a 37°C and 5% CO₂ atmosphere. In every medium, 0.2% of 10mg.mL⁻¹ gentamicin²⁹ is added (Gentamicin Gibco, 15710-049)

Substrate

The substrate is made of glass coverslips coated with adhesive molecules. In order to confine neuronal growth, the molecule can be deposited on limited, and controlled regions of the coverslip. This is done with photolithography techniques and has been explained in details in previous works, (see [154, 155] for most recent ones).

After cleaning with isopropanol the dried coverslips are exposed 30s to an O₂ plasma in order to prepare the surface for silanization. We introduce a dozen of coverslips with 100 μL of AB 109004 silane³⁰ in a vacuum chamber, rapidly after the plasma. The vacuum pump is activated for 20 minutes, and again 20 minutes after the coverslips are stored in a large petri dish tightly closed with parafilm. Silane is highly toxic and caution is needed during this step. It needs to be achieved under an extractor hood. Also, preparing a falcon tube of water to dispose of the silane pipette tip is a good habit.

In a clean room, S1805 positive photoresist is spincoated at 4000 rpm (with 4000 rpm.s⁻¹ acceleration) for 30s on the silane coated coverslips. After annealing it at 115°C for 1 minute, the coverslips are exposed to a 50-60 mJ.cm² UV light through a chosen mask. With wavelength of 435 nm, and the spectral lamp of the MJB4 mask aligner in the IPGG, this dose corresponds to a 5s exposure. The pattern is revealed after 1 min in the MF-26A developer. The coverslip is rinsed in

[154]: Tomba (2014), 'Primary brain cells in in vitro controlled microenvironments: single cell behaviors for collective functions'

[155]: Braini (2016), 'Approche biophysique des formes neuronales'

30: (3-methacryloxypropyl)trichlorosilane, 95%

31: PLO, Sigma P4957

32: Laminin, Sigma L2020

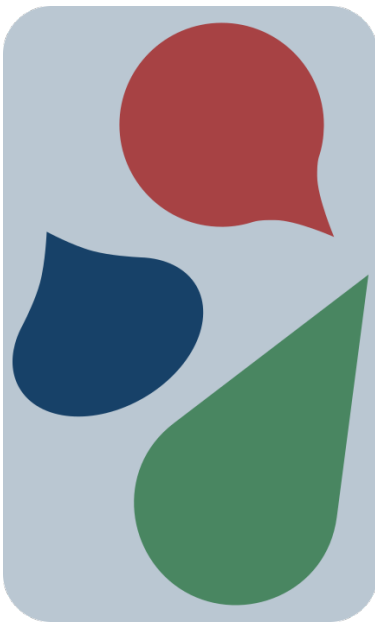


Figure 4.4: Patterns of adhesive proteins used for the photolithography mask. The tips have of 30° angle. **Green** pattern is created from a 1.5 mm in diameter disk, and imposing the tip to align with the circle tangents. **Red** pattern is created with the same constraint, but the tip is shortened with a curvature. **Blue** pattern is created with ellipses of width 1.5 mm and 1 mm height. These patterns are also created with a continuity of the tangents.

distilled water and dried with a vertical air jet. The coverslips can be stored in petri dish closed with parafilm for months.

The patterned coverslips are then exposed 5 minutes to an O_2 plasma. This step removes the silane where the resist is not, and prepare the glass surface to fix the adhesive molecules. It seems that this long plasma also make the photoresist easier to remove in the following steps. Neglecting the importance of this plasma has made many of my experiments unsuccessful. The poly-L-ornithine³¹ adhesive molecule is incubated overnight at $80\mu\text{g}\cdot\text{mL}^{-1}$ rapidly after the O_2 plasma. A $200\mu\text{L}$ drop is deposited on a clean and flat hydrophobic surface (a petri dish for instance, or parafilm). A coverslip is then carefully put on top of the drop, the photoresist pattern facing down. The petri dish is then tightly closed with parafilm to prevent evaporation and left aside overnight. After washing it in distilled water or D-PBS, the photoresist is removed in a 90s ultrasonic bath of pur ethanol. A deviation from the original protocol made me start with longer than 2min30s ultrasonic bath, although 1min30 should be enough providing the O_2 plasma is successful. After washing 2 times in distilled water, $10\mu\text{g}\cdot\text{mL}^{-1}$ laminin³² in distilled water is incubated for 45 minutes with the same protocol. The coverslips are washed 2 times and deposited in individual petri dishes with 1.5 mL of cell free seeding medium.

Poly-ornithine and laminin dilution can be done in calcium and magnesium free D-PBS unless the coverslips need to be dried. In this specific case, the dilution can be done in distilled water.

In unconstrained environment, the photolithography is not necessary and fluorodishes are coated with poly-ornithine and laminin with the same procedure. Fluorodish are specific petri dishes with glass bottom suited for microscopic imaging with strong magnification.

Mask design

In the EDR network model, neurons in-degree is directly related with the finite size of the culture. Closer to the boundaries, neurons create fewer connections because of the lack of close neighbours. Following this idea, I assumed that creating a sharp tip would increase the ratio border over surface, hence decrease locally the degree. Different values of the tip sharpness, as well as transitions to the circular part of the culture was tested, and can be seen in figure 4.5. The idea

behind all patterns is to reduce the number of sharp angles. I made sure the border gradient (the tangents) is continuous. 60 of these patterns fit in a 24x24 coverslip, allowing to test multiple tips angles.

Data acquisition

Probing individual cell

CytBow neurons

In order to quantify individual cell morphology in a dense biological environment one need to differentiate one specific cell from the others. Loulier et al. [156] developed the technology of multiaddressable genome-integrative color markers that are able to color label individual cells and follow their direct line of descent. I can use this technology in order to identify individual neurons. The colour labelling is expressed in the form of a fluorescent protein produced in the cytoplasm. Hence the mice's denomination: CytBow. In particular, neuronal cells of CytBow mice express 3 types of mutually exclusive fluorescent proteins [157–160] :

- ▶ the orange-red tdTomato ($\lambda_{abs} = 554\text{nm}$, $\lambda_{em} = 581\text{nm}$) or mCherry ($\lambda_{abs} = 587\text{nm}$, $\lambda_{em} = 610\text{nm}$) [157]
- ▶ the yellow-green mEYFP ($\lambda_{abs} = 515\text{nm}$, $\lambda_{em} = 528\text{nm}$) [158]
- ▶ the blue-green mCerulean ($\lambda_{abs} = 433\text{nm}$, $\lambda_{em} = 475\text{nm}$) [159] or mTurquoise2 ($\lambda_{abs} = 434\text{nm}$, $\lambda_{em} = 474\text{nm}$) [160]

Each cell in culture performed with CytBow mice can be colour coded, but with only 3 labels. Either the density is sufficiently small for this 3 colour neurons to rarely cross or the colour coded neurons must be only a fraction of the total population. We seek density close to several 100 mm^2 , and axons can grow up to a millimetre. Thus, one need to add wild type neurons, in a CytBow culture. Cultures with 20% CytBow³³ and 80% wild type has been successfully made on patterned substrate. The phenotypic instability of CytBow construction, and the strong reduction of mice availability after the Covid-19 pandemic made us choose another technology to keep our investigation going on. Note however, that the concentration of 20% colour coded cells was too high to identify individual cell morphology.

[156]: Loulier et al. (2014), 'Multiplex Cell and Lineage Tracking with Combinatorial Labels'

[157]: Shaner et al. (2004), 'Improved monomeric red, orange and yellow fluorescent proteins derived from *Discosoma* sp. red fluorescent protein'

[158]: Zacharias (2002), 'Partitioning of Lipid-Modified Monomeric GFPs into Membrane Microdomains of Live Cells'

[159]: Rizzo et al. (2004), 'An improved cyan fluorescent protein variant useful for FRET'

[160]: Goedhart et al. (2012), 'Structure-guided evolution of cyan fluorescent proteins towards a quantum yield of 93%'

33: Jean Livet's team at the Institut de la Vision kindly provided the mices

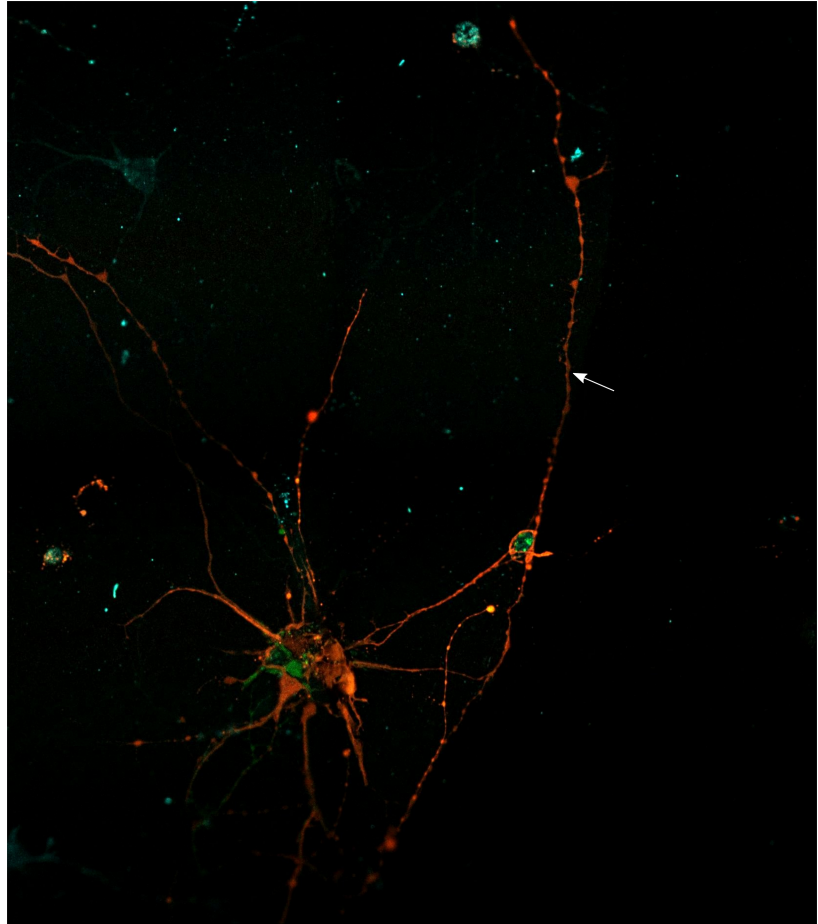


Figure 4.5: Photography of the border of a pattern with CytBow neurons at DIV4. One can see a small bundle of axon following the pattern boundary from top to bottom (**white arrow**). The green and red pseudocolours represent the mEYP and tdTomato proteins of CytBow construction.

Virus infection

34: Viral vector [wikipedia article](#)

35: unable to replicate by itself

*Viral vectors are tools commonly used by molecular biologists to deliver genetic material into cells.*³⁴

Lentiviruses are a subclass of virus able to target non-dividing cells like neurons. Also, it is possible to incorporate the green fluorescent protein (GFP) gene into a safe³⁵ and genetically stable lentivirus. The produced viral vector can be used to mark individual cells with GFP. A precise control of the infection is nonetheless require to control the fraction of probed neurons.

A solution of $10^7 - 10^8$ U.mL⁻¹ viral vector produced by Christian G. Specht's team, and stored at -80°C is introduced in the maintenance medium the day after plating (DIV1). It is assumed, after trying it once at DIV5, that infection in older culture are much less successful.

The quantity of added virus needs to be astutely adjusted to what one wants to observe. In order to set up a good statistical analysis I want as much images of neurons as possible, hence

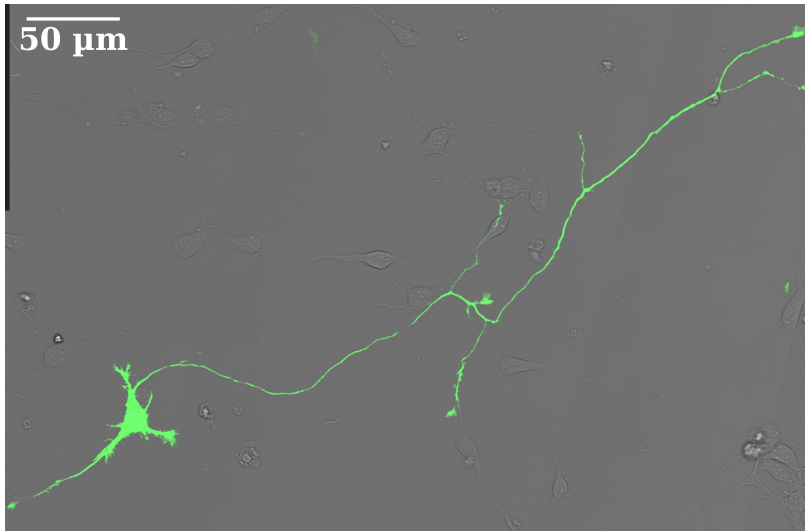


Figure 4.6: Phase contrast image of DIV 4 cortical neurons, with one expressing the GFP in pseudocolour.

the number of infected cells that express the GFP must be the highest possible. However, if too many cells cross one another it became impossible to properly characterize the single cell properties of the culture. For a cell of typical spatial extension e (see for example figure 4.6 the extension e corresponds to the diagonal, here $e = 500\mu\text{m}$), the density of cell expressing the GFP must scale as $d_{\text{GFP}} \sim \frac{1}{e^2}$. The number of cells expressing the GFP, and the quantity of virus added in the medium depends on the typical neuron size one wants to observe. This size depends on the neuron growth speed and age.

The larger the virus quantity, the higher the number of neurons one can observe, but the shorter these neurons can be observed. Thus, to observe neurons at late ages, one need very small quantity of virus and will only observe a few neurons expressing the GFP.

Surprisingly, the cell density is also to be taken into account. Indeed, the cell density expressing the GFP is 20% higher³⁶ in the cultures where I added 5 μL of viral solution compared to those where I added 10 μL . Taking the cell density into account, one find a monotonically increasing behavior of the ratio of density $\frac{d_{\text{GFP}}}{d}$, where d_{GFP} is the cell density expressing the GFP and d the total cell density. It is plausible that one need to take diffusion into account. The diffusion coefficient of virus in water is in the order of magnitude of $10\mu\text{m}^2.\text{s}^{-1}$ [161]. The virus concentration in the medium is close to 3.10^3mL^{-1} , thus the typical distance between two virus is 700 μm . It takes ~ 20 hours for a virus to diffuse over such distance, which suggest that diffusion is one of the limiting factor. Increasing the cell density increases the virus

36: This value takes all measurement into account

[161]: Bockstahler et al. (1962), 'The Molecular Weight and Other Biophysical Properties of Bromegrass Mosaic Virus'

37: If biological and adsorption mechanisms are indeed negligible with respect to diffusion processes

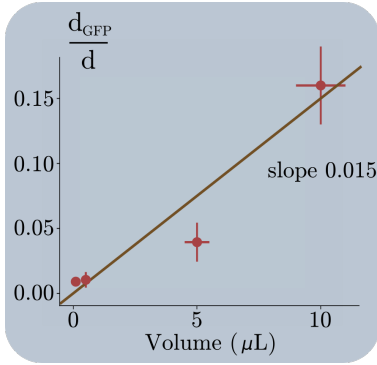


Figure 4.7: Ratio of cell density expressing the GFP, d_{GFP} and the total density d versus the volume of added virus. The line gives the approximate trend in the range we are interested in. Density were estimated by counted somata in images of $1\text{-}25\text{ mm}^{-2}$.

concentration gradient³⁷ which in turn, increase the diffusion efficiency by the same amount.

In open-air culture, with 2-3 mL of medium it seems that the cell density and the quantity of added virus are to be considered together to properly identify only a small sample of the whole neuronal network.

Figure 4.7 displays the ratio of densities versus the volume of virus solution added in the 3mL medium. There is no reason for the curve to be linear, however it gives a good approximation to set up the order of magnitude. The cell density that express the GFP can be written as:

$$d_{\text{GFP}} \approx d \times V_v \times 0.015$$

where d is the total density, and V_v the volume of virus (in μL), and 0.015 the slope (in μL^{-1}) computed in figure 4.7. One wants this density to match with $\frac{1}{e^2}$. Hence,

$$V_v(d, e) \approx \frac{1}{0.015 \times d \times e^2} \quad (4.4)$$

This equation is equivalent with saying that, if I want to observe a neuron of size e , in a culture of density d , I need to add a volume of virus V_v . For instance, a neuron with $e = 250\mu\text{m}$, in a culture of density 150 mm^{-2} can be observed with $7\mu\text{L}$. This is not an exact value but it is a good order of magnitude and corresponds to the experiments I conducted. If the density is higher, the number of cells expressing the GFP will be higher, thus the volume V_v needs to be lower. Moreover, if one looks for density $d_{\text{GFP}} \sim 1/e^2$ there is a good chance to overestimate the measurement towards smaller neurons of the culture. Since smaller ones are less likely to cross other neurons, they will be predominant in the statistics. Aiming for lower values that V_v in equation 4.4 is a good strategy. Fewer neurons will express the GFP but the statistics will be more consistent with the reality.

Table 4.1 shows the number of recorded neurons and the volume of virus added in each corresponding dish. One can see the second dissection fruitfulness, nonetheless it may have introduced a bias towards smaller neurons. When many neurons overlap and are not identifiable individually it is hard to estimate this bias. For instance, picture 4.9 shows that in a 20 mm^2 many neurons overlap and only a couple are

Table 4.1: Number of recorded neurons and volume of virus added in the 3 dissections from which the data are extracted. The number of recorded neurons per dish and the total per days in vitro per dissection is displayed on the right columns.

	Days In Vitro	Volume of virus V_v	Number of recorded neurons	
Dissection 1	4	1 μ l	8	29
			5	
			3	
	5	0.1 μ l	11	13
			2	
Dissection 2	4	5 μ l	35	47
			12	
	5	1 μ l	11	22
			11	
	6	0.5 μ l 0.05 μ l	24	46
22				
Dissection 3	4	1 μ l	23	31
			8	
	5	0.1 μ l	9	16
			7	
	6	0.01 μ l	3	6
3				

properly separable. These 3 dissections were used to set the quantity of virus and acquire morphological data, hence the heterogeneity and uneven representation of each culture.

Image recordings and Analysis

Images were recorded with a confocal microscope equipped with an oil-immersion 40x lens. For the GFP, the excitation is concentrated around the peak at 488 nm excited with a laser and the emission is concentrated around the 509 nm peak and above. Images were all 2048x2048 pixels and 228x228 μ m². Larger images were taken and merged together by the built-in feature of Leica software, LAS X. The microscope is equipped with a small incubator keeping the CO₂ concentration to 5% and heaters on the lens and petri dish holder set to provide a temperature close to 37°C on the petri dish.

High magnification under a microscope require a short distance between the lens and what we want to observe. Petri dishes are too thick for the 40x lens installed at the IPGG. This is the reason we use fluorodishes. However patterned cultures cannot be made in fluorodishes. It is possible to

[162]: Zhou et al. (2018), 'DeepNeuron'

[163]: Meijering et al. (2004), 'Design and validation of a tool for neurite tracing and analysis in fluorescence microscopy images'

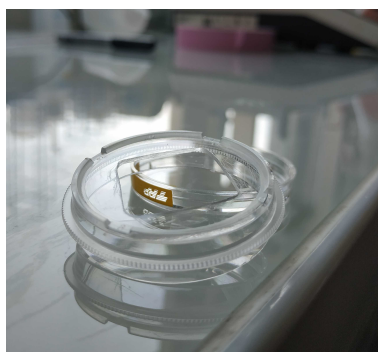


Figure 4.8: A drilled dish to support a glass coverslip.

use magnetic coverslip holders, but with those one needs to manipulate coverslips with living cells. Hence it is preferable, and much easier to make the coverslip holders by hand cutting through classical petri dishes (see figure 4.8) with a drilling machine. The coverslip is attached to the pierced dish after the photolithography with a thin layer of PDMS. This withstand the ultrasonic bath without any issue and the incubation of PLO can be realised with another glass coverslip on top of the droplet: the liquid is sandwiched between two coverslip.

There exist several software able to identify neuron morphology from confocal data. DeepNeuron [162] for instance uses deep learning to extract neuron morphology in multi dimensional images (up to 5D). NeuronJ [163] is an imageJ plugin that help reconstruct neuron morphology given the neurites' starting and ending point. This two examples seemed unefficient for what I wanted to do. On the one hand, DeepNeuron is highly fonctionnal but complex and on the other hand ImageJ needs a lot of inputs from the experimentalist. This motivated me to write a simple Python code able to extract neuron morphology from confocal data. I believe that since I was interested in neurons' firsts stages of development their spatial spread would not be too complex to solve. Retrospectively, it was probably not the best option and unconsciously motivated by the desire to learn image analysis in Python, perhaps more than a real need. However, the small software I developed does work well and shows that simple rules are able to extract neurons' morphology.

The first step are to identify the soma and neurite. This is simple since they have 2 different spatial scales. Somata ranges from 10 to 30 microns whereas neurites are smaller than a couple of microns in diameters. A simple convolution and thresholding of the binary fluorescent image will give the somata and neurite positions. One obtain two binary images where bright pixels belongs to the neuron's somata or neurite. Neurites are then reduced in size along their diameter in order to obtain a line of pixels with an efficient thinning algorithm [164]. Every pixel can be sorted out into 5 categories:

- ▶ The soma
- ▶ A neurite
- ▶ A branching point

[164]: Zhang et al. (1984) 'A fast parallel algorithm for thinning digital patterns'

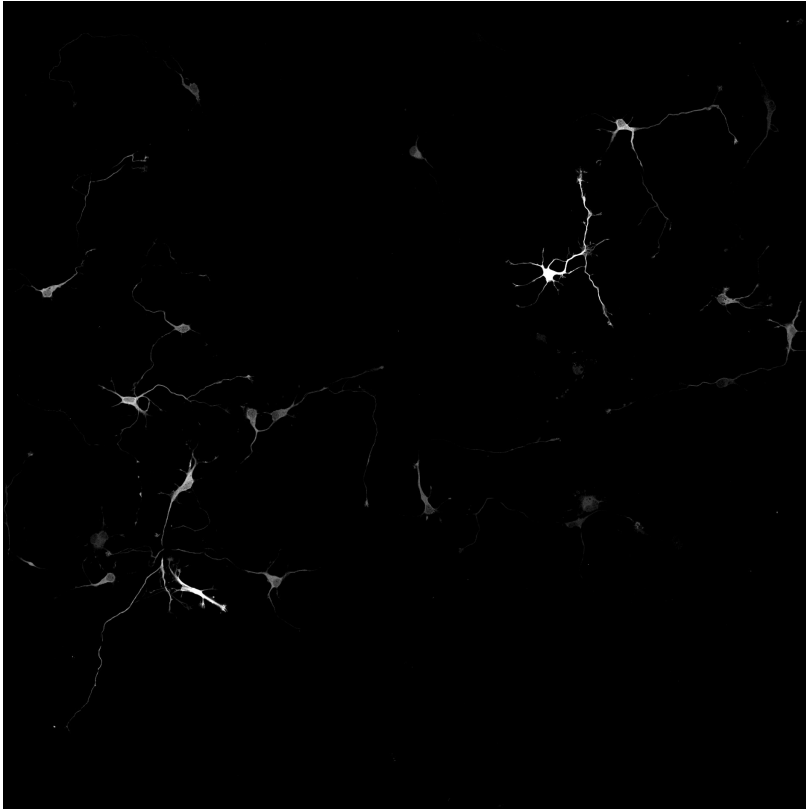


Figure 4.9: GFP fluorescent imaging from cortical cultures at DIV4. 5uL of virus was added and the image is 1.05x1.05 mm. One can estimate the cell density that express the GFP in this image close to 20 mm^{-2}

- ▶ A growth cone
- ▶ The background

The soma and background are identified in previous stages. Neurites, branching points and growth cones are identified according to their 8 closest pixels. A growth cone is the neurite end point, thus has only 1 bright neighbouring pixel. A neurite has 2 bright neighbouring pixels, and a branching point has at least 3. Figure 4.10 shows the extraction of neurons morphology with this method.

Note that with this definition a branching point is defined with several pixels. Figure 4.11 gives an example where the branching point is described by 3 pixels. For the following analysis, a single pixel is kept as a branching point. The others are set to the neurite category.

Then the neuron morphology is describe with a graph. Growth cones, branching points and the soma are the graph's nodes and neurites form the graph's edges. The edge direction corresponds to the direction of growth. Some direction are obvious: the growth starts from the soma, thus the node 'soma' has a null in-degree. Conversely the growth cone nodes have a in-degree of 1 and an out-degree of 0. When looking for the edge direction the most important rule is the following: if a

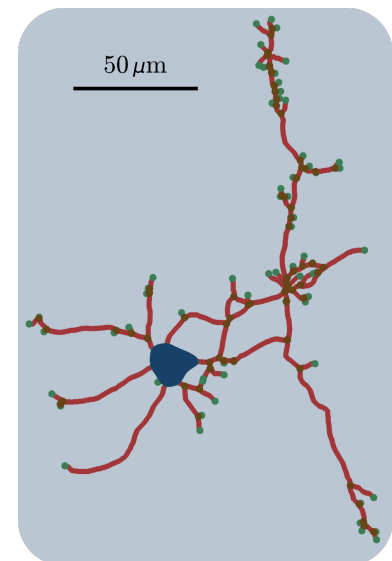


Figure 4.10: The different pixel categories are represented in this examples. The neuron come from the top right corner of figure 4.9. **Red** pixels are the neurites. **Blue** pixels are the soma. **Green** pixels are the branches tips, or growth cones. **Brown** pixels are the branching points.

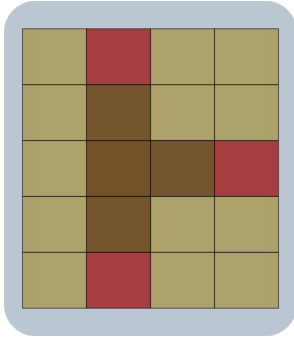


Figure 4.11: Background pixels are in gold, and bright pixels are in brown (branching point) or red (neurite). A branching point is described by more than one pixel. The three brown pixels belong to the branching point category because more than 2 of their neighbours are bright.

branching point, of total degree 3, has two outgoing links, necessarily the other one is in-coming. It is a form of conservation of mass.

These 3 simple rules are sufficient for many neurons. There is however a difficulty when crossing of neurites creates a loop in the tree structure of the graph. In order to solve this the first idea that comes to mind is to set a preferential direction according to the angle formed by each neurite in a branching point. Because of its rigidity, a neurite unlikely turn with an angle higher than $\sim 60^\circ$. The neurite average direction close to the branching point can be estimated with a linear regression of the pixelated skeleton (see figure 4.12 for the angle definition in a branching point). The unknown direction of growth can be chosen according to the smallest angle in the branching point. Surprisingly, this strategy is unefficient, and many mistakes were done. Because the skeleton is pixelated and a neurite is not a straight line the direction is badly approximated. With too few pixels the direction is highly dependent on the pixel size, and with too many the neurite starts to turn worsening the estimated direction quality. In order to overcome this difficulty, I set up another criteria taking into account the branches of two consecutive branching point.

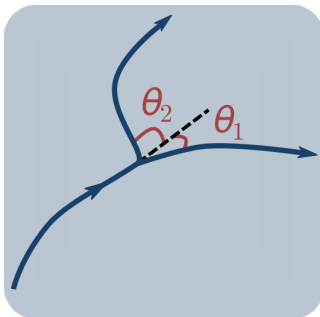


Figure 4.12: Definition of the angle in a branching point.

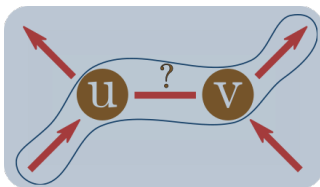


Figure 4.13: Schematic of the (u,v) branch. The encircled direction corresponds to the direction $u \rightarrow v$.

Let us suppose that we do not know the direction of the branch (u,v) , where u and v are two branching point of total degree 3 such that they both have one outgoing and one incoming edge. Then the direction $u \rightarrow v$ is associated with a neurite incoming in u and outgoing in v . This neurite is circled in blue in the schematic 4.13 and is associated with two angle in the branching point u and v . The sum can be compared with the equivalent one for $v \rightarrow u$ and find the best choice for the (u,v) edge direction. The best choice being the one with the smallest twist. This procedure can be done with degree higher than 3, for each edge one look for the best of all edges (the one with the smallest torsion). Figure 4.14 shows the edge direction in the same neuron from figure 4.10. Even with multiple crossing points the direction is the one a human eye would identify.

Definition of morphological structures

Let us set some definitions for the following analysis. When a single point is needed the soma position is approximated as the center of mass. Multiple neurites emerge

from the soma: one axon and several dendrites. The axon is identified as the longest neurite (computed with the curvilinear length, including branches). All other neurites are considered as dendrites. One neurite (axon, or dendrite) is considered as starting at the soma boundaries and end at all its growth cones or branch tips. One branch starts at a branching point along a neurite and ends up at a single growth cone. Thus, a neurite (axon or dendrite) is made of multiple branches, and I call the 'main' branch the longest one from the soma to a single growth cone.

Figure 4.15 shows one individual neuron at DIV6 in an homogeneous culture. This is an example of the image analysed through this process.

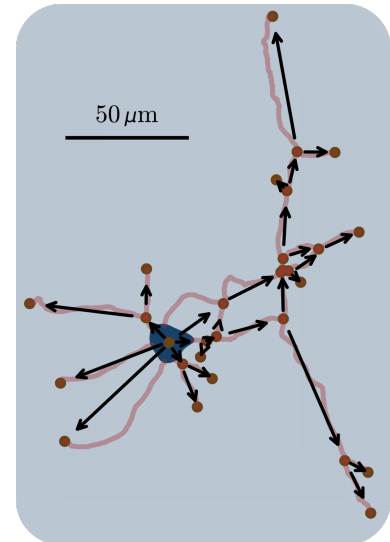
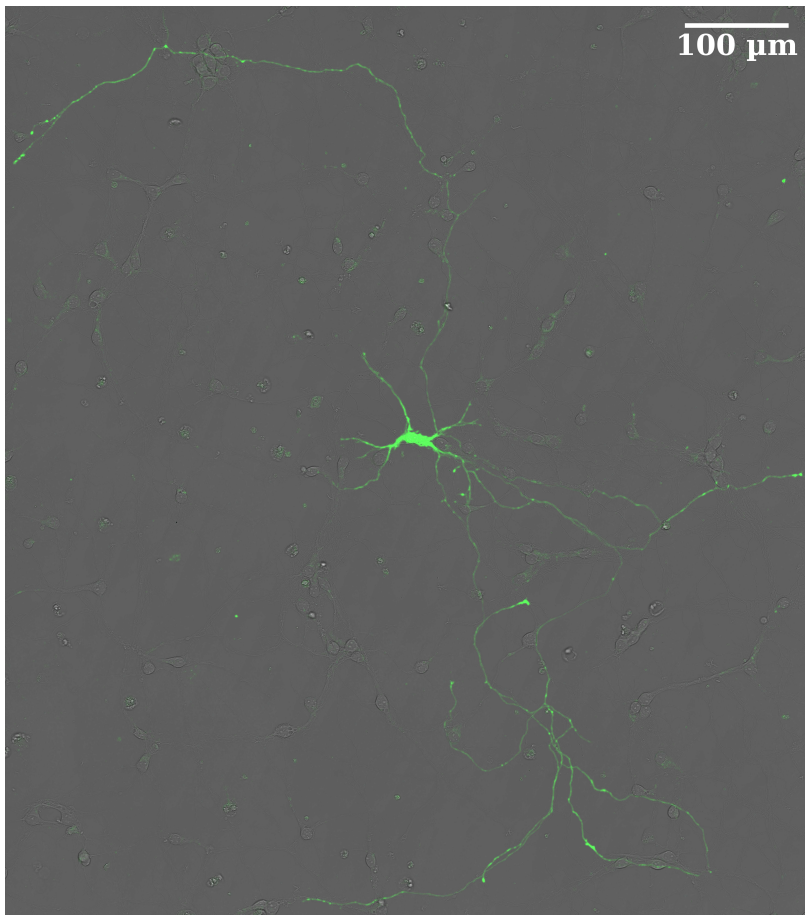


Figure 4.14: Neuron and morphological graph. Graph nodes are in brown: there are the soma, growth cone and branching points. The branches appears in light red.

Figure 4.15: Phase contrast image of a cortical culture of density 180 mm^{-2} , at DIV6 with a single neuron in green pseudocolour representing the GFP. The image is $780 \times 880 \text{ } \mu\text{m}^2$

Morphological quantities

In order to provide quantitative measurement for modeling of neuronal network, I am interested in the spatial spread of neurons. Does the growth cone stays in a relatively confined region close to the soma, or does it run far away in a straight

line? The tortuosity can quantify this behaviour: The tortuosity of a neurite following a path \mathcal{C} is the ratio of the total path length and the distance covered:

$$T = \frac{1}{\|\mathbf{r}_0 - \mathbf{r}_\infty\|} \int_{\mathcal{C}} \frac{\mathbf{s}}{\|\mathbf{s}\|} \cdot d\mathbf{s} \quad (4.5)$$

with \mathbf{r}_0 and \mathbf{r}_∞ the starting and ending point of the path \mathcal{C}

As described in the introduction (see page 89), the persistence length can accurately describe elongated streamlined systems like neurites. However, unlike polymer chains they are not susceptible to thermal fluctuations. Neurites persistence length may not be as easily related to the mechanical bending energy. For one thing they adhere to the substrate, and their shape may be influenced by and external signals (gradients of chemo-attractants/-repellants or mechanical stimuli) more than cytoskeleton rigidity³⁸. Also, this study propose to look at interacting neurons in culture which may impact the morphology more than the inner mechanical structure.

Nonetheless the 2D shape of neurites can be analysed with the same quantity l_p . Sometimes, [166, 167] the obtained quantity is called the path persistence length, as it is strictly speaking a geometrical observable of the path. The relationship between the path persistence length and the rigidity may not hold anymore, but the results will be of great value to improve interacting elongation models [168].

38: Note however, that laminin has been observed as a "permissive" substrate rather than an "instructive" one [165] regarding the elongation growth

[166]: Vikhorev et al. (2008), 'Bending Flexibility of Actin Filaments during Motor-Induced Sliding'

[167]: Duke et al. (1995), "'Gliding Assays" for Motor Proteins'

[168]: Kirkegaard et al. (2018), 'The role of tumbling frequency and persistence in optimal run-and-tumble chemotaxis'

[169]: Cifra (2004), 'Differences and limits in estimates of persistence length for semi-flexible macromolecules'

Calculation of the persistence length

Although other methods exists [169] I will compute the persistence length l_p as the correlation length of the unit tangent vector \vec{t}_s :

$$\langle \vec{t}_s \cdot \vec{t}_0 \rangle = \langle \cos(\theta_s - \theta_0) \rangle = \exp\left(-\frac{s}{l_p}\right) \quad (4.6)$$

with \vec{t}_s the tangent vector of the neurite path at a curvilinear position s .

In order to compute it with the experimental data I will look at every branches determined in the image analysis paragraph page 99. First I compute a B-spline approximation [170] of the branches so that the angles are not

[170]: Dierckx (1982), 'Algorithms for smoothing data with periodic and parametric splines'

constrained by the 2D pixelated grid. It is an efficient way to smooth the complex 2D neurite path. A linear fit of $\ln\langle\vec{t}_s \cdot \vec{t}_0\rangle$ versus the curvilinear distance s gives the persistence length.

4.3 Results

Morphological properties

Axon and dendrite length

In biological neuronal network, the typical connections length is govern by the axon and dendrite expansion. Figure 4.17 shows the total curvilinear length of axon and dendrites, branches included. First one must notice that the average value does not increase over time from DIV 5 to DIV 6 but stays relatively constant close to $750 \mu\text{m}$. On the one hand, there is probably an overestimation of small neurons at DIV 6 because of the increasing probability of overlapping in large neurons. On the other hand, the growth is highly multifactorial and variation of density, neuronal type and dissection may affect the total neurite length. Hence, the distribution may not be understood has a probability density: contrary to what the figure hints at DIV 6 small neurons are most probably not the majority.

However, this gives a typical length of $750 \mu\text{m}$ for axons and $250 \mu\text{m}$ for dendrites at DIV 5-6. These order of magnitude set the maximum distance possible for connections: neurons more than 1 mm apart from one another are very unlikely to create synaptic connections.

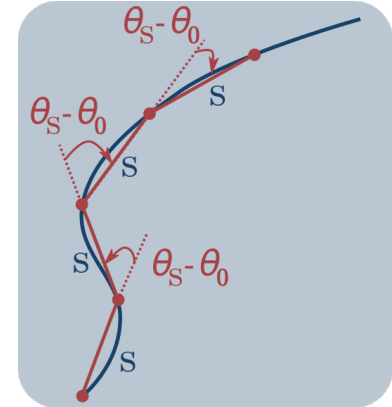
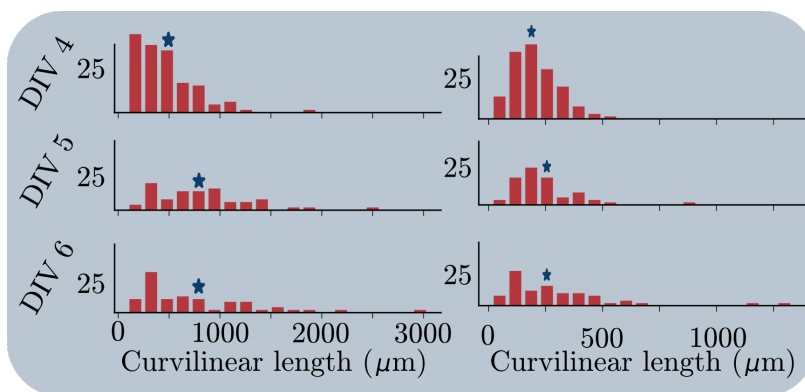


Figure 4.16: Schematic of the tangent angle $\theta(s)$ computed to estimate the persistence length. Red dots are separated by a curvilinear distance s along the neurite path here in blue.

Figure 4.17: Axon and dendrite total curvilinear length distribution. Branches are taken into account. The blue star is the mean.

39: A branch starts at a branching point, or the soma and ends at a growth cone

40: Tortuosity of a semi-circle

Branches tortuosity

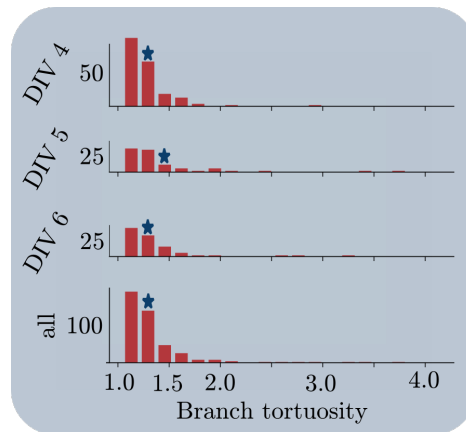
Since synapse formation depends on axon/dendrite contact, the probability distribution as function of the distance between two neurons has to be related to neurite tortuosity. With a high tortuosity, an axon cover a large surface increasing the possible contact with post-synaptic dendrites. Figure 4.18 shows the branches' tortuosity³⁹ distribution. It seems independent of the culture age and typical values are below⁴⁰ 1.6 with an average close to 4/3. Although some rare very high values are present, branches are best described with a relatively strong push forward and without many zigzags.

Hence, the typical branch size is 75% of its curvilinear length. The distance scale of the probability connection is then bounded above by 75% of the axon plus dendrite curvilinear length.

Figure 4.18: Branches tortuosity distribution defined in equation 4.5 as:

$$T = \frac{1}{\|\mathbf{r}_0 - \mathbf{r}_\infty\|} \int_{\mathcal{C}} \frac{\mathbf{s}}{\|\mathbf{s}\|} \cdot d\mathbf{s}$$

with \mathcal{C} being the branch path and \mathbf{r}_0 and \mathbf{r}_∞ the starting and ending point of the branch.



Branching

The ability to create multiple branches significantly increase the probability to create synapses. Bottom plot of figure 4.19 displays the number of branching points in axons and dendrites. There are on average 5-6 branching point in DIV6 axons, and 0.7 per dendrites.

Top plot of figure 4.19 shows the distribution of distances between two branching points. The typical value is close to 60 μm at all age for axons, and 20 μm in dendrites. In order to reproduce neurons morphology, the branching angle is displayed in figure 4.20. However, the branching angle is a local quantity and does not describe efficiently the spatial spread.⁴¹

41: At least up to DIV6

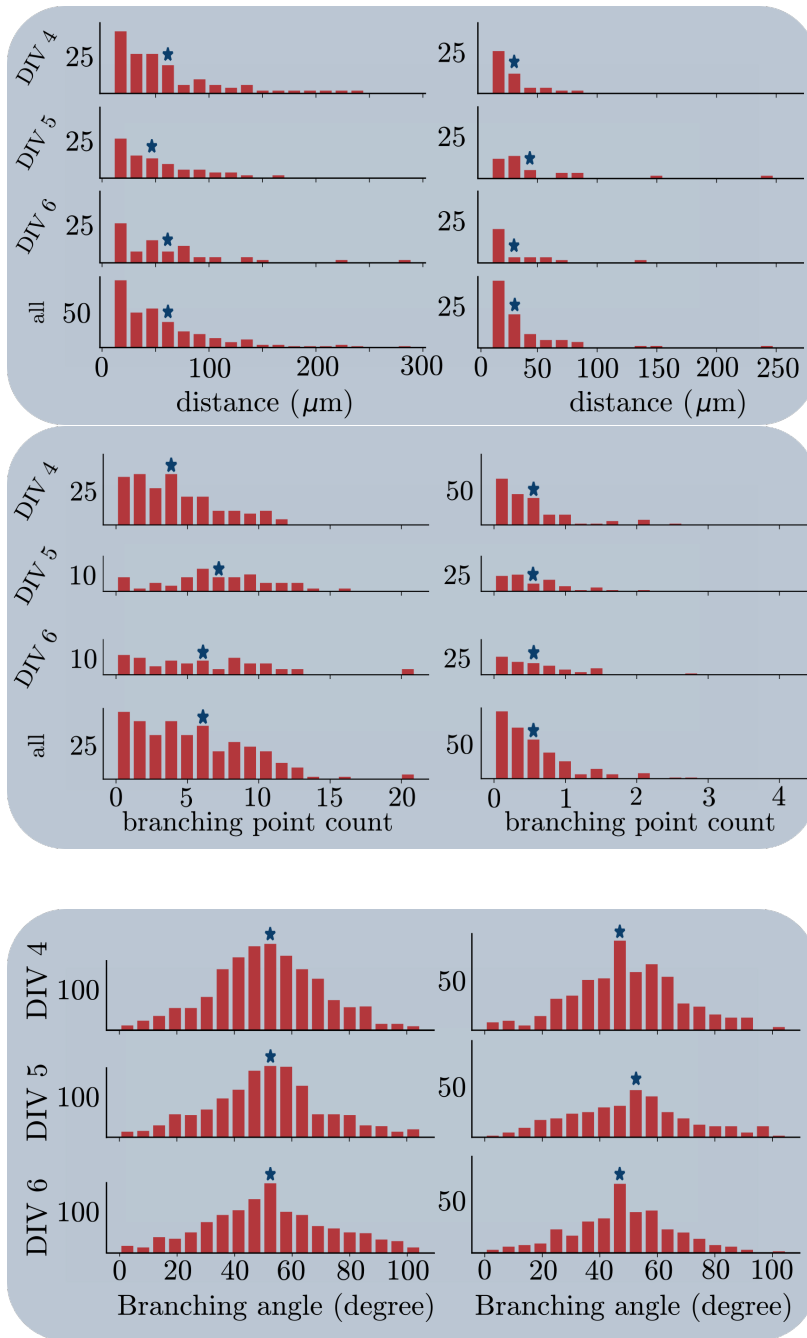


Figure 4.19: **Top** frame shows the distributions of curvilinear distance between two branching points. The blue star is the mean. **Bottom** frame shows the distributions of the number of branching point in the axon (**left**) and in dendrites (**right**).

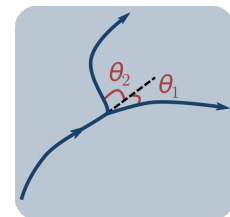


Figure 4.20: Distributions of the angle in at branching point in the axon (**left**) and dendrites (**right**). The blue star is the mean. The angle are computed according to the picture above showing two branching angle θ_1 and θ_2

Estimation of the network

In the elaboration of a theoretical model for networks of point-neuron⁴², the quantity one is looking for is the probability density of connection as function of the distance d between two neurons.

This quantity can be estimated with the probability that an axon has grown up to a certain distance from the pre-synaptic soma $P_{\text{growth}}(r_a)$ and the probability that a dendrite has grown up to a certain distance from the post-synaptic

42: Theoretical models that consider neurons as single points in the 2D space, like the ones we studied in the previous chapters

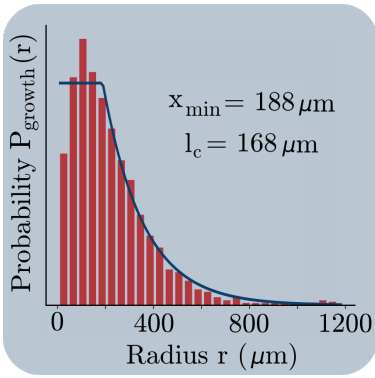


Figure 4.21: Presence probability of an axon branch at a distance r from the soma. The blue curve is a fit with function 4.7.

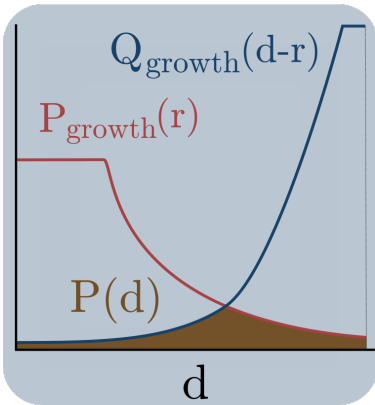


Figure 4.22: Schematic representation of the equation 4.8. $P_{\text{growth}}(r)$ and $Q_{\text{growth}}(d-r)$ are taken as function defined in equation 4.7, the connection probability $P(d)$ is directly related to the overlapping area. In this representation the pre-synaptic neuron is on the left side of the graph, and the post-synaptic neuron at the right side at a distance d .

soma $Q_{\text{growth}}(r_d)$. The probability that a synapse is created can be approximated as a uniform distribution over the contact length c and the interneuron distance can be written as $d \approx r_a + r_d - c$. As we have seen in the previous section, the axon length cannot be directly used here as the distance r_a . Because of the axon tortuosity, the probability P_{growth} becomes negligible below the average curvilinear length. Also, branching can increase the presence probability of an axon branch at a given distance r_a . Presence probability densities $P_{\text{growth}}(r_a)$ and $Q_{\text{growth}}(r_d)$ can be estimated from experimental data by counting the number of axon branch (respectively dendrites) at a given distance r_a (respectively r_d) from the soma. Figure 4.21 shows P_{growth} as function of the radius r from the soma at DIV6. One can expect that below a certain value r_{min} this probability plateau at a constant value because every neuron has at least one axon branch at this distance. r_{min} is the smallest radius whose circle encompass every axon recorded.

$$f(r) : r \mapsto p_o \left(1 + \Theta(r - r_{\text{min}}) \times \exp\left(-\frac{r}{l_c}\right) \right) \quad (4.7)$$

with l_c the exponential scale and p_o a normalization factor such that the integral over $[0, +\infty]$ is 1 and Θ the heaviside function.

Then, the probability of connection as function of the interneuron distance d can be computed as :

$$P(d) = q_o \int_0^d P_{\text{growth}}(r) \times Q_{\text{growth}}(d-r) \times R_o \, dr \quad (4.8)$$

with R_o the number of synapses per unit length of axo-dendritic crossing, $P_{\text{growth}}(r)$ the axon presence probability at a distance r from the pre-synaptic neuron and $Q_{\text{growth}}(d-r)$ the dendrite presence probability at a distance $d-r$ from the post-synaptic soma and q_o a normalization factor. This calculation is represented in figure 4.22.

The connection probability $P(d)$ is represented in figure 4.23, along with the correspondig mean connectivity length. shows that the mean connectivity length is increasing with the culture age. Values are in a good agreement with Barral et al. [79] who reported an average fonctionnal connection length of 400 μm in mature culture.

[79]: Barral et al. (2016), 'Synaptic scaling rule preserves excitatory-inhibitory balance and salient neuronal network dynamics'

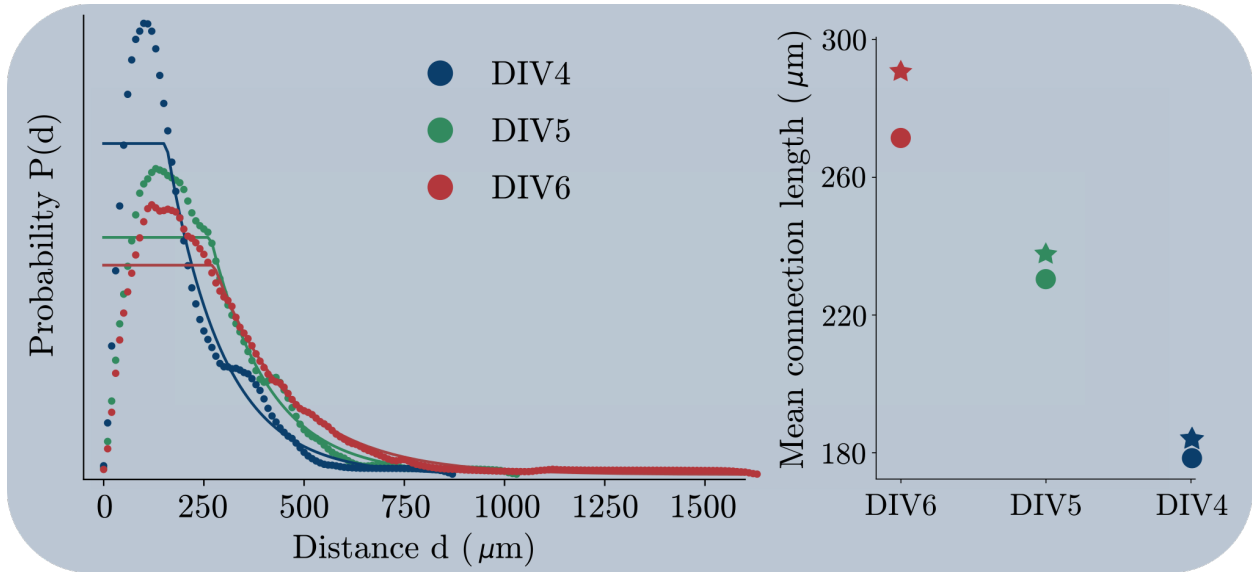


Figure 4.23: Left frame shows the connection probability as function of the inter neuron distance d . Experimental data is shown with the colored dots, and the lines shows the fit to a function described in eq. 4.7. Right frame shows the mean distance length computed with the experimental data (stars) and the fit (dots).

Growth properties

Growth ratio

In order to estimate neurons' preference in the axon or dendritic tree growth I defined the growth ratio as the ratio of the axon over the dendrites' curvilinear length:

$$G_r = \frac{L_{axon}}{L_{dendrites}} \quad (4.9)$$

Figure 4.24 displays the growth ratio distribution, and shows values similar at all ages with an average between 3 and 4. This is to relate with the total length in figure 4.17. The average axon length over the average dendrite lengths is also close to 3. Thus, on average slowly growing axons belong to neurons whose dendrites also grow slowly.

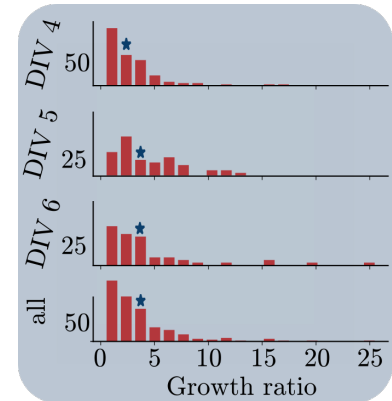


Figure 4.24: Growth ratio distribution. The blue star is the mean.

Growth cone speed

The main branch of the axon can be used to compute the growth cone speed as the ratio of the curvilinear length over the time duration. Since the growth is very slow the first 24 hours⁴³, I removed 24 hours from the days in vitro value. Right frame of figure 4.25 shows the distribution of growth cone speed. It appears homogeneous over the 3 DIV and close to $4 \mu\text{m}\cdot\text{h}^{-1}$. Reports [171, 172] in various systems and cell types have found the instantaneous growth cone speed

43: During the two first stage of development, only immature neurites develop and are 20 to 30 μm , which is 1 % of the axon total length

[171]: Ruchhoeft et al. (1997), 'Myosin functions in *Xenopus* retinal ganglion cell growth cone motility in vivo'

[172]: Tanaka et al. (1995), 'The role of microtubule dynamics in growth cone motility and axonal growth.'

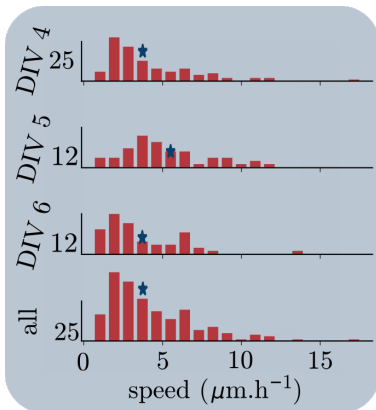


Figure 4.25: Growth cone speed distribution. The blue star is the mean.

to be close to $15 \mu\text{m}\cdot\text{h}^{-1}$. Firstly, growth cones dynamics is not a continuous process. Period of pausing and retraction can decrease significantly the long time averaged speed I compute here. Secondly, the growth cone motion may not entirely be reflected in the neurite path. Because of its inner mechanical structure and flexibility a neurite length may not be exactly equal to the distance covered by the growth cone. The persistence length can be of help to quantify this.

Persistence length

As explained in the previous section (see page 103), the persistence length is computed as the correlation length of the branches' direction: $\langle \mathbf{t}_s \cdot \mathbf{t}_o \rangle$. Experimental data shows that there are two regime:

- ▶ The **short range** (SR) regime: below $3 \mu\text{m}$, $\ln(\langle \mathbf{t}_s \cdot \mathbf{t}_o \rangle)$ follows a linear evolution as function of the curvilinear distance s with a persistence length close to $l_p^{\text{SR}} \approx 60 \mu\text{m}$. The average correlation coefficients is 0.97.
- ▶ The **long range** (LR) regime: above $10 \mu\text{m}$, $\ln(\langle \mathbf{t}_s \cdot \mathbf{t}_o \rangle)$ follows a linear evolution as function of the curvilinear distance s with a persistence length close to $l_p^{\text{LR}} \approx 500 \mu\text{m}$. The average correlation coefficients is 0.90.

Figure 4.26 shows the persistence lengths computed with neurons from all dishes, and gathered at single Days In Vitro. There is no obvious variation from DIV 4 to DIV 6 and one may assume that the true value is indeed independant on the culture age. Gathering every neuron at all days in vitro one find $l_p^{\text{LR}} = 487 \pm 38 \mu\text{m}$, and $l_p^{\text{SR}} = 59 \pm 6 \mu\text{m}$.

In order to better understand the double persistence length regime, let us look at some recorded images. Figure 4.28 shows an axon and its growth cone. One can observe that the axon follow a very sharp angle on a scale smaller than $10 \mu\text{m}$. Because of fluctuation in the surrounding adhesion caused by the laminin coating *and* close by neurons or axons, any neurite path can be steeply bend over angle that the cytoskeleton stiffness would not allow in a free environment. The cytoskeleton stiffness is most probably not impacted by the environment, but the interacting forces applied to the neurite are. Sharp bending of neurite because of its surroudings can also be found in figures 4.29. These extrem bending are responsible for the short range regime and the small persistence length. Figure 4.30 shows the middle part of an axon

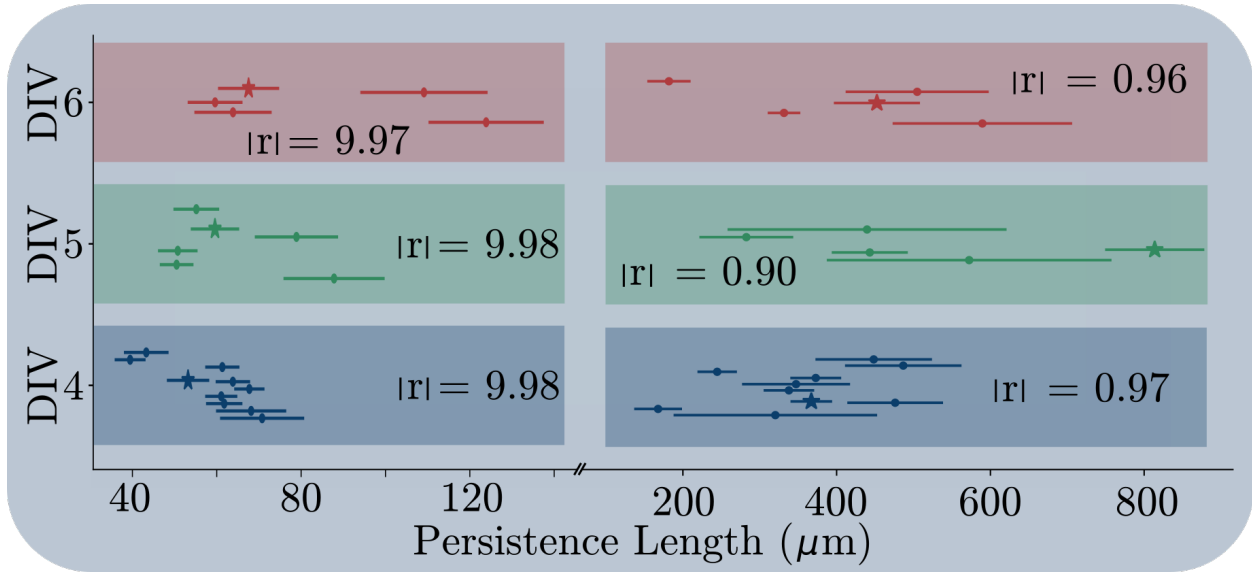


Figure 4.26: Persistence length computed with equation 4.6 for several days in vitro. Each point is calculated with every neuron in a single culture, and the star regroup every culture. The errorbars are computed with 3 times the standard deviation of the slope in the linear regression (under the assumption of residual normality).

at DIV6. One can see small fluctuations of the direction that seem to correlate with the surrounding biological material. However, there is no angle as sharp as the ones seen above. Indeed, as the neurite gets older, its stiffness increases. Also, the growth cone pull straighten the neurite. It results in an increased persistence length.

Figure 4.27 shows the correlation of the neurite orientation path as function of the curvilinear distance, agregating all the acquired data. The two regimes are clearly visible, and suggest that the path correlation can be written as:

$$\langle \vec{t}_s \cdot \vec{t}_0 \rangle \propto \exp\left(-\frac{s}{l_p^{LR}}\right) + \exp\left(-\frac{s}{l_p^{SR}}\right) \quad (4.10)$$

Perhaps a simplistic explanation is to relate the *short* range regime to the growth cone exploration with a very short memory scale and the *long* range to neurite stiffness. The cytoskeleton stability in high curvature regions can be assured by actin, much more flexible than microtubules.

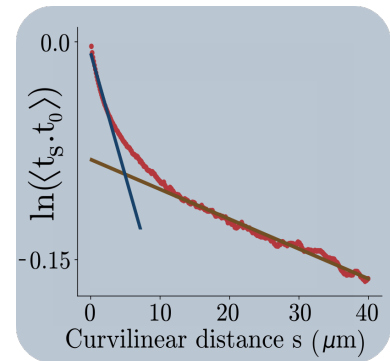


Figure 4.27: Correlation of neurite orientation path as function of the curvilinear distance, with the two *short* range and *long* range linear regression. in (resp.) blue and brown.

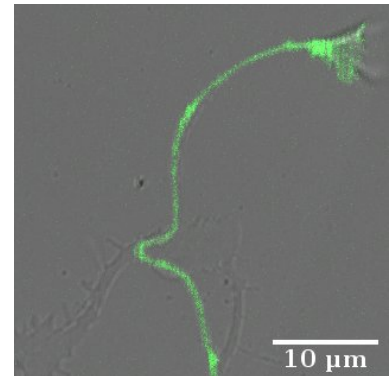


Figure 4.28: Image of an axon at DIV6 expressing the GFP with the surrounding in phase contrast.

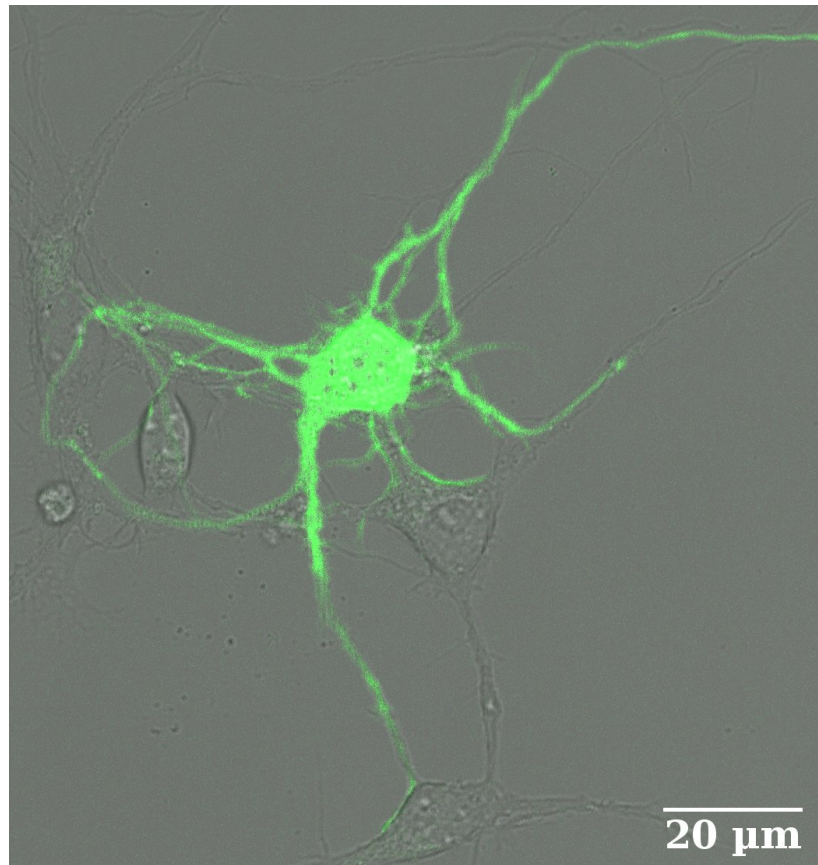


Figure 4.29: Image of a cortical neuron at DIV5 expressing the GFP with the surrounding in phase contrast.

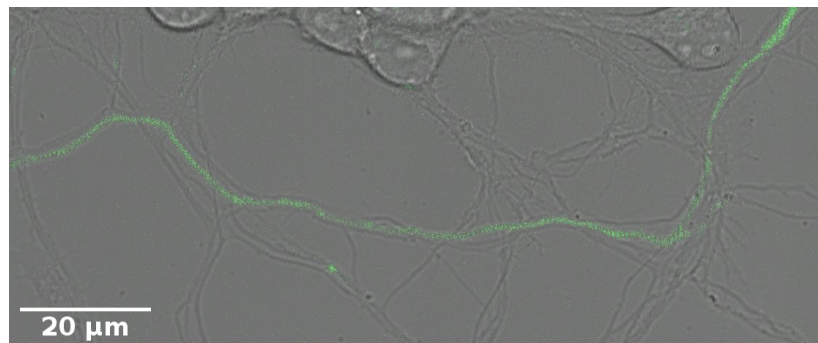


Figure 4.30: Image of an axon and its growth cone at DIV5 expressing the GFP with the surrounding in phase contrast.

**CONCLUDING REMARKS AND
PERSPECTIVES**

Understanding neuronal networks

Two regimes in the persistence length In my experimental study I have characterized cortical neurons' in two-dimensionnal cultures and there are two main properties that I want to highlight. Firstly, the analysis of neurites' paths, through the persistence length, has revealed two regimes that one may associate with two different mechanisms. This result can be directly used to improve theoretical models of neuronal growth with interacting neurons. The persistence length in the short range regime may come from the erratic motion of growth cone. The neurite stabilisation is made possible thanks to many interaction with neighboring biological materials (other neurons, or neurites, or glial cells). Without interaction the neurite path is probably much more constrained by its rigidity: just like a sewing thread being pull from its tip. The persistence length in the long range is much closer to values predicted for microtubules.

Connectivity length Secondly, I built a toy model for neuronal connection based on the probability for a pre-synaptic neuron to overlap a post-synaptic dendrite. The statistical analysis of a neurite presence probability as function of the distance from the soma has allowed us to take neurite stochastic morphological features (mainly branching and tortuosity) into account. The complex path between a pre-synaptic neuron, the synapse and the post synaptic neuron is approximated with a simple Euclidiene distance. Then, I was able to conclude on the *Euclidian* mean connectivity length. The specific values computed here must be treated with caution: the experimental data come from immature neurons and the final stages of development may influence strongly the result. Nonetheless, if these data are to be believed and the typical connection length is indeed considerably smaller than the axon length, it may reinforce the perception that neuronal networks are badly approximated by space-free networks.

Non regular dynamics of the QPM In exploring the Quorum Percolation Model in networks embedded in the two-dimensionnal space we have seen that the threshold rule of activation is sufficient to create a propagating front, from a random uniform excitation provided that the connection scale is small enough. We have highlighted evidences of a transition from a localized nucleation, invariant by rotation to a fractured propagation constrained by the network locality and the initial excitation. This complex dynamics of propagation seems related to the network ability to stop the activity. In both of these regimes, the model is unable to create a repetitive pattern of activation. Nucleation points and avalanches are not repeatedly happening in the same region of the culture.

A scale free dynamics ? The transition of spatio-temporal dynamics as the quorum threshold m is increased leads us to conjecture that spatial correlations can break down the discontinuous percolation transition and decreases the critical point m_c above which the transition is continuous. This is associated with a decrease of the initial excitation $f^*(m_c)$ needed to activate a large proportion of the network at this critical point m_c . A small excitation allowed us to properly identify avalanches of correlated activation and conjecture that a scale free dynamics may take place at the phase point of the spatial dynamics transition $(f^*, m_1(\lambda))$.

Orlandi et al. [49] and other teams have forwarded evidences of a strong regularity in the bursting dynamics of neuronal cultures. They proposed the concept of noise focusing: a dynamical amplification of noise towards specific regions of the culture able to initiate a system scale event. Here, we have shown that a simple threshold rule is not enough to produce a steady directed amplification: the Quorum Percolation Model in homogeneous networks embedded in space is not enough to produce a directed amplification of noise. Hence, regularity of nucleation points in the Noise Focusing Model necessarily comes from a dynamic absent in the Quorum Percolation Model.

High regularity of pacemakers The periodic steady state of neuronal cultures' activity can also be investigated in the framework of synchronization. Unsurprisingly, we have shown that synchronization of pacemaker neurons is able to reproduce high regularity in the spatio-temporal dynamics. The synchronization is govern by the network-neuron dynamics interaction: the nucleation process is characterized by a time scale dependent on neurons' inner dynamics, and the presence of leader neurons by the network locality. However, the synchronization process of relaxation oscillators lead the bursting steady state to a single nucleation point of activity. A complex map of nucleation point distribution like the one observed *in vitro* is not present in uniform networks of pacemakers. Also, the only pattern of propagation I have observed in this system are invariant by rotation and not constrained by the network structure. Uniform network of excitatory pacemakers is unable to stop the propagation in a given direction. One may ask if inhibition is able change the spatio-temporal pattern of burst initiation ?

An intriguing paradox Recordings of neuronal cultures activity are hard to reproduce because they display seemingly contradictory behaviour.

- ▶ **REGULARITY:** Neuronal bursts of activity are nucleated in a specific region of the culture, and with certain frequency of occurrence.
- ▶ **VARIABILITY:** There is a non trivial distribution of nucleation points in the 2D space and a most probably a variability in propagating front.
- ▶ **SYSTEM SCALE DYNAMICS:** Neuronal bursts are system scale events: the whole population is activated in a small time scale.
- ▶ **MULTI-SCALE DYNAMICS:** Along with the system scale bursts, there exists multiple scale of correlated activity (maybe distributed according to a power law)

What neuronal mechanism is fundamental to observe such complex activity ? The Quorum Percolation Model in networks embedded in space shows that a threshold rule of activation can reproduce the 3 last criteria but at different phase point. Synchronization of spatially embedded networks of pacemaker neurons is able to reproduce regular system scale events. Can the 4 criteria be met with these two ingredients ? Many teams study the self-organization of neuronal culture, and see in the scale free behaviour at a critical point a way to gather the 2 last criteria. Are self-organized critical systems able to reproduce the observed REGULARITY and VARIABILITY of neuronal bursting regime ?

Insights from experimental work Being able to work on real cultures has made me question the relevancy of trying to reproduce experimental data from different laboratories. I had the front row seat to see the difficulties for having homogeneous densities in culture of less than 1 mm². Even though I could not make any activity recordings, I had the opportunity (with recordings of Marx Montalà a student in Jordi Soriano's Team in Barcelona) to see that clusters of high density can lead a whole neuronal population activity for days. I have observed myself the morphological and growth speed differences between hippocampus and cortical cells, between different adhesive molecules, or environments (microfluidic chips, or open-air). I believe it makes sense to extrapolate those differences to neuronal activity, and thus question the motivation of theoretical works like my very own research. The *fundamental mechanism* I looked for may not be as fundamental or universal as one may want to believe. Being able to properly characterize and control hands on neuronal network make perfect sense in order to relate specific neuronal mechanisms to larger scale dynamics.

What I call an *intriguing paradox* may come from inner statistical variability of neuronal cultures: a cluster that act as a nucleation point increases the REGULARITY, whereas very homogeneous cultures may increase the VARIABILITY in spatio-temporal patterns of activity. A large proportion of pacemaker (for example in the hippocampus) may force the system towards forced oscillations and a SYSTEM SCALE DYNAMICS, whereas a higher proportion of irregularly firing neurons may drive the system towards a MULTI-SCALE DYNAMICS. Neurons' morphologies, and the network connectome bring there own complexity too: does a higher density culture increases or decreases the connectivity scale ? the axon tortuosity ? A population of neurons grown in small patterned tend to develop a large bundle of axon at the culture periphery. This bundle, absent in large cultures, undoubtedly impact the connectivity profile, and the observed activity. These characteristics are difficult, if not impossible, to implement in theoretical modelling, since we do not yet have a viable model of neuronal network activity. Thus, experimentally controlling these properties that we can only with difficulty model theoretically is probably the best way to establish a global understanding of neuron populations activity in culture.

APPENDIX

A

Neuronal culture confinement

In this appendix I describe multiple attempts to confine neuronal culture in the two-dimensional space. The goal is to obtain homogeneous cultures in the order of 1 mm^2 of various and controlled shape. As described in the main body, it can be achieved with photolithography techniques and coating of adhesive proteins in open-air culture.

The main issue with this technique is the large volume of medium required in open-air culture: 2-3 mL of medium drastically diminish the effective concentration of neurotrophic factors produced by glial cells and/or neurons themselves [173, 174]. Neurotrophic factors are families of small proteins that support the growth and survival of developing and mature neurons. Hence reducing the volume of medium can increase the survival rate and improve the growth.

The use of microfluidics chips can reduce the volume nanoliters and efficiently support the growth of neuronal population. Microfluidics devices have been extensively used in the recent years [175], not only because of the increase survival rate but because they are highly controllable, reproducible and flexible environments at the single cell precision or lower. I will present here 3 attempts to create affordable and easy to produce macrofluidics⁴⁵ suitable for confinement of neuronal population.

Business as usual The most simple approach is to use the very same patterned dishes I described in the main body and attach a millimeter scale roof on top of them. The roof can be made of two layers of biocompatible material like polydimethylsiloxane, PDMS. One layer form the main chamber: it is the exterior walls of the neuron's house we are building and has to be thicker than a neuron's height. The second layer

[173]: Walicke et al. (1986), 'Fibroblast growth factor promotes survival of dissociated hippocampal neurons and enhances neurite extension.'

[174]: Catapano et al. (2001), 'Specific Neurotrophic Factors Support the Survival of Cortical Projection Neurons at Distinct Stages of Development'

45: I call them macrofluidics, because they are much larger than typical chips. They are $\sim 100 \mu\text{L}$ in volume.

[175]: Millet et al. (2012) 'New perspectives on neuronal development via microfluidic environments'

is a flat roof with two opening: the inlet and outlet that allows to had or remove medium from the main chamber. Figure A.1 shows the two layers design that form the PDMS chip.

The fabrication is very simple. First, 30 mL of PDMS is first made with a 1:10 prepolymer to curing agent ratio, and air bubbles are removed in a vacuum chamber. The PDMS is poured in a 500 cm² culture dish or equivalent flat support. The PDMS has to cover the whole dish. It can easily be done by hand, making sure that no bubbles are created. Pouring 25 mL of PDMS results in an average layer of 500 μm. When pouring less than 25 mL the PDMS does not cover the whole dish, and the resulting thickness is actually often higher than 500 μm.

The PDMS can be stored in a 70° oven overnight or 2-3 hours. I suggest to let it rest overnight because of the cutting step: it seems to be more precise when the PDMS is harder. Although, precision is not a problem now. The chamber dimension being much larger than any relevant biological ones.

The PDMS layer is easily removed from the 500 cm² dish, which can be then re-use as many times as needed. The PDMS layer is then carefully deposited onto a plastic membrane with soft glue on it. The membrane hold PDMS layer when cutting it. An automatic mechanical cutter is then used to cut the PDMS layer into the 23x23 mm² square shape to fit the used cover-slips, along with the chamber and openings. In one 500 cm² PDMS layer I could fit around 20 chips (20 chambers, and 20 top). The individual layers are carefully removed from the plastic membrane⁴⁶ and washed several times in ethanol. Then, they are soaked 48 hours in water to remove ethanol.

The two layers are glued together with 30s O₂ plasma, making sure the top opening match with the chamber. This chip can then be fixed on the patterned cover-slip. There are two possibilities, first one is to use the 30s of O₂ plasma on both the PDMS chip and the cover-slip with photoresist still on. Then bond the two together and rapidly add the adhesive protein in the chamber to be coated on the cover-slip while the plasma is still active. Second one is to coat the adhesive protein on the coverslip, remove the photoresist, and dry the cover-slip before bonding with the chip. This prevents the use of plasma on the cover-slip and decreases the bond strength: the chip can peel off when adding medium, or washing the chamber doing this. However, with the first methods, the

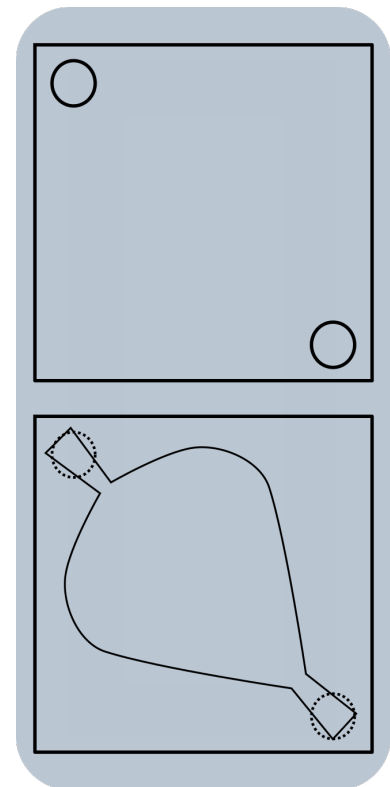


Figure A.1: Design of the macrofluidic chips. The top is only made of two circular openings, and the bottom is made of one large chamber with funnels that match the top openings. The dimension are th one of the cover-slips: 24x24 mm².
46: they tend to break down easily if not carefully handled. I found it usefull to peel them off from underneath with a pair of thin pliers.

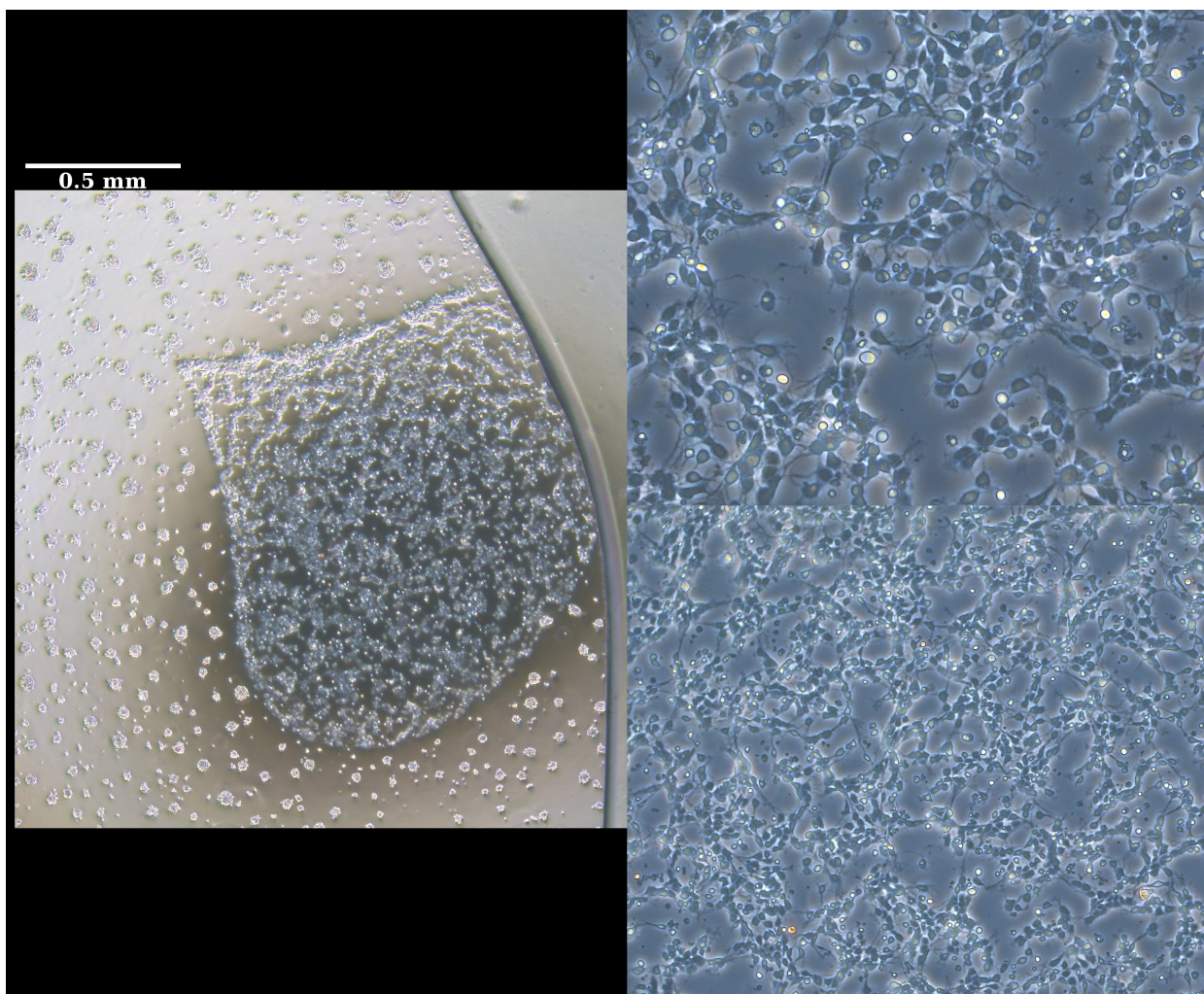


Figure A.2: Patterned culture of cortical neurons in a macrofluidic chip at DIV3. The droplet pattern is cut by the PDMS chamber. Small clusters of neurons form in the bulk outside of the pattern because there is no adhesive molecule.

photoresist is still on and the lift off need to be done afterwards.

Figure A.2 shows an example of a pattern substrate with macrofluidics chips on top. One can see the droplet pattern cut off by the PDMS chip.

Inverted patterns We understand that the problem come from the bond of the PDMS chip and patterned cover-slip coated with a vulnerable adhesive protein. With the inverted patterns technique, the photoresist is used to protect the adhesiv protein.

47: In a distilled water solution, to prevent crystallization when drying the cover-slip.

First the adhesive protein⁴⁷ is incubated in order to coat the whole cover-slip's surface. Photolithography is then used to create patterns of photoresist on top of the proteins in order

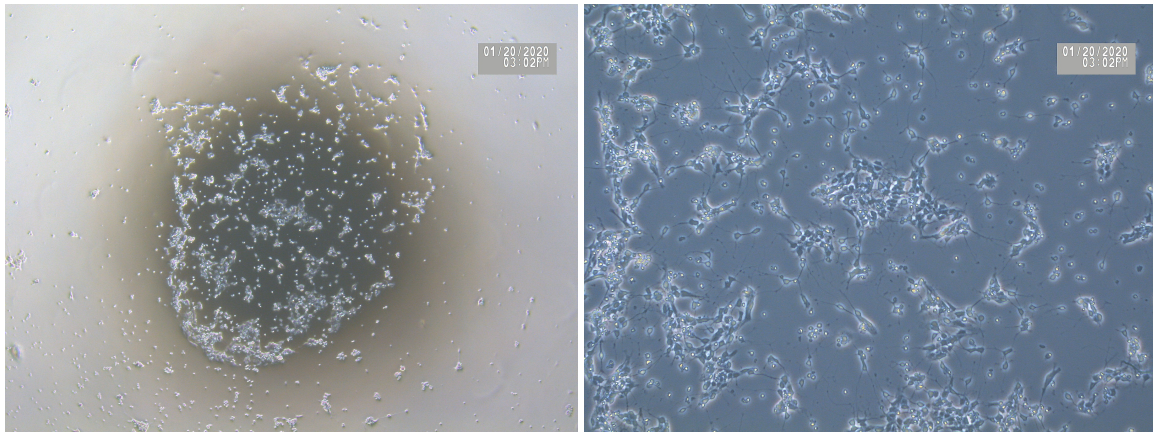


Figure A.3: DIV 3 culture of cortical neurons with inverse patterns.

to protect them. Silane can be added at this step in order to decrease cell adhesion outside of the desired patterns, and the chip can be bond with O₂ plasma on both the cover-slip with protected adhesive protein and the PDMS chip. This techniques has worked in a couple dishes, but only when the cell density was higher than what I was aiming for. Also, cells tend to cluster more intensely than in equivalent classic patterns.

Figure A.3 shows one pattern with this technique.

PDMS pattern I also tried to create pattern by cutting PDMS layers, which could be easily integrated into a chip. The difficulty here is to obtain patterns with a sufficiently good precision. Figure A.4 shows that the cutter tear the PDMS on the top surface, but the cut is much smoother on the bottom one. The PDMS thickness and stiffness are the two important parameter to avoid irregular and unwanted tear of the PDMS layer. Thickness of 500 μm seems to be in the good range, but thinner is good too. I believe that the PDMS should be sufficiently rigid, but I do not have enough hindsight to give more details.

Once cutted PDMS layers can be assembled with the roof chip and cover-slip with 30s of O₂ plasma bonding.

Manipulation of the chip Like every microfluidic systems, manipulating such confined environment can require some experience. First, you might notice from the sketch figure A.1 that the path from the roof opening to the chamber are narrower close to the chamber. I do not know where this

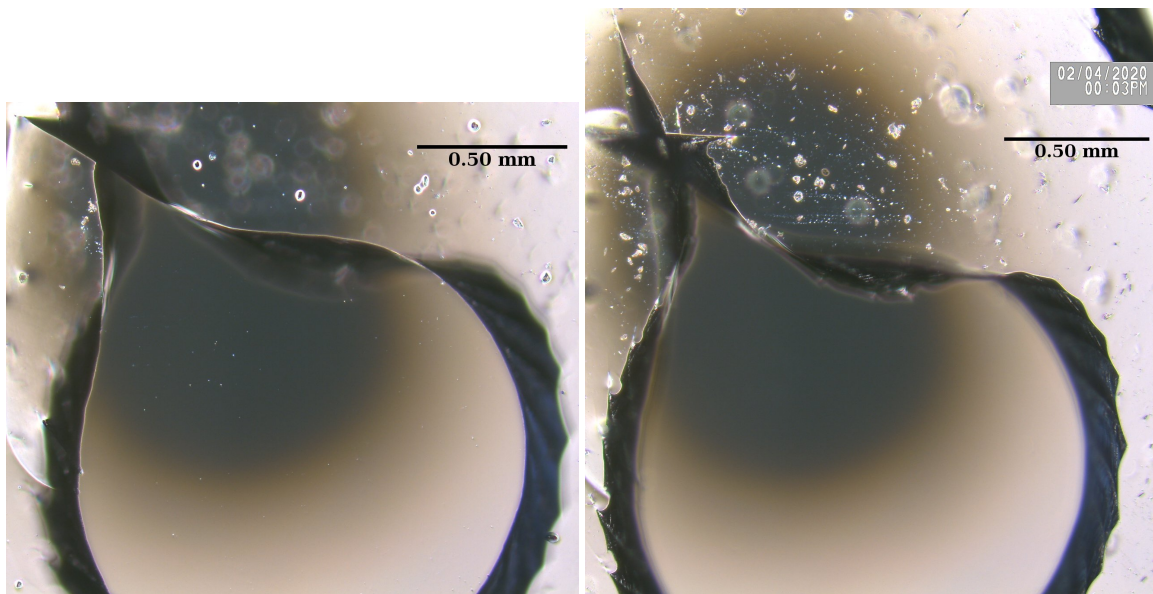


Figure A.4: Pattern made with $\sim 500 \mu\text{m}$ thick layer of PDMS. The left picture shows the bottom surface, with a smooth pattern edge. The right picture shows the top surface of the same pattern. There are many tears from the mechanical cutter.

48: I have not designed this chip

feature come from⁴⁸, but it is extremely useful. I have tried using larger funnel and adding any liquid in the chamber is a nightmare. With the narrow funnel one can fill it with the pipette tip and prevent the liquid from coming backwards.

When added any liquid in the chamber I found it useful to control the liquid by touching the PDMS roof with a pair of pliers, and decreasing locally the chamber height. This helps guiding the liquid towards the chamber boundaries symmetrically and prevent air bubbles to stay in the chamber. This is not an easy task, since you have to inject liquid with one hand and control the liquid with the other. Be careful not tear the PDMS roof. You can easily train with water, but note that changing the liquid and chamber coating will highly change the liquid behaviour in the chamber. For example, culture medium with cells is much more viscous, and do not flow as easily as ethanol in the chamber.

Finally, evaporation is something to keep in mind and adding medium almost every day is important to prevent air to enter the chamber. Maybe the chip design can be modified to add a little of medium. However, in order for my technique to work the top layer need to be flexible. If too thick, and not flexible enough adding liquid in the chamber may come as another challenge.

Bibliography

Here are the references in citation order.

- [1] W. A. Bentley. *Snowflakes in Photographs*. Google-Books-ID: 4O25SZtrMfkC. Courier Corporation, Sept. 6, 2012. 80 pp. (cited on page 2).
- [2] Andrew Adamatzky, ed. *Game of Life Cellular Automata*. London: Springer London, 2010. DOI: [10.1007/978-1-84996-217-9](https://doi.org/10.1007/978-1-84996-217-9). (Visited on 03/23/2021) (cited on page 3).
- [3] P. Rendell. 'A Universal Turing Machine in Conway's Game of Life'. In: *2011 International Conference on High Performance Computing Simulation*. 2011 International Conference on High Performance Computing Simulation. July 2011, pp. 764–772. DOI: [10.1109/HPCSim.2011.5999906](https://doi.org/10.1109/HPCSim.2011.5999906) (cited on page 3).
- [4] M Meister et al. 'Synchronous bursts of action potentials in ganglion cells of the developing mammalian retina'. In: *Science* 252.5008 (May 17, 1991), pp. 939–943. DOI: [10.1126/science.2035024](https://doi.org/10.1126/science.2035024). (Visited on 08/28/2019) (cited on page 3).
- [5] Daniel A. Butts et al. 'Retinal Waves Are Governed by Collective Network Properties'. In: *The Journal of Neuroscience* 19.9 (May 1, 1999), pp. 3580–3593. DOI: [10.1523/JNEUROSCI.19-09-03580.1999](https://doi.org/10.1523/JNEUROSCI.19-09-03580.1999). (Visited on 02/05/2019) (cited on pages 3, 51).
- [6] Matthew Cook. 'Universality in Elementary Cellular Automata'. In: *Complex Systems* (2004), p. 40 (cited on page 3).
- [7] Michael S. Gazzaniga. 'Neuroscience and the correct level of explanation for understanding mind'. In: *Trends in cognitive sciences* 14.7 (July 1, 2010), pp. 297–292. DOI: [10.1016/j.tics.2010.04.005](https://doi.org/10.1016/j.tics.2010.04.005). (Visited on 05/11/2021) (cited on page 4).
- [8] P.W. Anderson. 'More Is Different'. In: 177 (1972), p. 5 (cited on page 4).
- [9] Lluís Hernández-Navarro et al. 'Dominance of Metric Correlations in Two-Dimensional Neuronal Cultures Described through a Random Field Ising Model'. In: *Physical Review Letters* 118.20 (May 18, 2017). DOI: [10.1103/PhysRevLett.118.208101](https://doi.org/10.1103/PhysRevLett.118.208101). (Visited on 02/26/2019) (cited on pages 5, 54, 75).
- [10] Elad Schneidman et al. 'Weak pairwise correlations imply strongly correlated network states in a neural population'. In: *Nature* 440.7087 (Apr. 2006). Number: 7087 Publisher: Nature Publishing Group, pp. 1007–1012. DOI: [10.1038/nature04701](https://doi.org/10.1038/nature04701). (Visited on 03/24/2021) (cited on page 5).
- [11] Gasper Tkacik et al. 'Ising models for networks of real neurons'. In: *arXiv:q-bio/0611072* (Nov. 22, 2006). (Visited on 03/24/2021) (cited on page 5).
- [12] Danielle S. Bassett and Michael S. Gazzaniga. 'Understanding complexity in the human brain'. In: *Trends in Cognitive Sciences* 15.5 (May 2011), pp. 200–209. DOI: [10.1016/j.tics.2011.03.006](https://doi.org/10.1016/j.tics.2011.03.006). (Visited on 03/24/2021) (cited on pages 5, 6).
- [13] Patric Hagmann et al. 'Mapping the Structural Core of Human Cerebral Cortex'. In: *PLOS Biology* 6.7 (July 1, 2008). Publisher: Public Library of Science, e159. DOI: [10.1371/journal.pbio.0060159](https://doi.org/10.1371/journal.pbio.0060159). (Visited on 03/24/2021) (cited on page 5).

- [14] Emilio Salinas and Terrence J. Sejnowski. 'Correlated neuronal activity and the flow of neural information'. In: *Nature reviews. Neuroscience* 2.8 (Aug. 2001), pp. 539–550. DOI: [10.1038/35086012](https://doi.org/10.1038/35086012). (Visited on 09/04/2019) (cited on pages 5, 51).
- [15] L. F. Abbott and Wade G. Regehr. 'Synaptic computation'. In: *Nature* 431.7010 (Oct. 2004). Number: 7010 Publisher: Nature Publishing Group, pp. 796–803. DOI: [10.1038/nature03010](https://doi.org/10.1038/nature03010). (Visited on 03/24/2021) (cited on page 5).
- [16] Jessica S. Damoiseaux and Michael D. Greicius. 'Greater than the sum of its parts: a review of studies combining structural connectivity and resting-state functional connectivity'. In: *Brain Structure and Function* 213.6 (Oct. 1, 2009), pp. 525–533. DOI: [10.1007/s00429-009-0208-6](https://doi.org/10.1007/s00429-009-0208-6). (Visited on 03/24/2021) (cited on page 5).
- [17] Marcus E. Raichle and Abraham Z. Snyder. 'A default mode of brain function: A brief history of an evolving idea'. In: *NeuroImage* 37.4 (Oct. 2007), pp. 1083–1090. DOI: [10.1016/j.neuroimage.2007.02.041](https://doi.org/10.1016/j.neuroimage.2007.02.041). (Visited on 03/24/2021) (cited on page 5).
- [18] S. Herculano-Houzel. 'The remarkable, yet not extraordinary, human brain as a scaled-up primate brain and its associated cost'. In: *Proceedings of the National Academy of Sciences* 109 (Supplement_1 June 26, 2012), pp. 10661–10668. DOI: [10.1073/pnas.1201895109](https://doi.org/10.1073/pnas.1201895109). (Visited on 03/25/2021) (cited on page 6).
- [19] Rose G. Harrison et al. 'Observations of the living developing nerve fiber'. In: *The Anatomical Record* 1.5 (June 1, 1907), pp. 116–128. DOI: [10.1002/ar.1090010503](https://doi.org/10.1002/ar.1090010503). (Visited on 03/22/2021) (cited on page 7).
- [20] Jerome Pine. 'Recording action potentials from cultured neurons with extracellular microcircuit electrodes'. In: *Journal of Neuroscience Methods* 2.1 (Feb. 1, 1980), pp. 19–31. DOI: [10.1016/0165-0270\(80\)90042-4](https://doi.org/10.1016/0165-0270(80)90042-4). (Visited on 03/22/2021) (cited on page 7).
- [21] Guenter W. Gross, Ann N. Williams, and Jen H. Lucas. 'Recording of spontaneous activity with photoetched microelectrode surfaces from mouse spinal neurons in culture'. In: *Journal of Neuroscience Methods* 5.1 (Jan. 1, 1982), pp. 13–22. DOI: [10.1016/0165-0270\(82\)90046-2](https://doi.org/10.1016/0165-0270(82)90046-2). (Visited on 03/22/2021) (cited on pages 7, 8).
- [22] Johannes C. M. Schlachetzki et al. 'Studying neurodegenerative diseases in culture models'. In: *Brazilian Journal of Psychiatry* 35 (2013). Publisher: Associação Brasileira de Psiquiatria, S92–S100. DOI: [10.1590/1516-4446-2013-1159](https://doi.org/10.1590/1516-4446-2013-1159). (Visited on 03/26/2021) (cited on page 7).
- [23] M. A. Dichter. 'MODELS | The use of Cell Culture Models to Study Mechanisms Related to Epilepsy and Antiepileptic Drugs'. In: *Encyclopedia of Basic Epilepsy Research*. Ed. by Philip A. Schwartzkroin. Oxford: Academic Press, Jan. 1, 2009, pp. 808–814. DOI: [10.1016/B978-012373961-2.00322-2](https://doi.org/10.1016/B978-012373961-2.00322-2). (Visited on 03/25/2021) (cited on page 7).
- [24] Liqun Luo and Dennis D.M. O'Leary. 'Axon Retraction and Degeneration in Development and Disease'. In: *Annual Review of Neuroscience* 28.1 (2005). _eprint: <https://doi.org/10.1146/annurev.neuro.28.061604.135632>, pp. 127–156. DOI: [10.1146/annurev.neuro.28.061604.135632](https://doi.org/10.1146/annurev.neuro.28.061604.135632). (Visited on 03/25/2021) (cited on page 7).

- [25] Larry J. Millet et al. 'Guiding neuron development with planar surface gradients of substrate cues deposited using microfluidic devices'. In: *Lab on a Chip* 10.12 (2010). Publisher: Royal Society of Chemistry, pp. 1525–1535. DOI: [10.1039/C001552K](https://doi.org/10.1039/C001552K). (Visited on 03/22/2021) (cited on page 8).
- [26] Jean-Michel Peyrin et al. 'Axon diodes for the reconstruction of oriented neuronal networks in microfluidic chambers'. In: *Lab on a Chip* 11.21 (2011). Publisher: Royal Society of Chemistry, pp. 3663–3673. DOI: [10.1039/C1LC20014C](https://doi.org/10.1039/C1LC20014C). (Visited on 03/22/2021) (cited on page 8).
- [27] Bérange Déleglise et al. 'beta-amyloid induces a dying-back process and remote trans-synaptic alterations in a microfluidic-based reconstructed neuronal network'. In: *Acta Neuropathologica Communications* 2.1 (Sept. 25, 2014), p. 145. DOI: [10.1186/s40478-014-0145-3](https://doi.org/10.1186/s40478-014-0145-3). (Visited on 03/26/2021) (cited on page 8).
- [28] Bérange Déleglise et al. 'Synapto Protective Drugs Evaluation in Reconstructed Neuronal Network'. In: *PLOS ONE* 8.8 (Aug. 16, 2013). Publisher: Public Library of Science, e71103. DOI: [10.1371/journal.pone.0071103](https://doi.org/10.1371/journal.pone.0071103). (Visited on 03/26/2021) (cited on page 8).
- [29] Renaud Renault et al. 'Asymmetric axonal edge guidance: a new paradigm for building oriented neuronal networks'. In: *Lab on a Chip* 16.12 (2016), pp. 2188–2191. DOI: [10.1039/C6LC00479B](https://doi.org/10.1039/C6LC00479B). (Visited on 08/29/2019) (cited on page 8).
- [30] Csaba Forro et al. 'Electrophysiology Read-Out Tools for Brain-on-Chip Biotechnology'. In: *Micromachines* 12.2 (Feb. 2021). Number: 2 Publisher: Multidisciplinary Digital Publishing Institute, p. 124. DOI: [10.3390/mi12020124](https://doi.org/10.3390/mi12020124). (Visited on 03/26/2021) (cited on page 8).
- [31] Mirza Ali Mofazzal Jahromi et al. 'Microfluidic Brain-on-a-Chip: Perspectives for Mimicking Neural System Disorders'. In: *Molecular neurobiology* 56.12 (Dec. 2019), pp. 8489–8512. DOI: [10.1007/s12035-019-01653-2](https://doi.org/10.1007/s12035-019-01653-2). (Visited on 03/26/2021) (cited on page 8).
- [32] Daniel A. Wagenaar, Jerome Pine, and Steve M. Potter. 'An extremely rich repertoire of bursting patterns during the development of cortical cultures'. In: *BMC Neuroscience* 7.1 (Feb. 7, 2006), p. 11. DOI: [10.1186/1471-2202-7-11](https://doi.org/10.1186/1471-2202-7-11). (Visited on 04/07/2020) (cited on page 8).
- [33] Timothée Masquelier and Gustavo Deco. 'Network Bursting Dynamics in Excitatory Cortical Neuron Cultures Results from the Combination of Different Adaptive Mechanism'. In: *PLOS ONE* 8.10 (Oct. 11, 2013). Publisher: Public Library of Science, e75824. DOI: [10.1371/journal.pone.0075824](https://doi.org/10.1371/journal.pone.0075824). (Visited on 03/26/2021) (cited on pages 8, 9).
- [34] Samora Okujeni, Steffen Kandler, and Ulrich Egert. 'Mesoscale Architecture Shapes Initiation and Richness of Spontaneous Network Activity'. In: *The Journal of Neuroscience* 37.14 (Apr. 5, 2017), pp. 3972–3987. DOI: [10.1523/JNEUROSCI.2552-16.2017](https://doi.org/10.1523/JNEUROSCI.2552-16.2017). (Visited on 03/26/2021) (cited on page 8).
- [35] John M. Beggs and Dietmar Plenz. 'Neuronal Avalanches in Neocortical Circuits'. In: *The Journal of Neuroscience* 23.35 (Dec. 3, 2003), pp. 11167–11177. DOI: [10.1523/JNEUROSCI.23-35-11167.2003](https://doi.org/10.1523/JNEUROSCI.23-35-11167.2003). (Visited on 08/20/2018) (cited on pages 9, 10, 52).

- [36] J. M. Beggs. 'Neuronal Avalanches Are Diverse and Precise Activity Patterns That Are Stable for Many Hours in Cortical Slice Cultures'. In: *Journal of Neuroscience* 24.22 (June 2, 2004), pp. 5216–5229. DOI: [10.1523/JNEUROSCI.0540-04.2004](https://doi.org/10.1523/JNEUROSCI.0540-04.2004). (Visited on 08/20/2018) (cited on pages 9–12).
- [37] Dietmar Plenz and Tara C. Thiagarajan. 'The organizing principles of neuronal avalanches: cell assemblies in the cortex?' In: *Trends in Neurosciences* 30.3 (Mar. 2007), pp. 101–110. DOI: [10.1016/j.tins.2007.01.005](https://doi.org/10.1016/j.tins.2007.01.005). (Visited on 03/27/2021) (cited on pages 9, 10).
- [38] Per Bak and Chao Tang. 'Earthquakes as a self-organized critical phenomenon'. In: *Journal of Geophysical Research: Solid Earth* 94 (B11 Nov. 10, 1989), pp. 15635–15637. DOI: [10.1029/JB094iB11p15635](https://doi.org/10.1029/JB094iB11p15635). (Visited on 03/27/2021) (cited on page 9).
- [39] Marco Baiesi and Maya Paczuski. 'Scale-free networks of earthquakes and aftershocks'. In: *Physical Review E* 69.6 (June 2, 2004), p. 066106. DOI: [10.1103/PhysRevE.69.066106](https://doi.org/10.1103/PhysRevE.69.066106). (Visited on 03/27/2021) (cited on page 9).
- [40] Vidar Frette et al. 'Avalanche dynamics in a pile of rice'. In: *Nature* 379.6560 (Jan. 1996), pp. 49–52. DOI: [10.1038/379049a0](https://doi.org/10.1038/379049a0). (Visited on 03/27/2021) (cited on page 9).
- [41] V. Pasquale et al. 'Self-organization and neuronal avalanches in networks of dissociated cortical neurons'. In: *Neuroscience* 153.4 (June 2008), pp. 1354–1369. DOI: [10.1016/j.neuroscience.2008.03.050](https://doi.org/10.1016/j.neuroscience.2008.03.050). (Visited on 03/27/2021) (cited on page 10).
- [42] Mohammad Yaghoubi et al. 'Neuronal avalanche dynamics indicates different universality classes in neuronal cultures'. In: *Scientific Reports* 8.1 (Feb. 21, 2018), p. 3417. DOI: [10.1038/s41598-018-21730-1](https://doi.org/10.1038/s41598-018-21730-1). (Visited on 01/23/2019) (cited on pages 10, 52).
- [43] Janina Hesse and Thilo Gross. 'Self-organized criticality as a fundamental property of neural systems'. In: *Frontiers in Systems Neuroscience* 8 (2014). Publisher: Frontiers. DOI: [10.3389/fnsys.2014.00166](https://doi.org/10.3389/fnsys.2014.00166). (Visited on 05/11/2021) (cited on page 11).
- [44] Per Bak, Chao Tang, and Kurt Wiesenfeld. 'Self-organized criticality'. In: *Physical Review A* 38.1 (July 1, 1988), pp. 364–374. DOI: [10.1103/PhysRevA.38.364](https://doi.org/10.1103/PhysRevA.38.364). (Visited on 05/11/2021) (cited on page 11).
- [45] Jens Wilting et al. 'Operating in a Reverberating Regime Enables Rapid Tuning of Network States to Task Requirements'. In: *Frontiers in Systems Neuroscience* 12 (Nov. 6, 2018). DOI: [10.3389/fnsys.2018.00055](https://doi.org/10.3389/fnsys.2018.00055). (Visited on 02/15/2019) (cited on page 11).
- [46] Roxana Zeraati, Viola Priesemann, and Anna Levina. 'Self-organization toward criticality by synaptic plasticity'. In: *Frontiers in Physics* 9 (Apr. 22, 2021), p. 619661. DOI: [10.3389/fphy.2021.619661](https://doi.org/10.3389/fphy.2021.619661). (Visited on 05/11/2021) (cited on page 11).
- [47] Osame Kinouchi and Mauro Copelli. 'Optimal Dynamical Range of Excitable Networks at Criticality'. In: *Nature Physics* 2.5 (May 2006), pp. 348–351. DOI: [10.1038/nphys289](https://doi.org/10.1038/nphys289). (Visited on 05/11/2021) (cited on page 11).
- [48] John M Beggs. 'The criticality hypothesis: how local cortical networks might optimize information processing'. In: *Philosophical Transactions of the Royal Society A: Mathematical, Physical and Engineering Sciences* 366.1864 (Feb. 13, 2008), pp. 329–343. DOI: [10.1098/rsta.2007.2092](https://doi.org/10.1098/rsta.2007.2092). (Visited on 05/11/2021) (cited on page 11).

- [49] Javier G. Orlandi et al. 'Noise focusing and the emergence of coherent activity in neuronal cultures'. In: *Nature Physics* 9.9 (Sept. 2013), pp. 582–590. DOI: [10.1038/nphys2686](https://doi.org/10.1038/nphys2686). (Visited on 07/04/2018) (cited on pages 11, 12, 50, 51, 61, 76, 77, 115).
- [50] Davide Lonardoni et al. 'Recurrently connected and localized neuronal communities initiate coordinated spontaneous activity in neuronal networks'. In: *PLOS Computational Biology* 13.7 (July 27, 2017). Ed. by Francesco P. Battaglia, e1005672. DOI: [10.1371/journal.pcbi.1005672](https://doi.org/10.1371/journal.pcbi.1005672). (Visited on 07/04/2018) (cited on pages 12, 51, 52, 59, 61, 64, 70, 71).
- [51] M. Gandolfo et al. 'Tracking burst patterns in hippocampal cultures with high-density CMOS-MEAs'. In: *Journal of Neural Engineering* 7.5 (Aug. 2010), p. 056001. DOI: [10.1088/1741-2560/7/5/056001](https://doi.org/10.1088/1741-2560/7/5/056001). (Visited on 09/04/2019) (cited on page 12).
- [52] Danny Eytan and Shimon Marom. 'Dynamics and Effective Topology Underlying Synchronization in Networks of Cortical Neurons'. In: *Journal of Neuroscience* 26.33 (Aug. 16, 2006), pp. 8465–8476. DOI: [10.1523/JNEUROSCI.1627-06.2006](https://doi.org/10.1523/JNEUROSCI.1627-06.2006). (Visited on 09/04/2019) (cited on pages 12, 17, 20, 51, 52, 59, 68).
- [53] Yuji Ikegaya et al. 'Synfire Chains and Cortical Songs: Temporal Modules of Cortical Activity'. In: *Science* 304.5670 (Apr. 23, 2004). Publisher: American Association for the Advancement of Science Section: Research Article, pp. 559–564. DOI: [10.1126/science.1093173](https://doi.org/10.1126/science.1093173). (Visited on 03/30/2021) (cited on page 12).
- [54] J-P Eckmann et al. 'Leader neurons in population bursts of 2D living neural networks'. In: *New Journal of Physics* 10.1 (Jan. 31, 2008), p. 015011. DOI: [10.1088/1367-2630/10/1/015011](https://doi.org/10.1088/1367-2630/10/1/015011). (Visited on 07/04/2018) (cited on pages 12, 51, 52, 66, 68, 72).
- [55] Cyrille Zbinden. 'Leader neurons in living neural networks and in leaky integrate and fire neuron models'. PhD thesis. 2010. (Visited on 07/04/2018) (cited on page 12).
- [56] Marie B. Feller. 'Spontaneous Correlated Activity in Developing Neural Circuits'. In: 22 2 (1999), pp. 653–656 (cited on page 13).
- [57] Aaron G. Blankenship and Marla B. Feller. 'Mechanisms underlying spontaneous patterned activity in developing neural circuits'. In: *Nature reviews. Neuroscience* 11.1 (Jan. 2010), pp. 18–29. DOI: [10.1038/nrn2759](https://doi.org/10.1038/nrn2759). (Visited on 01/17/2019) (cited on pages 13, 16, 17).
- [58] Ege T. Kavalali. 'The mechanisms and functions of spontaneous neurotransmitter release'. In: *Nature Reviews Neuroscience* 16.1 (Jan. 2015), pp. 5–16. DOI: [10.1038/nrn3875](https://doi.org/10.1038/nrn3875). (Visited on 03/31/2021) (cited on page 13).
- [59] Pascal S. Kaeser and Wade G. Regehr. 'Molecular Mechanisms for Synchronous, Asynchronous, and Spontaneous Neurotransmitter Release'. In: *Annual review of physiology* 76 (2014), pp. 333–363. DOI: [10.1146/annurev-physiol-021113-170338](https://doi.org/10.1146/annurev-physiol-021113-170338). (Visited on 03/31/2021) (cited on page 13).
- [60] D. A. Sibarov and S. M. Antonov. 'Characteristics of Postsynaptic Currents in Primary Cultures of Rat Cerebral Cortical Neurons'. In: *Neuroscience and Behavioral Physiology* 45.4 (May 2015), pp. 431–439. DOI: [10.1007/s11055-015-0093-9](https://doi.org/10.1007/s11055-015-0093-9). (Visited on 03/31/2021) (cited on page 13).

- [61] Joel C. Miller. 'Equivalence of several generalized percolation models on networks'. In: *Physical Review E* 94.3 (Sept. 19, 2016), p. 032313. DOI: [10.1103/PhysRevE.94.032313](https://doi.org/10.1103/PhysRevE.94.032313). (Visited on 04/17/2020) (cited on page 13).
- [62] Eugene M. Izhikevich. *Dynamical systems in neuroscience: the geometry of excitability and bursting*. Computational neuroscience. OCLC: ocm65400606. Cambridge, Mass: MIT Press, 2007. 441 pp. (cited on pages 14, 62).
- [63] G. J. Baxter et al. 'Bootstrap percolation on complex networks'. In: *Physical Review E* 82.1 (July 1, 2010), p. 011103. DOI: [10.1103/PhysRevE.82.011103](https://doi.org/10.1103/PhysRevE.82.011103). (Visited on 04/30/2020) (cited on pages 14, 15).
- [64] Hamed Amini. 'Bootstrap Percolation in Living Neural Networks'. In: *Journal of Statistical Physics* 141.3 (Nov. 2010), pp. 459–475. DOI: [10.1007/s10955-010-0056-z](https://doi.org/10.1007/s10955-010-0056-z). (Visited on 05/14/2020) (cited on page 14).
- [65] Prabodh Shukla. 'Dynamics of bootstrap percolation'. In: *Pramana* 71.2 (Aug. 2008), pp. 319–329. DOI: [10.1007/s12043-008-0165-2](https://doi.org/10.1007/s12043-008-0165-2). (Visited on 05/04/2020) (cited on page 15).
- [66] Ilan Breskin. 'Connectivity in living neural networks'. PhD thesis. 2006. (Visited on 04/16/2020) (cited on pages 15, 19, 20).
- [67] Jean-Pierre Eckmann et al. 'The physics of living neural networks'. In: *Physics Reports. Nonequilibrium physics: From complex fluids to biological systems III. Living systems* 449.1 (Sept. 1, 2007), pp. 54–76. DOI: [10.1016/j.physrep.2007.02.014](https://doi.org/10.1016/j.physrep.2007.02.014). (Visited on 05/23/2019) (cited on page 15).
- [68] Jordi Soriano et al. 'Development of input connections in neural cultures'. In: *Proceedings of the National Academy of Sciences* 105.37 (Sept. 16, 2008), pp. 13758–13763. DOI: [10.1073/pnas.0707492105](https://doi.org/10.1073/pnas.0707492105). (Visited on 08/06/2019) (cited on pages 16, 19, 20).
- [69] S. Tazerart, L. Vinay, and F. Brocard. 'The Persistent Sodium Current Generates Pacemaker Activities in the Central Pattern Generator for Locomotion and Regulates the Locomotor Rhythm'. In: *Journal of Neuroscience* 28.34 (Aug. 20, 2008), pp. 8577–8589. DOI: [10.1523/JNEUROSCI.1437-08.2008](https://doi.org/10.1523/JNEUROSCI.1437-08.2008). (Visited on 02/01/2019) (cited on pages 16, 53, 54).
- [70] Sampsa T. Sipilä et al. 'Intrinsic bursting of immature CA3 pyramidal neurons and consequent giant depolarizing potentials are driven by a persistent Na⁺ current and terminated by a slow Ca²⁺-activated K⁺ current'. In: *European Journal of Neuroscience* 23.9 (2006). eprint: <https://onlinelibrary.wiley.com/doi/pdf/10.1111/j.1460-9568.2006.04757.x>, pp. 2330–2338. DOI: [10.1111/j.1460-9568.2006.04757.x](https://doi.org/10.1111/j.1460-9568.2006.04757.x). (Visited on 06/03/2020) (cited on pages 16, 53, 54).
- [71] Yaron Penn, Menahem Segal, and Elisha Moses. 'Network synchronization in hippocampal neurons'. In: *Proceedings of the National Academy of Sciences* 113.12 (Mar. 22, 2016), pp. 3341–3346. DOI: [10.1073/pnas.1515105113](https://doi.org/10.1073/pnas.1515105113). (Visited on 07/04/2018) (cited on pages 17, 51, 53, 73, 76).
- [72] Tanguy Fardet. 'Growth and activity of neuronal cultures'. PhD thesis. Paris: Paris Diderot, Sept. 18, 2018 (cited on pages 17, 21, 54).

- [73] Romain Brette and Wulfram Gerstner. ‘Adaptive Exponential Integrate-and-Fire Model as an Effective Description of Neuronal Activity’. In: *Journal of Neurophysiology* 94.5 (Nov. 1, 2005), pp. 3637–3642. DOI: [10.1152/jn.00686.2005](https://doi.org/10.1152/jn.00686.2005). (Visited on 07/04/2018) (cited on pages 17, 53, 73).
- [74] N. D. Mermin and H. Wagner. ‘Absence of Ferromagnetism or Antiferromagnetism in One- or Two-Dimensional Isotropic Heisenberg Models’. In: *Physical Review Letters* 17.22 (Nov. 28, 1966), pp. 1133–1136. DOI: [10.1103/PhysRevLett.17.1133](https://doi.org/10.1103/PhysRevLett.17.1133). (Visited on 03/30/2021) (cited on page 17).
- [75] Jean-Pierre Eckmann. ‘Leaders of neuronal cultures in a quorum percolation model’. In: *Frontiers in Computational Neuroscience* 4 (2010). DOI: [10.3389/fncom.2010.00132](https://doi.org/10.3389/fncom.2010.00132). (Visited on 07/04/2018) (cited on page 19).
- [76] Renaud Renault et al. ‘Effective non-universality of the quorum percolation model on directed graphs with Gaussian in-degree’. In: *Physica A: Statistical Mechanics and its Applications* 414 (Nov. 2014), pp. 352–359. DOI: [10.1016/j.physa.2014.07.028](https://doi.org/10.1016/j.physa.2014.07.028). (Visited on 05/12/2020) (cited on page 20).
- [77] Tanguy Fardet et al. ‘Effects of inhibitory neurons on the quorum percolation model and dynamical extension with the Brette–Gerstner model’. In: *Physica A: Statistical Mechanics and its Applications* 499 (June 1, 2018), pp. 98–109. DOI: [10.1016/j.physa.2018.02.002](https://doi.org/10.1016/j.physa.2018.02.002). (Visited on 05/12/2020) (cited on page 20).
- [78] Renaud Renault, Pascal Monceau, and Samuel Bottani. ‘Memory decay and loss of criticality in quorum percolation’. In: *Physical Review E* 88.6 (Dec. 20, 2013), p. 062134. DOI: [10.1103/PhysRevE.88.062134](https://doi.org/10.1103/PhysRevE.88.062134). (Visited on 05/04/2020) (cited on page 20).
- [79] Jérémie Barral and Alex D Reyes. ‘Synaptic scaling rule preserves excitatory–inhibitory balance and salient neuronal network dynamics’. In: *Nature Neuroscience* 19.12 (Dec. 2016), pp. 1690–1696. DOI: [10.1038/nn.4415](https://doi.org/10.1038/nn.4415). (Visited on 07/04/2018) (cited on pages 21, 76, 108).
- [80] Jian Gao, Tao Zhou, and Yanqing Hu. ‘Bootstrap percolation on spatial networks’. In: *Scientific Reports* 5.1 (Oct. 1, 2015). Number: 1 Publisher: Nature Publishing Group, p. 14662. DOI: [10.1038/srep14662](https://doi.org/10.1038/srep14662). (Visited on 05/19/2020) (cited on page 25).
- [81] David G. Kendall. ‘Branching Processes Since 1873’. In: *Journal of the London Mathematical Society* s1-41.1 (1966). _eprint: <https://londmathsoc.onlinelibrary.wiley.com/doi/pdf/10.1112/jlms/s1-41.1.385>, pp. 385–406. DOI: <https://doi.org/10.1112/jlms/s1-41.1.385>. (Visited on 04/20/2021) (cited on page 30).
- [82] Francis Galton. ‘Problem 4001’. In: *Educational Times* (1873), p. 17 (cited on page 30).
- [83] Linda J. S. Allen. *An Introduction to Stochastic Processes with Applications to Biology*. 0th ed. Chapman and Hall/CRC, Dec. 2, 2010. (Visited on 05/12/2021) (cited on page 31).
- [84] Martin Ester, Hans-Peter Kriegel, and Xiaowei Xu. ‘A Density-Based Algorithm for Discovering Clusters in Large Spatial Databases with Noise’. In: *Kdd* 96.34 (1996), p. 6 (cited on pages 44, 61).

- [85] Mallory Dazza et al. 'A novel methodology to describe neuronal networks activity reveals spatiotemporal recruitment dynamics of synchronous bursting states'. In: *Journal of Computational Neuroscience* (Apr. 27, 2021). DOI: [10.1007/s10827-021-00786-5](https://doi.org/10.1007/s10827-021-00786-5). (Visited on 05/12/2021) (cited on page 49).
- [86] Simona Olmi et al. 'Controlling seizure propagation in large-scale brain networks'. In: *PLOS Computational Biology* 15.2 (Feb. 25, 2019), e1006805. DOI: [10.1371/journal.pcbi.1006805](https://doi.org/10.1371/journal.pcbi.1006805). (Visited on 07/23/2019) (cited on page 50).
- [87] Marcello Massimini et al. 'The Sleep Slow Oscillation as a Traveling Wave'. In: *Journal of Neuroscience* 24.31 (Aug. 4, 2004), pp. 6862–6870. DOI: [10.1523/JNEUROSCI.1318-04.2004](https://doi.org/10.1523/JNEUROSCI.1318-04.2004). (Visited on 07/23/2019) (cited on pages 50, 51).
- [88] Alexander Paraskevov and Dmitry Zendrikov. 'A spatially resolved network spike in model neuronal cultures reveals nucleation centers, circular traveling waves and drifting spiral waves'. In: *bioRxiv* (Mar. 23, 2017). DOI: [10.1101/073981](https://doi.org/10.1101/073981). (Visited on 01/17/2019) (cited on pages 50–52, 61, 65, 70).
- [89] Christoph Kirst, Marc Timme, and Demian Battaglia. 'Dynamic information routing in complex networks'. In: *Nature Communications* 7 (Apr. 12, 2016), p. 11061. DOI: [10.1038/ncomms11061](https://doi.org/10.1038/ncomms11061). (Visited on 08/28/2019) (cited on page 50).
- [90] Maria V. Sanchez-Vives, Marcello Massimini, and Maurizio Mattia. 'Shaping the Default Activity Pattern of the Cortical Network'. In: *Neuron* 94.5 (June 7, 2017), pp. 993–1001. DOI: [10.1016/j.neuron.2017.05.015](https://doi.org/10.1016/j.neuron.2017.05.015). (Visited on 07/23/2019) (cited on page 50).
- [91] M. V. Sanchez-Vives. 'Slow wave activity as the default mode of the cerebral cortex'. In: *Archives Italiennes de Biologie* 497.23 (2015), pp. 69–73. DOI: [10.12871/000298292014239](https://doi.org/10.12871/000298292014239). (Visited on 08/28/2019) (cited on page 50).
- [92] Renaud Renault et al. 'Combining Microfluidics, Optogenetics and Calcium Imaging to Study Neuronal Communication In Vitro'. In: *PLOS ONE* 10.4 (Apr. 22, 2015), e0120680. DOI: [10.1371/journal.pone.0120680](https://doi.org/10.1371/journal.pone.0120680). (Visited on 08/29/2019) (cited on page 50).
- [93] Hideaki Yamamoto et al. 'Impact of modular organization on dynamical richness in cortical networks'. In: *Science Advances* 4.11 (Nov. 1, 2018), eaau4914. DOI: [10.1126/sciadv.aau4914](https://doi.org/10.1126/sciadv.aau4914). (Visited on 08/29/2019) (cited on pages 50, 51).
- [94] Elisenda Tibau et al. 'Neuronal spatial arrangement shapes effective connectivity traits of in vitro cortical networks'. In: *IEEE Transactions on Network Science and Engineering* (2018), pp. 1–1. DOI: [10.1109/TNSE.2018.2862919](https://doi.org/10.1109/TNSE.2018.2862919) (cited on page 50).
- [95] Maria V. Sanchez-Vives and David A. McCormick. 'Cellular and network mechanisms of rhythmic recurrent activity in neocortex'. In: *Nature Neuroscience* 3.10 (Oct. 2000), pp. 1027–1034. DOI: [10.1038/79848](https://doi.org/10.1038/79848). (Visited on 07/23/2019) (cited on page 50).
- [96] M. Derchansky et al. 'Transition to seizures in the isolated immature mouse hippocampus: a switch from dominant phasic inhibition to dominant phasic excitation'. In: *The Journal of Physiology* 586.2 (2008), pp. 477–494. DOI: [10.1113/jphysiol.2007.143065](https://doi.org/10.1113/jphysiol.2007.143065). (Visited on 01/17/2019) (cited on page 50).

- [97] David A McCormick and Diego Contreras. 'On The Cellular and Network Bases of Epileptic Seizures'. In: *Annual Review of Physiology* 63.1 (2001), pp. 815–846. DOI: [10.1146/annurev.physiol.63.1.815](https://doi.org/10.1146/annurev.physiol.63.1.815). (Visited on 01/17/2019) (cited on pages 50, 51).
- [98] Alessandro Maccione et al. 'Following the ontogeny of retinal waves: pan-retinal recordings of population dynamics in the neonatal mouse: Pan-retinal high-density retinal wave recordings'. In: *The Journal of Physiology* 592.7 (Apr. 1, 2014), pp. 1545–1563. DOI: [10.1113/jphysiol.2013.262840](https://doi.org/10.1113/jphysiol.2013.262840). (Visited on 08/20/2018) (cited on page 51).
- [99] Lyle Muller and Alain Destexhe. 'Propagating waves in thalamus, cortex and the thalamocortical system: Experiments and models'. In: *Journal of Physiology-Paris* 106.5 (Sept. 2012), pp. 222–238. DOI: [10.1016/j.jphysparis.2012.06.005](https://doi.org/10.1016/j.jphysparis.2012.06.005). (Visited on 04/23/2019) (cited on page 51).
- [100] Taras A. Gritsun, Joost le Feber, and Wim L. C. Rutten. 'Growth Dynamics Explain the Development of Spatiotemporal Burst Activity of Young Cultured Neuronal Networks in Detail'. In: *PLoS ONE* 7.9 (Sept. 19, 2012). Ed. by Thomas Wennekers, e43352. DOI: [10.1371/journal.pone.0043352](https://doi.org/10.1371/journal.pone.0043352). (Visited on 07/04/2018) (cited on pages 51, 52).
- [101] L. L. Bologna et al. 'Low-frequency stimulation enhances burst activity in cortical cultures during development'. In: *Neuroscience* 165.3 (Feb. 3, 2010), pp. 692–704. DOI: [10.1016/j.neuroscience.2009.11.018](https://doi.org/10.1016/j.neuroscience.2009.11.018). (Visited on 09/04/2019) (cited on page 51).
- [102] J. Stegenga et al. 'Analysis of Cultured Neuronal Networks Using Intraburst Firing Characteristics'. In: *IEEE Transactions on Biomedical Engineering* 55.4 (Apr. 2008), pp. 1382–1390. DOI: [10.1109/TBME.2007.913987](https://doi.org/10.1109/TBME.2007.913987). (Visited on 01/17/2019) (cited on page 51).
- [103] Michela Chiappalone et al. 'Dissociated cortical networks show spontaneously correlated activity patterns during in vitro development'. In: *Brain Research* 1093.1 (June 6, 2006), pp. 41–53. DOI: [10.1016/j.brainres.2006.03.049](https://doi.org/10.1016/j.brainres.2006.03.049). (Visited on 09/04/2019) (cited on pages 51, 52).
- [104] Xiao-Jing Wang and György Buzsáki. 'Gamma Oscillation by Synaptic Inhibition in a Hippocampal Interneuronal Network Model'. In: *The Journal of Neuroscience* 16.20 (Oct. 15, 1996), pp. 6402–6413. DOI: [10.1523/JNEUROSCI.16-20-06402.1996](https://doi.org/10.1523/JNEUROSCI.16-20-06402.1996). (Visited on 09/03/2019) (cited on page 51).
- [105] Johannes Zierenberg, Jens Wilting, and Viola Priesemann. 'Homeostatic Plasticity and External Input Shape Neural Network Dynamics'. In: *Physical Review X* 8.3 (July 20, 2018). DOI: [10.1103/PhysRevX.8.031018](https://doi.org/10.1103/PhysRevX.8.031018). (Visited on 08/26/2018) (cited on page 52).
- [106] Anna Levina and Michael Herrmann. 'Dynamical Synapses Give Rise to a Power-Law Distribution of Neuronal Avalanches'. In: *Nature Physics* (2006), p. 8 (cited on pages 52, 76).

- [107] Zenas C. Chao et al. 'Effects of Random External Background Stimulation on Network Synaptic Stability After Tetanization: A Modeling Study'. In: *Neuroinformatics* 3.3 (2005), p. 263. DOI: [10.1385/NI:3:3:263](https://doi.org/10.1385/NI:3:3:263). (Visited on 09/05/2019) (cited on page 52).
- [108] Katsunori Kitano and Tomoki Fukai. 'Variability v.s. synchronicity of neuronal activity in local cortical network models with different wiring topologies'. In: *Journal of Computational Neuroscience* 23.2 (Aug. 22, 2007), pp. 237–250. DOI: [10.1007/s10827-007-0030-1](https://doi.org/10.1007/s10827-007-0030-1). (Visited on 09/03/2019) (cited on page 52).
- [109] Jonathan Touboul and Alain Destexhe. 'Power-law statistics and universal scaling in the absence of criticality'. In: *Physical Review E* 95.1 (Jan. 4, 2017), p. 012413. DOI: [10.1103/PhysRevE.95.012413](https://doi.org/10.1103/PhysRevE.95.012413) (cited on page 52).
- [110] Jonathan Touboul and Alain Destexhe. 'Can Power-Law Scaling and Neuronal Avalanches Arise from Stochastic Dynamics?' In: *PLoS ONE* (Jan. 8, 2010). DOI: [10.1371/journal.pone.0008982](https://doi.org/10.1371/journal.pone.0008982) (cited on page 52).
- [111] Alberto Mazzoni et al. 'On the Dynamics of the Spontaneous Activity in Neuronal Networks'. In: *PLOS ONE* 2.5 (May 9, 2007), e439. DOI: [10.1371/journal.pone.0000439](https://doi.org/10.1371/journal.pone.0000439). (Visited on 02/05/2019) (cited on page 52).
- [112] Ellese Cotterill et al. 'A comparison of computational methods for detecting bursts in neuronal spike trains and their application to human stem cell-derived neuronal networks'. In: *Journal of Neurophysiology* 116.2 (Aug. 2016), pp. 306–321. DOI: [10.1152/jn.00093.2016](https://doi.org/10.1152/jn.00093.2016). (Visited on 06/07/2019) (cited on page 52).
- [113] Peter Dayan and L. F. Abbott. *Theoretical Neuroscience Computational and Mathematical Modeling of Neural Systems*. The MIT Press. 2000 (cited on pages 53, 55, 59).
- [114] A. Draguhn et al. 'Electrical coupling underlies high-frequency oscillations in the hippocampus in vitro'. In: *Nature* 394.6689 (July 1998), pp. 189–192. DOI: [10.1038/28184](https://doi.org/10.1038/28184). (Visited on 06/03/2020) (cited on pages 53, 54).
- [115] N. Rouach et al. 'Carbenoxolone Blockade of Neuronal Network Activity in Culture is not Mediated by an Action on Gap Junctions'. In: *The Journal of Physiology* 553.3 (2003). eprint: <https://physoc.onlinelibrary.wiley.com/doi/pdf/10.1113/jphysiol.2003.053439>, pp. 729–745. DOI: [10.1113/jphysiol.2003.053439](https://doi.org/10.1113/jphysiol.2003.053439). (Visited on 06/03/2020) (cited on pages 53, 54).
- [116] David Tsai et al. 'A very large-scale microelectrode array for cellular-resolution electrophysiology'. In: *Nature Communications* 8.1 (Nov. 27, 2017), pp. 1–11. DOI: [10.1038/s41467-017-02009-x](https://doi.org/10.1038/s41467-017-02009-x). (Visited on 12/10/2019) (cited on page 55).
- [117] Benjamin F Grewe et al. 'High-speed in vivo calcium imaging reveals neuronal network activity with near-millisecond precision'. In: *Nature Methods* 7.5 (May 2010), pp. 399–405. DOI: [10.1038/nmeth.1453](https://doi.org/10.1038/nmeth.1453). (Visited on 12/10/2019) (cited on page 55).
- [118] Arkady Pikovsky, Michael Rosenblum, and Jurgen Kurths. *Synchronization: A universal concept in nonlinear sciences*. 2001 (cited on page 55).
- [119] Fabian Pedregosa et al. 'Scikit-learn: Machine Learning in Python'. In: *Journal of Machine Learning Research* (2011), p. 6 (cited on page 61).

- [120] Sergio Faci-Lázaro, Jordi Soriano, and Jesús Gómez-Gardeñes. ‘Impact of targeted attack on the spontaneous activity in spatial and biologically inspired neuronal networks’. In: *Chaos: An Interdisciplinary Journal of Nonlinear Science* 29.8 (Aug. 1, 2019). Publisher: American Institute of Physics, p. 083126. DOI: [10.1063/1.5099038](https://doi.org/10.1063/1.5099038). (Visited on 09/22/2020) (cited on page 66).
- [121] Silmathoron and twardet. *twardet/NNGT: NNGT 2.3.0: improved (undirected) analysis and plots*. Feb. 23, 2021. DOI: [10.5281/zenodo.4557791](https://doi.org/10.5281/zenodo.4557791). (Visited on 05/12/2021) (cited on page 73).
- [122] Marc-Oliver Gewaltig and Markus Diesmann. ‘NEST (NEural Simulation Tool)’. In: *Scholarpedia* 2.4 (Apr. 5, 2007), p. 1430. DOI: [10.4249/scholarpedia.1430](https://doi.org/10.4249/scholarpedia.1430). (Visited on 08/28/2019) (cited on page 73).
- [123] E.M. Izhikevich. ‘Simple model of spiking neurons’. In: *IEEE Transactions on Neural Networks* 14.6 (Nov. 2003), pp. 1569–1572. DOI: [10.1109/TNN.2003.820440](https://doi.org/10.1109/TNN.2003.820440). (Visited on 09/18/2019) (cited on pages 73, 77).
- [124] Richard Naud et al. ‘Firing patterns in the adaptive exponential integrate-and-fire model’. In: *Biological Cybernetics* 99.4 (Nov. 2008), pp. 335–347. DOI: [10.1007/s00422-008-0264-7](https://doi.org/10.1007/s00422-008-0264-7). (Visited on 07/04/2018) (cited on page 73).
- [125] A. Levina, J. M. Herrmann, and T. Geisel. ‘Dynamical synapses causing self-organized criticality in neural networks’. In: *Nature Physics* 3.12 (Dec. 2007), pp. 857–860. DOI: [10.1038/nphys758](https://doi.org/10.1038/nphys758). (Visited on 05/12/2021) (cited on pages 76, 77).
- [126] Mukeshwar Dhamala, Viktor K. Jirsa, and Mingzhou Ding. ‘Transitions to Synchrony in Coupled Bursting Neurons’. In: *Physical Review Letters* 92.2 (Jan. 15, 2004), p. 028101. DOI: [10.1103/PhysRevLett.92.028101](https://doi.org/10.1103/PhysRevLett.92.028101). (Visited on 01/30/2019) (cited on page 76).
- [127] Misha Tsodyks, Asher Uziel, and Henry Markram. ‘Synchrony Generation in Recurrent Networks with Frequency-Dependent Synapses’. In: *Journal of Neuroscience* 20 (2000), p. 5 (cited on page 77).
- [128] Gabriele Baj et al. ‘Developmental and maintenance defects in Rett syndrome neurons identified by a new mouse staging system in vitro’. In: *Frontiers in Cellular Neuroscience* 8 (2014). Publisher: Frontiers. DOI: [10.3389/fncel.2014.00018](https://doi.org/10.3389/fncel.2014.00018). (Visited on 05/25/2021) (cited on pages 86, 87).
- [129] Carlos G Dotti, Christopher A Sullivan, and Gary A Banker. ‘The Establishment of Polarity by Hippocampal Neurons in Culture’. In: *The Journal of Neuroscience* (1988), p. 16 (cited on page 87).
- [130] Alfredo Cáceres, Bing Ye, and Carlos G. Dotti. ‘Neuronal Polarity: Demarcation, growth and commitment’. In: *Current opinion in cell biology* 24.4 (Aug. 2012), pp. 547–553. DOI: [10.1016/j.ceb.2012.05.011](https://doi.org/10.1016/j.ceb.2012.05.011). (Visited on 05/25/2021) (cited on page 87).
- [131] Stefanie Kaeck and Gary Banker. ‘Culturing hippocampal neurons’. In: *Nature Protocols* 1.5 (Dec. 2006), pp. 2406–2415. DOI: [10.1038/nprot.2006.356](https://doi.org/10.1038/nprot.2006.356). (Visited on 05/25/2021) (cited on page 87).

- [132] TI Fletcher, P De Camilli, and G Banker. 'Synaptogenesis in hippocampal cultures: evidence indicating that axons and dendrites become competent to form synapses at different stages of neuronal development'. In: *The Journal of Neuroscience* 14.11 (Nov. 1, 1994), pp. 6695–6706. DOI: [10.1523/JNEUROSCI.14-11-06695.1994](https://doi.org/10.1523/JNEUROSCI.14-11-06695.1994). (Visited on 01/07/2019) (cited on page 87).
- [133] Karunesh Ganguly et al. 'GABA Itself Promotes the Developmental Switch of Neuronal GABAergic Responses from Excitation to Inhibition'. In: *Cell* 105.4 (May 18, 2001), pp. 521–532. DOI: [10.1016/S0092-8674\(01\)00341-5](https://doi.org/10.1016/S0092-8674(01)00341-5). (Visited on 02/05/2019) (cited on page 88).
- [134] Joshua A Harrill et al. 'Ontogeny of biochemical, morphological and functional parameters of synaptogenesis in primary cultures of rat hippocampal and cortical neurons'. In: *Molecular Brain* 8.1 (2015), p. 10. DOI: [10.1186/s13041-015-0099-9](https://doi.org/10.1186/s13041-015-0099-9). (Visited on 05/20/2021) (cited on page 88).
- [135] Cecilia Conde and Alfredo Cáceres. 'Microtubule assembly, organization and dynamics in axons and dendrites'. In: *Nature Reviews Neuroscience* 10.5 (May 2009). Number: 5 Publisher: Nature Publishing Group, pp. 319–332. DOI: [10.1038/nrn2631](https://doi.org/10.1038/nrn2631). (Visited on 05/25/2021) (cited on page 88).
- [136] Charlotte H. Coles and Frank Bradke. 'Coordinating Neuronal Actin–Microtubule Dynamics'. In: *Current Biology* 25.15 (Aug. 3, 2015). Publisher: Elsevier, R677–R691. DOI: [10.1016/j.cub.2015.06.020](https://doi.org/10.1016/j.cub.2015.06.020). (Visited on 05/25/2021) (cited on page 88).
- [137] Kenneth B. Buck and James Q. Zheng. 'Growth Cone Turning Induced by Direct Local Modification of Microtubule Dynamics'. In: *The Journal of Neuroscience* 22.21 (Nov. 1, 2002), pp. 9358–9367. DOI: [10.1523/JNEUROSCI.22-21-09358.2002](https://doi.org/10.1523/JNEUROSCI.22-21-09358.2002). (Visited on 05/25/2021) (cited on page 88).
- [138] Riley Kellermeyer et al. 'The Role of Apoptotic Signaling in Axon Guidance'. In: *Journal of Developmental Biology* 6.4 (Dec. 2018). Number: 4 Publisher: Multidisciplinary Digital Publishing Institute, p. 24. DOI: [10.3390/jdb6040024](https://doi.org/10.3390/jdb6040024). (Visited on 05/25/2021) (cited on page 88).
- [139] Randal A. Koene et al. 'NETMORPH: A Framework for the Stochastic Generation of Large Scale Neuronal Networks With Realistic Neuron Morphologies'. In: *Neuroinformatics* 7.3 (Sept. 1, 2009), pp. 195–210. DOI: [10.1007/s12021-009-9052-3](https://doi.org/10.1007/s12021-009-9052-3). (Visited on 05/25/2021) (cited on page 88).
- [140] Susan M Maskery, Helen M Buettner, and Troy Shinbrot. 'Growth Cone Pathfinding: a competition between deterministic and stochastic events'. In: *BMC Neuroscience* 5.1 (2004), p. 22. DOI: [10.1186/1471-2202-5-22](https://doi.org/10.1186/1471-2202-5-22). (Visited on 05/25/2021) (cited on page 88).
- [141] Michael S. Smirnov et al. 'The effects of confinement on neuronal growth cone morphology and velocity'. In: *Biomaterials* 35.25 (Aug. 2014), pp. 6750–6757. DOI: [10.1016/j.biomaterials.2014.04.097](https://doi.org/10.1016/j.biomaterials.2014.04.097). (Visited on 05/21/2021) (cited on page 89).
- [142] Philipp Rauch et al. 'Forces from the rear: deformed microtubules in neuronal growth cones influence retrograde flow and advancement'. In: *New Journal of Physics* 15.1 (Jan. 18, 2013), p. 015007. DOI: [10.1088/1367-2630/15/1/015007](https://doi.org/10.1088/1367-2630/15/1/015007). (Visited on 05/04/2021) (cited on page 89).

- [143] A. P. Solon, M. E. Cates, and J. Tailleur. 'Active brownian particles and run-and-tumble particles: A comparative study'. In: *The European Physical Journal Special Topics* 224.7 (July 2015), pp. 1231–1262. DOI: [10.1140/epjst/e2015-02457-0](https://doi.org/10.1140/epjst/e2015-02457-0). (Visited on 05/06/2021) (cited on page 89).
- [144] F Gittes et al. 'Flexural rigidity of microtubules and actin filaments measured from thermal fluctuations in shape.' In: *Journal of Cell Biology* 120.4 (Feb. 15, 1993), pp. 923–934. DOI: [10.1083/jcb.120.4.923](https://doi.org/10.1083/jcb.120.4.923). (Visited on 05/04/2021) (cited on pages 89, 90).
- [145] Subra Suresh. 'Biomechanics and biophysics of cancer cells'. In: *Acta Biomaterialia* 3.4 (July 1, 2007), pp. 413–438. DOI: [10.1016/j.actbio.2007.04.002](https://doi.org/10.1016/j.actbio.2007.04.002). (Visited on 05/26/2021) (cited on page 89).
- [146] Waldemar Hällström et al. 'Fifteen-Piconewton Force Detection from Neural Growth Cones Using Nanowire Arrays'. In: *Nano Letters* 10.3 (Mar. 10, 2010), pp. 782–787. DOI: [10.1021/nl902675h](https://doi.org/10.1021/nl902675h). (Visited on 05/26/2021) (cited on page 89).
- [147] Jagannathan Rajagopalan, Alireza Tofangchi, and M. Taher A. Saif. 'Drosophila Neurons Actively Regulate Axonal Tension In Vivo'. In: *Biophysical Journal* 99.10 (Nov. 17, 2010), pp. 3208–3215. DOI: [10.1016/j.bpj.2010.09.029](https://doi.org/10.1016/j.bpj.2010.09.029). (Visited on 05/26/2021) (cited on page 89).
- [148] Lev Davidovitch Landau and Evgueni M Lifshitz. *Theory of Elasticity, Volume 7 of Course of Theoretical Physics*. 1959. (Visited on 05/07/2021) (cited on page 90).
- [149] Claudio Rivetti, Martin Guthold, and Carlos Bustamante. 'Scanning Force Microscopy of DNA Deposited onto Mica: Equilibration versus Kinetic Trapping Studied by Statistical Polymer Chain Analysis'. In: *Journal of Molecular Biology* 264.5 (Dec. 1996), pp. 919–932. DOI: [10.1006/jmbi.1996.0687](https://doi.org/10.1006/jmbi.1996.0687). (Visited on 05/06/2021) (cited on page 90).
- [150] J.A. Abels et al. 'Single-Molecule Measurements of the Persistence Length of Double-Stranded RNA'. In: *Biophysical Journal* 88.4 (Apr. 2005), pp. 2737–2744. DOI: [10.1529/biophysj.104.052811](https://doi.org/10.1529/biophysj.104.052811). (Visited on 05/06/2021) (cited on page 90).
- [151] Jonathon Howard. *Mechanics of Motor Proteins & the Cytoskeleton*. 2001 (cited on page 90).
- [152] Egor Dzyubenko et al. 'Colocalization of synapse marker proteins evaluated by STED-microscopy reveals patterns of neuronal synapse distribution in vitro'. In: *Journal of Neuroscience Methods* 273 (Nov. 2016), pp. 149–159. DOI: [10.1016/j.jneumeth.2016.09.001](https://doi.org/10.1016/j.jneumeth.2016.09.001). (Visited on 05/25/2021) (cited on page 91).
- [153] Audric Jan. 'Fasciculation axonale et dynamique du cône de croissance en environnement confiné'. PhD thesis. 2021 (cited on page 92).
- [154] Caterina Tomba. 'Primary brain cells in in vitro controlled microenvironments: single cell behaviors for collective functions'. In: (2014), p. 237 (cited on page 93).
- [155] Céline Braini. 'Approche biophysique des formes neuronales'. These de doctorat. Université Grenoble Alpes (ComUE), Dec. 16, 2016. (Visited on 04/28/2021) (cited on page 93).

- [156] Karine Loulier et al. 'Multiplex Cell and Lineage Tracking with Combinatorial Labels'. In: *Neuron* 81.3 (Feb. 5, 2014), pp. 505–520. DOI: [10.1016/j.neuron.2013.12.016](https://doi.org/10.1016/j.neuron.2013.12.016). (Visited on 04/29/2021) (cited on page 95).
- [157] Nathan C Shaner et al. 'Improved monomeric red, orange and yellow fluorescent proteins derived from *Discosoma* sp. red fluorescent protein'. In: *Nature Biotechnology* 22.12 (Dec. 2004), pp. 1567–1572. DOI: [10.1038/nbt1037](https://doi.org/10.1038/nbt1037). (Visited on 04/29/2021) (cited on page 95).
- [158] D. A. Zacharias. 'Partitioning of Lipid-Modified Monomeric GFPs into Membrane Microdomains of Live Cells'. In: *Science* 296.5569 (May 3, 2002), pp. 913–916. DOI: [10.1126/science.1068539](https://doi.org/10.1126/science.1068539). (Visited on 04/29/2021) (cited on page 95).
- [159] Mark A Rizzo et al. 'An improved cyan fluorescent protein variant useful for FRET'. In: *Nature Biotechnology* 22.4 (Apr. 2004), pp. 445–449. DOI: [10.1038/nbt945](https://doi.org/10.1038/nbt945). (Visited on 04/29/2021) (cited on page 95).
- [160] Joachim Goedhart et al. 'Structure-guided evolution of cyan fluorescent proteins towards a quantum yield of 93%'. In: *Nature Communications* 3.1 (Mar. 20, 2012). Number: 1 Publisher: Nature Publishing Group, p. 751. DOI: [10.1038/ncomms1738](https://doi.org/10.1038/ncomms1738). (Visited on 04/29/2021) (cited on page 95).
- [161] L. E. Bockstahler and P. Kaesberg. 'The Molecular Weight and Other Biophysical Properties of Bromegrass Mosaic Virus'. In: *Biophysical Journal* 2.1 (Jan. 1962), pp. 1–9. DOI: [10.1016/s0006-3495\(62\)86836-2](https://doi.org/10.1016/s0006-3495(62)86836-2) (cited on page 97).
- [162] Zhi Zhou et al. 'DeepNeuron: an open deep learning toolbox for neuron tracing'. In: *Brain Informatics* 5.2 (Dec. 2018), p. 3. DOI: [10.1186/s40708-018-0081-2](https://doi.org/10.1186/s40708-018-0081-2). (Visited on 05/03/2021) (cited on page 100).
- [163] E. Meijering et al. 'Design and validation of a tool for neurite tracing and analysis in fluorescence microscopy images'. In: *Cytometry* 58A.2 (Apr. 2004), pp. 167–176. DOI: [10.1002/cyto.a.20022](https://doi.org/10.1002/cyto.a.20022). (Visited on 05/03/2021) (cited on page 100).
- [164] T Y Zhang and C Y Suen. 'A fast parallel algorithm for thinning digital patterns'. In: 27.3 (1984), p. 4 (cited on page 100).
- [165] H. M. Buettner and R. N. Pittman. 'Quantitative effects of laminin concentration on neurite outgrowth in vitro'. In: *Developmental Biology* 145.2 (June 1, 1991), pp. 266–276. DOI: [10.1016/0012-1606\(91\)90125-M](https://doi.org/10.1016/0012-1606(91)90125-M). (Visited on 05/06/2021) (cited on page 104).
- [166] Petr G. Vikhorev, Natalia N. Vikhoreva, and Alf Månsson. 'Bending Flexibility of Actin Filaments during Motor-Induced Sliding'. In: *Biophysical Journal* 95.12 (Dec. 15, 2008), pp. 5809–5819. DOI: [10.1529/biophysj.108.140335](https://doi.org/10.1529/biophysj.108.140335). (Visited on 05/06/2021) (cited on page 104).
- [167] Thomas Duke, Timothy E. Holy, and Stanislas Leibler. "'Gliding Assays" for Motor Proteins: A Theoretical Analysis'. In: *Physical Review Letters* 74.2 (Jan. 9, 1995), pp. 330–333. DOI: [10.1103/PhysRevLett.74.330](https://doi.org/10.1103/PhysRevLett.74.330). (Visited on 05/06/2021) (cited on page 104).
- [168] Julius B Kirkegaard and Raymond E Goldstein. 'The role of tumbling frequency and persistence in optimal run-and-tumble chemotaxis'. In: *IMA Journal of Applied Mathematics* 83.4 (July 25, 2018), pp. 700–719. DOI: [10.1093/imamat/hxy013](https://doi.org/10.1093/imamat/hxy013). (Visited on 05/04/2021) (cited on page 104).

- [169] P. Cifra. 'Differences and limits in estimates of persistence length for semi-flexible macromolecules'. In: *Polymer* 45.17 (Aug. 5, 2004), pp. 5995–6002. DOI: [10.1016/j.polymer.2004.06.034](https://doi.org/10.1016/j.polymer.2004.06.034). (Visited on 05/21/2021) (cited on page 104).
- [170] P Dierckx. 'Algorithms for smoothing data with periodic and parametric splines'. In: *Computer Graphics and Image Processing* 20.2 (Oct. 1, 1982), pp. 171–184. DOI: [10.1016/0146-664X\(82\)90043-0](https://doi.org/10.1016/0146-664X(82)90043-0). (Visited on 05/07/2021) (cited on page 104).
- [171] Maureen L. Ruchhoeft and William A. Harris. 'Myosin functions in *Xenopus* retinal ganglion cell growth cone motility in vivo'. In: *Journal of Neurobiology* 32.6 (1997). _eprint: <https://onlinelibrary.wiley.com/doi/pdf/10.1002/%28SICI%291097-4695%2819970605%2932%3A6%3C567%3A%3AAID-NEU3%3E3.0.CO%3B2-Y,pp.567-578>. DOI: [https://doi.org/10.1002/\(SICI\)1097-4695\(19970605\)32:6<567::AID-NEU3>3.0.CO;2-Y](https://doi.org/10.1002/(SICI)1097-4695(19970605)32:6<567::AID-NEU3>3.0.CO;2-Y). (Visited on 05/21/2021) (cited on page 109).
- [172] E Tanaka, T Ho, and M W Kirschner. 'The role of microtubule dynamics in growth cone motility and axonal growth.' In: *Journal of Cell Biology* 128.1 (Jan. 1, 1995), pp. 139–155. DOI: [10.1083/jcb.128.1.139](https://doi.org/10.1083/jcb.128.1.139). (Visited on 05/21/2021) (cited on page 109).
- [173] P. Walicke et al. 'Fibroblast growth factor promotes survival of dissociated hippocampal neurons and enhances neurite extension.' In: *Proceedings of the National Academy of Sciences* 83.9 (May 1, 1986), pp. 3012–3016. DOI: [10.1073/pnas.83.9.3012](https://doi.org/10.1073/pnas.83.9.3012). (Visited on 05/25/2021) (cited on page 118).
- [174] Lisa A. Catapano et al. 'Specific Neurotrophic Factors Support the Survival of Cortical Projection Neurons at Distinct Stages of Development'. In: *The Journal of Neuroscience* 21.22 (Nov. 15, 2001), pp. 8863–8872. DOI: [10.1523/JNEUROSCI.21-22-08863.2001](https://doi.org/10.1523/JNEUROSCI.21-22-08863.2001). (Visited on 05/25/2021) (cited on page 118).
- [175] Larry J. Millet and Martha U. Gillette. 'New perspectives on neuronal development via microfluidic environments'. In: *Trends in neurosciences* 35.12 (Dec. 2012), pp. 752–761. DOI: [10.1016/j.tins.2012.09.001](https://doi.org/10.1016/j.tins.2012.09.001). (Visited on 05/25/2021) (cited on page 118).